

UCLA

UCLA Electronic Theses and Dissertations

Title

Spatial Control in Multi-Step, Multi-Catalyst Organometallic and Electrochemical Processes

Permalink

<https://escholarship.org/uc/item/8hs8n15z>

Author

Jolly, Brandon

Publication Date

2024

Peer reviewed|Thesis/dissertation

UNIVERSITY OF CALIFORNIA

Los Angeles

Spatial Control in Multi-Step, Multi-Catalyst
Organometallic and Electrochemical Processes

A dissertation submitted in partial satisfaction of the
requirements for the degree Doctor of Philosophy in Chemistry

by

Brandon Joseph Jolly

2024

© Copyright by
Brandon Joseph Jolly
2024

ABSTRACT OF THE DISSERTATION

Spatial Control in Multi-Step, Multi-Catalyst
Organometallic and Electrochemical Processes

by

Brandon Joseph Jolly

Doctor of Philosophy in Chemistry

University of California, Los Angeles, 2024

Professor Chong Liu, Chair

Multi-step processes, such as catalytic cycles, proceed through one or more intermediates that may participate in unwanted side reactions, leading to inefficiency and waste. Further, these intermediates may have a short shelf life and/or pose a safety concern. Thus, the development of methods to carry out multi-step processes to generate and utilize intermediates in one pass is of great desire. Biology manages its complex reaction network of multi-step, multi-enzyme processes by numerous means, namely spatial control via compartmentalization. By controlling where certain processes occur and the diffusion of key intermediates between reaction sites, biology efficiently carries out multiple concurrent reaction sequences efficiently with minimal competing pathways. For example, carboxysomes enhance the rate of CO₂ fixation by co-encapsulating

carbonic anhydrase and ribose 1,5-bisphosphate carboxylase-oxygenase while excluding deactivating oxygen (O_2). Inspired by spatial control in biology, my research seeks to adapt such methods of spatial control to construct efficient multi-step, multi-catalyst organometallic and electrochemical processes. In this manner, commodity chemicals can be produced from abundant feedstocks while obviating intermediate isolation and work up. Electrochemistry has emerged within the last few decades at the forefront of small molecule activation, particularly of environmental pollutants such as CO_2 , and organometallic chemistry is apt to further utilize products of electrochemical small molecule activation owing to decades of rich literature in homogeneous catalyst development. However, it is highly likely that catalyst - catalyst, catalyst - substrate, or substrate - substrate interference may impede the integration of multiple processes. Potential undesired interference may be circumvented by spatially separating while co-localizing the electro- and organometallic (or any type) catalysts in one reactor system allowing the transport of intermediates between them. The projects outlined below demonstrate the critical role spatial control and mass transport have in constructing efficient multi-step, multi-catalyst electro- and/or organometallic processes.

In the first research project (**Chapter 2**), we developed and applied a microkinetic model to extract design principles in compartmentalization of organometallic catalysis by a variety of micro- and nanostructures. Owing to fundamental understandings of compartmentalization in biology, the biocatalytic community has experimentally and theoretically studied *in vitro* confined enzyme cascades to develop efficient multi-enzyme pathways. However, the organometallic community has just recently begun to explore the positive impact spatial control via compartmentalization can have on transition metal catalysts. Additionally, no theoretical investigations that mathematically model confined organometallics have been reported, impeding

future development and optimization. Thus, we developed a mathematical model to study and predict under what set of kinetic and diffusive parameters would a particular compartment impart catalytic benefits to a multi-step organometallic process. An integral term in this work is called volumetric diffusive conductance (F_V), which describes a species' propensity for entry into and exit out of a particular compartment. From this work we derived that F_V should be tailored by tuning the confinement's surface area and volume to be equal to or less than the kinetics of the multi-step process. In this way, a compartment can competently retain intermediates along a reaction pathway to avoid counterproductive side reactions. This finding was verified by adapting our kinetic model to several experimentally confined organometallic systems.

Inspired by the work from **Chapter 2** in spatial control for multi-step processes, the research project outlined in **Chapter 3** seeks to spatially separate electrochemical CO₂ reduction (CO₂RR) to carbon monoxide (CO) and palladium (Pd) catalyzed CO and ethylene (C₂H₄) copolymerization to polyketone (PK) in collaboration with the Alex Miller lab from UNC Chapel Hill, and the Dunwei Wang lab at Boston College. The motivation for integrating these two catalytic processes via spatial control was to utilize CO₂ as a carbon source in polymer synthesis, obviate directly using toxic CO, and institute external control over polymer microstructure by tuning %CO incorporation electrochemically. Typical PK are alternating in nature (1:1 stoichiometry of CO:C₂H₄), which have high melt temperatures and are difficult to degrade. Much work has been devoted to catalyst development to produce non-alternating PK, which also requires variation in CO:C₂H₄ feed and temperature. The hypothesis for this effort is that by controlling the CO feed from CO₂RR to polyketone synthesis by varying applied current (i), we could prepare PK with a wide variety in %CO incorporation. To this end, PK with CO incorporation ranging from 4 - 50% were prepared using an appropriate non-alternating catalyst.

We next expanded on work from **Chapter 3** to integrate CO₂RR to hydroformylation for the preparation of aldehydes outlined in **Chapter 4**. A typical shortcoming of CO₂RR work is concomitant hydrogen evolution (HER). However, for hydroformylation, or put more broadly reactions using syngas (CO and H₂), simultaneous HER and CO production from CO₂RR would be desirable. In this work, we repurposed the typically unwanted HER in CO₂RR to fuel the rhodium (Rh) catalyzed hydroformylation of styrene with spatial co-localization and separation of the CO₂RR and hydroformylation components. Employing a typical Rh hydroformylation catalyst (HRh(CO)(PPh₃)₃ abbreviated as [Rh]), 97% aldehyde yield was obtained using a CO/H₂ feed from CO₂RR, with regioselectivity in line with prior reports for hydroformylation of styrene by [Rh]. Additionally, we synthesized and characterized a heterogenized version of [Rh] immobilized onto phosphine modified mesoporous silica (abbreviated as [Rh]/PPh₂/SiO₂) to allow catalyst recycling or to aid in future, more precise catalyst spatial control. [Rh]/PPh₂/SiO₂ demonstrated lowered observed catalytic activity, resulting in 43% aldehyde yield, likely due to changes in coordination environment and mass transport of substrates to heterogeneous Rh active sites. Nonetheless, this work, paired with work from **Chapter 3**, serves to expand the landscape of synthetic utility of CO₂ enabled by spatial control.

The final chapter of my dissertation (**Chapter 5**) aims to develop continuous flow amino acid cyclization to *N*-carboxyanhydrides (NCA) and ring opening polymerization (ROP) of NCAs as a step towards integrating the two to prepare polyamides from amino acids and CO₂. We targeted these two processes as ROP of NCAs liberates CO₂, and CO₂ could be recycled and utilized to synthesize NCAs from amino acids in an atom economical fashion. Further, we hypothesize spatial control of these two processes would allow for better control of monomer sequence compared with traditional NCA ROP. To integrate NCA synthesis and polymerization, we first developed

continuous flow systems for NCA synthesis and ROP separately, for later integration. In this manner, the two processes may be spatially separated in different flow reactors, where the products of one process may easily be funneled to the other via flow. Adapting conditions for NCA synthesis from amino acids and CO₂ developed by the Loi Do lab at the University of Houston, NCAs were prepared under flow conditions at moderate yields and greatly reduced CO₂ pressures compared to batch conditions. Additionally, employing a surface bound catalyst for NCA ROP developed by the Jeff Byers' lab at Boston College, NCA ROP was achieved at greatly accelerated rates compared to batch owing to enhanced mass transport by flow.

Throughout my graduate career, I have demonstrated how spatial control reminiscent of that developed by nature fosters the development of multi-step, multi-catalyst processes by allowing the efficient generation and utilization of key intermediates. A focal point of integrating chemical processes together is the mass transport between reaction sites, where judicious spatial control and continuous flow chemistry will be paramount. Such process integration has been demonstrated to lead to enhanced catalytic performance, as well as to develop new multi-step processes unattainable without spatial control.

This dissertation of Brandon Joseph Jolly is approved.

Paula Diaconescu

Alex Spokoyny

Ellen Sletten

Chong Liu, Committee Chair

University of California, Los Angeles

2024

DEDICATION

I dedicate this thesis to my family and friends: Mike and Nectar Jolly, my parents and extended family on both sides, Michael and Jenna Jolly, my brother and sister in law, The Phillips family, my in laws, Bernardo Guerrero, Blaine Baker, Dr. Patricia de la Torre, Valentino Perez, and Annalise Thompson, my college friends. Importantly, I thoroughly dedicate this thesis to Maggie and Alexan DerAlexanian, Carolyn and Joe Jolly, my maternal and paternal grandparents, all I do is done to make them proud or to smile down on me. Most importantly I dedicate this thesis to my wife and best friend, Cat Jolly. Thank you all for your incredible support, love, and friendship. None of this is possible without all of you, I love you all.

Table of Contents

Abstract of the Dissertation.....	ii
Table of Contents.....	ix
List of Figures.....	xii
List of Tables.....	xviii
Acknowledgements.....	xix
Vita.....	xxiii

Chapter 1. General Introduction.....	1
---	----------

Chapter 2. Developing a generalized kinetic model for compartmentalization of organometallic catalysis

Abstract.....	8
Introduction.....	9
Results and Discussion.....	13
Conclusion.....	29
References.....	31
Supplementary Information.....	38
Supplementary References.....	77

Chapter 3. Polyketones from carbon dioxide and ethylene by integrating electrochemical and organometallic catalysis

Abstract.....	79
---------------	----

Introduction.....	79
Results and Discussion.....	82
Conclusion.....	90
References.....	91
Supplementary Information.....	98
Supplementary References.....	149

Chapter 4. Integrated carbon dioxide reduction and hydroformylation

Abstract.....	151
Introduction.....	152
Results and Discussion.....	155
Conclusion.....	160
References.....	161
Supplementary Information.....	167
Supplementary References.....	179

Chapter 5. Continuous flow *N*-carboxyanhydride synthesis and polymerization

Abstract.....	180
Introduction.....	181
Results and Discussion.....	184
Conclusion.....	190
References.....	192
Supplementary Information.....	196

Supplementary References.....204

Chapter 6. Concluding Remarks.....205

List of Figures

Chapter 2. Developing a generalized kinetic model for compartmentalization of organometallic catalysis

Figure 2.1. Schematic of general compartmentalized and non-compartmentalized models.....	12
Figure 2.2. Plots of compartmentalized γ , R_I , and TOF as functions of rate constant k_2 and F_V compared to a non-compartmentalized system.....	20
Figure 2.3. Plots of compartmentalized γ , R_I , and TOF as functions of rate constant k_{e2} and F_V compared to a non-compartmentalized system.....	20
Figure S2.1. Compartmentalized rate of intermediate outflux (R_I) as a function of F_V and k_1 with first and second order ($m = 1, 2$) on initial catalyst concentration ($[Cat]$).....	68
Figure S2.2. Compartmentalized TOF as a function of F_V and k_1 for $m = 1$ and $m = 2$	69
Figure S2.3. Compartmentalized R_I as a function of F_V and k_2 or k_{e2} for $m = 2$	70
Figure S2.4. Compartmentalized TOF as a function of F_V and k_2 or k_{e2} for $m = 2$	71
Figure S2.5. Compartmentalized R_I and TOF as functions of F_V and k_2 for $m = 1$ under model $C_{Cat,total}$	72
Figure S2.6. Compartmentalized R_I and TOF as a function of F_V for $m = 1$ under model $C_{Cat,total}$	73
Figure S2.7. Comparison between compartmentalized and non-compartmentalized R_I and TOF as a function of k_2 for $m = 1$ under model $C_{Cat,total}$	74
Figure S2.8. Catalytic cycle for Fujiwari-Moritani palladium catalyzed olefin arylation operating in a tube-in-tube reactor.....	75
Figure S2.9. Catalytic cycle for Negishi palladium catalyzed cross couplings.....	76

Chapter 3. Polyketones from carbon dioxide and ethylene by integrating electrochemical and organometallic catalysis

Figure 3.1. Previous non-integrated polyketone synthesis reactions and our proposed electrochemical and organometallic integrated method.....	81
Figure 3.2. Synthesis of polyketones from CO ₂ and C ₂ H ₄ and varying %CO based on applied current.....	86
Figure 3.3. CO incorporation (%) and C-O stretching frequency as a function of the CO partial pressure.....	89
Figure S3.1. Photograph of high-pressure reactor fitted with electrochemical feedthroughs for integrated catalysis.....	102
Figure S3.2. Cyclic voltammograms of both Pd-PP and Pd-PP copolymerization catalysts.....	105
Figure S3.3. Analysis of high-pressure electrochemical carbon dioxide reduction (CO ₂) products carbon monoxide (CO) and dihydrogen (H ₂).....	107
Figure S3.4. Latimer diagram featuring the experimentally observed reduction potentials of Pd-PO and Pd-PP	107
Figure S3.5. GC-FIDm, GC-TCD, and potential vs. time trace from constant current electrolysis at 0.7 mA cm ⁻² for 24 h.....	108
Figure S3.6. ¹ H NMR spectrum of sample A from Table S3.2.....	114
Figure S3.7. ¹³ C{ ¹ H} NMR spectrum of sample A from Table S3.2.....	114
Figure S3.8. ¹ H NMR spectrum of sample B from Table S3.2.....	115
Figure S3.9. ¹³ C{ ¹ H} NMR spectrum of sample B from Table S3.2.....	115
Figure S3.10. ¹ H NMR spectrum of sample G from Table S3.2.....	116
Figure S3.11. ¹³ C{ ¹ H} NMR spectrum of sample A from Table S3.2.....	116

Figure S3.12. ^1H NMR spectrum of sample H from Table S3.2.....	116
Figure S3.13. $^{13}\text{C}\{^1\text{H}\}$ NMR spectrum of sample H from Table S3.2.....	116
Figure S3.14. ^1H NMR spectra of non-alternating polyketone sample N from Table S3.4 with variable %CO incorporation.....	119
Figure S3.15. ^1H NMR spectrum of sample K from Table S3.4.....	119
Figure S3.16. ^1H NMR spectrum of sample K from Table S3.4.....	120
Figure S3.17. ^1H NMR spectrum of sample M from Table S3.4.....	120
Figure S3.18. ^1H NMR spectrum of sample N from Table S3.4.....	121
Figure S3.19. ^1H NMR spectrum of sample O from Table S3.4.....	121
Figure S3.20. ^1H NMR spectrum of polyethylene from Table S3.3.....	122
Figure S3.21. ^1H NMR spectrum of <i>block</i> -polyethylene- <i>block</i> -alt-polyketone from Table S3.3....	122
Figure S3.22. ^1H NMR spectrum of a blend of polyethylene and alternating polyketone.....	123
Figure S3.23. Stack of ^1H NMR spectra of the various ethylene homopolymerization controls..	123
Figure S3.24. ATR-IR spectrum of sample K from Table S3.4.....	124
Figure S3.25. ATR-IR spectrum of sample M from Table S3.4.....	124
Figure S3.26. ATR-IR spectrum of sample O from Table S3.4.....	125
Figure S3.27. ^1H NMR spectrum of polyketone sample PO-1 from Table S3.5.....	130
Figure S3.28. $^{13}\text{C}\{^1\text{H}\}$ NMR spectrum of sample PO-1 from Table S3.5.....	130
Figure S3.29. ^1H NMR spectrum of polyketone sample PO-1 from Table S3.5.....	131
Figure S3.30. ^1H NMR spectrum of polyketone sample PO-2 from Table S3.5.....	131
Figure S3.31. ^1H NMR spectrum of polyketone sample PO-2 from Table S3.5.....	132
Figure S3.32. ^1H NMR spectrum of polyketone sample PO-3 from Table S3.5.....	132
Figure S3.33 $^{13}\text{C}\{^1\text{H}\}$ NMR spectrum of sample PO-3 from Table S3.5.....	133

Figure S3.34. ^1H NMR spectrum of polyketone sample PO-4 from Table S3.5.....	133
Figure S3.35. ^1H NMR spectrum of polyketone sample PO-5 from Table S3.5.....	134
Figure S3.36. ^1H NMR spectrum of polyketone sample PO-7 from Table S3.5.....	134
Figure S3.37. 2D DOSY NMR spectrum of polyketone sample PO-7 from Table S3.5.....	135
Figure S3.38. ^1H NMR spectrum of polyketone sample PO-9 from Table S3.5.....	135
Figure S3.39. 2D DOSY NMR spectrum of polyketone sample PO-9 from Table S3.5.....	136
Figure S3.40. ^1H NMR spectrum of polyketone sample PO-12 from Table S3.5.....	136
Figure S3.41. 2D DOSY NMR spectrum of polyketone sample PO-12 from Table S3.5.....	137
Figure S3.42. ^1H NMR spectrum of polyketone sample PP-2 from Table S3.5.....	137
Figure S3.43. ^1H NMR spectrum of polyketone sample PP-3 from Table S3.5.....	138
Figure S3.44. ^1H NMR spectrum of polyketone sample PP-7 from Table S3.5.....	138
Figure S3.45. $^{13}\text{C}\{^1\text{H}\}$ NMR spectrum of polyketone PP-7 from Table S3.5.....	139
Figure S3.46. ATR-IR spectrum of sample PO-1 from Table S3.5.....	140
Figure S3.47. ATR-IR spectrum of sample PO-3 from Table S3.5.....	140
Figure S3.48. ATR-IR spectrum of sample PO-7 from Table S3.5.....	141
Figure S3.49. ATR-IR spectrum of sample PO-9 from Table S3.5.....	141
Figure S3.50. ATR-IR spectrum of sample PO-12 from Table S3.5.....	142
Figure S3.51. ATR-IR spectrum of sample PO-13 from Table S3.5.....	142
Figure S3.52. ATR-IR spectrum of sample PP-1 from Table S3.5.....	143
Figure S3.53. ATR-IR spectrum of sample PP-2 from Table S3.5.....	143
Figure S3.54. ATR-IR spectrum of sample PP-3 from Table S3.5.....	144
Figure S3.55. ATR-IR spectrum of sample PP-4 from Table S3.5.....	144

Figure S3.56. SEC trace for sample PO-1 from Table S3.5.....	145
Figure S3.57. SEC trace for sample PO-2 from Table S3.5.....	145
Figure S3.58. SEC trace for sample PO-3 from Table S3.5.....	146
Figure S3.59. SEC trace for sample PO-4 from Table S3.5.....	146
Figure S3.60. SEC trace for sample PO-11 from Table S3.5.....	147
Figure S3.61. SEC trace for sample PO-13 from Table S3.5.....	147
Figure S3.62. SEC trace for sample PP-1 from Table S3.5.....	148
Figure S3.63. SEC trace for sample PP-2 from Table S3.5.....	148
 Chapter 4. Integrated carbon dioxide reduction and hydroformylation	
Figure 4.1. Integrated electrochemical CO ₂ reduction and hydroformylation.....	154
Scheme 4.1. Immobilization of HRh(CO)(PPh ₃) ₃ onto phosphine coated silica.....	156
Figure 4.2. Time course study of integrated electrochemical CO ₂ reduction and hydroformylation in a vial-in-vial reactor.....	159
Figure S4.1. ¹ H NMR of [Rh]/PPh ₂ /SiO ₂	172
Figure S4.2. ¹³ C NMR of [Rh]/PPh ₂ /SiO ₂	173
Figure S4.3. ³¹ P NMR of [Rh]/PPh ₂ /SiO ₂	174
Figure S4.4. ²⁹ Si NMR of [Rh]/PPh ₂ /SiO ₂	175
Figure S4.5. ATR-IR of [Rh]/PPh ₂ /SiO ₂	176
Figure S4.6. Chronopotentiometry traces from two separate experiments conducted at -0.5 mA cm ⁻² for 24 hours.....	177

Chapter 5. Continuous flow *N*-carboxyanhydride synthesis and polymerization

Figure 5.1. Targeted flow reactor scheme for integrated NCA synthesis and polymerization.....	182
Figure 5.2. Optimized conditions and percent yield for batch and flow synthesis of NCAs from amino acids with CO ₂	185
Figure 5.3. Reaction scheme of batch or flow SIP of sarcosine-NCA by a formal Fe(I) bisiminopyridine catalyst bound to a TiO ₂ coated FTO plate.....	187
Figure 5.4. Effect of varying residence time via flow rate on conversion and apparent rate constant k_f for a one pass NCA SIP.....	189
Figure S5.1. Alternate flow system configurations explored for flow <i>N</i> -benzylisatoic anhydride synthesis.....	198

List of Tables

Chapter 2. Developing a generalized kinetic model for compartmentalization of organometallic catalysis

Table S2.1. Expressions for compartmentalized and non-compartmentalized key reaction metrics.....65

Table S2.2. Expressions for compartmentalized and non-compartmentalized key reaction metrics for model $C_{Cat,total}$67

Chapter 3. Polyketones from carbon dioxide and ethylene by integrating electrochemical and organometallic catalysis

Table S3.1 Summary of CO₂ electrolysis experiments.....103

Table S3.2 Reaction outcomes and polymer characterization for CO/C₂H₄ copolymerization in 1,2-DCE at 25 °C.....112

Table S3.3 Compatibility testing and optimization of CO/C₂H₄ copolymerization.....118

Table S3.4 Temperature dependence of CO/C₂H₄ copolymerization by **Pd-PO**.....118

Table S3.5 Polyketone samples made from CO₂/C₂H₄ (using integrated catalysis).....127

Table S3.6 Integrated catalysis control experiments.....129

Chapter 4. Integrated carbon dioxide reduction and hydroformylation

Table S4.1. Experiments and controls in integrated electrochemical CO₂ reduction - hydroformylation.....170

Table S4.2. Integrated CO₂RR - hydroformylation time course study for both [Rh] and [Rh]/PPh₂/SiO₂.....171

Chapter 5. Continuous flow *N*-carboxyanhydride synthesis and polymerization

Table S5.1. Conditions and yields for flow NCA synthesis from a Custom DoE model.....199

Acknowledgements

First and foremost, I would like to thank my advisor and mentor Prof. Chong Liu for giving me the opportunity to conduct graduate research in his lab. I came into graduate school having prior experience in inorganic synthesis and photochemistry, a marginal overlap with Chong's research program in nanomaterials, microbiology, and electrochemistry. Nonetheless, he welcomed me into the lab and always worked with me to find projects which not only pertain to my background, but are also well interfaced with his interdisciplinary research program and my career interests in sustainable chemistry. He has provided invaluable mentorship, meticulously balancing both a hands off and hands on approach to give me the room to grow as a researcher, but also provide guidance wherever needed.

I would like to thank all members of the Chong Liu lab throughout my time in the lab for their support and guidance. Specifically, my thesis work would not have been possible if not for Dr. Ben Natinsky and Dr. Shuangning Xu and their guidance in everything research related, both in and out of lab. I would not have made it as far or have had the success I have had in graduate school without their influence. I also thank my fellow lab and cohort mates Yi Chen and Jingyu Wang for helping me out in lab whenever my research direction overlapped with their expertise. I am also forever grateful to my grad student friends outside of the Chong Liu lab at UCLA, as well as all UCLA Chemistry & Biochemistry staff from the graduate office, instrumentation staff, administrative personnel, shipping & receiving, maintenance, and janitorial. Together, they have all been integral in providing and maintaining my opportunity to conduct graduate research at UCLA. A big special thanks goes to Ricky Ruiz from shipping & receiving for making sure all our precious chemicals and supplies arrive timely and safely, and for knowing literally everyone's

names in the department. Another special thanks to the now CAO of the Earth, Planetary, and Space Sciences at UCLA Nick Baerg for his time as Student Services Manager in our department.

I thank all members of the National Science Foundation Center for Integrated Catalysis (NSF CIC). Being a part of this center was a monumental experience for me, getting to collaborate with great minds across the country on challenging problems taught me so much about different facets of chemistry I otherwise would likely not have been exposed to. I thank members of the following labs for their help in NSF CIC research projects: Prof Paula Diaconescu (UCLA), Prof Jeffery Byers and Prof Dunwei Wang (Boston College), Prof Alex Miller (UNC Chapel Hill), and Prof Loi Do (University of Houston).

I would not have even pursued a graduate level education if not for my time at Sonoma State University (SSU). I thank my advisor, Prof. Carmen Works, for giving me the opportunity to get my feet wet in chemical research. It is the work I did in her lab and the great mentorship she provided me that encouraged me and thoroughly prepared me to pursue graduate research. I'm forever grateful to everyone in Prof Works' lab, specifically Dr. Anne Nelson and Dr. Patricia de la Torre for their training and mentorship. I'd also like to thank Prof. Jon Fukuto who changed the way I view and think about problems in chemistry. I thank Prof. Monica Lares for her guidance both in my first, pivotal semester in college as well as throughout my undergraduate education. I would not have gotten through college if not for my classmates, specifically Annika Holm, Valeria Suarez, Bernardo Guerrero, Blaine Baker, Valentino Perez, Annalise Thompson, Nelson Wong, and so many others. I thank Cora Orme from the SSU Learning and Academic Resource Center for giving me the opportunity and thorough training to tutor throughout college, being a teaching assistant at UCLA was undoubtedly much easier in large part to Cora's mentorship in education. I

also thank my freshmen year roommate, and still friend to this day, Riley Lewis for always making me laugh and for always willing to jam to some old 70's rock.

I thank my family, of which I could produce a thesis length document of writing thanking them. I thank my uncle Dr. David Steenblock, for catching it early on that I had a knack for science and continuing to encourage me to pursue all that I have, and for the summer I spent tinkering with your lab equipment. I thank my mother's extended family, namely Noyemy Steenblock and Kevork DerAlexanian for always looking out for me (and for all the wonderful food throughout the years). I thank my paternal grandmother Carolyn Jolly for passing on her decades of experience and wisdom in education to me, which was proved invaluable in all of my teaching efforts, and for recruiting me to be a St. Louis Cardinals fan with her against the Cubs fans of the family. I thank my maternal grandmother Maggie DerAlexanian for her unconditional love, support, and outrageous sayings throughout my formative years, and for making it clear to everyone else I'm her favorite grandson. I thank my in laws, the Phillips family, specifically Denise, Greg, Greg II, Zach, and Kalie, for welcoming me with open arms into their family. Their support throughout the latter years of my graduate education have been paramount to my success and well being. I extend major gratitude to my brother and best friend since I was born, Michael "Jollerson" Jolly and his wife Jenna for always being there for me, supporting me in every way possible, and for always making me laugh.

I am beyond grateful in ways I cannot express through any combination of words for my parents, Mike and Nectar Jolly. I am very appreciative and lucky for my father's incredible work ethic for setting an example for me, and for ensuring my brother and I lived the best life we could. The countless 70+ hour weeks, or working over the weekends to support us have been a blessing, and I hope to reach a point in my career where I can give back to him and allow him (against his

will) to take some time off of work. Additionally, I could not have done all I have without my mother working 24/7 since I was born to raise me and my brother. It is undoubtedly the hardest job on the planet, and Michael and I are forever grateful for all she has done to make us who we are. All that I am capable of accomplishing is in one way or another very much attributed to their mentorship and guidance through the trials and tribulations of life. My accomplishments can additionally be ascribed to them forcing us to learn classical piano at a young age, sorry for ever resisting that, it is much appreciated. Though my name appears on the dissertation, and it will appear on my doctoral degree, it is equally as much their work as it is mine.

Lastly, I thank my wife, best friend, and business/marketing master turned amateur chemist, Cat Jolly. I cannot thank you enough for constantly supporting me, dealing with how annoying and cynical I get when there's incorrect science in a movie or TV show, for putting up with my erratic lab hours, taking interest in chemistry, being goofy with me, and for unconditionally loving me. I am very very lucky to have her in my life, and I look forward to what the future holds for us and our not so little puppy Scooby Jolly. Thank you for helping me get to where I am today.

I am forever indebted to everyone mentioned above, you all have made immeasurable contributions to my success and well-being, and for that I thank you all endlessly from the bottom of my heart.

VITA

EDUCATION

University of California, Los Angeles

Ph.D. Track Chemistry – Inorganic Concentration

M.S. Chemistry – Inorganic Concentration

Los Angeles, CA

Expected June 2024

March 2021

Sonoma State University

Rohnert Park, CA

Bachelor of Science: Chemistry

May 2019

SKILLS

- **Electrochemistry:** cyclic voltammetry, chronoamperometry, chronopotentiometry, high-pressure electrolysis
- **Continuous flow:** flow reactor design and implementation, packed bed reactor, bulk electrolysis in flow, Design of Experiment (DoE), computer aided design (CAD)
- **Synthetic:** Air/water free synthesis, purifications, column chromatography, recrystallization, materials fabrication
- **Characterization:** NMR (^1H , ^{13}C , ^{31}P), FTIR, UV-Vis, fluorescence spectroscopy, ICP-MS, GC, GCMS, LCMS, MS, TGA, EA
- **Software:** Adobe Illustrator, ChemDraw, JMP SAS, Igor Pro, Microsoft and Google Applications, Solidworks, Fusion 360, TopSpin, Mestrenova, Gamry Framework, CHI Electrochemical Workstation
- Experienced in communication of scientific data, collaborative environments, mentorship

SELECTED PUBLICATIONS

- (1) Natinsky, Benjamin S. *; Jolly, Brandon J. *; Dumas, David M.; Liu, Chong. Efficacy Analysis of Compartmentalization for Ambient CH_4 Activation Mediated by Rh^{II} Metalloradical in Nanowire Array. *Chemical Science* **2021**, *12*, 1818-1825
- (2) Jolly, Brandon J.; Davis, Ashton R.; Co, Nathalie H.; Diaconescu, Paula L.; Liu, Chong. A Generalized Kinetic Model for Compartmentalization of Organometallic Catalysis. *Chemical Science* **2022**, *13*, 1101-1110
- (3) Dodge, Henry M. *; Natinsky, Benjamin S. *; Jolly, Brandon J. *; Zhang, Haochuan; Mu, Yu; Chapp, Scott M.; Tran, Thi V.; Diaconescu, Paula L.; Do, Loi H.; Wang, Dunwei.; Liu, Chong.; Miller, Alexander J. M. Polyketones from Carbon Dioxide and Ethylene by Integrated Electrochemical and Organometallic Catalysis. *ACS Catalysis* **2023**, *13*, 4053-4059
- (4) Deng, Shijie. *; Jolly, Brandon J. *; Wilkes, James R.; Mu, Yu.; Byers, Jeffery A.; Do, Loi H.; Miller, Alexander J. M.; Wang, Dunwei.; Liu, Chong.; Diaconescu, Paula L. Spatiotemporal control for integrated catalysis. *Nature Reviews Methods Primers* **2023**, *3*, 28
- (5) Jolly, Brandon J.; Pung, Michael J.; Liu, Chong. Integrated electrochemical CO_2 reduction and hydroformylation. *Dalton. Trans.* **2024**, DOI:10.1039/D4DT00423J

*Co-first author

RESEARCH EXPERIENCE

University of California, Los Angeles

Los Angeles, CA

Graduate Researcher, Department of Chemistry and Biochemistry, Advisor: Chong Liu

August 2019 – Present

- Formulated a theory for confined organometallics and extracted design principle of tailoring compartment geometry to reaction kinetics to yield a 30% improvement in reaction efficiency

- Synthesized a library of proton coupled electron transfer active Os complexes leading to a fundamental understanding the role of ligand interactions on promoting concerted pathways

Center for Integrated Catalysis

Los Angeles, CA

Graduate Student Member, Advisor: Chong Liu

August 2020 – Present

- Designed flow system for the synthesis of *N*-carboxyanhydrides (NCA) from amino acids and CO₂ resulting in a rapid 10% improvement in selectivity over batch conditions using DoE
- Utilized CAD to build microfluidic reactors for surface-initiated polymerization (SIP) of NCAs
- Discovered how aided mass transport by flow accelerates observed rate of NCA SIP by 10,000x
- Integrated electrochemical CO₂ reduction to CO with ethylene copolymerization, resulting in 4 - 50% CO incorporation as a function of applied current
- Further integrated electrochemical CO₂RR to aldehyde synthesis via hydroformylation, achieving up to 97% aldehyde yield using CO and H₂ from CO₂RR
- Developed GCMS method for aldehyde products to study effect of applied current on regioselectivity
- Immobilized hydroformylation catalysts onto functionalized silica nanoparticles and prepared thin films by spin coating or drop casting

Sonoma State University

Rohnert Park, CA

Undergraduate Researcher, Department of Chemistry

August 2016 – May 2019

Advisor: Carmen Works

- Synthesized iron-iron hydrogenase models ([Fe-Fe]) and characterized spectroscopically
- Improved quantum yield of [Fe-Fe] by 50% through varying ligand framework
- Determined photochemical mechanism of [Fe-Fe], uncovering how solvent coordination alters kinetics of ligand (re)binding events over 10+ orders of magnitude

SELECTED PRESENTATIONS

- (1) **Oral Presentation** – ACS Undergraduate Research Symposium, “Synthesis and spectroscopic studies of [Fe-Fe] hydrogenase models” May 2019
- (2) **Oral Presentation** – ACS National Meeting, “Developing a general kinetic model for compartmentalization of organometallic catalysis” March 2022
- (3) **Oral Presentation** – ACS National Meeting, “Polyketones from carbon dioxide and ethylene by integrating electrochemical and organometallic catalysis” March 2023
- (4) **Poster** – 2023 Hawthorne Symposium, “Synthesis and electrochemical properties of pyridine derivatives of the proton coupled electron transfer active [Os(bpy)₂(py)(OH₂)]²⁺” Dec 2023

SELECTED LEADERSHIP AND COMMUNITY INVOLVEMENT

Sonoma State University Chemistry Club

August 2015 - May 2019

President, Vice President, Events Coordinator, Treasurer

- Planned outreach, social, and networking events with organizations on campus and local companies

University of California, Los Angeles Math and Physical Sciences Council

Sept 2020 - Present

Chemistry Department Representative, External Vice President

- Served as chemistry department elected representative

SELECTED AWARDS AND HONORS

- (1) ACS Undergraduate Physical Chemistry Award 2018
- (2) UCLA Graduate Dean’s Scholar Award 2019
- (3) Dissertation Year Fellowship 2023 – 2024

Chapter 1. General Introduction

Motivation: Spatial control in complex biological reaction pathways

Biology has evolved to manage its extensive complex reaction networks in numerous ways, with compartmentalization at the forefront.¹⁻³ Spatially co-localizing sequential reactions along a biosynthetic pathway ensures retention and utilization of ephemeral intermediates and therefore high reaction efficiency.¹⁻⁷ In the absence of such spatial control, key species would be free to participate in competing or deactivating pathways leading to low turnovers.⁵ For example, carboxysome microcompartments augment the rate of CO₂ fixation by encapsulating the cascade of carbonic anhydrase and ribose 1,5-bisphosphate carboxylase/oxygenase.^{3, 8} This allows this pathway to generate and retain high local CO₂ concentration while allowing the exclusion of deactivating O₂ within the carboxysome confinement. Analogously, the last two steps of tryptophan biosynthesis, conversion of indole-3-glycerol-phosphate to indole then to tryptophan, employs substrate-channeling bestowed by compartmentalized subunits of tryptophan synthase to enhance reaction efficiency.^{2,9} Here, a hydrophobic tunnel between the subunits retains the indole intermediate, which prevents its free diffusion and participation in deactivating side reactions.² With billions of years of evolution, spatial control by compartmentalization remains a staple of biology's ability to manage its complex network of often competing or incompatible biochemical reactions in a homogenous solution.

Building off fundamental discoveries of compartmentalization in biology, the biocatalytic community has made great strides in replicating such spatial control for the construction of *in vitro* enzyme cascades.^{4, 5, 7, 10-19} One example is the co-encapsulation of a three enzyme cascade comprising β -galactose, glucose oxidase, and horseradish peroxidase within a metal organic framework (MOF) pore.¹⁷ The co-localization of these three enzymes in close proximity resulted

in a fivefold rate enhancement for this cascade enabled by the retention of key intermediates within the MOF pore compartment. Following experimental work in *in vitro* enzyme cascade compartmentalization, theoretical studies on how compartments affect substrate/product transport and enzyme activity emerged in order to extract design principles for optimal enzyme compartmentalization.^{9, 15, 20} The success of spatial control in *in vitro* biocatalysis motivates the exploration of translating this phenomenon to other fields of catalysis for similar benefits. The work outlined in this dissertation is aimed at translating biological spatial control to organometallics and electrochemistry to construct efficient multi-step, multi-catalyst processes.

Precedence: Localized organometallic catalysis

Interdisciplinary work in interfacing organometallic catalysis with materials chemistry can enable spatial control down to the molecular level. Major achievements have been made in immobilizing organometallic species onto material surfaces by means such as direct bonding or through space interactions, with encapsulation within porous or nanostructured materials being a newer, promising avenue. For example, our lab previously reported how an anaerobic compartment generated by a reducing potential applied to a nanostructured electrode can allow O₂ sensitive methane activation via a Rh catalyst and oxidation to methanol to occur in proximity under ambient conditions.²¹ An observed five order of magnitude rate enhancement compared to no anaerobic compartment was ascribed to the retention and utilization of an O₂ sensitive Rh^{II} intermediate.^{21,}²² Advancements made in spatial control of organometallics and its reminiscent nature of biological compartmentalization motivate us to study and explore the effect of compartmentalizing organometallic catalysis towards developing multi-step, multi-catalyst processes.

This work: Intermediate generation and utilization enabled by spatial control in multi-step, multi-catalyst organometallic and electrochemical processes

The development of efficient complex reaction pathways operating in one pass presents an opportunity to convert abundant feedstocks or environmental pollutants to commodity chemicals, while obviating wasteful or problematic work ups with hazardous or ephemeral intermediates.²³ Electrochemistry and organometallic catalysis play integral roles in small molecule activation, while organometallic catalysis is also competent for follow up utilization of intermediates derived from small molecule activation. Therefore, the pairing of individual steps or catalysts is of great interest. However, a major potential complication of such an approach is interference between catalyst - catalyst, catalyst - substrate, substrate - substrate, and/or incompatibility in reaction conditions. We sought to adapt biological means of spatial control such as compartmentalization to reconcile these complications.

To start, we first developed a theoretical model of a general compartmentalized organometallic catalytic cycle. We elected to model a catalytic cycle as an exemplary multi-step process to extract design principles on how best to design a compartment to retain and utilize a key intermediate along the multi-step pathway. By modelling entry and exit of species into and out of a compartment and introducing competing reactions occurring outside of a confinement, we uncovered how the competition of mass transport as a function of compartment geometry and reaction kinetics affects observed catalytic performance. Such discoveries suggest that a compartment's geometry can be tailored to kinetics of a multi-step process to optimize performance within a confinement (**Chapter 2**). This design principle was verified by adapting our model to a small handful of established compartmentalized organometallic systems (**Chapter 2**). Next, we expanded on concepts from **Chapter 2** to integrate electrochemical CO₂ reduction (CO₂RR) and co-polymerization with ethylene to polyketone thermoplastics in separate compartments of a reactor. This allowed new reactivity in instituting an external handle over polymer microstructure via applied current density

enabled by spatial control (**Chapter 3**). Building off of work from **Chapter 3**, we integrated CO₂RR to hydroformylation with similar spatial control. Typically, concomitant hydrogen evolution (HER) in CO₂RR is undesired. However, hydroformylation requires CO and H₂, thus we repurposed this undesired HER to provide the synthetic equivalents for aldehyde synthesis in hydroformylation (**Chapter 4**). Another multi-step, multi-catalyst system we became interested in exploring, in collaboration, is the cyclization of amino acids to *N*-carboxyanhydrides (NCA) and polymerization of NCAs to polyamides with the use of flow chemistry (**Chapter 5**). In this work, we opted to employ separate flow systems as a means of spatial control, as well as connection between the two processes, to transform amino acids all the way to polyamides. NCAs often have a short shelf life owing to hydrolysis, but are attractive monomers for the synthesis of high molecular weight polyamides. Thus, an integrated approach whereby NCAs are generated and immediately consumed is desirable. We first developed and optimized flow systems for each separate process, as a step towards future integration.

References

1. Hurlley, S., Location, Location, Location. *Science* **2009**, *326*, 1205-1205.
2. Anderson, K. S.; Miles, E. W.; Johnson, K. A., Serine Modulates Substrate Channeling in Tryptophan Synthase. A Novel Intersubunit Triggering Mechanism. *J. Biol. Chem.* **1991**, *266*, 8020-8033.
3. Cannon, G. C.; Bradburne, C. E.; Aldrich, H. C.; Baker, S. H.; Heinhorst, S.; Shively, J. M., Microcompartments in Prokaryotes: Carboxysomes and Related Polyhedra. *Applied and Environmental Microbiology* **2001**, *67*, 5351-5361.
4. Conrado, R. J.; Varner, J. D.; Delisa, M. P., Engineering the spatial organization of metabolic enzymes: mimicking nature's synergy. *Curr. Opin. Biotechnol.* **2008**, *19*, 492-499.
5. Chen, A. H.; Silver, P. A., Designing Biological Compartmentalization. *Trends in Cell Biology* **2012**, *22*, 662-670.
6. Avalos, J. L.; Fink, G. R.; Stephanopoulos, G., Compartmentalization of Metabolic Pathways in Yeast Mitochondria Improves the Production of Branched-Chain Alcohols. *Nat. Biotechnol.* **2013**, *31*, 335-341.
7. Idan, O.; Hess, H., Origins of Activity Enhancement in Enzyme Cascades on Scaffolds. *ACS Nano* **2013**, *7*, 8658-8665.
8. Rae, B. D.; Long, B. M.; Whitehead, L. F.; Förster, B.; Badger, M. R.; Price, G. D., Cyanobacterial Carboxysomes: Microcompartments that Facilitate CO₂ Fixation. *J. Mol. Microbiol. Biotechnol.* **2013**, *23*, 300-307.
9. Chavan, K. S.; Calabrese Barton, S., Simulation of Intermediate Channeling by Nanoscale Confinement. *The Journal of Physical Chemistry C* **2018**, *122*, 14474-14480.

10. Wilner, O. I.; Weizmann, Y.; Gill, R.; Lioubashevski, O.; Freeman, R.; Willner, I., Enzyme cascades activated on topologically programmed DNA scaffolds. *Nature Nanotechnology* **2009**, *4*, 249-254.
11. Idan, O.; Hess, H., Diffusive transport phenomena in artificial enzyme cascades on scaffolds. **2012**, *7*, 769-770.
12. Jandt, U.; You, C.; Zhang, Y. H. P.; Zeng, A. P., Compartmentalization and Metabolic Channeling for Multienzymatic Biosynthesis: Practical Strategies and Modeling Approaches. *Adv. Biochem. Eng. Biotechnol.* **2013**, *137*, 41-65.
13. K uchler, A.; Yoshimoto, M.; Luginb uhl, S.; Mavelli, F.; Walde, P., Enzymatic reactions in confined environments. *Nature Nanotechnology* **2016**, *11*, 409-420.
14. Quin, M. B.; Wallin, K. K.; Zhang, G.; Schmidt-Dannert, C., Spatial organization of multi-enzyme biocatalytic cascades. *Org. Biomol. Chem.* **2017**, *15*, 4260-4271.
15. Zhang, Y.; Hess, H., Toward Rational Design of High-efficiency Enzyme Cascades. *ACS Catal.* **2017**, *7*, 6018-6027.
16. Chen, W.-H.; V azquez-Gonz alez, M.; Zoabi, A.; Abu-Reziq, R.; Willner, I., Biocatalytic Cascades Driven by Enzymes Encapsulated in Metal–Organic Framework Nanoparticles. *Nat. Catal.* **2018**, *1*, 689-695.
17. V azquez-Gonz alez, M.; Wang, C.; Willner, I., Biocatalytic Cascades Operating on Macromolecular Scaffolds and in Confined Environments. *Nat. Catal.* **2020**, *3*, 256-273.
18. Wang, C.; Yue, L.; Willner, I., Controlling biocatalytic cascades with enzyme–DNA dynamic networks. *Nat. Catal.* **2020**, *3*, 941-950.
19. Kracher, D.; Kourist, R., Recent developments in compartmentalization of chemoenzymatic cascade reactions. *Curr. Opin. Green Sustain. Chem.* **2021**, *32*, 100538.

20. Tsitkov, S.; Hess, H., Design Principles for a Compartmentalized Enzyme Cascade Reaction. *ACS Catal.* **2019**, *9*, 2432-2439.
21. Natinsky, B. S.; Lu, S.; Copeland, E. D.; Quintana, J. C.; Liu, C., Solution Catalytic Cycle of Incompatible Steps for Ambient Air Oxidation of Methane to Methanol. *ACS Cent. Sci.* **2019**, *5*, 1584-1590.
22. Natinsky, B. S.; Jolly, B. J.; Dumas, D. M.; Liu, C., Efficacy analysis of compartmentalization for ambient CH₄ activation mediated by a Rh^{II} metalloradical in a nanowire array electrode. *Chem. Sci.* **2021**, *12*, 1818-1825.
23. Deng, S.; Jolly, B. J.; Wilkes, J. R.; Mu, Y.; Byers, J. A.; Do, L. H.; Miller, A. J.; Wang, D.; Liu, C.; Diaconescu, P. L., Spatiotemporal control for integrated catalysis. *Nat. Rev. Methods Primers* **2023**, *3*, 28.

Chapter 2. Developing a generalized kinetic model for compartmentalization of organometallic catalysis

This chapter is a version of Jolly, B. J.; Co, N. H.; Davis, A. R.; Diaconescu, P. L.; Liu, C. "A generalized kinetic model for compartmentalization of organometallic catalysis." *Chem. Sci.* **2022**, *13*, 1101-1110.

Abstract

Compartmentalization is an attractive approach to enhance catalytic activity by retaining reactive intermediates and mitigating deactivating pathways. Such a concept has been well explored in biochemical and more recently, organometallic catalysis to ensure high reaction turnovers with minimal side reactions. However, a scarcity of theoretical framework towards confined organometallic chemistry impedes a broader utility for the implementation of compartmentalization. Herein, we report a general kinetic model and offer design guidance for a compartmentalized organometallic catalytic cycle. In comparison to a non-compartmentalized catalysis, compartmentalization is quantitatively shown to prevent the unwanted intermediate deactivation, boost the corresponding reaction efficiency (γ), and subsequently increase catalytic turnover frequency (*TOF*). The key parameter in the model is the volumetric diffusive conductance (F_V) that describes catalysts' diffusion propensity across a compartment's boundary. Optimal values of F_V for a specific organometallic chemistry are needed to achieve maximal values of γ and *TOF*. As illustrated in specific reaction examples, our model suggests that a tailored compartment design, including the use of nanomaterials, is needed to suit a specific organometallic catalytic cycle. This work provides justification and design principles for further exploration into compartmentalizing organometallics to enhance catalytic performance. The conclusions from this

work are generally applicable to other catalytic systems that need proper design guidance in confinement and compartmentalization.

Introduction

Compartmentalization has been well documented in biochemical literature as one method for achieving efficient *in vivo* tandem catalysis by encapsulating enzymes in well-defined micro- and nano-structures.¹⁻⁷ By controlling the diffusion of species in and out of compartment boundaries, nature is able to retain reactive or toxic intermediates, increase local substrate concentration, and mitigate deactivating or competing pathways.¹⁻⁷ For example, carboxysome microcompartments enhance the rate of CO₂ fixation by encapsulating the cascade of carbonic anhydrase and ribose 1,5-bisphosphate carboxylase/oxygenase to generate high local concentration of CO₂ and exclude deactivating O₂ within their polyhedral structures.^{8, 9} Also, the last two steps of tryptophan biosynthesis – the conversion of indole-3-glycerol-phosphate to indole and then to tryptophan – takes advantages of the substrate-channeling effect bestowed by compartmentalized subunits of tryptophan synthase.^{10, 11} Here, a hydrophobic tunnel between the two subunits retains the indole intermediate, which prevents its free diffusion and participation in deactivating side reactions.¹⁰ With billions of years of evolution, compartmentalization appears the mainstay of biology to manage the complex network of biochemical reactions that are frequently competing and incompatible with each other in a homogenous solution.

The success of natural compartmentalized enzyme cascades inspires the development of biomimetic synthetic catalysis with organometallic chemistry being the latest frontier. Multiple groups have employed well-defined spatial organization at the nano- and microscopic levels to construct *in vitro* biocatalytic and organometallic cascades with enhanced catalytic performance.^{2, 3, 12-16} Encapsulating NiFe hydrogenase in virus capsids improves its proteolytic and thermal

stability as well as enhances the rate of H₂ production.¹² Confining a biochemical cascade of β -galactose, glucose oxidase, and horse radish peroxidase in metal-organic frameworks led to an enhancement of reaction yield in comparison to a freely diffusing analogue.^{13, 14} The extent to which reaction yields are enhanced in confined enzyme cascades is reported to correlate with the distance between active sites, suggesting that spatial organization or localization of catalysts is beneficial in tandem or cascade reactions.¹⁵ In addition to biocatalysis, recently compartmentalization of organometallic catalysts has been experimentally demonstrated.¹⁷⁻²³ For example, our group employed a nanowire-array electrode to pair seemingly incompatible CH₄ activation based on O₂-sensitive rhodium (II) metalloradical (Rh(II)) with O₂-based oxidation for CH₃OH formation.^{17, 24} The application of a reducing potential to the nanowire array electrode created a steep O₂ gradient within the wire array electrode, such that an anoxic compartment was established at the bottom of the wires. As a result that was not observable for planar electrode without an anoxic region, a catalytic cycle was formed in which the air-sensitive Rh(II) activated CH₄ in the O₂-free region of the wire array electrode, while CH₃OH synthesis proceeded in the aerobic domain with O₂ as the terminal electron acceptor. The retainment of the ephemeral Rh(II) intermediate by the nanowire electrode for catalytic CH₄-to-CH₃OH conversion^{17, 24} encourages us to further explore the design principles of compartmentalizing cascades for higher turnovers with mitigated deactivation pathways.

We envision that a theoretical framework for organometallic catalysis will expand the use of compartmentalization for organometallic chemistry and beyond. In biochemistry, mathematical modeling of confined enzyme cascades has been well developed and offers the design principles in natural systems^{11, 25} and for engineered bio-compartments.^{11, 16, 25, 26} The models pinpoint a key parameter, volumetric diffusive conductance (F_V), which describes the diffusion propensity across

a compartment's boundary. F_V is determined by a compartment's surface-to-volume ratio and its boundary's permeability.^{26,27} An optimal value of F_V tailored to the specific biochemical reactions are needed in order to achieve better reactivity in comparison to the non-compartmentalized alternative. Similarly, we contend that further development of compartmentalized organometallic chemistry demands a similar quantitative design principle. In a model organometallic cycle that includes oxidative addition (OA), isomerization/migratory insertion (Iso/MI), and reductive elimination (RE) along with undesirable deactivation pathways,²⁸ what are the suitable values of the compartment's physical parameters for minimal deactivation and maximal turnover frequency (*TOF*) (Figure 2.1)? Unfortunately, there has been a paucity of theoretical treatment for this question despite the exciting progresses in experimental demonstration.¹⁷⁻²³ Such a lack of theoretical treatment motivates us to establish a general kinetic model and quantitatively investigate how compartmentalization will affect the competing reaction pathways and the corresponding turnover of the desired organometallic catalysis. The successful analysis of compartmentalization in organometallic catalysis, which bears the common features of catalysis in general, will pave the venue to analyze any catalytic cycle with synthetic compartments and confinement.

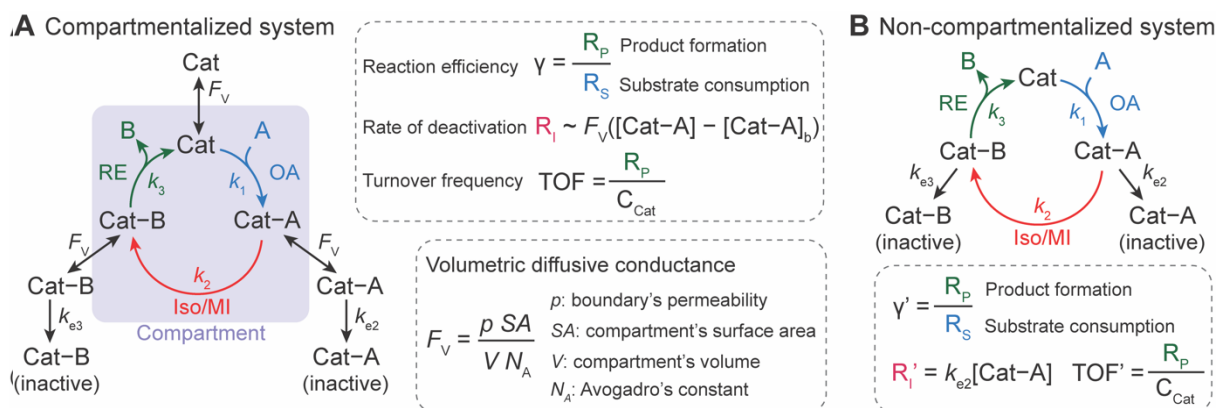


Figure 2.1 Schematic of a general compartmentalized catalytic cycle in organometallic chemistry (A) and the corresponding non-compartmentalized (freely diffusing) system (B). γ , reaction efficiency; R_S , rate of substrate consumption; R_I , rate of intermediate elimination; R_P , rate of product formation; TOF , turnover frequency; F_V , volumetric diffusive conductance; p , compartment boundary's permeability for catalytic intermediates; SA , compartment's surface area; V , compartment volume; N_A , Avogadro's constant; OA, oxidative addition (rate constant k_1); Iso/MI, isomerization/migratory insertion (rate constant k_2) in conjunction with a competing deactivation (rate constant k_{e2}); RE, reductive elimination (rate constant k_3) in conjunction with a competing deactivation (rate constant k_{e3}).

Here we report a general kinetic model and offer design guidance for a compartmentalized organometallic catalytic cycle. We took advantage of the established theoretical frameworks in biochemistry^{16, 25, 26} and applied such kinetic frameworks to a model compartmentalized cycle with competing deactivation pathways (Figure 2.1A),²⁸ and a non-compartmentalized counterpart as a control scenario (Figure 2.1B). Under assumptions and simplifications applicable to organometallic catalysis, as a proof-of-concept we examined three important metrics of this catalytic cycle in both compartmentalized and non-compartmentalized scenarios: (1) reaction efficiency (γ) that gauges the percentage of intermediates funneled towards desirable catalytic

turnover over deactivation pathways; (2) the deactivating rate of intermediate $Cat - A$ (R_I); and (3) the turnover frequency (TOF) that measures the steady-state catalytic rate despite intermediate deactivation. When compartments' F_V values are smaller than the intrinsic kinetics of the organometallic cycle in question, a compartmentalized system can significantly outperform a homogeneous counterpart with respect to γ and TOF with a lower value of R_I . We illustrated the general relationship for specific organometallic catalysis to achieve maximal γ and TOF . We additionally employed the developed model to analyze the experimental results in nanowire-based CH_4 activation,^{17, 29} the Fujiwara-Mirotani reaction,^{30, 31} and the Negishi coupling reaction.^{32, 33} The established kinetic model can be adapted to suit a plethora of catalytic cycles with synthetic compartments, offering a framework to be expanded on for advanced compartmentalization of general chemical catalysis.

RESULTS AND DISCUSSION

Our investigation starts with a hypothetical three-step organometallic cycle confined within a compartment in conjunction with multiple deactivation pathways in the exterior bulk solution (Figure 2.1A and Supplementary Information).²⁸ Catalytic species Cat of a presumed constant concentration in the bulk ($[Cat]_b \equiv C_{cat}$) diffuses into the compartment of volume V and bind substrate molecule A through oxidative addition to form intermediate species $Cat - A$, either pseudo-first-order ($m = 1$)³⁴⁻³⁷ or pseudo-second-order ($m = 2$)^{24, 38, 39} with respect to Cat (rate constant k_1). After a step of isomerization or migratory insertion (rate constant k_2) converts $Cat - A$ species to the product adduct $Cat - B$, the catalytic cycle is completed by the reductive elimination that transforms $Cat - B$ back to Cat with the release of product B (rate constant k_3). Here we presume that Cat , $Cat - A$ and $Cat - B$ intermediates all can diffuse across the compartment boundary and there are two possible competing deactivation pathways in the

homogenous solution outside the compartment. The deactivations of $Cat - A$ and $Cat - B$ are presumed pseudo-first-order with respect to the intermediates with rate constants k_{e2} and k_{e3} , respectively. Similarly, a non-compartmentalized system was constructed for the sake of comparison with the same set of kinetic reaction parameters (Figure 2.1B and Supplementary Information). The established compartmentalized and non-compartmentalized catalytic cycles are generally applicable to a broad range of organometallic catalysis with concurrent deactivation processes^{28, 40-42}, for which various deactivations have been well reviewed and comprehensively discussed in literature.⁴¹

For the compartmentalized scenario (Figure 2.1A), we additionally assign volumetric diffusive conductance (F_V) to quantitatively describe the extent of mass transport, predominantly diffusion-based, between the compartment and the surrounding bulk solution (Supplementary Information). As a measure of molecules' propensities to diffusively cross the compartment's boundary under a given concentration gradient, F_V is defined as the product of compartment boundary's permeability (ρ) and its total surface area (SA) while divided by Avogadro's constant (N_A) and the volume (V) of the corresponding compartment (Figure 2.1A).²⁶ In particular, p is proportional to the species' diffusion coefficients (D) and inversely proportional to the distance of diffusion path across the boundary.⁴³ In our analysis, we assume p remains constant for Cat , $Cat - A$ and $Cat - B$, given the fact that the catalytic center are frequently more bulky in comparison to the substrate/product, and the catalytic intermediates typically have similar diffusion coefficients despite the reaction-related adducts. We also assume that substrate A and product B are small enough that faster diffusion of A and B leads to minimal concentration gradients for A and B . Such assumption is also applicable to the practical applications when the substrates are used as the solvent in the catalysis. Under such assumptions, a single value of F_V for the catalytic intermediates is sufficient

to describe the effect of compartmentalization on a catalytic cycle. Because the value of ρ depends on the compartment's physical properties, the design of compartment's surface-to-volume ratio (SA/V) and materials' properties at the compartment's boundary has significant impacts on the value of F_V , and subsequently the overall catalytic turnover as will be discussed in this study.

In this work we aim to study the steady-state phenomena of compartmentalized catalysis. We assume constant, time-independent concentrations of Cat , $Cat - A$ and $Cat - B$ in both the compartment ($[Cat]$, $[Cat - A]$, and $[Cat - B]$, respectively) as well as the surrounding bulk solution ($[Cat]_b \equiv C_{cat}$ (vide supra), $[Cat - A]_b$ and $[Cat - B]_b$, respectively). Similarly, in the bulk solution substrate A is maintained at a constant concentration (C_A) and fast removal of product B is ensured ($[B] \rightarrow 0$). Such assumptions including $[Cat]_b \equiv C_{cat}$ pertain to a flow reactor with sufficient amount of catalysts or a batch reaction under high catalyst loading and low conversion (Supplementary Information). Alternatively, a constant total catalyst concentration including all catalytic species in the bulk can be presumed ($C_{Cat,total} \equiv [Cat]_b + [Cat - A]_b + [Cat - B]_b = constant$), Supplementary Information). We have analyzed the catalysis under both sets of assumptions. We note that the latter set of assumptions with a constant total catalyst concentration, more complicated to solve mathematically and labeled as “model $C_{Cat,total}$ ” in Supplementary Information, leads to similar conclusions and reinforces the general applicability of the following results solved when we assume $[Cat]_b \equiv C_{cat}$. Unless noted specifically, the results discussed below will be based on the former set of assumptions (Supplementary Information).

A set of steady-state kinetic equations are constructed to reflect both the compartmentalized and non-compartmentalized scenarios (equations S1–S5 and S67–S69) for an organometallic catalytic cycle following the analysis protocols established in biochemistry.²⁶ Comparing to the non-compartmentalized case that only includes reactions in the homogenous solution (equation

S67–69), the equations for the compartmentalized case (equation S1–5) additionally consider the reactions in the compartment as well as the mass transport across the boundary, whose magnitudes are governed by both the value of F_V and the concentration gradients across the compartment's boundary. Detailed mathematical treatment of the established equations can be found in Supplementary Information and a few key outputs of the model are evaluated here. As one of the proposed benefits of compartmentalization is the capability of retaining reactive intermediates within the compartment without significant catalyst deactivation in the bulk,^{2, 3, 14, 16} we are interested in evaluating the steady-state consumption rate of substrate A (R_S), the generation rate of product B (R_P), and the deactivation rate of intermediates $Cat - A$ (R_I) (Figure 2.1A). Moreover, in both compartmentalized and non-compartmentalized scenarios, we aim to analyze the rate of reaction, numerically represented as turnover frequency TOF , and the efficacy of transforming the substrate A into targeted product B , numerically represented as reaction efficiency γ that is defined as the percentage of intermediates funneled towards desirable catalytic turnover.¹⁶

²⁶ In both cases, γ is calculated as the ratio between the formation rate of product B and the consumption rate of substrate A . In the case of pseudo-first-order kinetics towards Cat in oxidative addition ($m = 1$), γ , $R_{I,m=1}$, and $TOF_{m=1}$ in a compartmentalized system can be expressed as,

$$\gamma = \frac{k_2 k_3}{(f_2 + k_2)(f_3 + k_3)} \quad (1)$$

$$R_{I,m=1} = \frac{k_1 k_{e2} F_V^2 C_{Cat} C_A}{(a_1 + F_V)(f_2 + k_2)(F_V + k_{e2})} \quad (2)$$

$$TOF_{m=1} = \frac{k_1 k_2 k_3 F_V C_A}{(a_1 + F_V)(f_2 + k_2)(f_3 + k_3)} \quad (3)$$

in which,

$$f_2 = \frac{F_V k_{e2}}{F_V + k_{e2}} \text{ and } f_3 = \frac{F_V k_{e3}}{F_V + k_{e3}} \quad (4)$$

$$a_1 = k_1 C_A - \frac{k_1 k_2 k_3 C_A}{(f_2 + k_2)(f_3 + k_3)} \quad (5)$$

In comparison under a non-compartmentalized scenario, the corresponding γ' , $R'_{I,m=1}$, and $TOF'_{m=1}$ are expressed as,

$$\gamma' = \frac{k_2 k_3}{(k_2 + k_{e2})(k_3 + k_{e3})} \quad (6)$$

$$R'_{I,m=1} = \frac{k_1 k_{e2} C_{cat} C_A}{k_2 + k_{e2}} \quad (7)$$

$$TOF'_{m=1} = \frac{k_1 k_2 k_3 C_A}{(k_2 + k_{e2})(k_3 + k_{e3})} \quad (8)$$

The mathematical expressions for γ , R_I , and TOF results, derived from Supplementary Information for the assumptions outlined in the main text and for model $C_{cat,total}$ respectively, are summarized in Table S1–S2 as a reference. The successful construction and mathematical derivation of a general kinetic model in organometallic catalysis warrants quantitative evaluation about the efficacy of compartmentalization under different reaction kinetics and compartment properties.

The derived analytical solutions to the established kinetic model allow us to numerically calculate the values of γ , R_I , and TOF in both compartmentalized and non-compartmentalized scenarios. Specifically, we set out to evaluate under what conditions compartmentalization is beneficial with a given set of parameters pertaining to the compartment's properties and kinetics of organometallic reactions. As an introductory example representative to a typical organometallic catalytic cycle, we assume that $C_{cat} = 1$ mM and $C_A = 10$ mM, as organometallic catalytic systems often operate

near 10 mol% catalyst loading.⁴⁰ Values of kinetic parameters are $k_1 \in [10^{-5}, 10^4] \text{ M}^{-1}\cdot\text{s}^{-1}$ ($m = 1$)³⁴⁻³⁷ or $k_1 \in [10^{-3}, 10^6] \text{ M}^{-2}\cdot\text{s}^{-1}$ ($m = 2$);^{17, 24, 38, 39} $k_2 \in [10^{-3}, 10^6] \text{ s}^{-1}$ ^{44, 45} and $k_3 = 10^6 \text{ s}^{-1}$.^{46, 47} When either k_1 or k_2 is not a variable of interest, they are set as $k_1 = 0.1 \text{ M}^{-1}\cdot\text{s}^{-1}$ ($m = 1$) or $10 \text{ M}^{-2}\cdot\text{s}^{-1}$ ($m = 2$) and $k_2 = 1 \times 10^3 \text{ s}^{-1}$.³⁴⁻³⁷ The selection of those kinetic parameters is based on reviews of oxidative addition and migratory insertion, as well as reported kinetic studies using techniques such as time resolved infrared spectroscopy for transient species on the intermediates during carbonylation and O₂ reduction and transfer, among others.^{17, 24, 34-39, 44, 45} The selection of k_3 parameter value implicitly assumes fast reductive elimination from $Cat - B$, which is supported by the observation that reductive eliminations are often not the rate-determining step in a catalytic cycle.^{46, 47} The values of deactivation kinetics k_{e2} for $Cat - A$ and k_{e3} for $Cat - B$ are selected with additional assumptions, given the dearth of reported kinetic values for the less exciting deactivation steps. As the reductive elimination from $Cat - B$ is sufficiently fast, our primary focus is to examine the deactivation from $Cat - A$ hence how the comparison between k_2 and k_{e2} will affect the overall catalysis. Subsequently we assign $k_{e3} = k_3 = 1 \times 10^6 \text{ s}^{-1}$ so that the rate of competing deactivation from $Cat - B$ is no lower than rate of reductive elimination. Similarly, when k_{e2} is not a variable of interest, we set $k_{e2} = k_2 = 1 \times 10^3 \text{ s}^{-1}$ to match the kinetics of isomerization/migratory insertion. Last, we set $F_V \in [30, 600] \text{ s}^{-1}$, whose range is estimated based on the diffusion coefficient of $9 \times 10^{-10} \text{ m}^2\cdot\text{s}^{-1}$ from tabulated organometallic catalysts,^{48, 49} as well as the geometry and properties of reported microscopic compartments in porous materials, supramolecular assemblies, nanoscopic micelles, and the use of nanowire array electrode in our previous work (see Supplementary Information).^{17-20, 29, 50, 51} Overall, our selection of kinetic values here represents an organometallic catalytic cycle whose oxidative addition step is turnover-limiting and the deactivation of yielded $Cat - A$ intermediate is the most critical issue, while the

fast reductive elimination leaves the deactivation of $Cat - B$ species secondary in terms of γ and TOF . With varying values of F_V and changing ratios between the values of k_2 and k_{e2} , the trend of compartmentalization's efficacy can be unveiled.

The numerically calculated values of γ , R_I , and TOF as a function of k_2 and F_V illustrate that compartmentalization generally outperforms the non-compartmentalized scenarios with a higher tolerance towards undesirable deactivation reactions (Figure 2.2). Under a fixed rate constant of deactivation ($k_{e2} = 1 \times 10^3 \text{ s}^{-1}$) and pseudo-first-order oxidative addition ($k_1 = 0.1 \text{ M}^{-1} \cdot \text{s}^{-1}$ for $m = 1$), values of γ , R_I , and TOF in a compartmentalized system are plotted as a function of both k_2 and F_V in Figure 2.2A to 2.2C. The rate of isomerization/migratory insertion (k_2) is understandably a predominant factor in all three plots. When k_2 is much smaller than the rate of deactivation (k_{e2}), γ approaches zero (Figure 2.2A) when the deactivation of $Cat - A$ outcompetes the step of isomerization/migratory insertion, which is concurrent with a higher rate of deactivation (R_I in Figure 2.2B) and lower TOF value (Figure 2.2C). Alternatively, when k_2 is much larger than k_{e2} and the deactivation step is less relevant, γ plateaus towards unity with concomitant increase in TOF (Figure 2.2A,C). Despite the dominant role of k_2 , whether or not the system is compartmentalized strongly affects the values of γ , R_I , and TOF (Figure 2.2D to 2.2F). While the trend is generally applicable for all values of F_V , a specific case ($F_V = 320 \text{ s}^{-1}$) that corresponds to the nanowire array

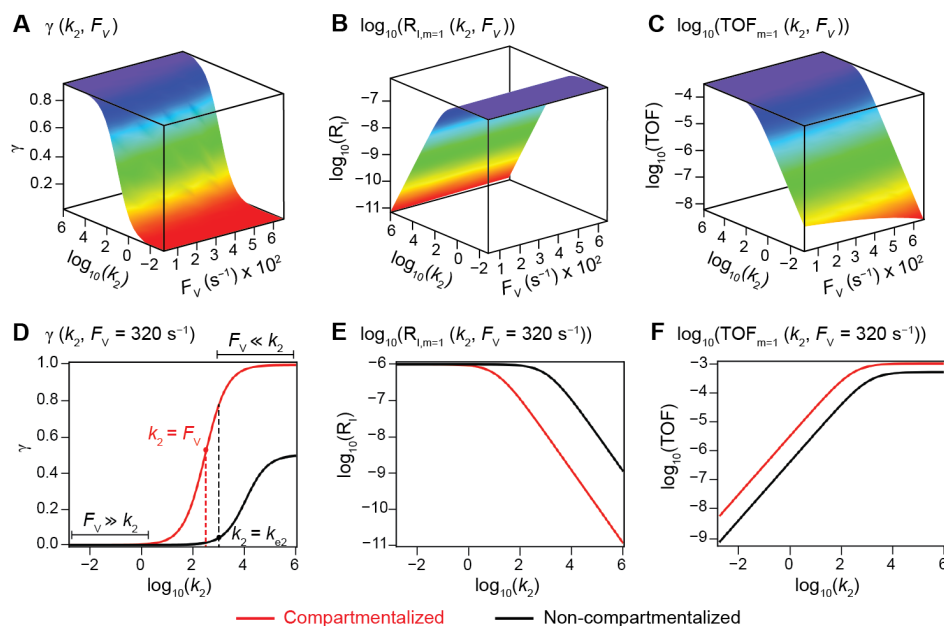


Figure 2.2 Reaction efficiency (γ , **A** and **D**), logarithmic of intermediate outflux rate ($\log_{10}(R_I)$, **B** and **E**), and logarithmic of turnover frequency ($\log_{10}(TOF)$, **C** and **F**) as a function of volumetric diffusive conductance (F_V) and logarithmic of the rate constant for isomerization or migratory insertion (Iso/MI) ($\log_{10}(k_2)$). **A** to **C**, compartmentalized scenario depicted in Figure 2.1A. **D** to **F**, comparisons between compartmentalized (red trace, when $F_V = 320 \text{ s}^{-1}$) and non-compartmentalized (black trace) scenarios. $m = 1$, $k_1 = 0.1 \text{ M}^{-1} \cdot \text{s}^{-1}$ notwithstanding **A** and **D**, $k_{e2} = 1 \times 10^3 \text{ s}^{-1}$, $k_3 = k_{e3} = 1 \times 10^6 \text{ s}^{-1}$. The selection of those exemplary values is based on literature reports on the kinetics of relevant organometallic systems (vide supra).

electrode for CH_4 -to- CH_3OH conversion in our previous work,¹⁷ illustrates under which situation the advantages of compartmentalization will be observed. As the value of k_2 increases, the compartmentalized scenario observes an increase of reaction efficiency γ in a sigmoidal fashion when k_2 approaches the value of F_V (red trace in Figure 2.2D); in contrast, γ in a non-compartmentalized case (black trace in Figure 2.2D) won't increase until k_2 approaches the value of k_{e2} . Similarly, with $F_V \ll k_{e2}$ and under a reasonably large value of k_2 , compartmentalization

suppresses the rate of deactivation R_I (Figure 2.2E) and increases the TOF by roughly no less than one order of magnitude (Figure 2.2F). Evaluations assuming pseudo-second-order kinetics towards Cat in the step of oxidative addition ($m = 2$) lead to the same conclusion (Figures S2.3A and S2.4A). Those observations suggest that the strategy of compartmentalization allows a catalytic cycle to be much more tolerant towards undesirable side reactions, as long as F_V is much smaller than k_{e2} ($F_V \ll k_{e2}$) with a judicious compartment design.

Additional examination suggests that a less “leaky” compartment, or one less prone to diffusive loss of intermediate, with smaller F_V value should be more effective than one with a relatively larger F_V . Here the extent of leakiness is relevant to the reactions of interests and a “leaky” compartment is defined as one whose F_V is much larger than the one of k_2 ($F_V \gg k_2$), with about one or two orders of magnitude of difference (a factor of 10 to 100) as shown in Figure 2.2D, because the difference of γ values between compartmentalization and non-compartmentalization is the biggest when $F_V < k_2 \ll k_{e2}$. Such a trend is more apparent when γ , R_I , and TOF were plotted as a function of F_V under fixed values of k_2 and k_{e2} (Figure 2.3A to 2.3C). In both situations when $m = 1$ and $m = 2$, a larger value of F_V leads to smaller values of γ and TOF and large value of R_I . This suggests that a more “leaky” compartment is not sufficient to conserve the yielded intermediates and is more prone to deactivation than one with a small F_V . A similar conclusion can be obtained when investigating the dependence of γ , R_I , and TOF as a function of F_V and k_{e2} (Figure 2.3D to 2.3F, Figure S2.3B and S2.4B). Significant decrease of γ and increase of R_I was observed at high F_V values, particularly when the values of k_{e2} are so large that the deactivation is much faster than the isomerization/migratory insertion step and intermediate $Cat - A$ has a much shorter life time once it diffuses out of the compartment.

The above noted observations can be mathematically rationalized from our derived equations.

When the value of F_V is similar to or even larger than k_{e2} or k_{e3} ($F_V \gtrsim k_{e2}$ or k_{e3}),

$$f_2|_{F_V \gtrsim k_{e2}} = \frac{F_V k_{e2}}{F_V + k_{e2}} = k_{e2} \quad \text{and} \quad f_3|_{F_V \gtrsim k_{e3}} = \frac{F_V k_{e3}}{F_V + k_{e3}} = k_{e3} \quad (9)$$

This will lead to $\gamma \approx \gamma'$, i.e. the reaction efficiency is not significantly altered with compartmentalization in comparison to the non-compartmentalized case.

Alternatively, when $F_V \ll k_{e2}$ or k_{e3} , we have

$$f_2|_{F_V \ll k_{e2}} = \frac{F_V k_{e2}}{F_V + k_{e2}} = F_V \quad \text{and} \quad f_3|_{F_V \ll k_{e3}} = \frac{F_V k_{e3}}{F_V + k_{e3}} = F_V \quad (10)$$

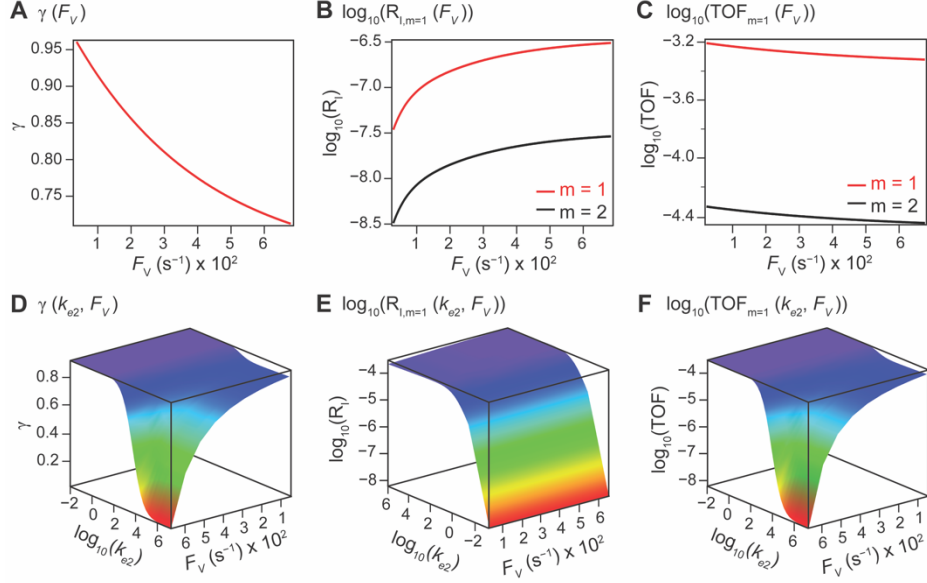


Figure 2.3 In a compartmentalized system, reaction efficiency (γ , **A** and **D**), logarithmic of intermediate outflux rate ($\log_{10}(R_I)$, **B** and **E**), and logarithmic of turnover frequency ($\log_{10}(TOF)$, **C** and **F**) as a function of volumetric diffusive conductance (F_V) and logarithmic of the rate constant for *Cat* – *A* deactivation ($\log_{10}(k_{e2})$). The axis of F_V and $\log_{10}(k_{e2})$ in **D** and **F** are inverted for the sake of presentation clarity. $k_1 = 0.1 \text{ M}^{-1}\cdot\text{s}^{-1}$ and $10 \text{ M}^{-2}\cdot\text{s}^{-1}$ for $m = 1$ and 2 , respectively, notwithstanding **A** and **D**. $k_2 = k_{e2} = 1 \times 10^3 \text{ s}^{-1}$. $k_3 = k_{e3} = 1 \times 10^6 \text{ s}^{-1}$.

This leads to

$$\gamma|_{F_V \ll k_{e2} \& k_{e3}} = \frac{k_2 k_3}{(f_2 + k_2)(f_3 + k_3)} = \frac{k_2 k_3}{(F_V + k_2)(F_V + k_3)} = \frac{1}{\left(\frac{F_V}{k_2} + 1\right)\left(\frac{F_V}{k_3} + 1\right)} \quad (11)$$

$$TOF_{m=1}|_{F_V \ll k_{e2} \& k_{e3}} = \frac{k_1 k_2 k_3 F_V C_A}{\left(k_1 C_A - \frac{k_1 k_2 k_3 C_A}{(F_V + k_2)(F_V + k_3)} + F_V\right)(F_V + k_2)(F_V + k_3)} \quad (12)$$

The equations noted above suggest that optimal, near-unity reaction efficiency γ , high *TOF*, and low R_I values would be obtained when $F_V \ll k_2$ and k_3 , which is consistent with our observations in Figure 2.2. Under our above-stated assumption that isomerization/migratory insertion is the

turnover-limiting step ($k_2 \ll k_3$), $\gamma = 0.9$ and 0.99 when $F_V/k_2 = 0.11$ and 0.01 , respectively. The corresponding expression of TOF can be simplified as,

$$TOF_{m=1}|_{F_V \ll k_{e2} \& k_{e3}} = k_2 \frac{1}{1 + \left(1 + \frac{F_V}{k_2}\right) \frac{k_2}{k_1 C_A}} \quad (13)$$

$$TOF_{m=1}|_{F_V \ll k_{e2} \& k_{e3}} \approx k_2 \frac{k_1 C_A}{k_2 + k_1 C_A} \quad \text{when } \frac{F_V}{k_2} \rightarrow 0 \quad (14)$$

The monotonic yet asymptotic increase of TOF values suggests that maximal TOF will be achieved when $F_V/k_2 \rightarrow 0$.

Lastly, when a constant total catalyst concentration including all catalytic species in the bulk is presumed (“model $C_{Cat,total}$ ”, $C_{Cat,total} \equiv [Cat]_b + [Cat - A]_b + [Cat - B]_b = constant$, Supplementary Information), the calculated values of R_I and TOF as functions of F_V and k_2 displayed little difference to the above-mentioned observations (Figures S2.5 to S2.7), while the derived expressions of γ are identical under both assumptions (Table S2.1 and S2.2). Such observations suggest that slight variation in the assumptions of the developed model does not significantly alter how the compartment’s F_V impacts the kinetics of overall catalysis.

The established kinetic model and the numerical evaluation offers an affirmative answer to the efficacy of compartmentalized organometallic catalysis and, if needed, what is the desired properties of the established compartment. When the rate constants of the steps in the catalytic cycle (k_2 and k_3) are commensurate with or greater than the rate constants of deactivation steps (k_{e2} and k_{e3}), i.e. $k_2 \gtrsim k_{e2}$ and $k_3 \gtrsim k_{e3}$, compartmentalization is not necessary since the intrinsic reactivity of catalysis is sufficiently fast with respect to undesirable side reactions. Compartmentalization should be considered under $k_2 < k_{e2}$ and $k_3 < k_{e3}$, when the intrinsic reactivities of the catalytic cycle cannot outcompete the deactivation pathways. The efficacy of

compartmentalization will be observable, as long as the compartment's volumetric diffusive conductance F_V is much smaller than k_{e2} or k_{e3} ($F_V \ll k_{e2}$ or k_{e3}). Nonetheless, one interesting conclusion from our analysis is that maximal efficacy of compartmentalization (reaction efficiency $\gamma \rightarrow 1$) demands F_V to be smaller not only than the rate constants of deactivation steps (k_{e2} and k_{e3}) but also than the rate constants of steps in the catalytic cycle (k_2 and k_3). This requirement for maximal γ stems from the fact that a “leaky” compartment with large F_V is not sufficient to conserve the yielded intermediates and is prone to deactivation. Practically, such a requirement is indeed a blessing for organometallic chemistry. As typical organometallic studies do not commonly characterize the deactivating side reactions, there lacks detailed kinetic information the values of k_{e2} or k_{e3} in comparison to the knowledge about catalytic kinetics (k_2 and k_3). Because we posit that criteria of $F_V < k_2$ and $F_V < k_3$ are sufficient for a compartment to “revive” a catalytic cycle unfunctional in a homogenous solution, kinetic information of the in-cycle steps (k_2 and k_3) is sufficient for future design of functional compartmentalization.

The feasibility of obtaining the range of F_V from the kinetics of the proposed catalytic cycle offers more guidance for the materials design for the compartment. As F_V is proportional to the compartment boundary's permeability (ρ) and its surface-to-volume ratio (SA/V),²⁶ multiple synthetic handles could be applied to achieve a desirable F_V value. A less permeable interface at the boundary of compartment as well as smaller surface-to-volume ratio will help to reduce the mass transport hence the value of F_V . Characterization techniques that help determine encapsulation geometry and assess permeability, such as electron microscopies and chromatographic methods, should be welcomed for more detailed mechanistic investigations in experimental demonstration.⁵²⁻⁵⁵ One interesting result from this argument is that a compartment of extremely small dimension, for example of nanoscopic scale, may not be necessarily beneficial,

because nanoscopic dimensions with their large surface-to-volume ratio may create a “leaky” compartment. Here we set $F_V \gg k_2$ as the criterion for a “leaky” compartment that poorly retains intermediates (vide supra), when there is minimal difference in reaction efficiency γ between a compartmentalized and non-compartmentalized system (Figure 2.2D). As F_V is calculated by a compartment’s surface-to-volume ratio (SA/V), its boundary’s permeability (ρ), and the Avogadro’s constant (N_A),²⁶ a “leaky” compartment for a specific catalysis satisfies the following equations,

$$F_V \equiv \frac{SA}{V} \cdot \frac{\rho}{N_A} \gg k_2 \quad \& \quad \frac{SA}{V} \gg \frac{k_2 \cdot N_A}{\rho} \quad (15)$$

Provided a compartment’s surface-to-volume ratio (SA/V) or chemicals’ permeability across the compartment’s boundary (ρ) is sufficiently large, our model predicts that compartmentalization will not be beneficial. In addition, the opposite inequality may be used to design optimal compartmentalized catalysis ($F_V \ll k_2$). Careful compartment design tailored to the specific kinetics of the catalytic cycle is recommended before experimental implementation.

The developed model remains generally applicable in the presence of mass transport heterogeneity in the compartment. As a first-order approximation, a mean-field average diffusion coefficient D is sufficient to describe the permeation of molecules through a compartment at ensemble level as long as the compartment’s porosity is isotropic, based on single-molecule studies of molecular diffusion in mesoporous silica and polymer films.^{56, 57} In the presence of anisotropy such as highly aligned pores or in our previous work’s nanowire arrays, a mean-field averaged diffusion coefficient D is still good enough to account for the diffusion phenomena in the specific direction.^{58, 59} In cases where anisotropic diffusion exists, the values of anisotropic ρ normal to the compartment’s boundary should be used when calculating F_V . Moreover, in scenarios in where

drastically heterogeneous D values are apparent inside a single compartment, an effective value of \bar{F}_V will be derived based on the volume-weighted average of F_V across the whole compartment, similar to the studies in metabolic microcompartments.²⁵ The order of magnitudes of the derived \bar{F}_V will be sufficient for the initial design of the compartmentalized catalysis, before further optimizations and detailed analysis proceed.

We caution that our established model only considers the mass transport of catalysts and assumes an unconditionally fast supply of substrate A and quick removal of product B . While such assumptions have their real-life correspondence under certain circumstances (*vide supra*), the currently established model is incapable of accounting for the possible mass-transport limitation for the substrate and product, which could be induced by a small F_V value recommended by the model presented here. Given that, we cautioned that a lower bound of F_V exists for optimal performance in practical applications, and an unnecessarily small value of F_V could be detrimental to the compartment design. This argument is corroborated by our prior work that utilizes nanowire array electrode to pair CH_4 activation from O_2 -sensitive metalloporphyrin with CH_3OH generation with O_2 as the terminal oxidant.^{17, 29} An increase of the nanowire array's length, corresponding to a smaller value of F_V (Supplementary Information), was experimentally observed to yield an increased rate of CH_4 activation until the reaction rate plateaued for nanowire arrays of 27 μm length.^{17, 29} Such experimental results illustrate the presence of a lower bound of F_V for optimal performance, when the mass transport of substrate CH_4 is probably limited due to the increased length of the nanowire array.

We employed our model and analyzed the benefits of compartmentalizing the Fujiwara-Moritani reaction, which is a Pd-catalyzed oxidative C-C coupling reactions.^{30, 31} In such a catalysis, stoichiometric oxidant is needed to regenerate the catalytically active Pd(II) species,^{30, 31} yet the

presence of spent oxidant can inhibit the reaction and result in mediocre yields.^{31, 60} Therefore, one possible strategy of reconciling such an incompatibility is to compartmentalize the Pd-based catalysts. Based on the available kinetic data reported in literature,⁶⁰ we translated our generally applicable model into the Fujiwara-Moritani reaction (Figure S2.8) and established the mathematical relationship that correlates volumetric diffusive conductance (F_V) with reaction efficiency (γ), the rate of catalyst deactivation (R_I), and turnover frequency (TOF) (Supplementary Information). We compared the values of γ , R_I , and TOF between the compartmentalized and non-compartmentalized cases. While the homogenous non-compartmentalized scenario yields $\gamma \sim 10^{-2}$ and $R_I \sim 10^{-5} \text{ s}^{-1}$, our model predicts that at $F_V \sim 10^{-5} \text{ s}^{-1}$, about 100 times smaller than the kinetic constant k_2 for the turnover-limiting step,⁶⁰ compartmentalization significantly decreases the rate of deactivation ($R_I = 2 \times 10^{-11} \text{ s}^{-1}$) and increase the reaction efficiency ($\gamma = 0.99$). Indeed, a recent experimental demonstration of compartmentalized Fujiwara-Moritani reaction with a “tube-in-tube” design is consistent with our model’s prediction.⁶¹ With an estimated $F_V \sim 10^{-28} \text{ s}^{-1}$ that well surpasses the criterion $F_V \ll k_2$ (vide supra), the model predicts little catalyst deactivation and high reaction efficiency ($\gamma \sim 1$ and $R_I \sim 10^{31} \text{ s}^{-1}$). Such predictions are consistent with the experimental observations⁶¹ and illustrate the utility of our model.

In another example, we analyzed the Negishi coupling reaction³² operating within a MOF confinement and concluded that compartmentalization of this reaction may have marginal benefits in the context of mitigating side reactions. In such a reaction, Ni or Pd catalysts enable the cross-coupling reactions between organic halides and organozinc, organoaluminum, or organozirconium compounds.^{32, 33} Detailed kinetic information is available for the coupling between an aryl iodide compound with an aliphatic zinc chloride³³ and we similarly established the kinetic model (Figure S2.9, and Supplementary Information). We found that in the non-compartmentalized scenario, γ

is close to unity already ($\gamma \sim 1$) because the deactivation steps (k_{e2} and $k_{e3} \sim 2 \times 10^{-3} \text{ s}^{-1}$) are slow in comparison to the steps in the catalytic cycle (k_1 and $k_2 \sim 1 \sim 10 \text{ M}^{-1} \cdot \text{s}^{-1}$; $k_3 \sim 0.5 \text{ s}^{-1}$). This suggests that benefits of compartmentalizing the Negishi coupling reaction will not be significant in the context of mitigating side reactions and boost reaction efficiency. Indeed, the model predicts that compartmentalization may even lower the TOF in comparison to the non-compartmentalized case, since benefits of preventing already negligible side reactions is outweighed by the mass transport of catalyst. Overall, the developed model represents a viable tool to pick the catalytic reactions that are suitable for the study of compartmentalization.

CONCLUSION

In this study, we developed a general kinetic framework for compartmentalizing organometallic catalysis with competing deactivation reactions in the bulk solution. Compartmentalization is only necessary under $k_2 < k_{e2}$ and $k_3 < k_{e3}$, when the intrinsic reactivities of the catalytic cycle cannot outcompete the deactivation pathways. Under such situations, the kinetic model predicts that careful compartment design with suitable values of volumetric diffusive conductance ($F_V \ll k_2$ and $F_V \ll k_3$ of at least one or two orders of magnitude difference) is capable of achieving maximal reaction efficiency (γ) and turnover frequency (TOF). Under our stated assumption that isomerization/migratory insertion is the turnover-limiting step ($k_2 \ll k_3$), the criterion of minimal deactivation and maximal TOF is equivalent to $F_V/k_2 = 0.11$ and 0.01 for $\gamma = 0.9$ and 0.99 , respectively, in order for the established compartment to minimize intermediate elimination and maximize catalysis. It is intriguing that the kinetics of deactivation steps are not needed for the design of compartment, as long as it is known that $k_2 < k_{e2}$ and $k_3 < k_{e3}$. As discussed with the examples of nanowire-based CH_4 activation,^{17, 29} Fujiwara-Mirotani reaction,^{30, 31} and the Negishi coupling reaction,^{32, 33} a tailored compartment design, including the use of nanomaterials, is

needed to suit a specific organometallic catalysis. Such insights will assist in future *a priori* design of compartmentalized organometallics for enhanced catalytic performance. Moreover, the developed quantitative model is applicable to any general catalytic cycle particularly in the liquid phase, because the model includes the general features of any catalysis: multiple reaction steps connected in a cyclic fashion, the existence of turnover-limiting step, the interference from deactivation/competing reactions, and the issue of mass transport in the proximity of active sites. The conclusions and design principles obtained from the reported model is adaptable to suit most if not any catalytic cycles with synthetic compartments and confinements, offering a framework to be expanded on for advanced compartmentalization of general chemical catalysis.

References

1. Hurtley, S., Location, Location, Location. *Science* **2009**, *326*, 1205-1205.
2. Chen, A. H.; Silver, P. A., Designing Biological Compartmentalization. *Trends in Cell Biology* **2012**, *22*, 662-670.
3. Jandt, U.; You, C.; Zhang, Y. H. P.; Zeng, A. P., Compartmentalization and Metabolic Channeling for Multienzymatic Biosynthesis: Practical Strategies and Modeling Approaches. *Adv. Biochem. Eng. Biotechnol.* **2013**, *137*, 41-65.
4. Alam, M. T.; Olin-Sandoval, V.; Stincone, A.; Keller, M. A.; Zelezniak, A.; Luisi, B. F.; Ralser, M., The self-inhibitory nature of metabolic networks and its alleviation through compartmentalization. *Nat. Commun.* **2017**, *8*, 1-13.
5. Avalos, J. L.; Fink, G. R.; Stephanopoulos, G., Compartmentalization of Metabolic Pathways in Yeast Mitochondria Improves the Production of Branched-Chain Alcohols. *Nat. Biotechnol.* **2013**, *31*, 335-341.
6. Tu, B. P., Logic of the Yeast Metabolic Cycle: Temporal Compartmentalization of Cellular Processes. *Science* **2005**, *310*, 1152-1158.
7. Zecchin, A.; Stapor, P. C.; Gouveia, J.; Carmeliet, P., Metabolic pathway compartmentalization: an underappreciated opportunity? *Curr. Opin. Biotechnol.* **2015**, *34*, 73-81.
8. Cannon, G. C.; Bradburne, C. E.; Aldrich, H. C.; Baker, S. H.; Heinhorst, S.; Shively, J. M., Microcompartments in Prokaryotes: Carboxysomes and Related Polyhedra. *Applied and Environmental Microbiology* **2001**, *67*, 5351-5361.

9. Rae, B. D.; Long, B. M.; Whitehead, L. F.; Förster, B.; Badger, M. R.; Price, G. D., Cyanobacterial Carboxysomes: Microcompartments that Facilitate CO₂ Fixation. *J. Mol. Microbiol. Biotechnol.* **2013**, *23*, 300-307.
10. Anderson, K. S.; Miles, E. W.; Johnson, K. A., Serine Modulates Substrate Channeling in Tryptophan Synthase. A Novel Intersubunit Triggering Mechanism. *J. Biol. Chem.* **1991**, *266*, 8020-8033.
11. Chavan, K. S.; Calabrese Barton, S., Simulation of Intermediate Channeling by Nanoscale Confinement. *The Journal of Physical Chemistry C* **2018**, *122*, 14474-14480.
12. Jordan, P. C.; Patterson, D. P.; Saboda, K. N.; Edwards, E. J.; Miettinen, H. M.; Basu, G.; Thielges, M. C.; Douglas, T., Self-Assembling Biomolecular Catalysts for Hydrogen Production. *Nat. Chem.* **2016**, *8*, 179-185.
13. Chen, W.-H.; Vázquez-González, M.; Zoabi, A.; Abu-Reziq, R.; Willner, I., Biocatalytic Cascades Driven by Enzymes Encapsulated in Metal–Organic Framework Nanoparticles. *Nat. Catal.* **2018**, *1*, 689-695.
14. Vázquez-González, M.; Wang, C.; Willner, I., Biocatalytic Cascades Operating on Macromolecular Scaffolds and in Confined Environments. *Nat. Catal.* **2020**, *3*, 256-273.
15. Idan, O.; Hess, H., Origins of Activity Enhancement in Enzyme Cascades on Scaffolds. *ACS Nano* **2013**, *7*, 8658-8665.
16. Zhang, Y.; Hess, H., Toward Rational Design of High-efficiency Enzyme Cascades. *ACS Catal.* **2017**, *7*, 6018-6027.
17. Natinsky, B. S.; Lu, S.; Copeland, E. D.; Quintana, J. C.; Liu, C., Solution Catalytic Cycle of Incompatible Steps for Ambient Air Oxidation of Methane to Methanol. *ACS Cent. Sci.* **2019**, *5*, 1584-1590.

18. Leenders, S. H. A. M.; Gramage-Doria, R.; De Bruin, B.; Reek, J. N. H., Transition Metal Catalysis in Confined Spaces. *Chem. Soc. Rev.* **2015**, *44*, 433-448.
19. Lu, J.; Dimroth, J.; Weck, M., Compartmentalization of Incompatible Catalytic Transformations for Tandem Catalysis. *J. Am. Chem. Soc.* **2015**, *137*, 12984-12989.
20. Rayder, T. M.; Bensalah, A. T.; Li, B.; Byers, J. A.; Tsung, C.-K., Engineering Second Sphere Interactions in a Host–Guest Multicomponent Catalyst System for the Hydrogenation of Carbon Dioxide to Methanol. *J. Am. Chem. Soc.* **2021**, *143*, 1630-1640.
21. Simms, R. W.; Cunningham, M. F., Compartmentalization of Reverse Atom Transfer Radical Polymerization in Miniemulsion. *Macromolecules* **2008**, *41*, 5148-5155.
22. Smeets, N. M. B.; Heuts, J. P. A.; Meuldijk, J.; Cunningham, M. F.; Van Herk, A. M., Evidence of Compartmentalization in Catalytic Chain Transfer Mediated Emulsion Polymerization of Methyl Methacrylate. *Macromolecules* **2009**, *42*, 7332-7341.
23. Wang, K.; Jordan, J. H.; Hu, X. Y.; Wang, L., Supramolecular Strategies for Controlling Reactivity within Confined Nanospaces. *Angew. Chem. Int. Ed.* **2020**, *59*, 13712-13721.
24. Wayland, B. B.; Ba, S.; Sherry, A. E., Activation of Methane and Toluene by Rhodium(II) Porphyrin Complexes. *J. Am. Chem. Soc.* **1991**, *113*, 5305-5311.
25. Hinzpeter, F.; Gerland, U.; Tostevin, F., Optimal Compartmentalization Strategies for Metabolic Microcompartments. *Biophys. J.* **2017**, *112*, 767-779.
26. Tsitkov, S.; Hess, H., Design Principles for a Compartmentalized Enzyme Cascade Reaction. *ACS Catal.* **2019**, *9*, 2432-2439.
27. Berg, H. C., *Random Walks in Biology*. Princeton University Press: 1993.
28. Miessler, G.; Tarr, D., *Inorganic Chemistry, 2004*. Vol. 1, p 2-3.

29. Natinsky, B. S.; Jolly, B. J.; Dumas, D. M.; Liu, C., Efficacy analysis of compartmentalization for ambient CH₄ activation mediated by a Rh^{II} metalloradical in a nanowire array electrode. *Chem. Sci.* **2021**, *12*, 1818-1825.
30. Moritani, I.; Fujiwara, Y., Aromatic substitution of styrene-palladium chloride complex. *Tetrahedron Letters* **1967**, *8*, 1119-1122.
31. Fujiwara, Y.; Moritani, I.; Danno, S.; Asano, R.; Teranishi, S., Aromatic substitution of olefins. VI. Arylation of olefins with palladium (II) acetate. *J. Am. Chem. Soc.* **1969**, *91*, 7166-7169.
32. Negishi, E.; King, A. O.; Okukado, N., Selective carbon-carbon bond formation via transition metal catalysis. 3. A highly selective synthesis of unsymmetrical biaryls and diarylmethanes by the nickel-or palladium-catalyzed reaction of aryl-and benzylzinc derivatives with aryl halides. *The Journal of organic chemistry* **1977**, *42*, 1821-1823.
33. Zhang, H.; Luo, X.; Wongkhan, K.; Duan, H.; Li, Q.; Zhu, L.; Wang, J.; Batsanov, A. S.; Howard, J. A.; Marder, T. B., Acceleration of Reductive Elimination of [Ar-Pd-C] by a Phosphine/Electron-Deficient Olefin Ligand: A Kinetic Investigation. *Chemistry—A European Journal* **2009**, *15*, 3823-3829.
34. Labinger, J. A., Tutorial on Oxidative Addition. *Organometallics* **2015**, *34*, 4784-4795.
35. Breno, K. L.; Pluth, M. D.; Landorf, C. W.; Tyler, D. R., Aqueous Phase Organometallic Catalysis Using (MeCp)₂Mo(OH)(H₂O)⁺. Intramolecular Attack of Hydroxide on Organic Substrates. *Organometallics* **2004**, *23*, 1738-1746.
36. Ellis, P. R.; Pearson, J. M.; Haynes, A.; Adams, H.; Bailey, N. A.; Maitlis, P. M., Oxidative Addition of Alkyl Halides to Rhodium(I) and Iridium(I) Dicarbonyl Diiodides:

- Key Reactions in the Catalytic Carbonylation of Alcohols. *Organometallics* **1994**, *13*, 3215-3226.
37. Espenson, J. H.; Pestovsky, O.; Huston, P.; Staudt, S., Organometallic Catalysis in Aqueous Solution: Oxygen Transfer to Bromide. *J. Am. Chem. Soc.* **1994**, *116*, 2869-2877.
38. Ju, T. D.; Lang, R. F.; Roper, G. C.; Hoff, C. D., Oxidative Addition of Butanethiol and Thiophenol to the $\bullet\text{Cr}(\text{CO})_3\text{C}_5\text{Me}_5$ Radical. Kinetic and Thermodynamic Study of a Third-Order Reaction and Its Catalysis. *J. Am. Chem. Soc.* **1996**, *118*, 5328-5329.
39. Heiden, Z. M.; Rauchfuss, T. B., Homogeneous Catalytic Reduction of Dioxygen Using Transfer Hydrogenation Catalysts. *J. Am. Chem. Soc.* **2007**, *129*, 14303-14310.
40. Astruc, D., *Organometallic chemistry and catalysis*. Springer: 2007; Vol. 291.
41. Crabtree, R. H., Deactivation in Homogeneous Transition Metal Catalysis: Causes, Avoidance, and Cure. *Chem. Rev.* **2015**, *115*, 127-150.
42. Meißner, A.; Alberico, E.; Drexler, H.-J.; Baumann, W.; Heller, D., Rhodium diphosphine complexes: a case study for catalyst activation and deactivation. *Catal. Sci. Technol.* **2014**, *4*, 3409-3425.
43. Stein, W., *Transport and diffusion across cell membranes*. Elsevier Inc.: 1986.
44. Ford, P. C.; Massick, S., Time Resolved Spectroscopic Studies Relevant to Reactive Intermediates in Homogeneous Catalysis. The Migratory Insertion Reaction. *Coord. Chem. Rev.* **2002**, *226*, 39-49.
45. Massick, S. M.; Ford, P. C., Use of a High-Pressure/Variable-Temperature Infrared Flow Cell To Examine the Reaction Kinetics of the Migratory Insertion Intermediate ($\eta^5\text{-C}_5\text{H}_5$)Fe(CO)C(O)CH₃ by Time-Resolved Spectroscopy. *Organometallics* **1999**, *18*, 4362-4366.

46. Nilsson, P.; Wendt, O. F., Kinetic Investigation of a PC(sp^3)P pincer palladium (II) complex in the Heck reaction. *J. Organomet. Chem.* **2005**, *690*, 4197-4202.
47. Jin, L.; Zhang, H.; Li, P.; Sowa Jr, J. R.; Lei, A., What is the Rate of the Csp²–Csp² Reductive Elimination Step? Revealing an Unusually Fast Ni-Catalyzed Negishi-Type Oxidative Coupling Reaction. *J. Am. Chem. Soc.* **2009**, *131*, 9892-9893.
48. Pregosin, P. S.; Kumar, P. G. A.; Fernández, I., Pulsed Gradient Spin–Echo (PGSE) Diffusion and ¹H,¹⁹F Heteronuclear Overhauser Spectroscopy (HOESY) NMR Methods in Inorganic and Organometallic Chemistry: Something Old and Something New. *Chem. Rev.* **2005**, *105*, 2977-2998.
49. Drago, D.; Pregosin, P. S.; Pfaltz, A., Selective anion effects in chiral complexes of iridium via diffusion and HOESY data: relevance to catalysis. *Chem. Commun.* **2002**, 286-287.
50. Bender, T. A.; Morimoto, M.; Bergman, R. G.; Raymond, K. N.; Toste, F. D., Supramolecular Host-Selective Activation of Iodoarenes by Encapsulated Organometallics. *J. Am. Chem. Soc.* **2019**, *141*, 1701-1706.
51. Qu, P.; Kuepfert, M.; Hashmi, M.; Weck, M., Compartmentalization and Photoregulating Pathways for Incompatible Tandem Catalysis. *J. Am. Chem. Soc.* **2021**, *143*, 4705-4713.
52. Huang, C.; Liu, C.; Chen, X.; Xue, Z.; Liu, K.; Qiao, X.; Li, X.; Lu, Z.; Zhang, L.; Lin, Z.; Wang, T., A Metal–Organic Framework Nanosheet-Assembled Frame Film with High Permeability and Stability. *Advanced Science* **2020**, *7*, 1903180.
53. Li, W.; Zhang, Y.; Xu, Z.; Meng, Q.; Fan, Z.; Ye, S.; Zhang, G., Assembly of MOF Microcapsules with Size-Selective Permeability on Cell Walls. *Angew Chem Int Ed Engl* **2016**, *55*, 955-9.

54. Lei, L.; Zhang, Q.; Shi, S.; Zhu, S., Breathable Microgel Colloidosome: Gas-Switchable Microcapsules with O₂ and CO₂ Tunable Shell Permeability for Hierarchical Size-Selective Control Release. *Langmuir* **2017**, *33*, 6108-6115.
55. Haldoupis, E.; Watanabe, T.; Nair, S.; Sholl, D. S., Quantifying Large Effects of Framework Flexibility on Diffusion in MOFs: CH₄ and CO₂ in ZIF-8. *ChemPhysChem* **2012**, *13*, 3449-3452.
56. Dong, B.; Mansour, N.; Huang, T.-X.; Huang, W.; Fang, N., Single molecule fluorescence imaging of nanoconfinement in porous materials. *Chem. Soc. Rev.* **2021**, *50*, 6483-6506.
57. Dong, B.; Pei, Y.; Zhao, F.; Goh, T. W.; Qi, Z.; Xiao, C.; Chen, K.; Huang, W.; Fang, N., In situ quantitative single-molecule study of dynamic catalytic processes in nanoconfinement. *Nat. Catal.* **2018**, *1*, 135-140.
58. Jung, C.; Kirstein, J.; Platschek, B.; Bein, T.; Budde, M.; Frank, I.; Müllen, K.; Michaelis, J.; Bräuchle, C., Diffusion of oriented single molecules with switchable mobility in networks of long unidimensional nanochannels. *J. Am. Chem. Soc.* **2008**, *130*, 1638-1648.
59. Feil, F.; Cauda, V.; Bein, T.; Bräuchle, C., Direct visualization of dye and oligonucleotide diffusion in silica filaments with collinear mesopores. *Nano Lett.* **2012**, *12*, 1354-1361.
60. Mulligan, C. J.; Parker, J. S.; Hii, K. K., Revisiting the mechanism of the Fujiwara–Moritani reaction. *Reaction Chemistry & Engineering* **2020**, *5*, 1104-1111.
61. Ferlin, F.; Anastasiou, I.; Carpisassi, L.; Vaccaro, L., Aerobic waste-minimized Pd-catalysed C–H alkenylation in GVL using a tube-in-tube heterogeneous flow reactor. *Green Chem.* **2021**, *23*, 6576-6582.

Supplementary Information

Kinetic models for compartmentalized and non-compartmentalized scenarios with assumptions stated in the main text

The steps of a chosen general catalytic cycle are shown in Figure 2.1A and are outlined in the main text. Here, C_{Cat} represents the concentration of the initial catalyst in bulk. C_{Cat} is assumed to be present in excess of $[Cat]$, which represents the initial catalyst concentration in the compartment. Therefore, C_{Cat} is assumed to negligibly change during the course of the cascade catalysis, and it is thus treated as a constant.

Mathematical derivation of compartmentalized scenarios

Here, we solve for key reaction metrics for a compartmentalized catalytic cycle under the assumptions stated in the first section of the results and discussion of the main text. The steady state kinetic equations for catalytic species in the compartmentalized system are:

$$\frac{d[Cat]}{dt} = F_V(C_{Cat} - [Cat]) + k_3[Cat - B] - k_1[Cat]^m C_A = 0 \quad (S1)$$

$$\frac{d[Cat - A]}{dt} = -F_V([Cat - A] - [Cat - A]_b) + k_1[Cat]^m C_A - k_2[Cat - A] = 0 \quad (S2)$$

$$\frac{d[Cat - A]_b}{dt} = F_V([Cat - A] - [Cat - A]_b) - k_{e2}[Cat - A]_b = 0 \quad (S3)$$

$$\frac{d[Cat - B]}{dt} = -F_V([Cat - B] - [Cat - B]_b) + k_2[Cat - A] - k_3[Cat - B] = 0 \quad (S4)$$

$$\frac{d[Cat - B]_b}{dt} = F_V([Cat - B] - [Cat - B]_b) - k_{e3}[Cat - B]_b = 0 \quad (S5)$$

Expressions for F_V and $k_{e2/3}$ are shown in Section S3. From Equation S5, $[Cat - B]_b$ may be solved for:

$$F_V[Cat - B] - F_V[Cat - B]_b - k_{e3}[Cat - B]_b = 0 \quad (S6)$$

$$F_V[Cat - B] = F_V[Cat - B]_b + k_{e3}[Cat - B]_b \quad (S7)$$

$$[Cat - B]_b(F_V + k_{e3}) = F_V[Cat - B] \quad (S8)$$

$$[Cat - B]_b = \frac{F_V[Cat - B]}{F_V + k_{e3}} \quad (S9)$$

Inputting Equation S9 into Equation S4, $[Cat - B]$ may be solved for:

$$-F_V[Cat - B] + F_V[Cat - B]_b + k_2[Cat - A] - k_3[Cat - B] = 0 \quad (S10)$$

$$k_2[Cat - A] = F_V[Cat - B] - F_V[Cat - B]_b + k_3[Cat - B] \quad (S11)$$

$$k_2[Cat - A] = F_V[Cat - B] - F_V \left(\frac{F_V[Cat - B]}{F_V + k_{e3}} \right) + k_3[Cat - B] \quad (S12)$$

$$k_2[Cat - A] = [Cat - B] \left(F_V - \frac{F_V^2}{F_V + k_{e3}} + k_3 \right) \quad (S13)$$

$$[Cat - B] = \frac{k_2[Cat - A]}{\frac{F_V k_{e3}}{F_V + k_{e3}} + k_3} \quad (S14)$$

$$f_n = \frac{F_V k_{en}}{F_V + k_{en}} \quad (S15)$$

$$[Cat - B] = \frac{k_2[Cat - A]}{f_3 + k_3} \quad (S16)$$

From Equation S3, $[Cat - A]_b$ may be solved for:

$$F_V([Cat - A] - [Cat - A]_b) - k_{e2}[Cat - A]_b = 0 \quad (S17)$$

$$F_V[Cat - A] - F_V[Cat - A]_b - k_{e2}[Cat - A]_b = 0 \quad (S18)$$

$$F_V[Cat - A] = [Cat - A]_b(F_V + k_{e2}) \quad (S19)$$

$$[Cat - A]_b = \frac{F_V[Cat - A]}{F_V + k_{e2}} \quad (S20)$$

Inputting Equation S20 into Equation S2, $[Cat - A]$ may be solved for:

$$-F_V([Cat - A] - [Cat - A]_b) + k_1[Cat]^m[A] - k_2[Cat - A] = 0 \quad (S21)$$

$$k_1[Cat]^m C_A = F_V[Cat - A] - F_V[Cat - A]_b + k_2[Cat - A] \quad (S22)$$

$$k_1[Cat]^m C_A = F_V[Cat - A] - F_V \left(\frac{F_V[Cat - A]}{F_V + k_{e2}} \right) + k_2[Cat - A] \quad (S23)$$

$$[Cat - A] = \frac{k_1[Cat]^m C_A}{F_V - \frac{F_V^2}{F_V + k_{e2}} + k_2} \quad (S24)$$

$$[Cat - A] = \frac{k_1[Cat]^m C_A}{f_2 + k_2} \quad (S25)$$

Rearranging S1 to solve for $[Cat]$ when $m = 1, 2$

$$F_V(C_{Cat} - [Cat]) + k_3[Cat - B] - k_1[Cat]^m C_A = 0 \quad (S26)$$

$$k_1[Cat]^m C_A + F_V[Cat] - F_V C_{Cat} - k_3[Cat - B] = 0 \quad (S27)$$

Input solution for $[Cat - B]$ (S16) and $[Cat - A]$ (S25)

$$k_1[Cat]^m C_A + F_V[Cat] - F_V C_{Cat} - k_3 \left(\frac{k_2[Cat - A]}{f_3 + k_3} \right) = 0 \quad (S28)$$

$$k_1[Cat]^m C_A + F_V[Cat] - F_V C_{Cat} - \frac{k_1 k_2 k_3 [Cat]^m C_A}{(f_2 + k_2)(f_3 + k_3)} = 0 \quad (S29)$$

$$\left(k_1 C_A - \frac{k_1 k_2 k_3 C_A}{(f_2 + k_2)(f_3 + k_3)} \right) [Cat]^m + F_V[Cat] - F_V C_{Cat} = 0 \quad (S30)$$

$$\text{defining } a_1 = k_1 C_A - \frac{k_1 k_2 k_3 C_A}{(f_2 + k_2)(f_3 + k_3)} \quad (S31)$$

When $m = 1$

$$a_1[Cat] + F_V[Cat] - F_V C_{Cat} = 0 \quad (S32)$$

$$(a_1 + F_V)[Cat] = F_V C_{Cat} \quad (S33)$$

$$[Cat] = \frac{F_V C_{Cat}}{a_1 + F_V} \quad (S34)$$

When $m = 2$

$$a_1[Cat]^2 + F_V[Cat] - F_V C_{Cat} = 0 \quad (S35)$$

$$[Cat] = \frac{-F_V \pm \sqrt{F_V^2 - 4(a_1)(-F_V C_{Cat})}}{2a_1} \quad (S36)$$

$$[Cat] = \frac{-F_V + \sqrt{F_V^2 + 4a_1 F_V C_{Cat}}}{2a_1} \quad (S37)$$

Key Reaction Metrics: Compartmentalized

$$R_{S,m} = k_1 [Cat]^m C_A \quad (S38)$$

$$R_{I,m} = F_V ([Cat - A] - [Cat - A]_b) \quad (S39)$$

$$R_{P,m} = k_3 [Cat - B] \quad (S40)$$

$$\gamma_m = \frac{R_{P,m}}{R_{S,m}} \quad (S41)$$

$$TOF_m = \frac{R_{P,m}}{m C_{Cat}} \quad (S42)$$

Solving for R_S when $m = 1$ by inputting S34 into S38

$$R_{S,m=1} = k_1 [Cat] C_A \quad (S43)$$

$$R_{S,m=1} = \frac{k_1 F_V C_{Cat} C_A}{a_1 + F_V} \quad (S44)$$

Solving for R_S when $m = 2$ by inputting S37 into S38

$$R_{S,m=2} = k_1 [Cat]^2 C_A \quad (S45)$$

$$R_{S,m=2} = k_1 \left(\frac{-F_V + \sqrt{F_V^2 + 4a_1 F_V C_{Cat}}}{2a_1} \right)^2 C_A \quad (S46)$$

Simplifying R_I (S39)

$$R_{I,m} = F_V \left(\frac{k_1 [Cat]^m C_A}{f_2 + k_2} - \frac{F_V \left(\frac{k_1 [Cat]^m C_A}{f_2 + k_2} \right)}{F_V + k_{e2}} \right) \quad (S47)$$

$$R_{I,m} = F_V k_1 [Cat]^m C_A \left(\frac{1}{f_2 + k_2} - \frac{F_V}{(f_2 + k_2)(F_V + k_{e2})} \right) \quad (S48)$$

$$R_{I,m} = \frac{k_1 k'_{e2} F_V [Cat]^m C_A}{(f_2 + k_2)(F_V + k_{e2})} \quad (S49)$$

Solving for R_I when $m = 1$ by inputting S34 into S49

$$R_{I,m=1} = \left(\frac{k_1 k_{e2} F_V C_A}{(f_2 + k_2)(F_V + k_{e2})} \right) [Cat] \quad (S50)$$

$$R_{I,m=1} = \frac{k_1 k_{e2} F_V^2 C_{cat} C_A}{(a_1 + F_V)(f_2 + k_2)(F_V + k_{e2})} \quad (S51)$$

Solving for R_I when $m = 2$ by inputting S37 into S49

$$R_{I,m=2} = \left(\frac{k_1 k_{e2} F_V C_A}{(f_2 + k_2)(F_V + k_{e2})} \right) [Cat]^2 \quad (S52)$$

$$R_{I,m=2} = \frac{k_1 k_{e2} F_V C_A}{(f_2 + k_2)(F_V + k_{e2})} \left(\frac{-F_V + \sqrt{F_V^2 + 4a_1 F_V C_{cat}}}{2a_1} \right)^2 \quad (S53)$$

Simplifying R_P (S40)

$$R_{P,m} = k_3 [Cat - B] \quad (S54)$$

$$R_{P,m} = \frac{k_1 k_2 k_3 [Cat]^m C_A}{(f_2 + k_2)(f_3 + k_3)} \quad (S55)$$

Solving for R_P when $m = 1$ by inputting S34 into S55

$$R_{P,m=1} = \frac{k_1 k_2 k_3 C_A}{(f_2 + k_2)(f_3 + k_3)} [Cat] \quad (S56)$$

$$R_{P,m=1} = \frac{k_1 k_2 k_3 F_V C_{cat} C_A}{(a_1 + F_V)(f_2 + k_2)(f_3 + k_3)} \quad (S57)$$

Solving for R_P when $m = 2$ by inputting S37 into S55

$$R_{P,m=2} = \frac{k_1 k_2 k_3 C_A}{(f_2 + k_2)(f_3 + k_3)} [Cat]^2 \quad (S59)$$

$$R_{P,m=2} = \frac{k_1 k_2 k_3 C_A}{(f_2 + k_2)(f_3 + k_3)} \left(\frac{-F_V + \sqrt{F_V^2 + 4a_1 F_V C_{cat}}}{2a_1} \right)^2 \quad (S60)$$

Solving for γ (S41)

$$\gamma_m = \frac{k_3 [Cat - B]}{k_1 [Cat]^m [A]} \quad (S61)$$

$$\gamma_m = \frac{k_3 \left(\frac{k_2 [Cat - A]}{f_3 + k_3} \right)}{k_1 [Cat]^m [A]} \quad (S62)$$

$$\gamma_m = \frac{k_2 k_3 \left(\frac{k_1 [Cat]^m C_A}{f_2 + k_2} \right)}{k_1 [Cat]^m [A] (f_3 + k_3)} \quad (S63)$$

$$\gamma = \frac{k_2 k_3}{(f_2 + k_2)(f_3 + k_3)} \quad (S64)$$

Solving for TOF_m when $m = 1, 2$ by inputting S57 or S60 into S42

$$TOF_{m=1} = \frac{k_1 k_2 k_3 F_V C_A}{(a_1 + F_V)(f_2 + k_2)(f_3 + k_3)} \quad (S65)$$

$$TOF_{m=2} = \frac{k_1 k_2 k_3 C_A}{2C_{Cat}(f_2 + k_2)(f_3 + k_3)} \left(\frac{-F_V + \sqrt{F_V^2 + 4a_1 F_V C_{Cat}}}{2a_1} \right)^2 \quad (S66)$$

Mathematical derivation of non-compartmentalized scenarios

The rates of species within the general catalytic cycle under the non-compartmentalized framework are generated by dropping diffusive (F_V) terms and bulk concentrations from the compartmentalized framework to generate the following under steady state:

$$\frac{d[Cat]}{dt} = k_3[Cat - B] - k_1[Cat]^m C_A = 0 \quad (S67)$$

$$\frac{d[Cat - A]}{dt} = k_1[Cat]^m C_A - k_2[Cat - A] - k_{e2}[Cat - A] = 0 \quad (S68)$$

$$\frac{d[Cat - B]}{dt} = k_2[Cat - A] - k_3[Cat - B] - k_{e3}[Cat - B] = 0 \quad (S69)$$

Solving for $[Cat - B]$ from S69

$$k_2[Cat - A] - k_3[Cat - B] - k_{e3}[Cat - B] = 0 \quad (S70)$$

$$[Cat - B](k_3 + k_{e3}) = k_2[Cat - A] \quad (S71)$$

$$[Cat - B] = \frac{k_2[Cat - A]}{k_3 + k_{e3}} \quad (S72)$$

Solving for $[Cat - A]$ from S68

$$k_1[Cat]^m C_A - k_2[Cat - A] - k_{e2}[Cat - A] = 0 \quad (S73)$$

$$[Cat - A](k_2 + k_{e2}) = k_1[Cat]^m C_A \quad (S74)$$

$$[Cat - A] = \frac{k_1[Cat]^m C_A}{k_2 + k_{e2}} \quad (S75)$$

Key Reaction Metrics: Non-Compartmentalized

$$R_{S,m} = k_1[Cat]^m C_A \quad (S38)$$

$$R_{I,m} = k_{e2}[Cat - A] \quad (S76)$$

$$R_{P,m} = k_3[Cat - B] \quad (S40)$$

$$\gamma_m = \frac{R_{P,m}}{R_{S,m}} \quad (S41)$$

$$TOF_m = \frac{R_{P,m}}{m[Cat]} \quad (S42)$$

Solving for R_I where $m = 1, 2$ by inputting S75 into S76

$$R_I = k_{e2}[Cat - A] \quad (S77)$$

$$R_I = k_{e2} \left(\frac{k_1[Cat]^m C_A}{k_2 + k_{e2}} \right) \quad (S78)$$

$$R_I = \frac{k_1 k_{e2} [Cat]^m C_A}{k_2 + k_{e2}} \quad \text{with } m = 1, 2 \quad (S79)$$

Solving for $R_{P3,m}$ where $m = 1, 2$ by inputting S72 into S40

$$R_{P,m} = k_3[Cat - B] \quad (S80)$$

$$R_{P,m} = k_3 \left(\frac{k_1 k_2 [Cat]^m C_A}{(k_2 + k_{e2})(k_3 + k_{e3})} \right) \quad (S81)$$

$$R_{P,m} = \frac{k_1 k_2 [Cat]^m C_A}{(k_2 + k_{e2})(k_3 + k_{e3})} \quad m = 1, 2 \quad (S82)$$

Solving for γ_m

$$\gamma_m = \frac{k_3[Cat - B]}{k_1[Cat]^m C_A} \quad (S83)$$

$$\gamma_m = \frac{k_1 k_2 [Cat]^m C_A}{(k_2 + k_{e2})(k_3 + k_{e3})} \quad (S84)$$

$$\gamma = \frac{k_2 k_3}{(k_2 + k_{e2})(k_3 + k_{e3})} \quad (S85)$$

Solving for TOF_m where $m = 1, 2$ by inputting S82 into S42

$$TOF_{m=1} = \frac{k_1 k_2 k_3 C_A}{(k_2 + k_{e2})(k_3 + k_{e3})} \quad (S86)$$

$$TOF_{m=2} = \frac{k_1 k_2 k_3 [Cat] C_A}{2(k_2 + k_{e2})(k_3 + k_{e3})} \quad (S87)$$

To mirror the assumption made in the prior compartmentalized scenario (section S1A) that C_{Cat} is present in excess of compartmentalized $[Cat]$, here we assume the extent of $[Cat]$ consumption in a non-compartmentalized cycle with deactivations is minimal relative to its regeneration, therefore $[Cat] \approx C_{Cat} = 1$ mM. Limitations associated with this assumption are addressed in section S3 by introducing a $C_{Cat, total}$ term and are shown to yield negligible difference in mechanistic conclusions.

Derivation of F_V for a nanowire array as a nanoscopic compartment in solution

We expand on our previous derivation of term $F_V = F/VN_A$, where F is diffusive conductance in $M s^{-1}$, V is either the volume of the compartment or the bulk (denoted V_b), and N_A is Avogadro's number.^{1,2} In brief, F is defined as the product of compartment permeability (ρ), surface area (SA),

and Avogadro's number (N_A). We define permeability in terms diffusion coefficient (D), diffusion path to enter the compartment (Δx), and nanowire length (L) as follows:

$$\rho \approx \frac{D}{\Delta x} \quad (\text{S88})$$

We approximate that the compartment is established roughly halfway down the wire based on our prior work, therefore $\Delta x \sim 0.5 \times L$.⁴ Combining p with SA and N_A , we obtain:

$$F \approx \frac{D * SA * N_A}{0.5 * L} \quad (\text{S89})$$

In order to obtain the flux of particular species, we normalize F to $V \times N_A$, which we define as F_V . We derive V in terms of $0.5 \times SA$ and length of the compartment along the nanowire, $L - \Delta x = 0.5 \times L$, to obtain:

$$F_V = \frac{F}{VN_A} \approx \frac{\frac{D \times SA \times N_A}{0.5 * L}}{0.5 \times SA \times 0.5 \times L \times N_A} \approx \frac{8D}{L^2} \quad (\text{S90})$$

We make a first order approximation where substrate and product molecules A and B are relatively small, therefore D is not significantly changed throughout the course of the cycle and we assume all catalytic species have the same D and flux governed by the same F_V value.⁴ In the example of a nanowire array, F_V is only a function of nanowire length L . We suspect that this approximation may be extended to other processes to tune F_V solely based on nanostructure geometry. However, we note one limitation of this derivation of F_V is that it assumes equal probability for a molecule to diffuse in and out of the compartment at every nanowire length. Our approach to reconcile this issue is to take an integral weighted average of F_V at each nanowire length. Therefore, we use the following expression to explicitly calculate F_V at various L , ranging from 10 – 50 μm based on previous experimental work.⁴

$$\frac{\int_L^0 F_V(L)w(L)dL}{\int_L^0 w(L) dL} \quad (\text{S91})$$

To account for bulk volume (V_b) in deactivation steps, we introduce k'_{en} terms for the compartmentalized system, using $Cat - A$ as an example.

$$\frac{d[Cat - A]}{dt} = \frac{F}{V_b N_A} ([Cat - A] - [Cat - A]_b) - k_{e2} [Cat - A]_b = 0 \quad (\text{S92})$$

$$\frac{d[Cat - A]}{dt} = \frac{F}{V N_A} ([Cat - A] - [Cat - A]_b) - k_{e2} \frac{V_b}{V} [Cat - A]_b = 0 \quad (\text{S93})$$

$$\frac{d[Cat - A]}{dt} = F_V ([Cat - A] - [Cat - A]_b) - k'_{e2} [Cat - A]_b = 0 \quad (\text{S94})$$

$$k'_{en} = k_{en} \frac{V_b}{V} \quad (\text{S95})$$

By using k'_{en} ($n = 2, 3$), we allow the previous F_V equation with the volume of the compartment and subsequent calculations to be utilized throughout the model. In addition, we make a similar approximation that $k'_{en} \approx k_n$ for eliminations to be considered. For simplicity, only k_{en} is listed in the main text and throughout the derivations, however for compartmentalized systems, k'_{en} should be used.

Kinetic models for compartmentalized and non-compartmentalized scenarios for model

$C_{Cat,total}$

We note the assumption that initial catalyst concentration in the bulk ($[Cat]_b$) does not change over time and that C_{Cat} may be used as a constant may not always hold true. Here in this scenario, we introduce $[Cat]_b$ and $C_{Cat,total}$ terms to avoid treating catalyst concentration as a constant.

Mathematical derivation of compartmentalized scenarios for model $C_{Cat,total}$

Equations S1 – S5 are the same, however we introduce eq S88 to account for $[Cat]_b$ and $C_{Cat,total}$.

$$\frac{d[Cat]}{dt} = -F_V([Cat] - [Cat]_b) + k_3[Cat - B] - k_1[Cat]^m C_A = 0 \quad (S1)$$

$$\frac{d[Cat - A]}{dt} = -F_V([Cat - A] - [Cat - A]_b) + k_1[Cat]^m C_A - k_2[Cat - A] = 0 \quad (S2)$$

$$\frac{d[Cat - A]_b}{dt} = F_V([Cat - A] - [Cat - A]_b) - k_{e2}[Cat - A]_b = 0 \quad (S3)$$

$$\frac{d[Cat - B]}{dt} = -F_V([Cat - B] - [Cat - B]_b) + k_2[Cat - A] - k_3[Cat - B] = 0 \quad (S4)$$

$$\frac{d[Cat - B]_b}{dt} = F_V([Cat - B] - [Cat - B]_b) - k_{e3}[Cat - B]_b = 0 \quad (S5)$$

$$C_{Cat,total} = [Cat] + [Cat]_b + [Cat - A] + [Cat - A]_b + [Cat - B] + [Cat - B]_b \quad (S96)$$

Expressions for $[Cat - A]$ (S25), $[Cat - A]_b$ (S20), $[Cat - B]$ (S16), and $[Cat - B]_b$ (S9) are unchanged from the scenario without $C_{Cat,total}$. Now solving for $[Cat]_b$ from S96:

$$[Cat]_b = \frac{C_{Cat,total}}{[Cat] + [Cat - A] + [Cat - A]_b + [Cat - B] + [Cat - B]_b} \quad (S97)$$

$$[Cat]_b = \frac{C_{Cat,total}}{[Cat] + \left(\frac{k_1[Cat]^m C_A}{f_2 + k_2}\right) + \left(\frac{F_V[Cat - A]}{F_V + k_{e2}}\right) + \left(\frac{k_1 k_2 k_3 [Cat]^m C_A}{(f_2 + k_2)(f_3 + k_3)}\right) + \frac{F_V[Cat - B]}{F_V + k_{e3}}} \quad (S98)$$

$$[Cat]_b = \frac{C_{Cat,total}}{[Cat] + \frac{k_1[Cat]^m C_A}{f_2 + k_2} + \frac{k_1 F_V [Cat]^m C_A}{(f_2 + k_2)(F_V + k_{e2})} + \frac{k_1 k_2 k_3 [Cat]^m C_A}{(f_2 + k_2)(f_3 + k_3)} + \frac{k_1 k_2 k_3 F_V [Cat]^m C_A}{(f_2 + k_2)(f_3 + k_3)(F_V + k_{e3})}} \quad (S99)$$

Solving for $[Cat]_b$ when $m = 1$:

$$[Cat]_{b,m=1} = \frac{C_{Cat,total}}{[Cat] \left(1 + \frac{k_1 C_A}{f_2 + k_2} + \frac{k_1 F_V C_A}{(f_2 + k_2)(F_V + k_{e2})} + \frac{k_1 k_2 k_3 C_A}{(f_2 + k_2)(f_3 + k_3)} + \frac{k_1 k_2 k_3 F_V C_A}{(f_2 + k_2)(f_3 + k_3)(F_V + k_{e3})}\right)} \quad (S100)$$

$$a_2 = 1 + \frac{k_1 C_A}{f_2 + k_2} + \frac{k_1 F_V C_A}{(f_2 + k_2)(F_V + k_{e2})} + \frac{k_1 k_2 k_3 C_A}{(f_2 + k_2)(f_3 + k_3)} + \frac{k_1 k_2 k_3 F_V C_A}{(f_2 + k_2)(f_3 + k_3)(F_V + k_{e3})} \quad (S101)$$

$$[Cat]_b = \frac{C_{Cat,total}}{a_2} [Cat]^{-1} \quad (S102)$$

Solving for $[Cat]$ when $m = 1$:

$$-F_V([Cat] - [Cat]_b) + k_3[Cat - B] - k_1[Cat]C_A = 0 \quad (S103)$$

$$-F_V[Cat] + F_V \left(\frac{C_{Cat,total}}{a_2} [Cat]^{-1} \right) + \frac{k_1 k_2 k_3 [Cat] C_A}{(f_2 + k_2)(f_3 + f_3)} - k_1 [Cat] C_A = 0 \quad (S104)$$

$$-F_V[Cat] + F_V \left(\frac{C_{Cat,total}}{a_2} [Cat]^{-1} \right) + a_1 [Cat] = 0 \quad (S105)$$

$$-F_V[Cat]^2 + \frac{F_V C_{Cat,total}}{a_2} + a_1 [Cat]^2 = 0 \quad (S106)$$

$$[Cat]^2 (F_V - a_1) = \frac{F_V C_{Cat,total}}{a_2} \quad (S107)$$

$$[Cat] = \sqrt{\frac{F_V C_{Cat,total}}{a_2 (F_V - a_1)}} \quad (S108)$$

Solving for $[Cat]_b$ when $m = 2$:

$$[Cat]_{b,m=2} = \frac{C_{Cat,total}}{[Cat] + \frac{k_1 [Cat]^2 C_A}{f_2 + k_2} + \frac{k_1 F_V [Cat]^2 C_A}{(f_2 + k_2)(F_V + k_{e2})} + \frac{k_1 k_2 k_3 [Cat]^2 C_A}{(f_2 + k_2)(f_3 + f_3)} + \frac{k_1 k_2 k_3 F_V [Cat]^2 C_A}{(f_2 + k_2)(f_3 + f_3)(F_V + k_{e3})}} \quad (S109)$$

$$[Cat]_{b,m=2} = \frac{C_{Cat,total}}{[Cat] + [Cat]^2 \left(\frac{k_1 C_A}{f_2 + k_2} + \frac{k_1 F_V C_A}{(f_2 + k_2)(F_V + k_{e2})} + \frac{k_1 k_2 k_3 C_A}{(f_2 + k_2)(f_3 + f_3)} + \frac{k_1 k_2 k_3 F_V C_A}{(f_2 + k_2)(f_3 + f_3)(F_V + k_{e3})} \right)} \quad (S110)$$

$$a_3 = \frac{k_1 C_A}{f_2 + k_2} + \frac{k_1 F_V C_A}{(f_2 + k_2)(F_V + k_{e2})} + \frac{k_1 k_2 k_3 C_A}{(f_2 + k_2)(f_3 + f_3)} + \frac{k_1 k_2 k_3 F_V C_A}{(f_2 + k_2)(f_3 + f_3)(F_V + k_{e3})} \quad (S111)$$

$$[Cat]_{b,m=2} = C_{Cat,total} ([Cat] + a_3 [Cat]^2)^{-1} \quad (S112)$$

Solving for $[Cat]$ when $m = 2$:

$$-F_V([Cat] - [Cat]_b) + k_3[Cat - B] - k_1[Cat]C_A = 0 \quad (S113)$$

$$-F_V[Cat] + F_V(C_{Cat,total}([Cat] + a_3[Cat]^2)^{-1}) + \frac{k_1k_2k_3[Cat]C_A}{(f_2 + k_2)(f_3 + f_3)} - k_1[Cat]C_A = 0 \quad (S114)$$

$$-F_V[Cat] + F_V(C_{Cat,total}([Cat] + a_3[Cat]^2)^{-1}) + a_1[Cat] = 0 \quad (S115)$$

$$-F_V[Cat]([Cat] + a_3[Cat]^2) + F_VC_{Cat,total} + a_1[Cat]([Cat] + a_3[Cat]^2) = 0 \quad (S116)$$

$$-F_V[Cat]^2 - F_Va_3[Cat]^3 + F_VC_{Cat,total} + a_1[Cat]^2 + a_3[Cat]^3 = 0 \quad (S117)$$

$$(a_3 - F_V)[Cat]^3 + (a_1 - F_V)[Cat]^2 + F_VC_{Cat,total} = 0 \quad (S118)$$

Defining $b = (a_3 - F_V)$, $c = (a_1 - F_V)$, $d = F_VC_{Cat,total}$, a general solution is:

$$[Cat] = \frac{1}{3} \left(\frac{\sqrt[3]{-27b^2d + 3\sqrt{3}\sqrt{27b^4d^2 + 4b^2c^3d} - 2c^3}}{\sqrt[3]{2b}} + \frac{\sqrt[3]{2c^2}}{b\sqrt[3]{-27b^2d + 3\sqrt{3}\sqrt{27b^4d^2 + 4b^2c^3d} - 2c^3}} - \frac{c}{b} \right) \quad (S119)$$

Key Reaction Metrics: Compartmentalized

$$R_{I,m} = F_V([Cat - A] - [Cat - A]_b) \quad (S39)$$

$$\gamma_m = \frac{R_{P,m}}{R_{S,m}} \quad (\text{S41})$$

$$TOF_m = \frac{R_{P,m}}{m[Cat]_0} \quad (\text{S42})$$

γ does not change from when accounting for $C_{Cat,total}$ as $[Cat - A]$ and $[Cat - B]$ do not change, leaving the solution previously obtained where γ does not depend on $[Cat]$ (S61-64).

Solving for R_I when $m = 1$:

$$R_{I,m} = F_V([Cat - A] - [Cat - A]_b) \quad (\text{S120})$$

Using prior simplification of R_I (S49) since $[Cat - A]$ and $[Cat - A]_b$ do not change:

$$R_{I,m} = \frac{k_1 k_{e2} F_V [Cat]^m C_A}{(f_2 + k_2)(F_V + k_{e2})} \quad (\text{S121})$$

$$R_{I,m=1} = \frac{k_1 k_{e2} F_V C_A}{(f_2 + k_2)(F_V + k_{e2})} \sqrt{\frac{F_V C_{Cat,total}}{a_2(F_V - a_1)}} \quad (\text{S122})$$

Solving for TOF when $m = 1$:

$$TOF_m = \frac{R_{P,m}}{m C_{Cat,total}} \quad (\text{S42})$$

$$TOF_{m=1} = \frac{k_1 k_2 k_3 [Cat] C_A}{C_{Cat,total} (f_2 + k_2) (f_3 + f_3)} \quad (S123)$$

$$TOF_{m=1} = \frac{k_1 k_2 k_3 C_A}{(f_2 + k_2) (f_3 + f_3)} \sqrt{\frac{F_V}{C_{Cat,total} a_2 (F_V - a_1)}} \quad (S124)$$

Mathematical derivation of non-compartmentalized scenarios for model $C_{Cat,total}$

Here, we derive an analogous non-compartmentalized framework under model $C_{Cat,total}$ to compare to the non-compartmentalized scenario derived in section S1B with the original assumptions from the main text. Eq S67 – 69 remain the same, however we introduce eq S125 to solve for $[Cat]$ in terms of $C_{Cat,total}$. We note that again γ is unchanged from Section 1 when accounting for $C_{Cat,total}$ (S64).

$$C_{Cat,total} = [Cat] + [Cat - A] + [Cat - B] \quad (S125)$$

Inputting expressions for $[Cat - A]$ (S75) and $[Cat - B]$ (S72), which are unchanged when accounting for $C_{Cat,total}$.

$$C_{Cat,total} = [Cat] + \frac{k_1 [Cat] C_A}{k_2 + k_{e2}} + \frac{k_1 k_2 [Cat] C_A}{(k_2 + k_{e2})(k_3 + k_{e3})} \quad (S126)$$

$$C_{Cat,total} = [Cat] \left(1 + \frac{k_1 C_A}{k_2 + k_{e2}} + \frac{k_1 k_2 C_A}{(k_2 + k_{e2})(k_3 + k_{e3})} \right) \quad (S127)$$

$$a_4 = 1 + \frac{k_1 C_A}{k_2 + k_{e2}} + \frac{k_1 k_2 C_A}{(k_2 + k_{e2})(k_3 + k_{e3})} \quad (S128)$$

$$[Cat] = \frac{C_{Cat,total}}{a_4} \quad (S129)$$

The non-compartmentalized simplification of R_I (S79) is unchanged, therefore $R_{I,m=1}$ under this scenario can be derived as the following:

$$R_{I,m=1} = \frac{k_1 k_{e2} C_{Cat,total} C_A}{a_4 (k_2 + k_{e2})} \quad (S130)$$

Solving for $TOF_{m=1}$ starting from S42:

$$TOF_{m=1} = \frac{k_1 k_2 k_3 C_A}{a_4 (k_2 + k_{e2}) (k_3 + k_{e3})} \quad (S131)$$

Calculation of γ , TOF, and R_I for tube-in-tube Fujiwara-Mirotani reaction.

In the confines of the kinetic model developed in this study and established mechanistic understanding of Pd catalyzed olefin arylation (Fujiwara-Mirotani),⁵⁻⁷ shown schematically in Figure S2.8 operating in the tube-in-tube reactor,⁸ we arrive at the below steady state compartmentalized expressions. (S132 – S136). We assign the Pd(II) species as Pd , the amide carbonyl coordinated intermediate species as $Pd - A$, and the aryl bound species as $Pd - B$, analogous to the generic Cat , $Cat - A$, and $Cat - B$ species utilized earlier. C_{aryl} refers to the concentration of the aryl substrate, and C_{olefin} represents the concentration of the olefin substrate.

$$\frac{d[Pd]}{dt} = F_V(C_{Pd} - [Pd]) + k_3[Pd - B]C_{olefin} - k_1[Pd]^m C_{aryl} = 0 \quad (S132)$$

$$\frac{d[Pd - A]}{dt} = -F_V([Pd - A] - [Pd - A]_b) + k_1[Pd]^m C_{aryl} - k_2[Pd - A] = 0 \quad (S133)$$

$$\frac{d[Pd - A]_b}{dt} = F_V([Pd - A] - [Pd - A]_b) - k_{e2}[Pd - A]_b = 0 \quad (S134)$$

$$\frac{d[Pd - B]}{dt} = -F_V([Pd - B] - [Pd - B]_b) + k_2[Pd - A] - k_3[Pd - B]C_{olefin} = 0 \quad (S135)$$

$$\frac{d[Pd - B]_b}{dt} = F_V([Pd - B] - [Pd - B]_b) - k_{e3}[Pd - B]_b = 0 \quad (S136)$$

Below are the resultant expressions for compartmentalized γ , R_I , and TOF , with γ being unchanged from S64, and with R_I and TOF containing the appropriate palladium, aryl and olefin substrate concentration terms.

$$\gamma = \frac{k_2 k_3 C_{olefin}}{(f_2 + k_2)(f_3 + k_3 C_{olefin})} \quad (S137)$$

$$R_I = \left(\frac{k_1 k_{e2} F_V C_{aryl}}{(f_2 + k_2)(F_V + k_{e2})} \right) [Pd_{cat}] \quad (S138)$$

$$TOF = \frac{k_1 k_2 k_3 F_V C_{aryl} C_{olefin}}{(a_1 + F_V)(f_2 + k_2)(f_3 + k_3 C_{olefin})} \quad (S139)$$

The expressions for non-compartmentalized γ' , R_I' , and TOF' are as follows.

$$\gamma' = \frac{k_2 k_3 C_{olefin}}{(k_2 + k_{e2})(k_3 C_{olefin} + k_{e3})} \quad (\text{S140})$$

$$R_I' = \frac{k_1 k_{e2} [Pd_{cat}] C_{aryl}}{k_2 + k_{e2}} \quad (\text{S141})$$

$$TOF' = \frac{k_1 k_2 k_3 C_{aryl} C_{olefin}}{(k_2 + k_{e2})(k_3 C_{olefin} + k_{e3})} \quad (\text{S142})$$

An approximate F_V was estimated based the tube-in-tube reactor as follows:

$$F_V = \frac{\left(\frac{D}{\Delta x}\right) SA}{V N_A} \quad (\text{S143})$$

Here, surface area (SA), volume (V), and diffusion path (Δx) are calculated from reported dimensions of the reactor, taken to be cylindrical. Similar to our treatment of a nanowire array generated compartment (Supplementary Information), an average diffusion path of half of the diameter is utilized. Using a representative 2 m long reactor with a radius of 1 mm, as well as an approximate diffusion coefficient (D) on the order of magnitude of $10^{-10} \text{ m}^2 \text{ s}^{-1}$ (see also Supplementary Information for common Pd catalysts diffusion coefficient), F_V is estimated to be 10^{-28} s^{-1} . This is corroborated by Pd leaching studies,⁸ which also lead to $F_V \sim 10^{-28} \text{ s}^{-1}$. This approximate value was determined by converting a typical leaching rate⁸ of 0.1 ppm hr^{-1} to diffusive conductance (F in M s^{-1}), and finally to volumetric diffusive conductance (F_V , in s^{-1}) using $F_V = F/VN_A$.

Kinetic data from was compiled from prior reports,^{6,7} with $k_1 \sim 2 \text{ M}^{-1} \text{ s}^{-1}$, $k_2 \sim 3 \times 10^{-3} \text{ s}^{-1}$, $k_3 \sim 0.15 \text{ M}^{-1} \text{ s}^{-1}$, $k_{e2} \sim 3 \times 10^{-5} \text{ s}^{-1}$, and $k_{e3} \sim 5 \text{ s}^{-1}$. Concentrations were set to 1×10^{-6} , 0.1, and 0.25

M for the Pd catalyst, aryl and olefin substrate respectively, following literature reports at low catalyst loading.^{7,8} Taking the above into consideration, we obtain $\gamma \sim 1$, $R_I \sim 3 \times 10^{-31} \text{ s}^{-1}$, and $TOF \sim 0.5 \text{ s}^{-1}$ for the compartmentalized Fujiwara-Mirotani reaction. The non-compartmentalized treatment in comparison leads to $\gamma \sim 8 \times 10^{-3}$, $R_I \sim 7 \times 10^{-5} \text{ s}^{-1}$, and $TOF \sim 5 \times 10^{-3} \text{ s}^{-1}$. Such an analysis confirms on a theoretical basis the benefits of compartmentalization to this system over a homogeneous analogue and demonstrates the validity of our model. Though we note reported TOF for the tube-in-tube reactor is lower (0.005^{-1}),⁸ suggesting our analysis is an overestimate of true TOF .

Calculation of γ , TOF, and R_I for the Negishi reaction.

In this section, we analyze palladium catalyze cross coupling (Negishi reaction),^{9,10} as a hypothetical compartmentalized system and non-compartmentalized analogue. We arrive at the below equations following its catalytic cycle, shown schematically in Figure S2.9.

$$\frac{d[Pd]}{dt} = F_V(C_{Pd} - [Pd]) + k_3[Pd - B] - k_1[Pd]^m C_{ArI} = 0 \quad (S144)$$

$$\frac{d[Pd - A]}{dt} = -F_V([Pd - A] - [Pd - A]_b) + k_1[Pd]^m C_{ArI} - k_2[Pd - A] C_{CyZnCl} = 0 \quad (S145)$$

$$\frac{d[Pd - A]_b}{dt} = F_V([Pd - A] - [Pd - A]_b) - k_{e2}[Pd - A]_b = 0 \quad (S146)$$

$$\frac{d[Pd - B]}{dt} = -F_V([Pd - B] - [Pd - B]_b) + k_2[Pd - A] C_{CyZnCl} - k_3[Pd - B] = 0 \quad (S147)$$

$$\frac{d[Pd - B]_b}{dt} = F_V([Pd - B] - [Pd - B]_b) - k_{e3}[Pd - B]_b = 0 \quad (S148)$$

Here, the initial catalyst species, $[Pd]$ (typically $Pd(PR_3)X_2$) is labelled as Pd , the aryl iodide bound species post oxidative addition is labelled $Pd - A$, and the aryl cyclohexyl bound species pre reductive elimination is labelled $Pd - B$, with the substrate taken as the aryl iodide (ArI). For the compartmentalized system, we chose to confine this reaction within the metal organic framework (MOF) with formula $\{Cu_6Sr[(S,S)\text{-Mecysmox}]_3(OH)_2(H_2O)\}15H_2O$ (Mecysmox = bis[S-methylcysteine]oxalyl diamide), because it is well characterized and has been shown to stabilize a Pd catalyst within its pores.¹¹ We have averaged the diffusion coefficient based on previous studies on Pd complexes as $6 \times 10^{-10} \text{ m}^2 \cdot \text{s}^{-1}$.¹² An F_V value for this system was approximated accounting for geometric constraints of the MOF compartments¹² using the definition of F_V displayed in Figure 2.1 and discussed in Supplementary Information (eq S143).

$$F_V = \frac{\left(\frac{D}{\Delta x}\right) SA}{VN_A} \quad (\text{S143})$$

Here, surface area (SA), volume (V), and diffusion path (Δx) are calculated from crystallographic data of above mentioned MOF's hexagonal pores, with an average diffusion path (Δx) taken as half the distance needed to enter the pore.¹² Using geometric equations for the surface area and volume of hexagonal prisms, we estimate $F_V \sim 10^{-15} \text{ s}^{-1}$.

Next, applying our kinetic framework for a compartmentalized system, we arrive at the following equations for the Negishi reaction operating within MOFs.

$$\gamma = \frac{k_2 k_3 C_{CyZnCl}}{(f_2 + k_2 C_{CyZnCl})(f_3 + k_3)} \quad (\text{S149})$$

$$R_I = \left(\frac{k_1 k_{e2} F_V C_{ArI}}{(f_2 + k_2 C_{CyZnCl})(F_V + k_{e2})} \right) [Pd] \quad (\text{S150})$$

$$TOF = \frac{k_1 k_2 k_3 F_V C_{ArI} C_{CyZnCl}}{(a_1 + F_V)(f_2 + k_2 C_{CyZnCl})(f_3 + k_3)} \quad (S151)$$

The expressions for non-compartmentalized γ' , R_I' , and TOF' are as follows.

$$\gamma' = \frac{k_2 k_3 C_{CyZnCl}}{(k_2 C_{CyZnCl} + k_{e2})(k_3 + k_{e3})} \quad (S152)$$

$$R_I' = \frac{k_1 k_{e2} [Pd] C_{ArI}}{k_2 C_{CyZnCl} + k_{e2}} \quad (S153)$$

$$TOF' = \frac{k_1 k_2 k_3 C_{ArI} C_{CyZnCl}}{(k_2 C_{CyZnCl} + k_{e2})(k_3 + k_{e3})} \quad (S154)$$

Concentrations were set to 1×10^{-3} , 1×10^{-2} , and 0.1 M for the Pd catalyst, aryl iodide and alkyl zinc chloride substrates respectively, following literature reports.^{9,10} Applying $k_1 \sim 10 \text{ M}^{-1} \text{ s}^{-1}$, $k_2 \sim 3 \text{ M}^{-1} \text{ s}^{-1}$, $k_3 \sim 5 \text{ s}^{-1}$, and $k_{e2} \sim k_{e3} \sim 2 \times 10^{-3} \text{ s}^{-1}$,¹⁰ the Negishi reaction operating within the specified MOF yields $\gamma \sim 1$, $R_I \sim 10^{-19} \text{ s}^{-1}$ and $TOF \sim 0.2$. The homogeneous analogue is predicted to result in $\gamma \sim 0.98$, $R_I \sim 10^{-6} \text{ s}^{-1}$ and $TOF \sim 0.5$. This example serves to demonstrate that when a non-compartmentalized reaction already performs at or near $\gamma \sim 1$ and moderate TOF , with deactivation kinetics being much slower than the kinetics of the catalytic cycle, compartmentalization is not necessary and may even worsen catalytic performance.

Table S2.1 Expressions for compartmentalized and non-compartmentalized key reaction metrics

Physical terms	Scenarios	m ^d	Expression	Equation number
γ^a	Compartmentalized	–	$\frac{k_2 k_3}{(f_2 + k_2)(f_3 + k_3)}$	1, S64
	Non-compartmentalized	–	$\frac{k_2 k_3}{(k_2 + k_{e2})(k_3 + k_{e3})}$	6, S85
R_I^b	Compartmentalized	1	$\frac{k_1 k_{e2} F_V^2 C_{cat} C_A}{(a_1 + F_V)(f_2 + k_2)(F_V + k_{e2})}$	2, S51
		2	$\frac{k_1 k_{e2} F_V C_A}{(f_2 + k_2)(F_V + k_{e2})} \left(\frac{-F_V + \sqrt{F_V^2 + 4a_1 F_V C_{cat}}}{2a_1} \right)^2$	S53
	Non-compartmentalized	1	$\frac{k_1 k_{e2} C_{cat} C_A}{k_2 + k_{e2}}$	7, S79
		2	$\frac{k_1 k_{e2} C_{cat}^2 C_A}{k_2 + k_{e2}}$	S79
TOF^c	Compartmentalized	1	$\frac{k_2 + k_{e2}}{k_1 k_2 k_3 F_V C_A}$	3, S65
		2	$\frac{k_2 + k_{e2}}{(a_1 + F_V)(f_2 + k_2)(f_3 + k_3)}$	S66
	Non-compartmentalized	1	$\frac{k_1 k_2 k_3 C_A}{2C_{cat}(f_2 + k_2)(f_3 + k_3)} \left(\frac{-F_V + \sqrt{F_V^2 + 4a_1 F_V C_{cat}}}{2a_1} \right)^2$	S66
		2	$\frac{k_1 k_2 k_3 C_A}{(k_2 + k_{e2})(k_3 + k_{e3})}$	8, S86
			$\frac{k_1 k_2 k_3 C_{cat} C_A}{2(k_2 + k_{e2})(k_3 + k_{e3})}$	S87

^a γ – reaction efficiency, assesses the ratio of product formation to substrate consumption, ^b R_I – rate of intermediate outflux/elimination, assessment of a compartment’s or freely diffusing system’s tendency to lose a key intermediate to diffusion to the bulk and/or deactivation, ^c TOF – turnover frequency, product turnovers per unit time normalized to catalyst concentration, ^d order with respect to

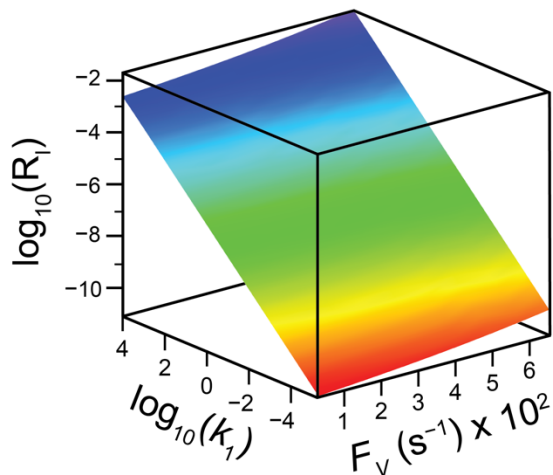
Cat, denoted as $m = 1$ or 2 , describes first or second order dependence of the oxidative addition step on catalyst concentration. Term a_1 is a consolidation of various kinetic and diffusive parameters used for simplicity (equation S31).

Table S2.2 Expressions for compartmentalized and non-compartmentalized key reaction metrics for model $C_{Cat,total}$

Physical terms	Scenarios	m^d	Expression	Equation number
γ^a	Compartmentalized	–	$\frac{k_2 k_3}{(f_2 + k_2)(f_3 + k_3)}$	1, S64
	Non-compartmentalized	–	$\frac{k_2 k_3}{(k_2 + k_{e2})(k_3 + k_{e3})}$	6, S85
R_I^b	Compartmentalized	1	$\frac{k_1 k_{e2} F_V C_A}{(f_2 + k_2)(F_V + k_{e2})} \sqrt{\frac{F_V C_{Cat,total}}{a_2 (F_V - a_1)}}$	S122
	Non-compartmentalized	1	$\frac{k_1 k_{e2} C_{Cat,total} C_A}{a_4 (k_2 + k_{e2})}$	S130
TOF^c	Compartmentalized	1	$\frac{k_1 k_2 k_3 C_A}{(f_2 + k_2)(f_3 + k_3)} \sqrt{\frac{F_V}{C_{Cat,total} a_2 (F_V - a_1)}}$	S124
	Non-compartmentalized	1	$\frac{k_1 k_2 k_3 C_A}{a_4 (k_2 + k_{e2})(k_3 + k_{e3})}$	S131

This alternative mathematical model, while arithmetically more complex, treats the concentration of all catalytic species more rigorously with minimal changes to mechanistic insights compared to the mathematical model used in the main text (compare Figure 2.2B–C, 2.2E–F, 2.3B–C to Supplemental Figures S2.5–2.7). ^a γ – reaction efficiency, assesses the ratio of product formation to substrate consumption, ^b R_I – rate of intermediate outflux/elimination, assessment of a compartment’s or freely diffusing system’s tendency to lose a key intermediate to diffusion to the bulk and/or deactivation, ^c TOF – turnover frequency, product turnovers per unit time normalized to catalyst concentration, ^d order with respect to Cat , denoted as $m = 1$ or 2 , describes first or second order dependence of the oxidative addition step on catalyst concentration. Terms a_1 , a_2 , and a_4 are consolidations of various kinetic and diffusive parameters used for simplicity (equations: a_1 – S31, a_2 – S101, a_4 – S128).

A $\log_{10}(R_{I,m=1}(k_1, F_V))$



B $\log_{10}(R_{I,m=2}(k_1, F_V))$

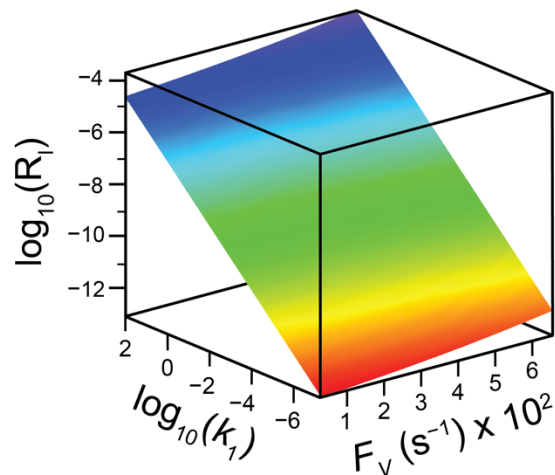
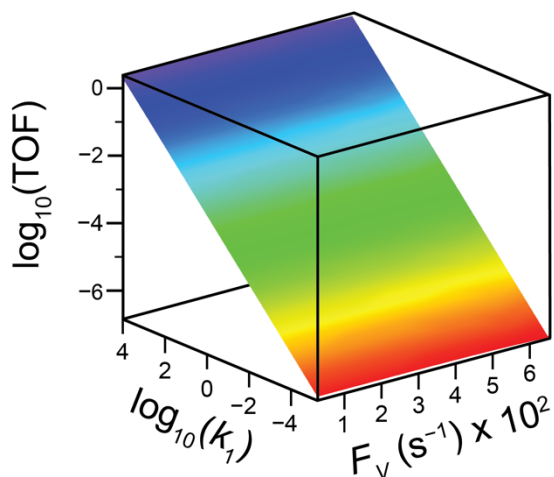


Figure S2.1 Graphical representations of compartmentalized rate of intermediate outflux (R_I) as a function of volumetric diffusive conductance (F_V) and logarithm of rate constant for oxidative addition (k_1) for (A) $m = 1$ and (B) $m = 2$ both set at rate constants for isomerization/migratory insertion and competing *Cat* – A elimination, $k_2 = k_{e2} = 1 \times 10^3 \text{ s}^{-1}$, and rate constants for reductive elimination and competing *Cat* – B elimination $k_3 = k_{e3} = 1 \times 10^6 \text{ s}^{-1}$.

A $\log_{10}(\text{TOF}_{m=1}(k_1, F_V))$



B $\log_{10}(\text{TOF}_{m=2}(k_1, F_V))$

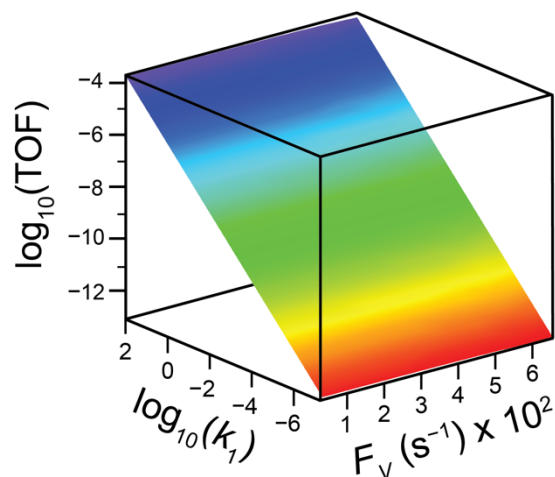
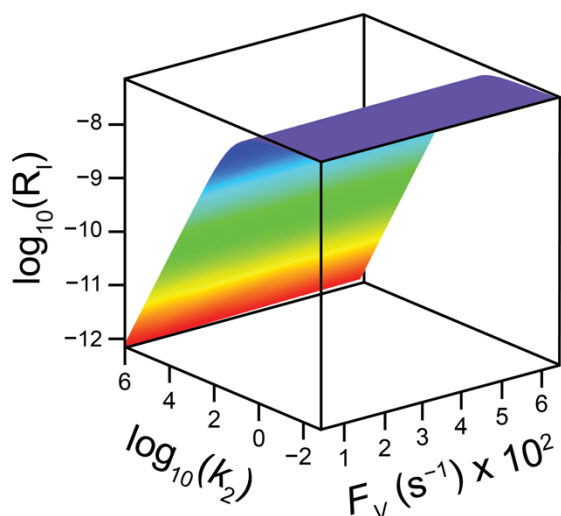


Figure S2.2 Graphical representations of compartmentalized turnover frequency (TOF) as a function of volumetric diffusive conductance (F_V) and logarithm of rate constant for oxidative addition (k_1) for (A) $m = 1$ and (B) $m = 2$ both set at rate constants for isomerization/migratory insertion and competing $\text{Cat} - A$ elimination, $k_2 = k_{e2} = 1 \times 10^3 \text{ s}^{-1}$, and rate constants for reductive elimination and competing $\text{Cat} - B$ elimination $k_3 = k_{e3} = 1 \times 10^6 \text{ s}^{-1}$.

A $\log_{10}(R_{l,m=2}(k_2, F_V))$



B $\log_{10}(R_{l,m=2}(k_{e2}, F_V))$

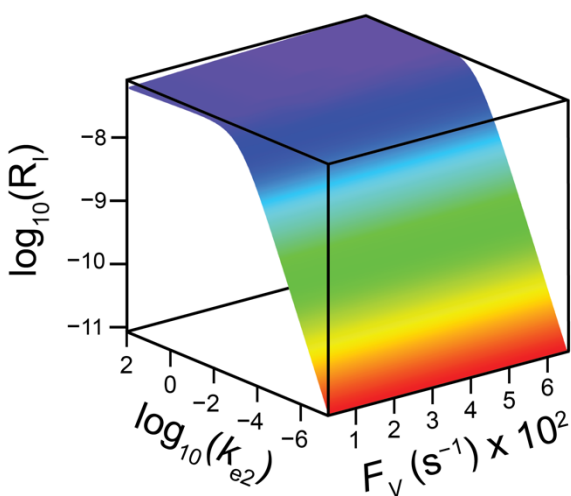
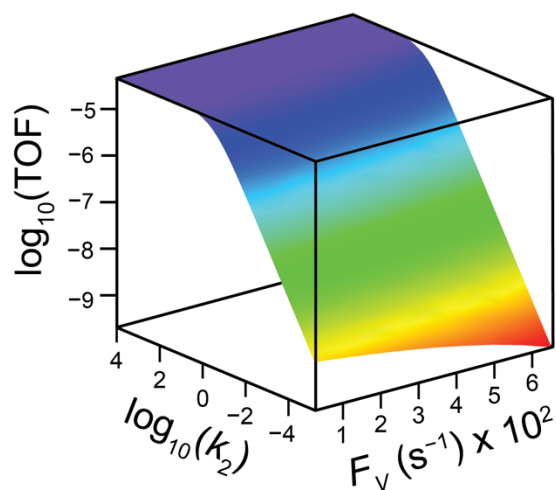


Figure S2.3 Graphical representations of compartmentalized rate of intermediate outflux (R_l) as a function of volumetric diffusive conductance (F_V) and logarithm of rate constant for isomerization/migratory insertion (k_2) for $m = 2$ (**A**) at rate constant for oxidative addition $k_1 = 10 \text{ M}^{-2} \text{ s}^{-1}$, rate constant for *Cat* - A elimination $k_{e2} = 1 \times 10^3 \text{ s}^{-1}$, and rate constant for reductive elimination and competing *Cat* - B elimination $k_3 = k_{e3} = 1 \times 10^6 \text{ s}^{-1}$. (**B**) R_l as a function of F_V and logarithm of rate constant for *Cat* - A elimination (k_{e2}) for $m = 2$ at $k_1 = 10 \text{ M}^{-2} \text{ s}^{-1}$, $k_2 = 1 \times 10^3 \text{ s}^{-1}$, and $k_3 = k_{e3} = 1 \times 10^6 \text{ s}^{-1}$.

A $\log_{10}(\text{TOF}_{m=2}(k_2, F_V))$



B $\log_{10}(\text{TOF}_{m=2}(k_{e2}, F_V))$

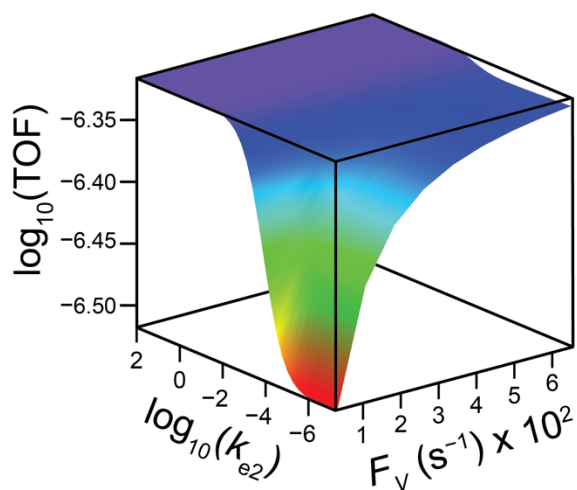
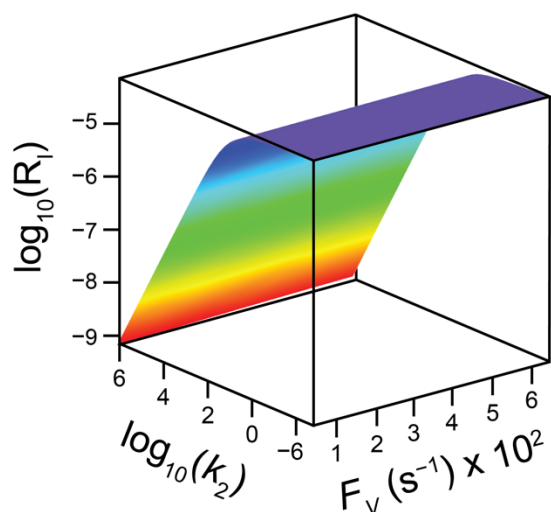


Figure S2.4 Graphical representations of compartmentalized turnover frequency (TOF) as a function of volumetric diffusive conductance (F_V) and logarithm of rate constant for isomerization/migratory insertion (k_2) for $m = 2$ (**A**) at rate constant for oxidative addition $k_1 = 10 \text{ M}^{-2} \text{ s}^{-1}$, rate constant for $\text{Cat} - A$ elimination $k_{e2} = 1 \times 10^3 \text{ s}^{-1}$, and rate constant for reductive elimination and competing $\text{Cat} - B$ elimination $k_3 = k_{e3} = 1 \times 10^6 \text{ s}^{-1}$. (**B**) TOF as a function of F_V and logarithm of rate constant for $\text{Cat} - A$ elimination (k_{e2}) for $m = 2$ at $k_1 = 10 \text{ M}^{-2} \text{ s}^{-1}$, $k_2 = 1 \times 10^3 \text{ s}^{-1}$, and $k_3 = k_{e3} = 1 \times 10^6 \text{ s}^{-1}$.

A $\log_{10}(R_{l,m=1}(k_2, F_V))$



B $\log_{10}(\text{TOF}_{m=1}(k_2, F_V))$

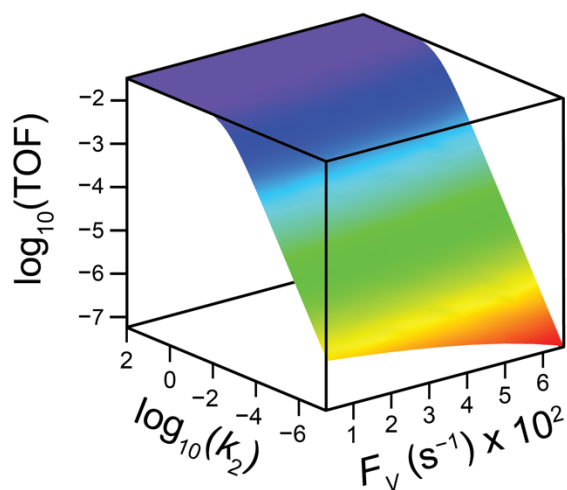
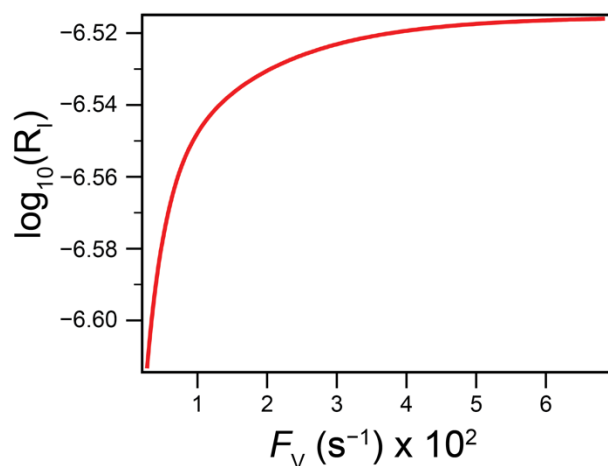


Figure S2.5 Graphical representations of compartmentalized rate of intermediate outflux (R_l) (**A**) and turnover frequency (TOF) (**B**) under model $C_{\text{Cat},\text{total}}$ as a function of volumetric diffusive conductance (F_V) and logarithm of rate constant for isomerization/migratory insertion (k_2) for $m = 1$. Both panels are set at rate constant for oxidative addition $k_1 = 0.1 \text{ M}^{-1} \text{ s}^{-1}$, rate constant for $\text{Cat} - A$ elimination $k_{e2} = 1 \times 10^3 \text{ s}^{-1}$, and rate constant for reductive elimination and competing $\text{Cat} - B$ elimination $k_3 = k_{e3} = 1 \times 10^6 \text{ s}^{-1}$.

A $\log_{10}(R_{l,m=1}(F_V))$



B $\log_{10}(TOF_{m=1}(F_V))$

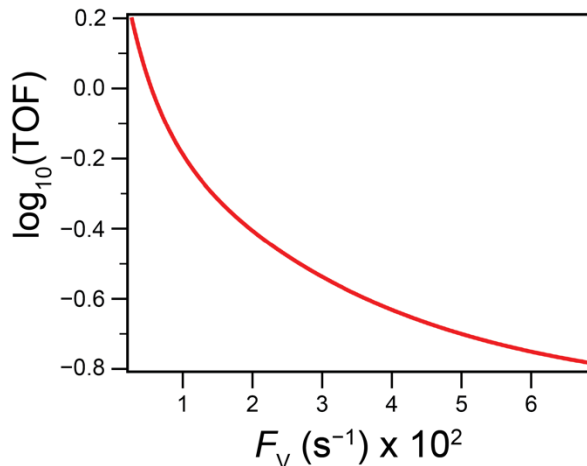


Figure S2.6 Graphical representations of compartmentalized rate of intermediate outflux (R_l) (**A**) and turnover frequency (TOF) (**B**) under model $C_{Cat,total}$ as a function of volumetric diffusive conductance (F_V) for $m = 1$. Both panels are set at rate constant for oxidative addition $k_1 = 0.1 \text{ M}^{-1} \text{ s}^{-1}$, rate constant for isomerization/migratory insertion and $Cat - A$ elimination $k_2 = k_{e2} = 1 \times 10^3 \text{ s}^{-1}$, and rate constant for reductive elimination and competing $Cat - B$ elimination $k_3 = k_{e3} = 1 \times 10^6 \text{ s}^{-1}$.

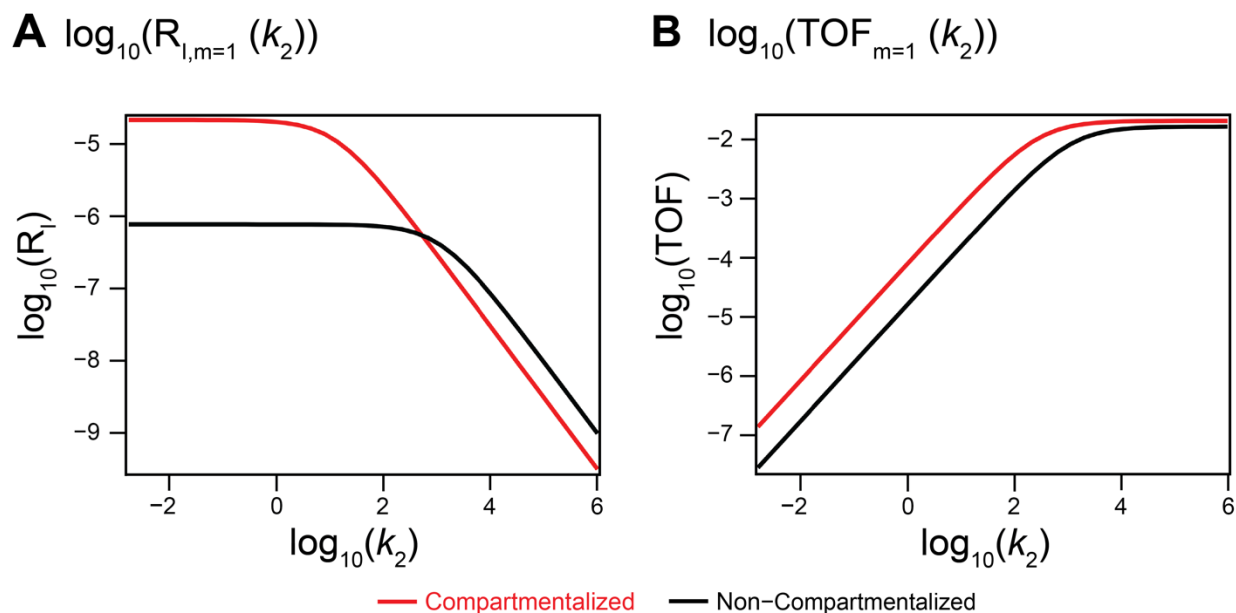


Figure S2.7 Comparison between compartmentalized and non-compartmentalized rate of intermediate outflux (R_I) (A) and turnover frequency (TOF) (B) under model $C_{Cat,total}$ as a function of logarithm of rate constant for isomerization/migratory insertion (k_2) for $m = 1$. Both panels are set at rate constant for oxidative addition $k_1 = 0.1 \text{ M}^{-1} \text{ s}^{-1}$, rate constant for $Cat - A$ elimination $k_{e2} = 1 \times 10^3 \text{ s}^{-1}$, and rate constant for reductive elimination and competing $Cat - B$ elimination $k_3 = k_{e3} = 1 \times 10^6 \text{ s}^{-1}$. The compartmentalized trace in both panels are set to volumetric diffusive conductance (F_V) of 320 s^{-1} .

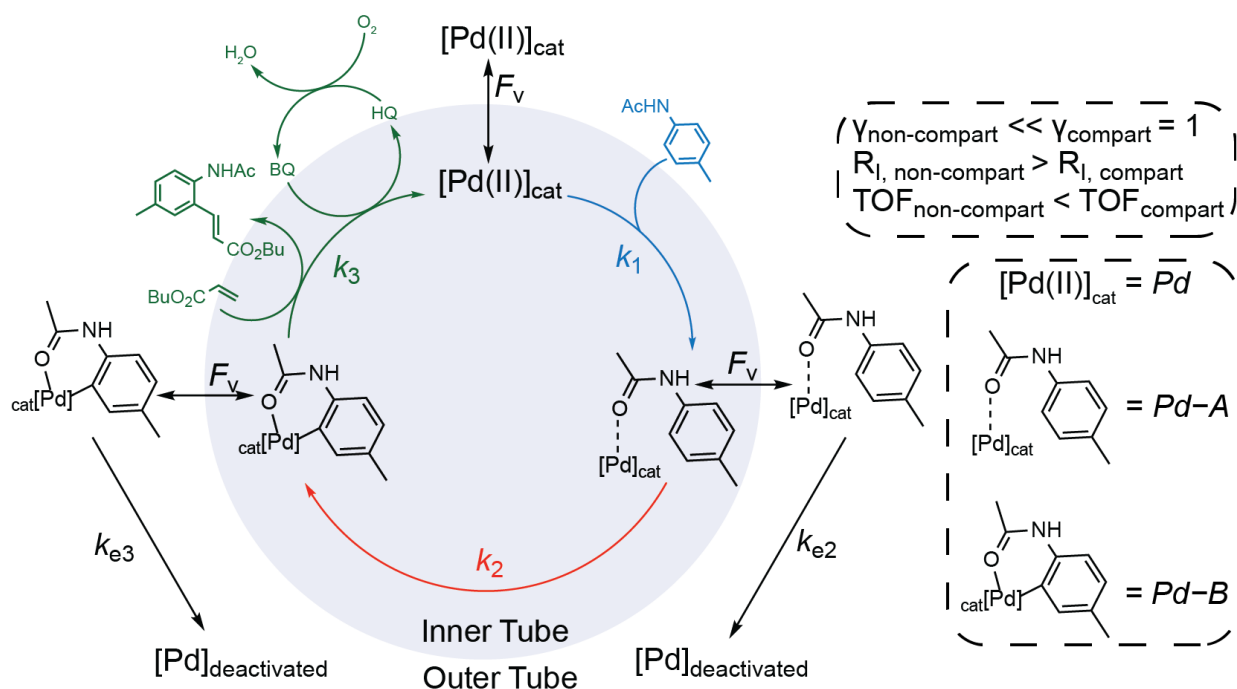


Figure S2.8 Schematic of compartmentalized palladium catalyzed olefin arylation (Fujiwara-Moritani, FM, reaction)⁵⁻⁷ operating in a tube-in-tube reactor⁸ used in Supplementary Information. F_V - volumetric diffusive conductance, k_1 , k_2 , and k_3 - rate constants for catalytic steps of FM, and k_{e2} and k_{e3} - rate constants for deactivation of palladium species by oxidizing media, BQ - benzoquinone, HQ - hydroquinone, γ - reaction efficiency, R_i - intermediate outflux and subsequent elimination, and TOF - turnover frequency, compart - compartmentalized, non-compart – non-compartmentalized. Terms Pd , $Pd - A$, and $Pd - B$ are abbreviations used in the Supplemental Information.

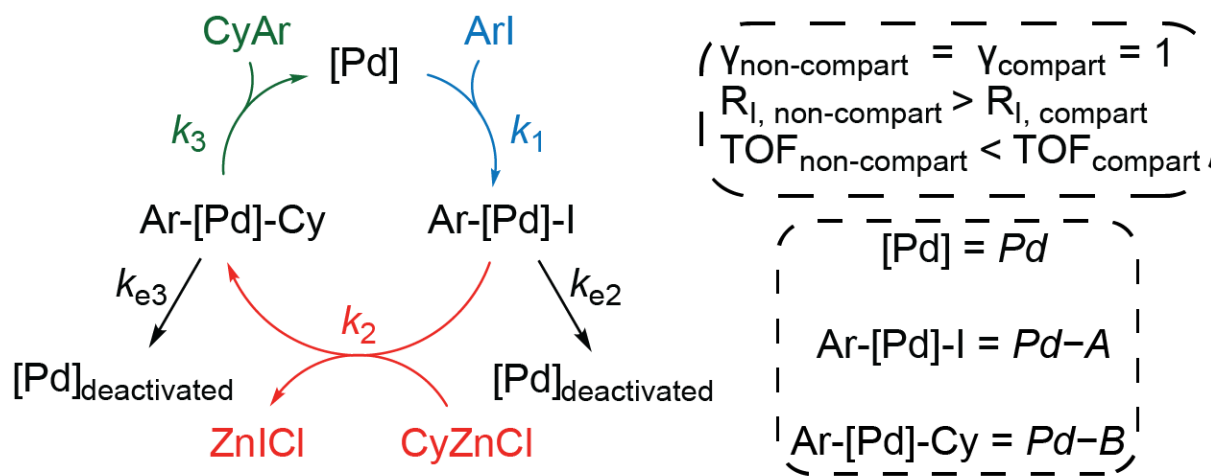


Figure S2.9 Schematic of palladium catalyzed olefin arylation (Negishi reaction)^{9,10} used in Supplementary Information as a non-compartmentalized and hypothetical compartmentalized within a MOF system. F_V - volumetric diffusive conductance, k_1 , k_2 , and k_3 - rate constants for catalytic steps of the Negishi reaction, and k_{e2} and k_{e3} - rate constants for deactivation of palladium species, Ar - aryl, Cy - cyclohexyl, γ - reaction efficiency, R_I - intermediate outflux and subsequent elimination, and TOF - turnover frequency, compart - compartmentalized, non-compart – non-compartmentalized. Terms Pd , $Pd - A$, and $Pd - B$ are abbreviations used in the Supplemental Information.

Additional references

1. Tsitkov, S.; Hess, H. Design Principles for a Compartmentalized Enzyme Cascade Reaction. *ACS Catal.*, 2019, **9**, 2432-2439.
2. Natinsky, B. S.; Jolly, B. J.; Dumas, D. M.; Liu, C. Efficacy analysis of compartmentalization for ambient CH₄ activation mediated by a Rh^{II} metalloradical in a nanowire array electrode. *Chem. Sci.*, 2021, **12**, 1818-1825.
3. Stein, W. *Transport and diffusion across cell membranes*, Elsevier Inc., 1986.
4. Natinsky, B. S.; Lu, S.; Copeland, E. D.; Quintana, J. C.; Liu, C. Solution Catalytic Cycle of Incompatible Steps for Ambient Air Oxidation of Methane to Methanol. *ACS Cent. Sci.*, 2019, **5**, 1584-1590.
5. Moritani, I.; Fujiwara, Y. Aromatic substitution of styrene-palladium chloride complex. *Tetrahedron Lett.*, 1967, **8**, 1119-1122.
6. Fujiwara, Y.; Moritani, I.; Danno, S.; Asano, R.; Teranishi, S. Aromatic substitution of olefins. VI. Arylation of olefins with palladium (II) acetate. *JACS.*, 1969, **91**, 7166-7169.
7. Mulligan, C. J.; Parker, J. S.; Hii, K. K. Revisiting the mechanism of the Fujiwara–Moritani reaction. *React. Chem. Eng.*, 2020, **5**, 1104–1111.
8. Ferlin, F.; Anastasiou, I.; Carpisassi, L.; Vaccaro, L. Aerobic waste-minimized Pd-catalysed C–H alkenylation in GVL using a tube-in-tube heterogeneous flow reactor. *Green Chem.*, 2021, **23**, 6576-6582.
9. Negishi, E.; King, A. O.; Okukado, N. Selective carbon-carbon bond formation via transition metal catalysis. 3. A highly selective synthesis of unsymmetrical biaryls and diarylmethanes by the nickel-or palladium-catalyzed reaction of aryl-and benzylzinc derivatives with aryl halides. *J. Org. Chem.*, 1977, **42**, 1821-1823.

10. Zhang, H.; Luo, X.; Wongkhan, K.; Duan, H.; Li, Q.; Zhu, L.; Wang, J.; Batsanov, A. S.; Howard, J. A.; Marder, T. B. Acceleration of Reductive Elimination of [Ar-Pd-C] by a Phosphine/Electron-Deficient Olefin Ligand: A Kinetic Investigation. *Chem. Eur. J.*, 2009, **15**, 3823-3829.
11. Tiburcio, E.; Greco, R.; Mon, M.; Ballesteros-Soberanas, J.; Ferrando-Soria, J. s.; López-Haro, M.; Hernández-Garrido, J. C.; Oliver-Meseguer, J.; Marini C.; Boronat, M. Soluble/MOF-Supported Palladium Single Atoms Catalyze the Ligand-, Additive-, and Solvent-Free Aerobic Oxidation of Benzyl Alcohols to Benzoic Acids. *J. Am. Chem. Soc.*, 2021, **143**, 2581-2592.
12. Ananikov, V. P.; Zalesskiy, S. S.; Kachala, V. V.; Beletskaya, I. P. NMR approach for the identification of dinuclear and mononuclear complexes: The first detection of [Pd(SPh)₂(PPh₃)₂] and [Pd₂(SPh)₄(PPh₃)₂]-The intermediate complexes in the catalytic carbon-sulfur bond formation reaction. *J. Organomet. Chem.*, 2011, **696**, 400-405.

Chapter 3. Polyketones from Carbon Dioxide and Ethylene by Integrating Electrochemical and Organometallic Catalysis

This chapter is a version of Dodge, H. M.; Natinsky, B. S.; Jolly, B. J.; Zhang, H. C.; Mu, Y.; Chapp, S. M.; Tran, T. V.; Diaconescu, P. L.; Do, L. H.; Wang, D. W.; Liu, C.; Miller, A. J. M., Polyketones from Carbon Dioxide and Ethylene by Integrating Electrochemical and Organometallic Catalysis. *ACS Catal.* **2023**, *13*, 4053-4059.

Abstract

The utilization of carbon dioxide in polymer synthesis is an attractive strategy for sustainable materials. Electrochemical CO₂ reduction would offer a natural starting point for producing monomers, but the conditions of electrocatalysis are often drastically different from the conditions of organometallic coordination-insertion polymerization. Reported here is a strategy for integrating electrochemical and organometallic catalysts that enables polyketone synthesis from CO₂ and ethylene in a single multicompartment reactor. Polyketone materials that are up to 50% derived from CO₂ can be prepared in this way. Potentiostatic control over the CO-producing catalyst enables the controlled generation of low-pressure CO, which in conjunction with a palladium phosphine sulfonate organometallic catalyst enables copolymerization to nonalternating polyketones with the CO content tuned based on the applied current density.

Introduction

The majority of synthetic plastics, adhesives, and other polymer materials are derived from fossil fuels. The environmental consequences are significant, as preparation of monomers releases large amounts of CO₂ to the atmosphere.^{1, 2} To address this challenge, scientists have long sought to utilize carbon dioxide as the source of carbon (and possibly oxygen) in polymer synthesis (Figure

3.1A).³ Polycarbonates prepared via copolymerization of CO₂ and epoxides represent a major success story in this area.⁴⁻⁸ Routes from CO₂ to polyurethanes and polyureas have also been developed. Chemistry combining CO₂ and olefins nascent, with CO₂/butadiene copolymers (29 wt% CO₂) representing a recent breakthrough.⁹⁻¹⁵ However, general strategies for accessing high-performance olefin-based polymeric materials from CO₂ are lacking.

Polyketone materials¹⁶⁻¹⁸ attracted our attention as a possible target for improving sustainability in polymer synthesis. The copolymer of carbon monoxide and ethylene with a perfectly alternating microstructure (referring to the orientation and ordering of the monomer subunits), poly(1-oxo-trimethylene), is a prototypical polyketone. Prepared most commonly using molecular palladium catalysts, poly(1-oxo-trimethylene) materials have many properties associated with attractive engineering thermoplastics, such as high melting points, excellent impact performance, and sturdy chemical resistance.¹⁹ A few catalysts also produce “nonalternating” polyketones under specific conditions (elevated temperature, low CO pressure relative to ethylene pressure) that feature several ethylene units between each carbonyl group.²⁰⁻²² These materials have lower melting temperatures and improved solubility, which can enhance processability.⁷ At extremely low CO incorporation, nonalternating polyketone behaves more like polyethylene, a material for which mass production infrastructure is already in place.^{7, 8} A recent study demonstrated nickel-catalyzed CO/C₂H₄ copolymerization with as little as 0.3 mol% CO content, accessing materials that could be processed like polyethylene while also featuring facile degradation pathways due to the isolated ketone functional groups.⁸

To date, polyketones have been prepared from CO and C₂H₄, which are industrially sourced from fossil fuels. This process is typically run under high pressures of CO, which can pose safety concerns due to its high toxicity. Methods for sustainable CO production have been developed,²³⁻

²⁵ but there is an opportunity to improve efficiency by developing the fundamental catalysis tools needed to integrate electrochemical CO₂ reduction with organometallic polymerization catalysis (Figure 3.1B). Initial progress has been made in this area, albeit in low pressure applications.²⁶⁻²⁸ Often times, however, electrochemical and organometallic catalysts require starkly different reaction conditions for optimal performance. The electroreduction of CO₂ typically employs an aqueous electrolyte at room temperature and 1 bar CO₂,²⁹⁻³¹ while palladium-catalyzed polyketone

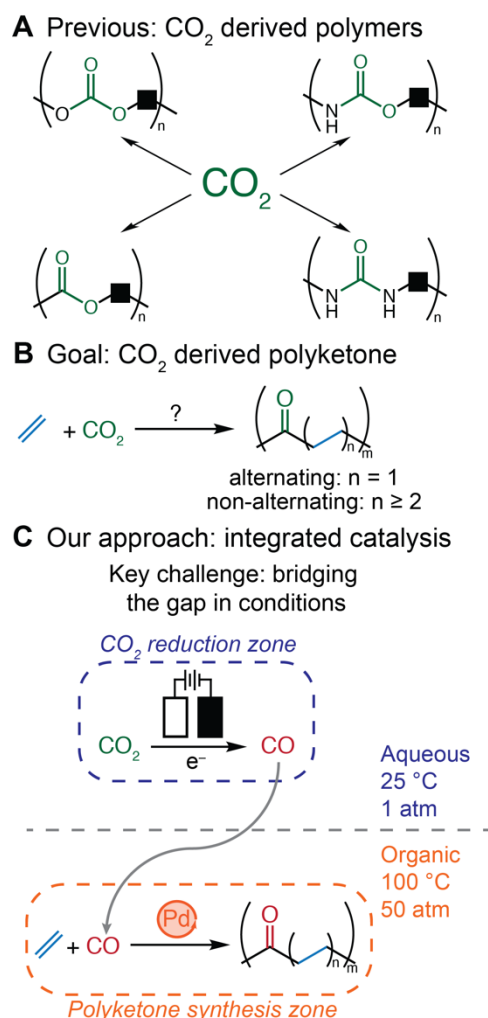


Figure 3.1 Previous non-integrated polyketone synthesis reactions and our proposed electrochemical/organometallic integrated method.

synthesis typically utilizes organic solvents at elevated temperatures ($>80\text{ }^{\circ}\text{C}$) and high pressures ($>20\text{ bar}$).^{19, 32, 33}

Polyketone materials in which each carbonyl unit is derived from carbon dioxide are reported here, accessed through the integration of heterogeneous electrocatalytic CO_2 reduction to CO and homogeneous organometallic CO/ C_2H_4 copolymerization catalysis in a multicompartiment reactor (Figure 3.1C). Overcoming incompatibility challenges through reactor design and development of suitable reaction conditions enables the synthesis of perfectly alternating polyketone that is *50 wt% CO_2 -derived by mass*. With a different organometallic palladium complex in the same integrated catalysis reactor, nonalternating polyketones were prepared *with the extent of CO_2 -derived carbonyl linkages controlled electrochemically*.

Results and Discussion

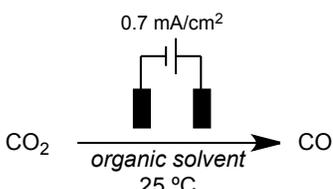
We began by identifying reaction conditions where electrochemical and organometallic catalysts could be coupled. The solvent, temperature, and pressure conditions were considered key factors. Initial studies sought nonaqueous CO_2 electroreduction using heterogeneous metal electrodes. High activity and fewer chain transfer events were observed in organic solvents during polyketone synthesis catalyzed by organometallic Pd complexes, relative to aqueous conditions.^{19, 32, 33} However, data on electrochemical CO generation from CO_2 in nonaqueous solvents is limited.³⁴⁻
³⁶ Three polar aprotic solvents were tested: 1,2-dichloroethane (1,2-DCE), 1,2-difluorobenzene (1,2-DFB), and *N,N*-dimethylformamide (DMF), all with the addition of 5% v/v methanol (MeOH) as a proton donor and 0.25 M tetrabutylammonium hexafluorophosphate (TBAPF_6) as an electrolyte (Table 3.1A). A bespoke high-pressure electrochemical reactor capable of supplying varying pressures of CO_2 and C_2H_4 was designed in order to enhance CO yield and limit mass transport limitations (Figure S1).

Gold is amongst the most CO selective catalysts in aqueous electrolytes,^{37, 38} so we were surprised to find that gold sputtered on carbon paper or supported on titanium produced almost no CO in 1,2-DCE, 1,2-DFB, or DMF as quantified by online gas chromatography (GC) (Table S3.1). Palladium foil showed more promising results for CO₂ electroreduction in nonaqueous media (Table 3.1A and S3.1). The Faradaic efficiency for CO₂ reduction to CO (FE_{CO}) after 24 h was only ca. 1% in 1,2-DFB. Although the FE_{CO} increased to 2.5% in 1,2-DCE, this solvent was problematic because of a competing hydrodechlorination reaction that produced C₂H₄ and C₂H₆ (observed via GC analysis).^{39, 40} DMF with 5% v/v MeOH was more promising, with CO formed in the 5-19% FE_{CO} range. Using DMF without added MeOH led to even higher selectivity, 35-44% FE_{CO}, and extending the reaction time results in ca. 0.5 bar CO produced. These conditions were chosen for further studies. The FE_{CO} in DMF was higher than reports of Pd foil in water (FE_{CO} = 13%)⁴¹⁻⁴³ and similar to Pd foil in methanol (FE_{CO} ~ 40%).⁴¹⁻⁴⁴ Concomitant hydrogen evolution was also observed in these CO₂ electrolyses experiments, with faradaic efficiencies (FE_{H2}) ranging from 1 – 67% depending on the conditions (see Supplementary Information and Table S3.1 for more details).

Having identified promising conditions for nonaqueous CO generation, we turned to two classic organometallic CO/C₂H₄ copolymerization catalysts (Figure 3.2). Some of the first reports of organometallic polyketone synthesis utilized 1,2-bis(diphenylphosphino)propane (dppp),^{32, 45} so we prepared the cationic palladium methyl complex [(dppp)Pd(Me)(MeCN)][BAr^F₄] (**Pd-PP**, Ar^F is 3,5-bis(trifluoromethyl)phenyl).⁴⁶ This catalyst produces perfectly alternating polyketone (ca. 1 “mistake” per 10⁵ insertions).⁴⁷ The neutral catalyst (PO)Pd(Me)(pyridine) (**Pd-PO**, PO is *o*-Ar₂PC₆H₄SO₃ with Ar being *o*-MeO-C₆H₄) was the first catalyst reported to furnish nonalternating polyketone.^{16, 17} Alkyl complexes with weakly bound MeCN and pyridine ligands have been

shown to initiate polymerization without requiring any chemical activator, and to carry out the individual polymerization steps at low temperatures.^{16, 47}

A

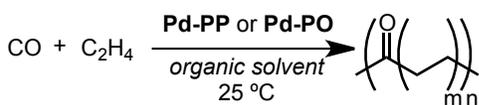


0.7 mA/cm²

CO₂ $\xrightarrow[\text{organic solvent, 25 °C}]{} \text{CO}$

Electrodes	Solvent	Time (h)	<i>P</i> _{CO₂} (bar) initial	<i>P</i> _{C₂H₄} (bar) initial	FE _{CO} (%)	<i>P</i> _{CO} (bar) final
Au-Ti	DMF (10% MeOH)	2	8	15	7	0.008
Pd	DMF (5% MeOH)	3	7	7	19	0.028
Pd	DMF (5% MeOH)	12	7	7	5	0.032
Pd	DMF	24	7	7	44	0.531
Pd	1,2-DCE (5% MeOH)	24	5	5	3	0.002

B



CO + C₂H₄ $\xrightarrow[\text{organic solvent, 25 °C}]{\text{Pd-PP or Pd-PO}}$ 

Catalyst	Solvent	<i>P</i> _{CO} (bar)	<i>P</i> _{C₂H₄} (bar)	Activity (g mmol ⁻¹ h ⁻¹)	<i>M</i> _n (Đ)
Pd-PO	1,2-DCE	0.5	0.5	0	-
Pd-PO	1,2-DCE	0.5	7	0.064	3580 (1.8)
Pd-PO	1,2-DCE	10	10	0.105	6380 (1.5)
Pd-PO	DMF (40 °C)	0.5	10.5	0.27	-
Pd-PP	1,2-DCE	0.5	0.5	0.197	-
					24160 (2.2)
Pd-PP	1,2-DCE	0.5	10	0.166	5070 (1.0)
					1930 (1.1)
Pd-PP	1,2-DCE	10	10	0.819	21370 (7.3)
Pd-PP	DMF	0.5	10	0.43	-

Table 3.1 Selected experiments independently optimizing reaction conditions for CO₂ reduction and copolymerization. (A) Electrochemical CO₂ reduction in nonaqueous solvent at low temperature. (B) CO/C₂H₄ copolymerization in nonaqueous solvent at low temperature.

Focusing on room temperature copolymerization, we subjected **Pd-PP** and **Pd-PO** to a range of conditions, varying solvent, catalyst loading, and reactant pressures. The findings are summarized in Table 3.1B and S3.2–S3.4. Polymer is still formed at 0.5 bar each of CO and C₂H₄ at room temperature in reactions catalyzed by **Pd-PP**. In contrast, the neutral catalyst **Pd-PO**, which generally exhibits lower activity than **Pd-PP**, did not form any polymer at 1 bar total pressure. At 0.5 bar CO and 7 bar C₂H₄, however, appreciable polymerization activity was apparent. Neither H₂ nor CO₂ gas interfered with the copolymerization, confirming that these species presenting during electrocatalysis do not inhibit the copolymerization. Based on the copolymerization studies, we targeted 7 bar C₂H₄ for integration with electrochemical CO generation.

The electrochemical reactor was charged with DMF/TBAPF₆ electrolyte containing the 5 mM of **Pd-PP** or **Pd-PO** and held at constant current, but formation of Pd black was observed along with traces of polymer. Cyclic voltammograms collected in DMF with 0.25 M TBAPF₆ revealed irreversible reductions for **Pd-PP** ($E_{p,c} \sim -2.9$ V vs ferrocenium/ ferrocene, Fc⁺/Fc) and **Pd-PO** ($E_{p,c} \sim -2.48$ V vs Fc⁺/Fc) (Figure S3.2). These reduction potentials are unfortunately more positive than what is required to reach 0.7 mA/cm² electrolysis current density for CO production (-3.71 V vs. Fc⁺/Fc).

To combat the degradation of the polymerization catalyst under CO₂ reduction potentials, a vial-in-a-vial approach was adopted as depicted in Figure 3.2. Taking advantage of the intermediate CO being a gas, the electrocatalytic material and molecular catalyst were physically separated under a shared headspace in the pressure reactor.

The high-pressure reactor containing DMF and 0.25 M TBAPF₆ as electrolyte and a vial of DMF containing **Pd-PP** was charged with 7 bar CO₂ and 7 bar C₂H₄, and a current density of 0.7 mA·cm⁻² was applied for 24 h at room temperature while both chambers were stirred. CO was produced

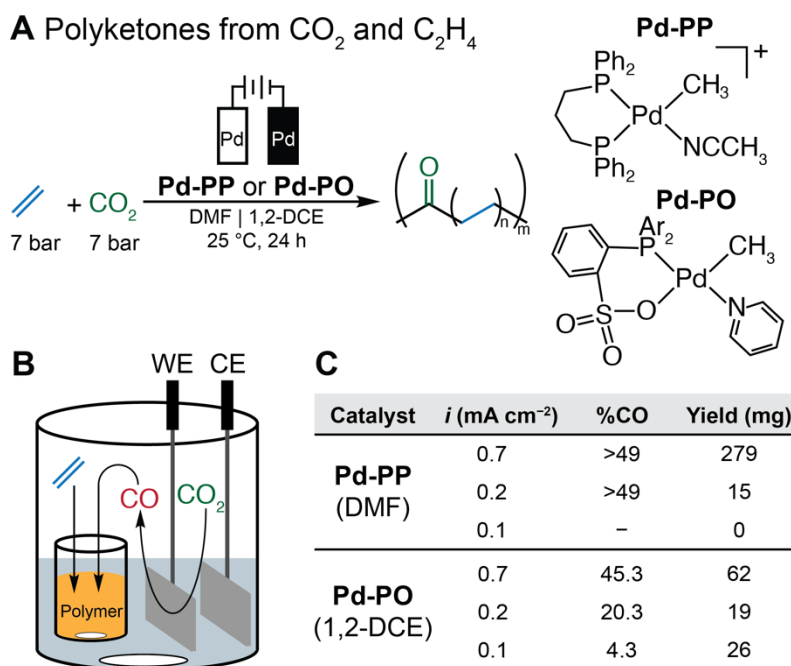


Figure 3.2 Synthesis of polyketones from CO₂ and C₂H₄. (A) Reaction scheme and catalyst structures (Ar = *o*-MeO-C₆H₄). (B) Reactor design showing outer compartment (DMF solution depicted in blue) with electrochemical components and inner compartment (DMF or 1,2-DCE solution containing organometallic Pd catalyst, depicted in yellow).

with a similar efficiency to electrolyses in the absence of the polymerization catalyst (37% F_{CO}, Table S3.5). An off-white precipitate was observed in the vial containing **Pd-PP** at the end of the reaction. The solid was isolated, washed with acidified MeOH and characterized by ¹H and ¹³C nuclear magnetic resonance (NMR) spectroscopy, attenuated total reflectance infrared spectroscopy (ATR-IR) spectroscopy, and size exclusion chromatography (SEC). NMR analysis in a 1,1,1,3,3,3-hexafluoro-2-propanol (HFIP)/C₆D₆ (4:1) mixture revealed the signatures a perfectly alternating microstructure (>49% CO content), as expected for the type of catalyst employed.¹⁶ ATR-IR spectra for each polymer sample featured a C=O stretch at 1692 cm⁻¹, consistent with alternating polyketone (>49% CO incorporation).⁷ In these initial experiments, we chose DMF for the solvent in both compartments of the reactor. The polymer yield was comparable

when DMF was used for the electrochemical compartment and 1,2-DCE was employed in the copolymerization compartment (Table S3.5). The SEC trace (HFIP eluent) and NMR analysis of the degree of polymerization (DP) show that the polymers produced via integrated catalysis have similar molecular weight as those produced from CO, with high-dispersity number average molecular weights (M_n) in the range of 4,000-18,000 g/mol and sometimes featuring multimodal distributions (Table S3.5). The high-pressure electrochemical reactor and reaction conditions overcome apparent incompatibility to enable the dual electrochemical/organometallic catalytic synthesis of polyketone that *is 50% CO₂-derived by weight*.

Next, we decided to explore the possibility of electrochemical control over co-monomer concentration by varying of the applied current density to the Pd foil cathode. Using **Pd-PP** as the organometallic catalyst, the applied current density was varied from 0.7 to 0.1 mA·cm⁻². The yield dropped as the current density was lowered and P_{CO} decreased (from 0.45 to 0.01 bar, Figure 3.2). In cases where polymer formed, it was perfectly alternating polyketone (>49% CO incorporation). Either in the absence of an external applied current or under N₂ instead of CO₂, integrated catalysis with **Pd-PP** yielded no precipitate. Integrated trials using ¹³CO₂ as a pre-monomer yielded a dramatically intensified ¹³C NMR peak at ~212 ppm for the carbonyl carbon of the polyketone (Figure S45).

The same reactor was next employed for reactions using **Pd-PO**, a catalyst previously reported to produce nonalternating polyketones (typical conditions are 110 °C, $P_{C_2H_4}$ = 30 bar, P_{CO} = 5 bar).^{17, 21, 48, 49} The high-pressure reactor was charged with DMF and 0.25 M TBAPF₆ in the main electrochemical compartment and 1,2-DCE containing **Pd-PO** in the polymerization compartment, and pressurized to 7 bar CO₂ and 7 bar C₂H₄. A current density ranging from 0.7 to 0.1 mA·cm⁻² was applied for 24 h at room temperature. At 0.5 and 0.7 mA·cm⁻² applied current

density, where 0.25-0.5 bar partial pressures of CO were generated, polymers with predominantly alternating microstructure were produced in integrated catalysis featuring **Pd-PO**. But at 0.3 mA·cm⁻² applied current density and below, where the CO partial pressure was as low as 0.002 bar after the reaction, the NMR spectra show signals for multiple repeating C₂H₄ units diagnostic of nonalternating polyketone. As the degree of CO incorporation in the polyketone copolymer decreases, solubility in HFIP decreases, but solubility in 1,1,2,2-tetrachloroethane (TCE) increases. NMR spectra were thus collected in both HFIP at 25 °C and TCE-*d*₂ at 100 °C for microstructure analysis.

Figure 3 reveals correlated trends in the %CO incorporation determined by NMR spectroscopy and the C=O stretches observed by ATR-IR spectroscopy as a function of applied current density (and CO generated during electrolysis). The polymers ranged from almost perfectly alternating (>45% CO) when the CO pressure approached 0.5 bar, to very low CO content of 3-6% at less than 0.01 bar CO. The potentiostat therefore provides a means of fine-tuning the degree of CO incorporation in the polymer.

The NMR and IR spectroscopic data, along with SEC data showing a monomodal distribution of polymer molecular weights, point to nonalternating polyketone materials, rather than mixtures of polyethylene and alternating polyketone. Further support comes from DOSY NMR spectra, which show that the resonance for CH₂ repeat units far from ketone groups have the same diffusion coefficient as the CH₂ units adjacent to ketone units, confirming they are part of the same nonalternating polyketone polymer. We prepared authentic samples of both an alternating polyketone / polyethylene block copolymer and a physical blend of alternating polyketone and polyethylene produced by these catalysts, and the NMR and IR signatures are distinct (Figure S3.23). Although **Pd-PO** does catalyze slow ethylene homopolymerization at room temperature

under 7 bar C₂H₄ (Table S3.6), we hypothesize that even the small amounts of CO formed at early times effectively inhibit any of this potential side reaction. Furthermore, chain end analysis is consistent with minimal chain transfer, preventing release of polyethylene before CO incorporation.

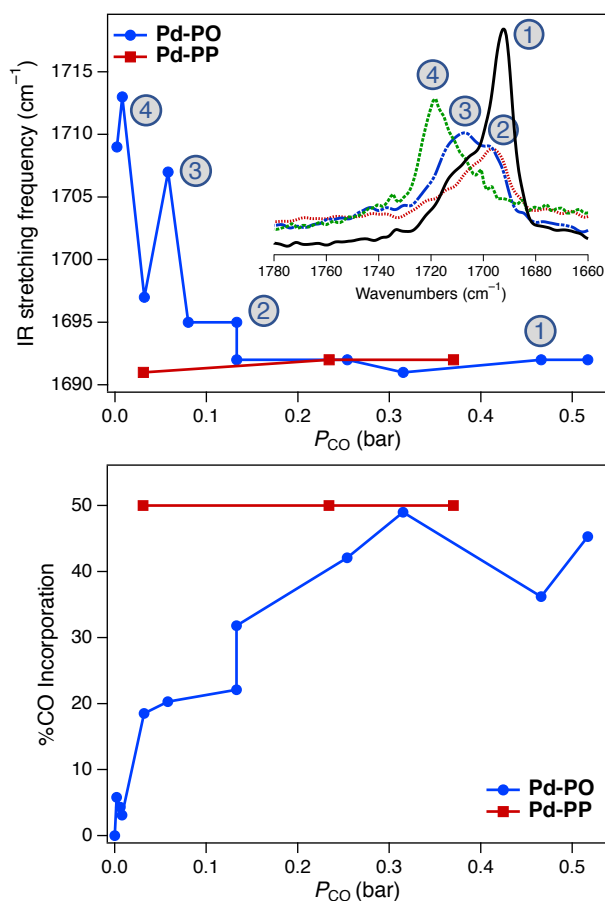


Figure 3.3 CO incorporation (%) and C-O stretching frequency (top) plotted as a function of the CO partial pressure for catalyst used (bottom). The partial pressure of CO is modulated by the applied current density.

The generation of nonalternating polyketone at room temperature by **Pd-PO** in the integrated system was rather surprising. When 0.5 bar CO was used directly in copolymerizations under conditions similar to integrated catalysis, the %CO incorporation was 47%; even at just 0.1 bar

(charging 1 bar CO, then 9 bar N₂ and venting), the material was predominantly *alternating* polyketone (44% CO, $\nu_{\text{CO}} = 1692 \text{ cm}^{-1}$). Only at elevated temperatures (80-100 °C), with a 20:1 C₂H₄:CO ratio, did the CO content drop below 20% (**Table S3.4**). We attribute the ability to generate nonalternating polymer to the controlled production of small amounts of CO using electrochemistry. The integrated system readily produces the very low CO levels needed to access nonalternating materials in one pot from CO₂. Such materials are promising because they are more readily degraded than polyethylene itself.^{8, 22, 50-52}

Conclusion

Integrating electrochemical and organometallic catalysis enables the synthesis of CO₂-derived polyketones. This report provides a blueprint for approaching the challenge of catalyst integration for seemingly incompatible reaction conditions, using a unique reactor design and systematic variation of reaction parameters to achieve suitable conditions for co-catalysis. Furthermore, integrated catalysis produces polyketone materials of variable composition, with the molecular weight and degree of CO incorporation controlled by the choice of organometallic catalyst and applied current density, offering new opportunities in sustainable polymer synthesis.

References

1. Zhu, Y.; Romain, C.; Williams, C. K., Sustainable polymers from renewable resources. *Nature*, **2016**, *540*, 354-362.
2. Zhang, X.; Fevre, M.; Jones, G. O.; Waymouth, R. M., Catalysis as an enabling science for sustainable polymers. *Chem. Rev.* **2018**, *118*, 839-885.
3. Grignard, B.; Gennen, S.; Jérôme, C.; Kleij, A. W.; Detrembleur, C., Advances in the use of CO₂ as a renewable feedstock for the synthesis of polymers. *Chem. Soc. Rev.* **2019**, *48*, 4466-4514.
4. Coates, G. W.; Moore, D. R., Discrete metal-based catalysts for the copolymerization of CO₂ and epoxides: discovery, reactivity, optimization, and mechanism. *Angew. Chem. Int. Ed.* **2004**, *43*, 6618-6639.
5. Klaus, S.; Lehenmeier, M. W.; Anderson, C. E.; Rieger, B., Recent advances in CO₂/epoxide copolymerization—New strategies and cooperative mechanisms. *Coord. Chem. Rev.* **2011**, *255*, 1460- 1479.
6. Lu, X.-B.; Ren, W.-M.; Wu, G.-P., CO₂ copolymers from epoxides: catalyst activity, product selectivity, and stereochemistry control. *Acc. Chem. Res.* **2012**, *45*, 1721-1735.
7. Soomro, S. S.; Cozzula, D.; Leitner, W.; Vogt, H.; Müller, T. E., The Microstructure and Melt Properties of CO–Ethylene Copolymers With Remarkably Low CO Content. *Polym. Chem.* **2014**, *5*, 3831-3837.
8. Baur, M.; Lin, F.; Morgen, T. O.; Odenwald, L.; Mecking, S., Polyethylene materials with in-chain ketones from nonalternating catalytic copolymerization. *Science* **2021**, *374*, 604-607.

9. Nakano, R.; Ito, S.; Nozaki, K., Copolymerization of carbon dioxide and butadiene via a lactone intermediate. *Nat. Chem.* **2014**, *6*, 325-331.
10. Tang, S.; Zhao, Y.; Nozaki, K., Accessing divergent main-chain-functionalized polyethylenes via copolymerization of ethylene with a CO₂/butadiene-derived lactone. *J. Am. Chem. Soc.* **2021**, *143*, 17953-17957.
11. Tang, S.; Nozaki, K., Advances in the Synthesis of Copolymers from Carbon Dioxide, Dienes, and Olefins. *Acc. Chem. Res.* **2022**, *55*, 1524-1532.
12. Liu, M.; Sun, Y.; Liang, Y.; Lin, B.-L., Highly efficient synthesis of functionalizable polymers from a CO₂/1,3-butadiene-derived lactone. *ACS Macro Lett.* **2017**, *6*, 1373-1378.
13. Yue, S.; Bai, T.; Xu, S.; Shen, T.; Ling, J.; Ni, X., Ring-Opening Polymerization of CO₂-Based Disubstituted δ -Valerolactone toward Sustainable Functional Polyesters. *ACS Macro Lett.* **2021**, *10*, 1055-1060.
14. Garcia Espinosa, L. D.; Williams-Pavlantos, K.; Turney, K. M.; Wesdemiotis, C.; Eagan, J. M., Degradable Polymer Structures from Carbon Dioxide and Butadiene. *ACS Macro Lett.* **2021**, *10*, 1254-1259.
15. Rapagnani, R. M.; Dunscomb, R. J.; Fresh, A. A.; Tonks, I. A., Tunable and recyclable polyesters from CO₂ and butadiene. *Nat. Chem.* **2022**, *14*, 877-883.
16. Luo, R.; Newsham, D. K.; Sen, A., Palladium-Catalyzed Nonalternating Copolymerization of Ethene and Carbon Monoxide: Scope and Mechanism. *Organometallics* **2009**, *28*, 6994-7000.
17. Drent, E.; van Dijk, R.; van Ginkel, R.; van Oort, B.; Pugh, R. I., The first example of palladium catalysed non-perfectly alternating copolymerisation of ethene and carbon monoxide. *Chem. Commun.* **2002**, 964-965.

18. Bettucci, L.; Bianchini, C.; Claver, C.; Suarez, E. J. G.; Ruiz, A.; Meli, A.; Oberhauser, W., Ligand Effects in the Non-Alternating CO–Ethylene Copolymerization by Palladium(II) Catalysis. *Dalton Trans.* **2007**, 5590-5602.
19. Vavasori, A.; Ronchin, L., Polyketones: synthesis and applications. *Encyclopedia of Polymer Science and Technology* **2002**, 1-41.
20. Chen, C.; Anselment, T. M. J.; Fröhlich, R.; Rieger, B.; Kehr, G.; Erker, G., *o*-Diarylphosphinoferrocene Sulfonate Palladium Systems for Nonalternating Ethene–Carbon Monoxide Copolymerization. *Organometallics* **2011**, *30*, 5248-5257.
21. Hearley, A. K.; Nowack, R. J.; Rieger, B., New single-site palladium catalysts for the nonalternating copolymerization of ethylene and carbon monoxide. *Organometallics* **2005**, *24*, 2755-2763.
22. Chen, S.-Y.; Pan, R.-C.; Chen, M.; Liu, Y.; Chen, C.; Lu, X.-B., Synthesis of Nonalternating Polyketones Using Cationic Diphosphazane Monoxide-Palladium Complexes. *J. Am. Chem. Soc.* **2021**, *143*, 10743-10750.
23. Appel, A. M.; Bercaw, J. E.; Bocarsly, A. B.; Dobbek, H.; DuBois, D. L.; Dupuis, M.; Ferry, J. G.; Fujita, E.; Hille, R.; Kenis, P. J., Frontiers, opportunities, and challenges in biochemical and chemical catalysis of CO₂ fixation. *Chem. Rev.* **2013**, *113*, 6621-6658.
24. Francke, R.; Schille, B.; Roemelt, M., Homogeneously catalyzed electroreduction of carbon dioxide—methods, mechanisms, and catalysts. *Chem. Rev.* **2018**, *118*, 4631-4701.
25. Shin, H.; Hansen, K. U.; Jiao, F., Techno-economic assessment of low-temperature carbon dioxide electrolysis. *Nat. Sustain.* **2021**, *4*, 911-919.

26. Jensen, M. T.; Rønne, M. H.; Ravn, A. K.; Juhl, R. W.; Nielsen, D. U.; Hu, X.-M.; Pedersen, S. U.; Daasbjerg, K.; Skrydstrup, T., Scalable carbon dioxide electroreduction coupled to carbonylation chemistry. *Nat. Commun.* **2017**, *8*, 1-8.
27. Shi, Y.; Xia, C.; Huang, Y.; He, L., Electrochemical Approaches to Carbonylative Coupling Reactions. *Chem. Asian J.* **2021**, *16*, 2830-2841.
28. Nielsen, D. U.; Hu, X.-M.; Daasbjerg, K.; Skrydstrup, T., Chemically and electrochemically catalysed conversion of CO₂ to CO with follow-up utilization to value-added chemicals. *Nat. Catal.* **2018**, *1*, 244-254.
29. Zhang, S.; Fan, Q.; Xia, R.; Meyer, T. J., CO₂ reduction: from homogeneous to heterogeneous electrocatalysis. *Acc. Chem. Res.* **2020**, *53*, 255-264.
30. Kumar, B.; Brian, J. P.; Atla, V.; Kumari, S.; Bertram, K. A.; White, R. T.; Spurgeon, J. M., New trends in the development of heterogeneous catalysts for electrochemical CO₂ reduction. *Catal. Today* **2016**, *270*, 19-30.
31. Zhao, G.; Huang, X.; Wang, X.; Wang, X., Progress in catalyst exploration for heterogeneous CO₂ reduction and utilization: a critical review. *J. Mater. Chem. A* **2017**, *5*, 21625-21649.
32. Drent, E.; Budzelaar, P. H., Palladium-catalyzed alternating copolymerization of alkenes and carbon monoxide. *Chem. Rev.* **1996**, *96*, 663-682.
33. Bianchini, C.; Meli, A., Alternating copolymerization of carbon monoxide and olefins by single-site metal catalysis. *Coord. Chem. Rev.* **2002**, *225*, 35-66.
34. Jiang, C.; Nichols, A. W.; Machan, C. W., A look at periodic trends in d-block molecular electrocatalysts for CO₂ reduction. *Dalton Trans.* **2019**, *48*, 9454-9468.

35. Rohr, B. A.; Singh, A. R.; Gauthier, J. A.; Statt, M. J.; Nørskov, J. K., Micro-kinetic model of electrochemical carbon dioxide reduction over platinum in non-aqueous solvents. *Phys. Chem. Chem. Phys.* **2020**, *22*, 9040-9045.
36. Jones, J. P.; Prakash, G. S.; Olah, G. A., Electrochemical CO₂ reduction: recent advances and current trends. *Isr. J. Chem.* **2014**, *54*, 1451-1466.
37. Vickers, J. W.; Alfonso, D.; Kauffman, D. R., Electrochemical carbon dioxide reduction at nanostructured gold, copper, and alloy materials. *Energy Technol.* **2017**, *5*, 775-795.
38. Chen, C.; Zhang, B.; Zhong, J.; Cheng, Z., Selective electrochemical CO₂ reduction over highly porous gold films. *J. Mater. Chem. A* **2017**, *5*, 21955-21964.
39. Gan, G.; Li, X.; Wang, L.; Fan, S.; Mu, J.; Wang, P.; Chen, G., Active Sites in Single-Atom Fe-N_x-C Nanosheets for Selective Electrochemical Dechlorination of 1, 2-Dichloroethane to Ethylene. *ACS Nano* **2020**, *14*, 9929-9937.
40. Gan, G.; Fan, S.; Li, X.; Wang, J.; Bai, C.; Guo, X.; Tade, M.; Liu, S., Nature of Intrinsic Defects in Carbon Materials for Electrochemical Dechlorination of 1, 2-Dichloroethane to Ethylene. *ACS Catal.* **2021**, *11*, 14284-14292.
41. Noda, H.; Ikeda, S.; Oda, Y.; Imai, K.; Maeda, M.; Ito, K., Electrochemical reduction of carbon dioxide at various metal electrodes in aqueous potassium hydrogen carbonate solution. *Bull. Chem. Soc. Jpn.* **1990**, *63*, 2459-2462.
42. Gao, D.; Zhou, H.; Wang, J.; Miao, S.; Yang, F.; Wang, G.; Wang, J.; Bao, X., Size-dependent electrocatalytic reduction of CO₂ over Pd nanoparticles. *J. Am. Chem. Soc.* **2015**, *137*, 4288-4291.

43. Gao, D.; Zhou, H.; Cai, F.; Wang, D.; Hu, Y.; Jiang, B.; Cai, W.-B.; Chen, X.; Si, R.; Yang, F., Switchable CO₂ electroreduction via engineering active phases of Pd nanoparticles. *Nano Res.* **2017**, *10*, 2181-2191.
44. Saeki, T.; Hashimoto, K.; Kimura, N.; Omata, K.; Fujishima, A., Electrochemical reduction of CO₂ with high current density in a CO₂ + methanol medium at various metal electrodes. *J. Electroanal. Chem.* **1996**, *404*, 299-302.
45. Drent, E.; Van Broekhoven, J.; Doyle, M., Efficient palladium catalysts for the copolymerization of carbon monoxide with olefins to produce perfectly alternating polyketones. *J. Organomet. Chem.* **1991**, *417*, 235- 251.
46. Fujita, T.; Nakano, K.; Yamashita, M.; Nozaki, K., Alternating copolymerization of fluoroalkenes with carbon monoxide. *J. Am. Chem. Soc.* **2006**, *128*, 1968-1975.
47. Shultz, C. S.; Ledford, J.; DeSimone, J. M.; Brookhart, M., Kinetic studies of migratory insertion reactions at the (1, 3-Bis (diphenylphosphino) propane) Pd (II) center and their relationship to the alternating copolymerization of ethylene and carbon monoxide. *J. Am. Chem. Soc.* **2000**, *122*, 6351-6356.
48. Bettucci, L.; Bianchini, C.; Claver, C.; Suarez, E. J. G.; Ruiz, A.; Meli, A.; Oberhauser, W., Ligand effects in the non-alternating CO–ethylene copolymerization by palladium (II) catalysis. *Dalton Trans.* **2007**, 5590-5602.
49. Chen, C.; Anselment, T. M.; Fröhlich, R.; Rieger, B.; Kehr, G.; Erker, G., *o*-Diarylphosphinoferrocene Sulfonate Palladium Systems for Nonalternating Ethene–Carbon Monoxide Copolymerization. *Organometallics* **2011**, *30*, 5248-5257.
50. Andrady, A. L., Weathering of polyethylene (LDPE) and enhanced photodegradable polyethylene in the marine environment. *J. Appl. Polym. Sci.* **1990**, *39*, 363-370.

51. Andrady, A.; Pegram, J.; Song, Y., Studies on enhanced degradable plastics. II. Weathering of enhanced photodegradable polyethylenes under marine and freshwater floating exposure. *J. Environ. Polym. Degrad.* **1993**, *1*, 117-126.
52. Hartley, G. H.; Guillet, J., Photochemistry of ketone polymers. I. Studies of ethylene-carbon monoxide copolymers. *Macromolecules* **1968**, *1*, 165-170.

Supplementary Information

Reagents and Materials

General considerations for reagents and materials. The commercial reagents used in the various procedures were used as received unless specified. The deionized (DI) water that was used throughout the experiments came from a Millipore Milli-Q Water Purification System. N,N-dimethylformamide (DMF) and 1,2-dichloroethane were dried over 3 Å molecular sieves for at least 24 h prior to use. Pd(*o*-Ar₂PC₆H₄SO₃)(Me)(pyridine) (**Pd-PO**, Ar = *o*-MeO-C₆H₄) was synthesized according to the literature procedure.¹ Chloride complex (dppp)Pd(Me)(Cl) (dppp is 1,2-bis(diphenylphosphino)propane) and methyl complex [(dppp)Pd(Me)(MeCN)][BAr^F₄] (**Pd-PP**, Ar^F is 3,5-bis(trifluoromethyl)phenyl) were synthesized according to literature procedures.^{2,3}

*Synthesis of [(dppp)Pd(Me)(MeCN)][BAr^F₄] (**Pd-PP**).* The complex was prepared analogously to the literature procedure.⁴ A 20 mL vial was charged with (dppp)Pd(Me)(Cl) (0.165 g, 0.290 mmol), NaBAr^F₄ (0.257 g, 0.290 mmol), MeCN (0.30 mL), and dichloromethane (10 mL). After being allowed to stir at room temperature for 15 h, the mixture was filtered and the filtrate was concentrated under vacuum to yield an orange solid (0.3988 g, 96%) with spectroscopic data closely matching prior reports.^{2,3}

*Synthesis of Pd(*o*-Ar₂PC₆H₄SO₃)(Me)(pyridine) (**Pd-PO**).* The complex was prepared analogously to the literature procedure.¹ To a solution of 2-[di(2-methoxyphenyl)phosphino] benzenesulfonic acid (0.506 g, 1.25 mmol) in dichloromethane (5 mL) was added a solution of Pd(*N,N,N',N'*-tetramethylethylenediamine)(CH₃)₂ (0.318 g, 1.25 mmol) in dichloromethane (5 mL). The cloudy mixture was stirred at room temperature for 1 h, then pyridine (0.509 mL, 6.29 mmol) was added via syringe. Upon pyridine addition, the mixture turned a clear pale yellow, and was allowed to stir for an additional 30 min. The solution was then concentrated under vacuum to a total volume

of about 5 mL. Diethyl ether (15 mL) was added, resulting in a fine precipitate. The pale yellow solids were collected by filtration, washed three times with diethyl ether (10 mL), and dried under vacuum (0.694 g, 91%). The spectroscopic data closely matched prior reports.¹

Electrochemical Methods and CO₂ Electroreduction to CO Studies

Electrochemical methods. Electrochemistry was performed using a Gamry Instruments Interface 1000-E or Biologic VMP3 potentiostat. The electrolyte solution was composed of 0.25 M TBAPF₆ dissolved in the organic solvent of choice: DMF, 1,2-dichloroethane (1,2-DCE), or 1,2-difluorobenzene (1,2-DFB). A custom-designed high-pressure electrochemical reactor (Parr Instruments) was used (**Figure S3.1**). The solution volume was 200 mL and the gas headspace volume was ca. 750 mL (the value used for Faradaic efficiency calculations). The reactor was pressurized with the desired amount of CO₂ (and optionally C₂H₄). A two-electrode configuration was utilized under constant applied current (I_{appl}) and the headspace was sampled before and after electrolysis using a gas chromatograph (GC). **Table S3.1** summarizes the optimization of CO₂ reduction in this cell. After the reaction, the electrodes were sequentially rinsed and sonicated in acetone, DI water, and dilute nitric acid. To determine the potential at the working electrode, a Ag⁺/Ag pseudo-reference electrode with a glass frit was added and the output potential was calibrated versus the ferrocenium/ferrocene reduction potential.

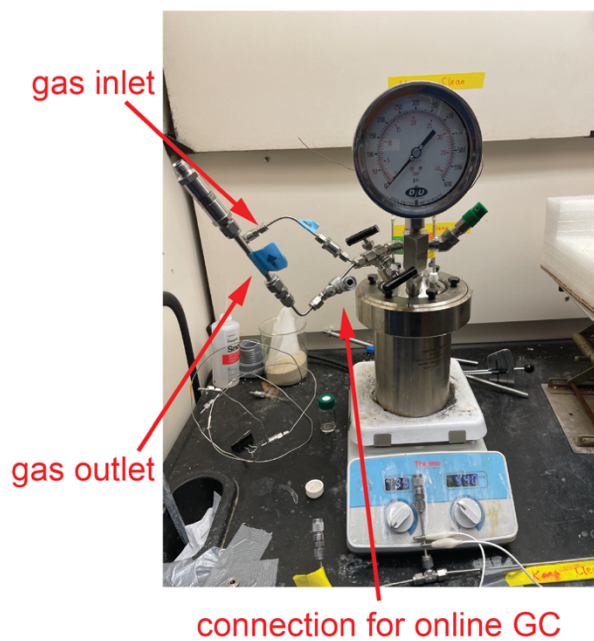
In a representative experiment, the working electrode and counter/reference electrode were both comprised of Pd foil with an average surface area of ~130 cm². Constant current electrolysis was conducted for 24 h under a constant I_{appl} of 90 mA resulting in a current density of 0.7 mA·cm⁻². CO₂ gas (Airgas, 99.999 %) and C₂H₄ gas (Airgas, 99.9 %) were charged into the high-pressure reactor such that the total pressure was 14 bar ($P_{\text{CO}_2}/P_{\text{C}_2\text{H}_4} = 1$). The gas headspace of the reactor was sampled via online detection with a GC before and after electrolysis.

Gas product quantification from CO₂ electrolysis. The gas products of CO₂ reduction were quantified via online detection with a GC (SRI 8610C). For electrolyses carried out at 0.5 mA cm⁻² or higher, the headspace sample was diluted at a ratio of 5/83 using air to avoid saturating the detector. The valve oven temperature was set to 175 °C. The carrier gas was argon which was supplied at a pressure of 15 psi and a flow rate of 40 mL/min. Upon sample injection, the initial column temperature was held at 50 °C for 1 min, after which the temperature ramp rate was 20 °C/min with a final temperature of 90 °C. The column temperature was held at 90 °C for 3.75 min. Then, at a ramp rate of 30 °C/min, the temperature was increased to 210 °C. Three columns were utilized within the GC in the following order: a 0.5 m Haysep-D pre-column, a 2 m MoleSieve5A column, and a 2 m Haysep-D column. Both a flame ionization detector equipped with a methanizer (FIDm) and a thermal conductivity detector (TCD) were used for sample quantification. Hydrogen was supplied to the FID from a H₂-100 Hydrogen Generator at a pressure of 20 psi and a flow rate of 30 mL/min. Air was also supplied to the FIDm at a pressure of 5 psi and a flow rate of 250 mL/min. CO was quantified at a retention time of ~5.45 min on the spectrum obtained from the FIDm and H₂ was quantified at a retention time of ~1.25 min on the spectrum obtained from the TCD. The amount of CO and H₂ produced was quantified with a standard calibration gas mixture (0.5 % CO₂, 0.5 % CO, 0.5 % H₂, and 0.5 % O₂ in N₂). The proton source in CO₂ electrolyses experiments with no added H⁺ source is likely adventitious water, which is documented in other non-aqueous CO₂ reduction systems.^{5, 6} Additionally, reports of water content in common organic solvents prepared over molecular sieves, analogous to this study, show appreciable residual water by Karl Fischer titrations.⁷

Cyclic voltammetry of Pd complexes. Cyclic voltammograms of both Pd complexes were collected on a CH Instruments 630D potentiostat in an argon-filled glovebox. In separate experiments, DMF

solutions containing 0.25 M TBAPF₆ and either 1 mM **Pd-PP** or 1 mM **Pd-PO** were added to glass vial equipped with a Teflon cap fitted with electrode and gas inlet/outlet ports. The working electrode was a 3 mm diameter glassy carbon disc, with a Pt wire counter electrode, a Ag⁺/Ag pseudo-reference electrode. Voltammograms were collected at scan rates of 50, 100, 200, and 500 mV/s. The reported data are after *iR* correction. Cyclic voltammograms of ferrocene were also conducted to calibrate the potentials of Ag⁺/Ag pseudo-reference electrode. Voltammograms are shown in **Figure S3.2**.

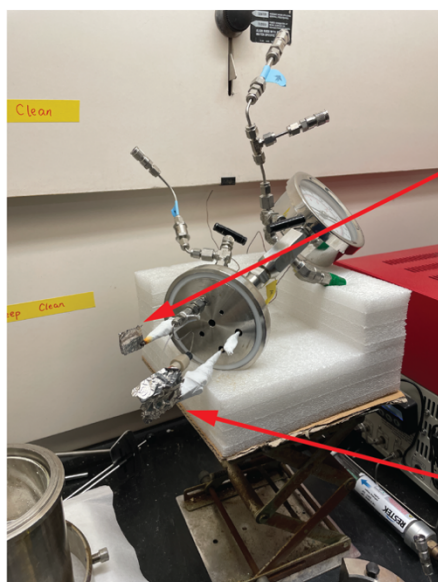
A Outside view of high-pressure reactor



B Inside view of high-pressure reactor



C Electrode placement in high-pressure reactor



D External electrode connections

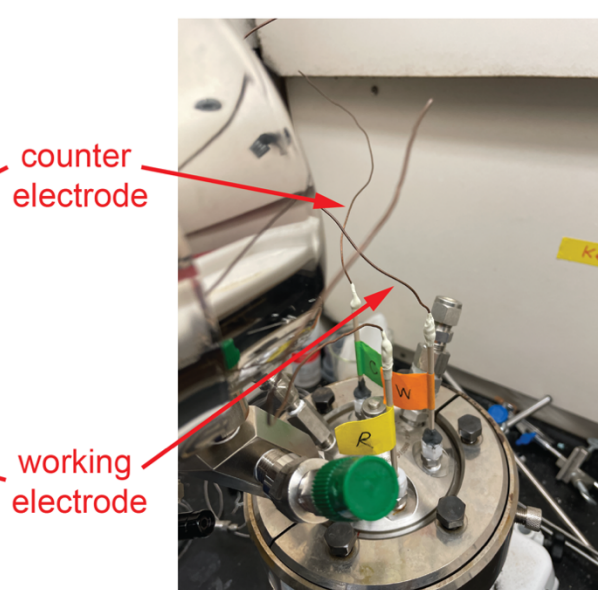


Figure S3.1 Photograph of high-pressure reactor fitted with electrochemical feedthroughs for integrated catalysis. (A) outside view, (B) inside view of reactor, (C) working and counter electrodes (Pd foil), and (D) external electrode connections.

Table S3.1 Summary of CO₂ electrolysis experiments (without an organometallic catalyst present).

Working electrode	Counter electrode	Solvent	Additive	Current density (mA/cm ²)	Time (h)	Temp. (°C)	<i>P</i> _{CO₂} (bar) ^a	<i>P</i> _{Total} (bar) ^b	FE _{CO} (%)	<i>P</i> _{CO} (bar) ^c	FE _{H₂} (%)
Pd foil	Pd foil	1,2-DCE	5 % MeOH	0.45	6	25	1	1	~15	N/A ^d	~12
Pd foil	Pd foil	1,2-DCE	5 % MeOH	0.45	6	40	1	1	< 1	N/A	~4
Pd foil	Pd foil	1,2-DCE	5 % MeOH	0.45	6	60	1	1	< 1	N/A	~8
Pd foil	Pd wire	1,2-DCE	5 % MeOH	1.20	12	25	5	10	0.3	0.0003	2.5
Pd foil	FTO ^e	1,2-DCE	5 % MeOH	0.70	6	25	5	10	5.3	0.003	1.0
Pd foil	Pd foil	1,2-DCE	5 % MeOH	0.70	24	25	5	10	2.5	0.002	1.7
Au-C ^f	Au-C ^f	1,2-DCE	5 % MeOH	0.70	1.5	25	8	23	10	< 0.0001	22.3
Pd foil	Pd foil	1,2-DFB	5 % MeOH	0.45	6	25	1	1	~21	N/A	~11
Pd foil	Pd foil	1,2-DFB	5 % MeOH	0.45	6	40	1	1	< 1	N/A	~6
Pd foil	Pd foil	1,2-DFB	5 % MeOH	0.45	6	60	1	1	< 1	N/A	~7
Pd foil	Pd foil	1,2-DFB	5 % MeOH	0.70	12	25	6	12	12.4	0.019	19.4
Pd foil	Pd foil	1,2-DFB	5 % MeOH	0.70	24	25	6	12	1.3	0.004	29.3
Pd foil	FTO ^e	1,2-DFB	5 % MeOH	0.70	24	25	6	12	< 1	0.0001	23.4
Au-C ^f	Au-C ^f	1,2-DFB	5 % MeOH	0.70	2	25	8	23	< 1	< 0.0001	25.5
Au-Ti ^g	Au-Ti ^g	1,2-DFB	5 % MeOH	0.70	2	25	8	23	< 1	< 0.0001	22.1
Pd foil	Pd foil	DMF	5 % MeOH	0.70	3	25	7	14	18.8	0.028	31.5
Pd foil	Pd foil	DMF	5 % MeOH	0.70	6	25	7	14	14.4	0.043	45.1
Pd foil	Pd foil	DMF	5 % MeOH	0.70	12	25	7	14	17.2	0.103	58.4
Pd foil	Pd foil	DMF	5 % MeOH	0.70	24	25	7	14	7.9	0.095	67.8
Au-Ti ^g	Au-Ti ^g	DMF	10 % H ₂ O + 5 mM CsCO ₃	0.70	15	25	8	23	7.5	0.056	20.5
Au-Ti ^g	Au-Ti ^g	DMF	10 % MeOH	0.70	2	25	8	23	6.5	0.008	35.7
Pd foil	Pd foil	DMF	5 % H ₂ O	0.70	12	25	7	14	5.3	0.032	41.0
Pd foil	Pd foil	DMF	3 % CH ₃ CO ₂ H	0.70	12	25	7	14	3.9	0.006	47.6
Pd foil	Pd foil	DMF	None	0.70	24	25	7	14	86.0	0.518	0.9
Pd foil	Pd foil	DMF	None	0.70	24	25	7	14	44.1	0.531	22.3
Pd foil	Pd foil	DMF	None	0.70	24	25	7	14	34.6	0.493	32.3

^a CO₂ pressure reading prior to electrolysis. ^b Total pressure reading prior to electrolysis (sum of

CO₂ and C₂H₄ pressure). ^c Pressure of CO measured post electrolysis via on-line GC analysis of

reactor head space. ^d total CO pressure was unable to be quantified because a flow cell open to air was utilized for this experiment. ^e FTO is fluorine-doped tin oxide ^fAu-C is gold sputtered on carbon. ^gAu-Ti is gold sputtered on titanium.

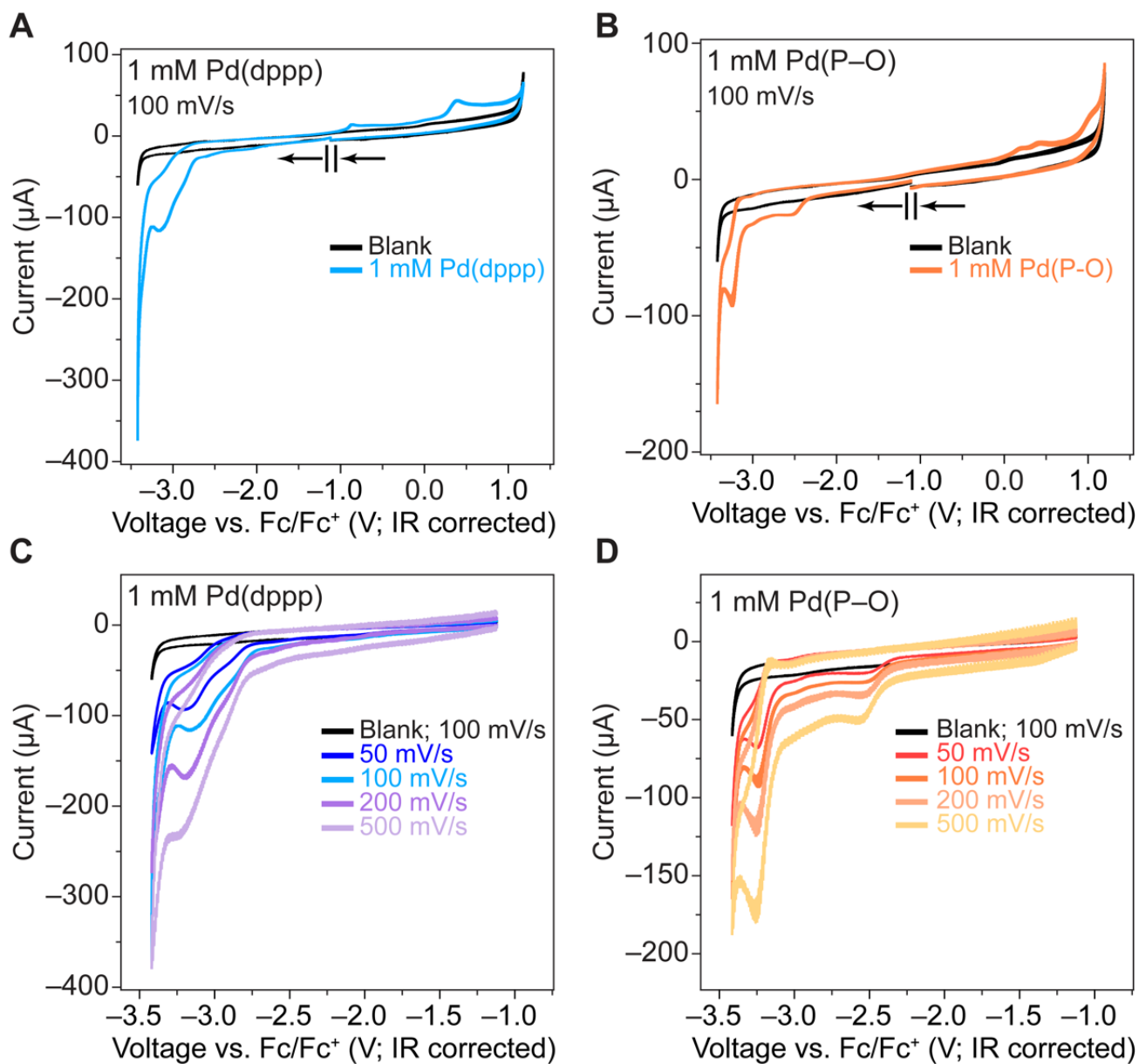


Figure S3.2 Cyclic voltammograms of both **Pd-PP** and **Pd-PP** copolymerization catalysts. (A) blank trace (black, no Pd) and 1 mM **Pd-PP** (light blue) and (B) blank trace (black, no Pd) and 1 mM **Pd-PO** (orange) at a scan rate of 100 mV/s. (C) 1 mM **Pd-PP** at scan rates of 50 mV/s (navy blue), 100 mV/s (light blue), 200 mV/s (purple), and 500 mV/s (light purple) (D) 1 mM **Pd-PO** at scan rates of 50 mV/s (red), 100 mV/s (dark orange), 200 mV/s (orange), and 500 mV/s (light

orange). Glassy carbon working electrode, platinum wire counter electrode, and Ag/Ag⁺ pseudo-reference electrode. 0.25 M tetrabutylammonium hexafluorophosphate in DMF. Potentials, after *iR* compensation, are referenced to the ferrocene/ferrocenium redox couple (Fc/Fc⁺).

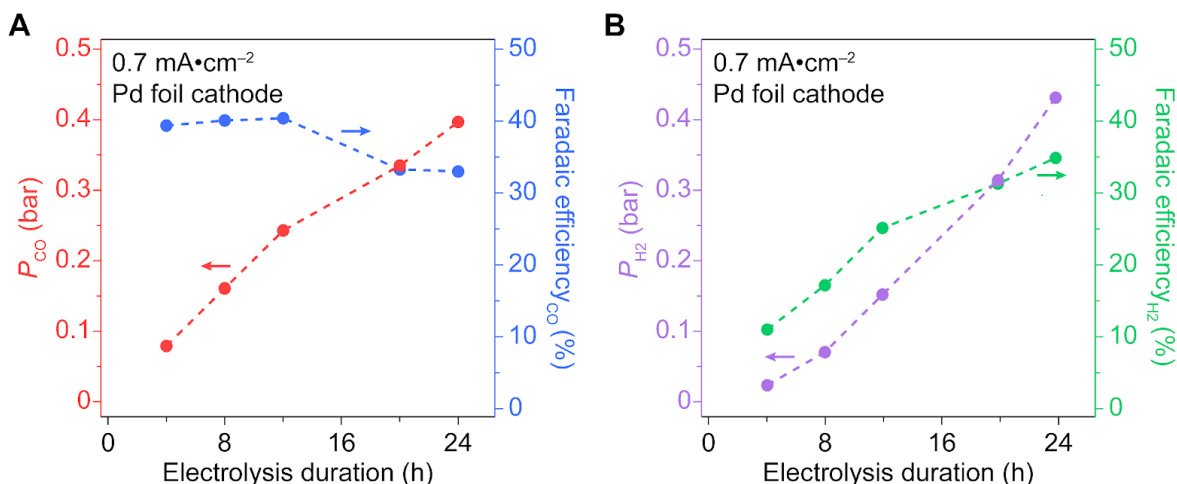


Figure S3.3 Analysis of high-pressure electrochemical carbon dioxide reduction (CO_2) products carbon monoxide (CO) and dihydrogen (H_2) generated at a palladium (Pd) foil cathode over a 24 hour time period at a constant current density of $0.7 \text{ mA}\cdot\text{cm}^{-2}$. **(A)** The CO partial pressure (red) and the respective Faradaic efficiency for CO (blue) upon sampling every 4 h. **(B)** The H_2 partial pressure (purple) and the respective Faradaic efficiency for H_2 (green) upon sampling every 4 h. The gas headspace was characterized and quantified with a gas chromatograph. The working electrode and counter/reference electrodes are both Pd foil. The electrolyte solution is comprised of 0.25 M tetrabutylammonium hexafluorophosphate dissolved in DMF.

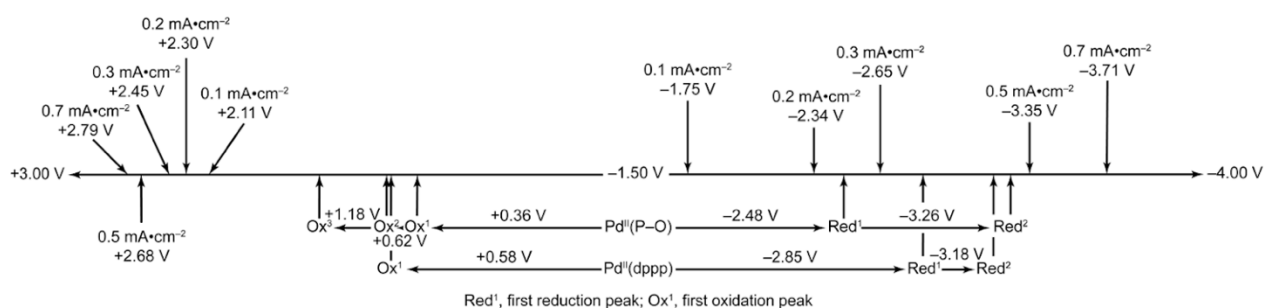


Figure S3.4 Latimer diagram featuring the experimentally observed reduction potentials of the two Pd complexes utilized (**Pd-PO** and **Pd-PP**) alongside the experimental potentials at the working and counter electrodes at each current density applied during the integrated catalysis reactions.

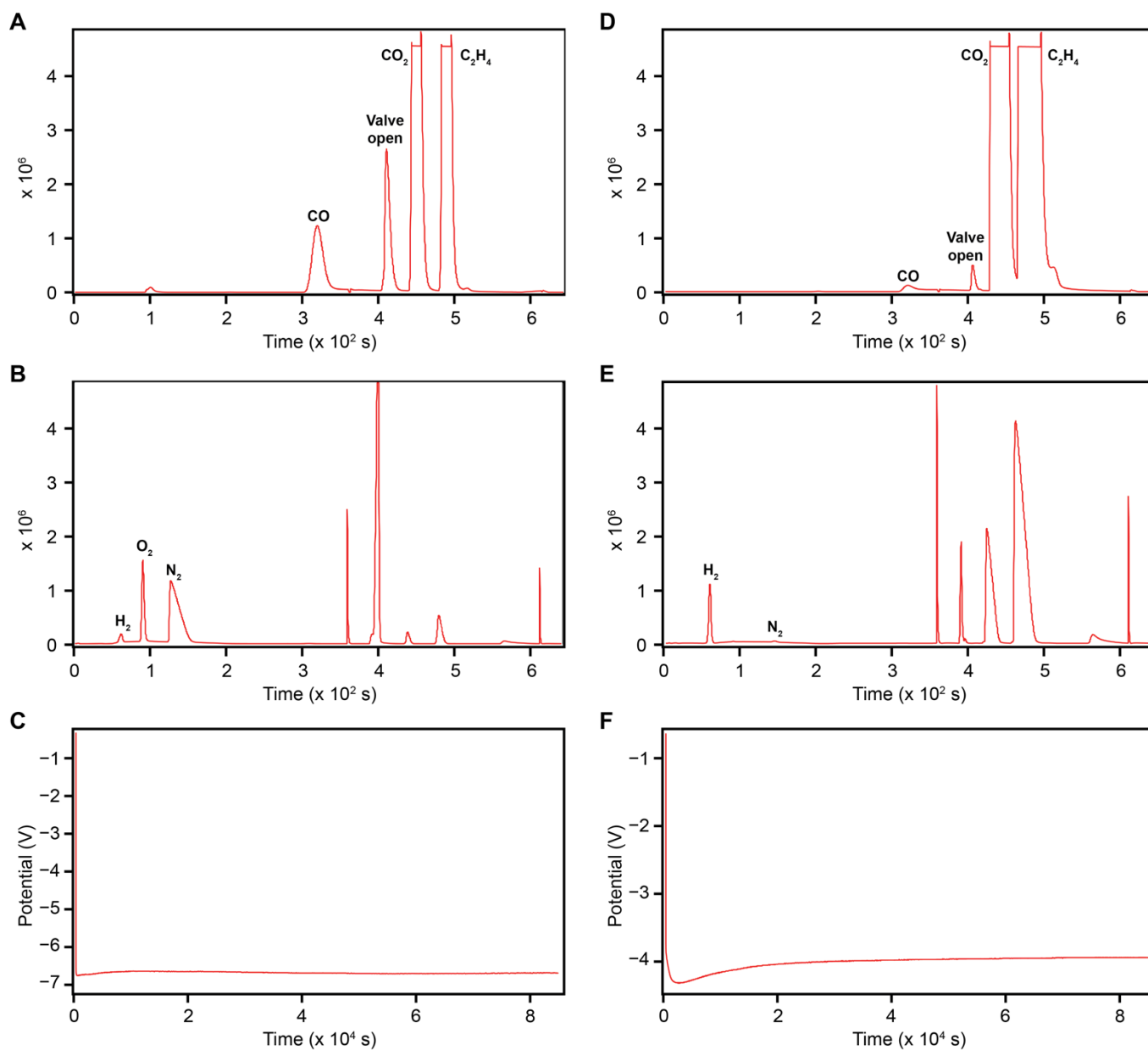


Figure S3.5 (A) GC-FIDm, (B) GC-TCD, and (C) potential vs. time trace from constant current electrolysis at 0.7 mA cm^{-2} for 24 h with Pd foil working and counter/reference electrodes in 0.25 M TBAPF_6 in DMF integrated with **Pd-PO** in 1,2-DCE under 7 bar CO_2 and 7 bar C_2H_4 . (D) GC-FIDm, (E) GC-TCD, and (F) potential vs. time trace from constant current electrolysis at 0.1 mA cm^{-2} for 24 h with Pd foil working and counter/reference electrodes in 0.25 M TBAPF_6 in DMF integrated with **Pd-PP** in DMF under 7 bar CO_2 and 7 bar C_2H_4 .

Polymerization Catalysis Methods and CO/C₂H₄ Copolymerization Studies

Catalytic CO/C₂H₄ copolymerization. In a nitrogen-filled glovebox, a 5 mM stock solution of Pd catalyst was prepared in the solvent of choice. Aliquots (1 mL) of the stock solution were transferred to 2 mL vials via syringe (3-5 vials in total). The vials were sealed with caps that have pre-cut septa designed to allow gas to enter upon pressurization, and placed in a Cat18 high pressure reactor (HEL Group). The reactor was sealed and brought outside the glovebox. The reactor was placed on a heating/stirring plate and connected to a high-pressure gas manifold equipped with CO, C₂H₄, and N₂ gas lines. CO was added to the desired pressure first. To reach a CO pressure of 0.5 bar, the reactor was first pressurized to 20 bar with carbon monoxide and nitrogen (10 bar each) and then vented to atmospheric pressure. To reach a CO pressure of 0.1 bar, the reactor was first pressurized to 10 bar CO and vented three times, ending with a vent to 1 bar CO. Then, the total pressure was brought to 10 bar using N₂ ($P_{N_2} = 9$ bar), and vented back to 1 bar (0.1 bar CO, 0.9 bar N₂). Once the desired CO pressure was reached, the reactor was pressurized with C₂H₄ gas. To end the reaction, the reactor was vented to atmospheric pressure and the vials were retrieved. The contents of the vials were combined into a single scintillation vial. MeOH (10 mL) and 35% HCl (0.6 mL) were added and the mixture was stirred vigorously for at least 4 h. The solids were then collected by vacuum filtration and dried under vacuum.

NMR spectroscopic characterization of copolymers. ¹H NMR and ¹³C{¹H} NMR spectra were recorded on Bruker AV400 or 500MHz spectrometers. Chemical shifts for protons are reported in parts per million (ppm) relative to tetramethylsilane, referenced using the residual protio solvent resonances. Isolated polymer samples were analyzed by ¹H and ¹³C{¹H} NMR. Polyketone samples were dissolved in a 4/1 mixture of 1,1,1,3,3,3-hexafluoro-2-propanol (HFIP) / C₆D₆ and the data was acquired at 298 K. If the sample was not fully soluble or if resonances associated with

multiple ethylene insertions were apparent, additional samples were prepared in 1,1,2,2-tetrachloroethane-d₂ (TCE-d₂) and the data was acquired at 100 °C. The percentage of CO incorporation (%CO) was quantified by ¹H NMR spectroscopy in TCE-d₂ at 100 °C according to reported procedures,⁸ as described in Figure S3.14, except as noted (i.e. for samples that were perfectly alternating). Chain ends were apparent in most NMR spectra, providing additional insight into the polymerization reactions. Triplets at 1.12 and 0.95 ppm (TCE-d₂), or at 0.82 and 0.74 ppm (HFIP/C₆D₆), are assigned as ethyl ketone –C(O)CH₂CH₃ and *n*-alkyl –CH₂CH₂CH₂CH₃ groups, respectively. These are noteworthy for being most likely formed by protonolysis of a Pd–CH₂CH₂R species during acidic workup, thereby providing evidence of good catalyst control over the polymerization. This would also suggest that the other chain end is the methyl ketone –C(O)CH₃ group coming from initiation by the Pd–CH₃ complex, and a singlet at ca. 2.45 ppm consistent with this assignment is present in HFIP/C₆D₆ spectra. Alkene chain ends derived from β-hydrogen elimination chain transfer were only observed in a few samples from CO/C₂H₄ copolymerization run at high temperature. Copolymerization both from CO and CO₂ in the integrated reactor led to spectroscopically similar materials, with analogous chain ends, indicating similar control in each reaction. When the polymerization is controlled, NMR spectroscopy can be used to obtain the degree of polymerization (DP) and thus provide a secondary estimate of M_n . Equation S1 can be used to determine the DP, using the ratio of integrals of the in-chain signals and the two chain end signals (Figure S3.6). For alternating polyketone samples, the DP equation simplifies considerably because only the polyketone signal and ethyl ketone chain end are present. Although the DP calculations rely on assumptions, and are thus considered estimates, NMR analyses of several representative samples aligned nicely with the M_n values determined by size exclusion chromatography.

$$DP = \frac{(2 \cdot 0.25 \cdot I_A) + (2 \cdot 0.5 \cdot I_B) + (0.5 \cdot I_C) + (0.25 \cdot I_D) - (0.66 \cdot I_{CE1}) - (0.66 \cdot I_{CE2})}{(0.33 \cdot I_{CE1}) + (0.33 \cdot I_{CE2})} \quad (S1)$$

Where I_A is the integral of the $-C(O)CH_2CH_2-$ unit, I_B is the integral of the first bridging methylene that links polyketone and polyethylene runs, I_C is the integral of the second methylene that links polyketone and polyethylene runs, I_D is the integral of the $-CH_2CH_2-$ unit, I_{CE1} is the integral of the methyl of the ethyl ketone chain end $-C(O)CH_2CH_3$, and I_{CE2} is the integral of the methyl of the n -alkyl chain end, $-CH_2CH_2CH_2CH_3$. 1H - 1H COSY spectra reveal the chain-end methylene quartets to be under peaks B (CE1) and C (CE2), so the integration of these peaks is subtracted in eq S1. Figure S14 shows the assignments. Equation S2 can be used to determine the M_n from NMR analysis.

$$M_n (NMR) = (DP) \left(28.01 \frac{g}{mol} \right) \left(\frac{\%CO}{100} \right) + (DP) \left(28.05 \frac{g}{mol} \right) \left(1 - \frac{\%CO}{100} \right) + \left(29.06 \frac{g}{mol} + 15.03 \frac{g}{mol} \right) \quad (S2)$$

Where DP is the degree of polymerization (number of enchaind monomer units) from eq S1, and %CO is determined as described above and in Figure S3.14, and the final term represents the mass of the methyl and ethyl chain end groups. A few representative samples were examined using equations S1 and S2 to compare M_n from NMR and SEC: Sample A from Table S2 has M_n of 6380 g/mol from SEC, and NMR from analysis has a DP of 228 and M_n of 6430 g/mol. Sample K from Table S2 has M_n of 3580 g/mol from SEC, and from NMR analysis has a DP of 86 and M_n of 2450 g/mol. Sample PO-1 from Table S5 has M_n 1260 from SEC, and from NMR analysis has a DP of 25 and M_n of 744 g/mol.

Infrared spectroscopic analysis. Attenuated total reflectance-infrared spectroscopy (ATR-IR) was employed to observe the C–O stretching frequency in the polymer. ATR-IR spectra of polymers were acquired on a ThermoScientific Nicolet iS5 with germanium ATR attachment or Bruker Alpha with diamond ATR attachment. The IR stretches of ketones reflect the density of carbonyl

moieties in the polymer chain.⁹ Non-alternating polyketones with low CO content exhibit shifts around 1712 cm⁻¹, whereas alternating polyketones exhibit a shift of 1692 cm⁻¹.

Size exclusion chromatography (SEC) polymer characterization. Size exclusion chromatography (SEC) for alternating polyketone samples was performed at 40 °C using an Agilent Technologies 1260 Infinity Series liquid chromatography system (G1310B isocratic pump, G1329A autosampler, G1316A column compartment, G1362A refractive index detector). The system was equipped with one Agilent HFIPgel guard column (PL HFIPgel Guard, 50 x 4.6 mm, 9 μm) and two Agilent HFIPgel HPLC columns (PL1514-5900HFIP, 4.6 × 250 mm, 9 μm). Experiments were run using a solution of 20 mM sodium trifluoroacetate (CF₃COONa) dissolved in HFIP as the mobile phase at a flow rate of 0.300 mL·min⁻¹. Column calibration was performed with narrow-dispersity poly(methyl methacrylate) (PMMA) standards. SEC for non-alternating polyketone samples was performed using a Malvern high-temperature GPC instrument equipped with refractive index, viscometer, and light scattering detectors at 150 °C with 1,2,4-trichlorobenzene (stabilized with 125 ppm BHT) as the mobile phase. A calibration curve was established using polystyrene standards in triple detection mode. All molecular weights reported are based on the triple detection method.

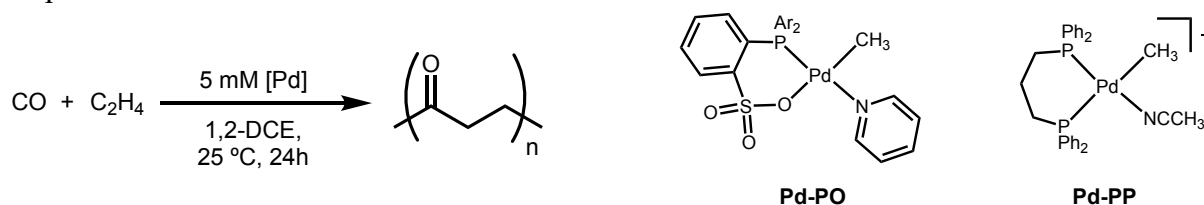


Table S3.2 Reaction outcomes and polymer characterization for CO/C₂H₄ copolymerization in 1,2-DCE at 25 °C.

Catalyst	Sample	P _{CO} (bar)	P _{C₂H₄} (bar)	Polymer yield (g)	Activity (g mmol ⁻¹ h ⁻¹)	M _n	%CO	Đ
	I	0.5	0.5	0	0	-	-	-
Pd-PO	K	0.5	7	0.023	0.064	3580	>49 ^a	1.8
	G	0.5	10	0.018	0.029	3250	49.0 ^a	1.9
	E	0.5	20	0.037	0.062	4120	45.6 ^a	3.0
	C	5	10	0.062	0.103	4810	>49 ^a	1.5
	A	10	10	0.063	0.105	6380	>49 ^a	1.5

	L	0.1	7	0.0057	0.0159	-	43.6	-
	J	0.5	0.5	0.118	0.197	-	>49 ^a	-
Pd-PP	H	0.5	10	0.099	0.166	2416 0 5070 1930	>49 ^a	2.2 1.0 1.1
	F	0.5	20	0.085	0.142	2863 0 4300	>49 ^a	2.2 1.1
	D	5	10	0.461	0.769	1950 0	>49 ^a	5.8
	B	10	10	0.491	0.819	2137 0	>49 ^a	7.3

^a The %CO incorporation calculated from the ¹H NMR spectrum at 25°C in HFIP.

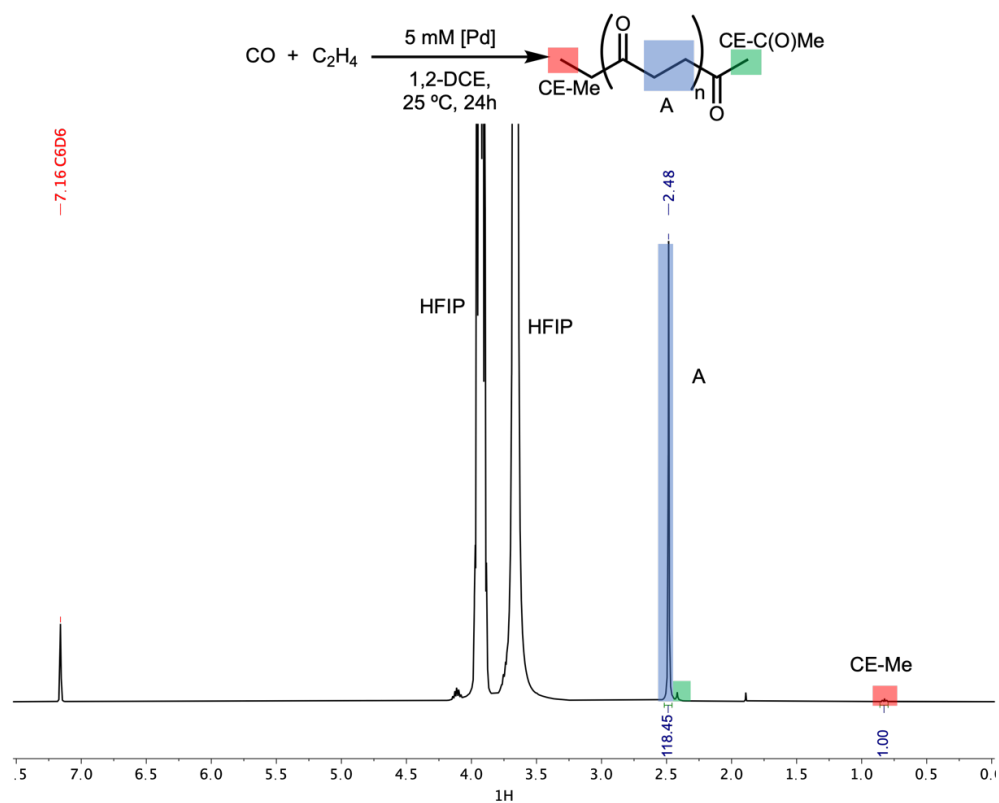


Figure S3.6 ^1H NMR spectrum of sample A from Table S3.2 (4:1 HFIP/ C_6D_6 , 25°C), highlighting the chain end signals used for calculating degree of polymerization.

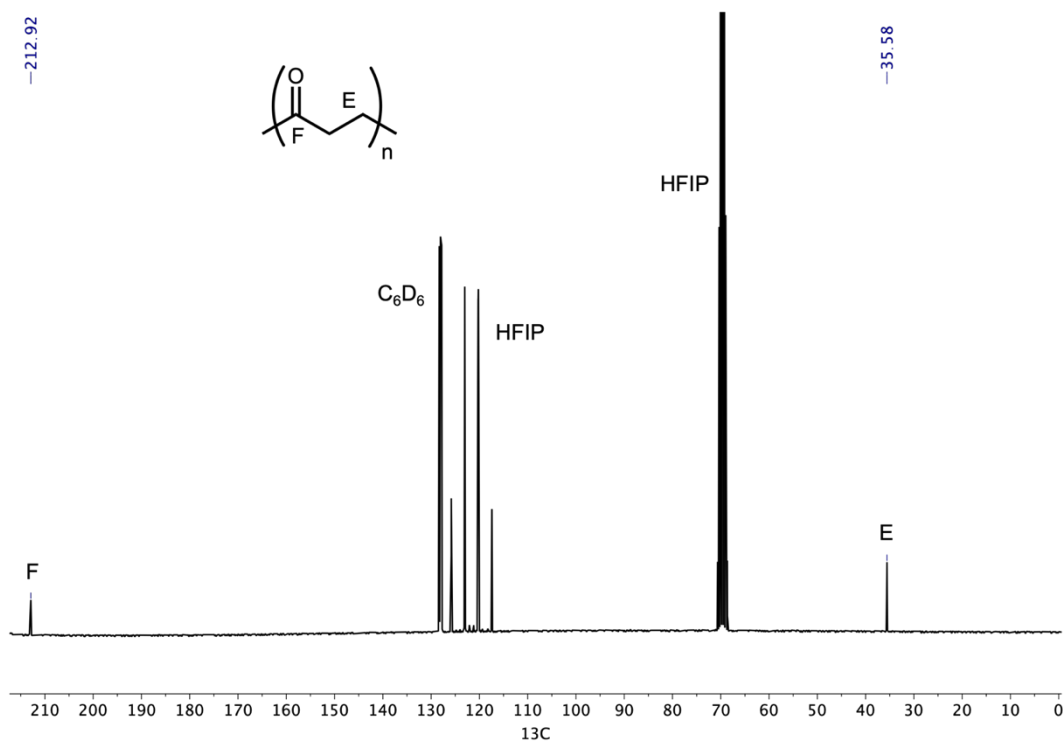


Figure S3.7 $^{13}\text{C}\{^1\text{H}\}$ NMR spectrum of sample A from Table S3.2 (4:1 HFIP/ C_6D_6 , 25°C).

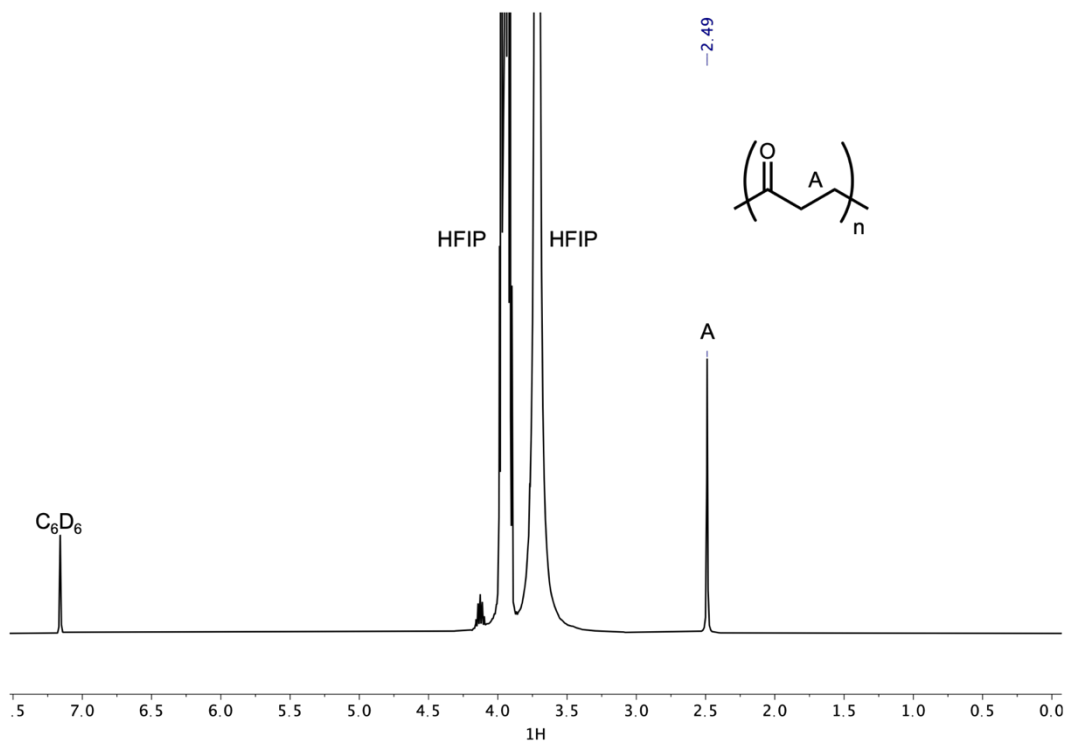


Figure S3.8 ^1H NMR spectrum of sample B from Table S3.2 (4:1 HFIP/ C_6D_6 , 25 °C).

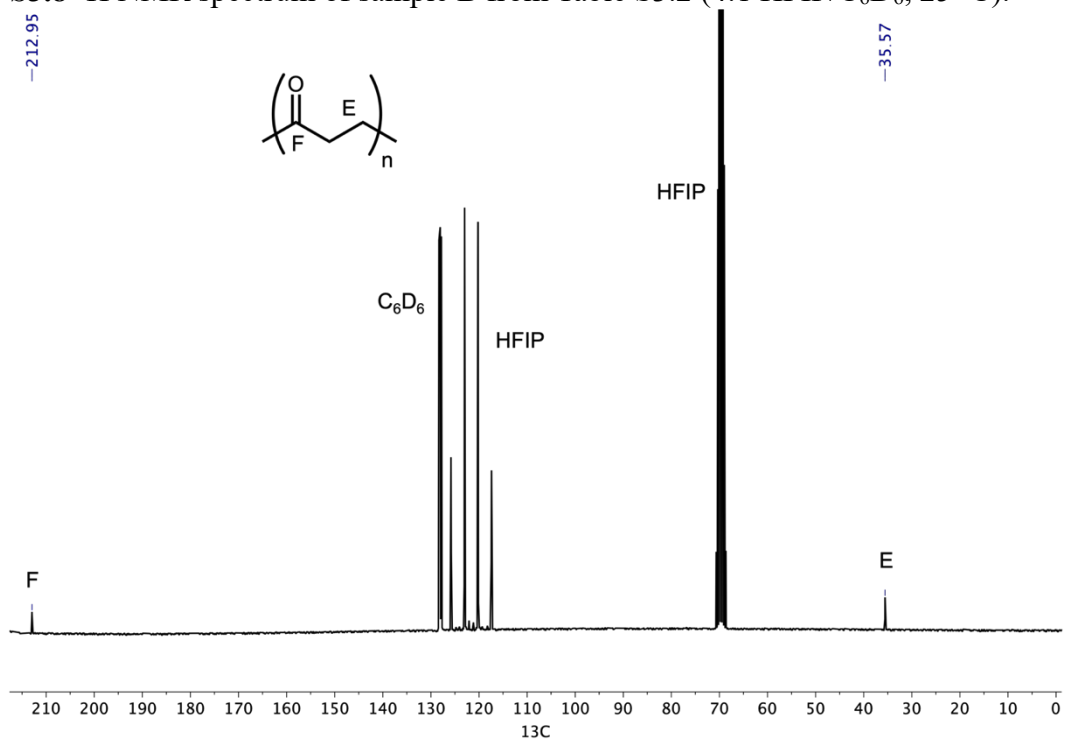


Figure S3.9 $^{13}\text{C}\{^1\text{H}\}$ NMR spectrum of sample B from Table S3.2 (4:1 HFIP/ C_6D_6 , 25 °C).

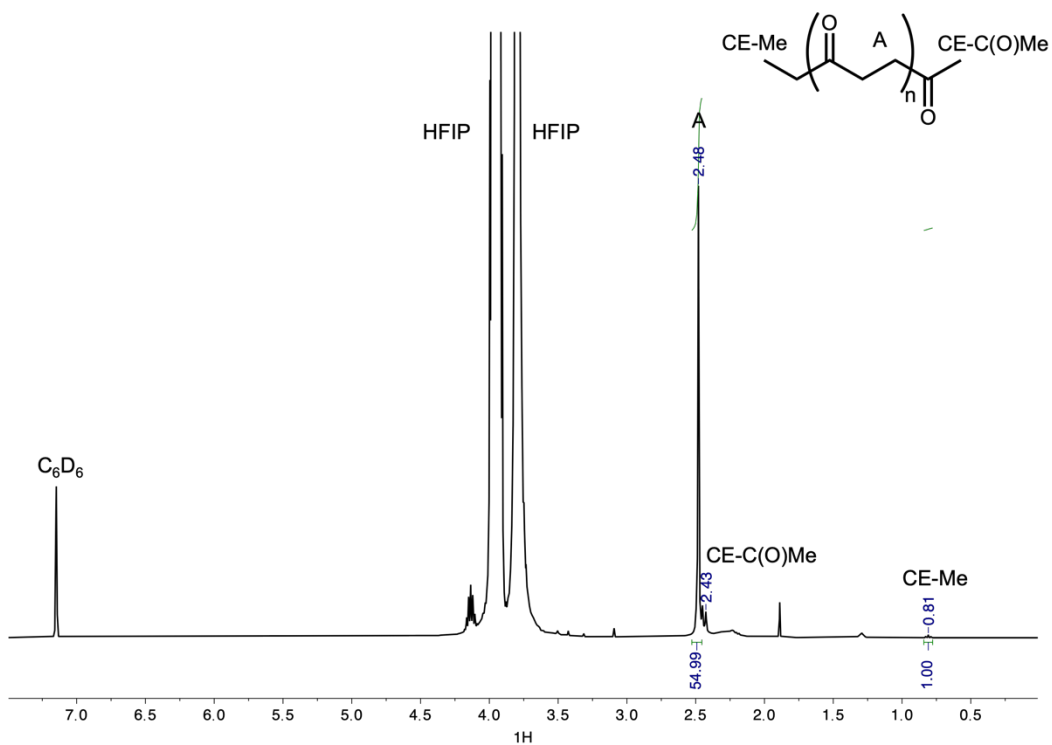


Figure S3.10 ^1H NMR spectrum of sample G from Table S3.2 (4:1 HFIP/ C_6D_6 , 25 $^\circ\text{C}$).

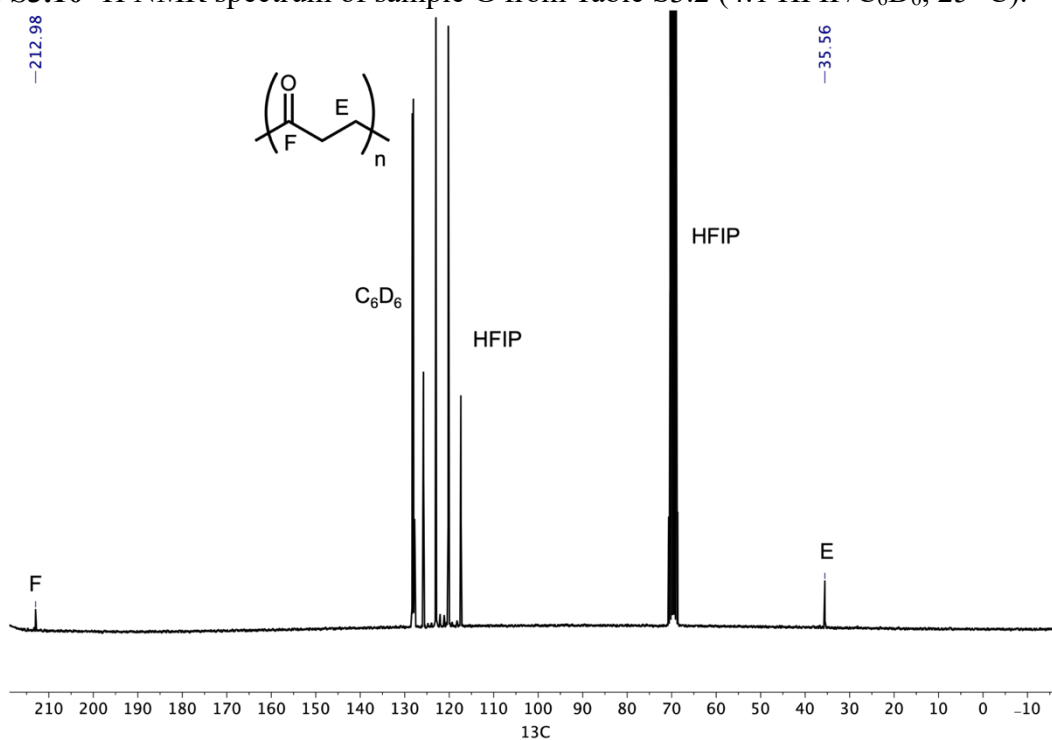


Figure S3.11 $^{13}\text{C}\{^1\text{H}\}$ NMR spectrum of sample G from Table S3.2 (4:1 HFIP/ C_6D_6 , 25 $^\circ\text{C}$).

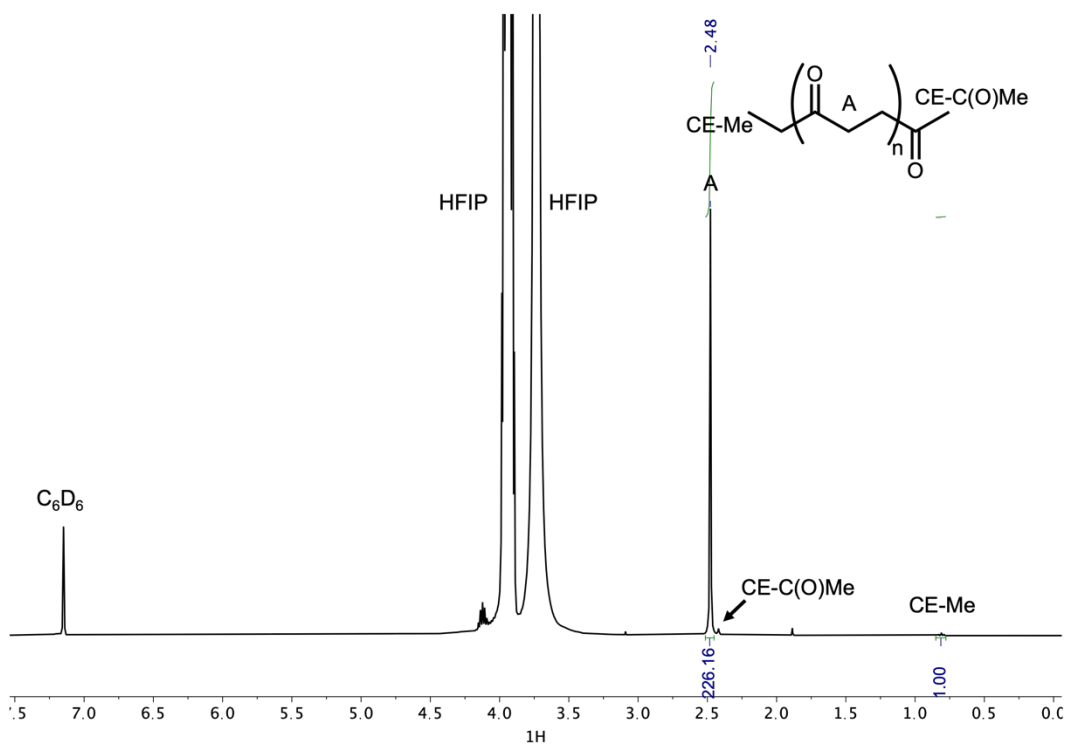


Figure S3.12 ^1H NMR spectrum of sample H from Table S3.2 (4:1 HFIP/ C_6D_6 , 25 $^\circ\text{C}$).

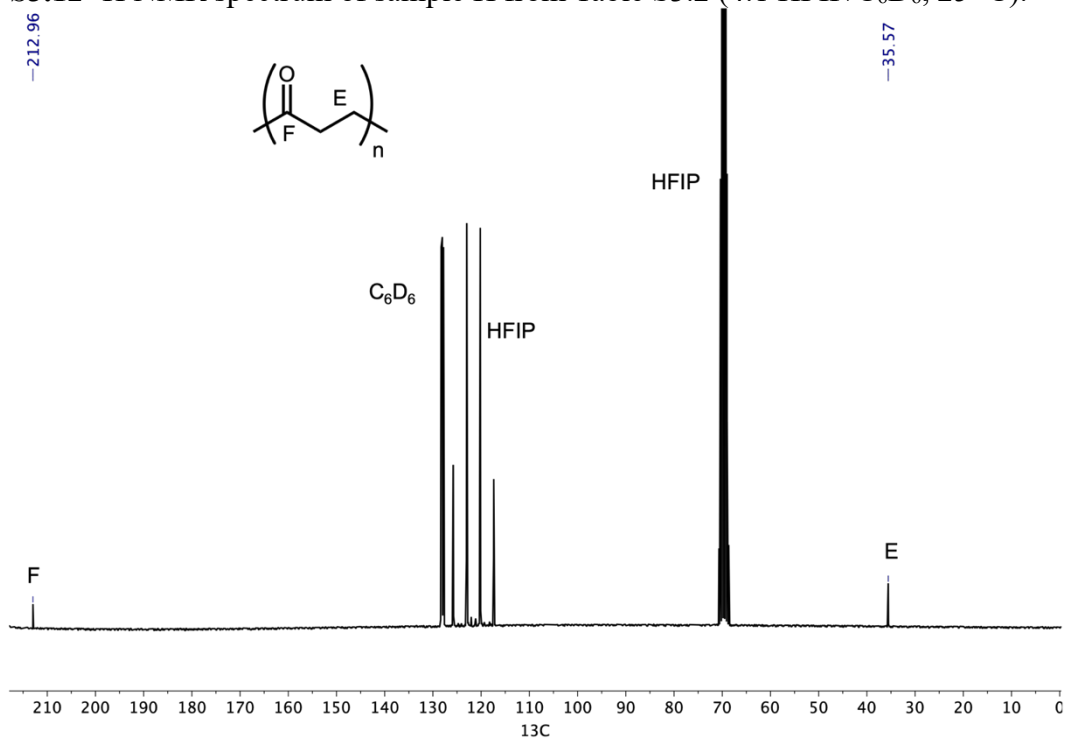
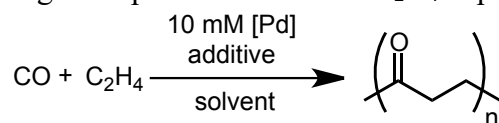
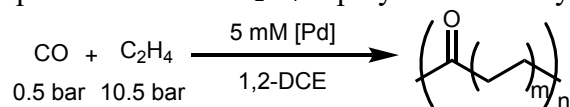


Figure S3.13 $^{13}\text{C}\{^1\text{H}\}$ NMR spectrum of sample H from Table S3.2 (4:1 HFIP/ C_6D_6 , 25 $^\circ\text{C}$).

Table S3.3 Compatibility testing and optimization of CO/C₂H₄ copolymerization.

Catalyst	Solvent	T (°C)	Reaction time (h)	P _{CO} (bar)	P _{C₂H₄} (bar)	P _{CO₂} (bar)	P _{H₂} (bar)	Yield (mg)	Activity (g·mmol Pd ⁻¹ ·h ⁻¹)
Pd-PO	1,2-DCE	40	2	0.5	10.5	0	0	22.5	0.75
Pd-PO	1,2-DCE	40	2	1	11	1	0	26.9	0.45
Pd-PO	1,2-DCE	40	2	1	10	10	0	32.6	0.54
Pd-PO	1,2-DCE	40	2	1	11	11	1	33.0	0.55
Pd-PO ^a	1,2-DCE	25	24	0.5	10.5	0	0	45.0	0.08
Pd-PO	1,2-DCE	40	24	0.5	10.5	0	0	123.3	0.17
Pd-PO	1,2-DCE	25	24	0	10	0	0	101.5	0.28
Pd-PO ^b	1,2-DCE	60	3	0/10 ^b	10	0	0	279.2	6.2
Pd-PO	1,2-DFB	40	2	0.5	10.5	0	0	9.1	0.3
Pd-PO	DMF	40	2	0.5	10.5	0	0	16.0	0.27
Pd-PP ^a	DMF	25	24	0.5	10	0	0	102.0	0.43

^a Carried out at 5 mM Pd. ^b After 1 h at 60 °C with 10 bar C₂H₄ and 0 bar CO, 10 bar CO was introduced (while maintaining 10 bar C₂H₄) and the reaction was allowed to run for 2 h at 60 °C.

Table S3.4 Temperature dependence of CO/C₂H₄ copolymerization by Pd-PO.

Sample	Temp. (°C)	Time (h)	Activity (g mmol Pd ⁻¹ h ⁻¹)	% CO incorporation	IR CO stretch (cm ⁻¹)
K	25	24	0.08	47	1688
L	40 ^a	24	0.17	30	
M	60	24	0.53	28	1704
N	80 ^a	2	1.73	19	
O	100	2	13.7	6.3	1711

^a 10 mM Pd

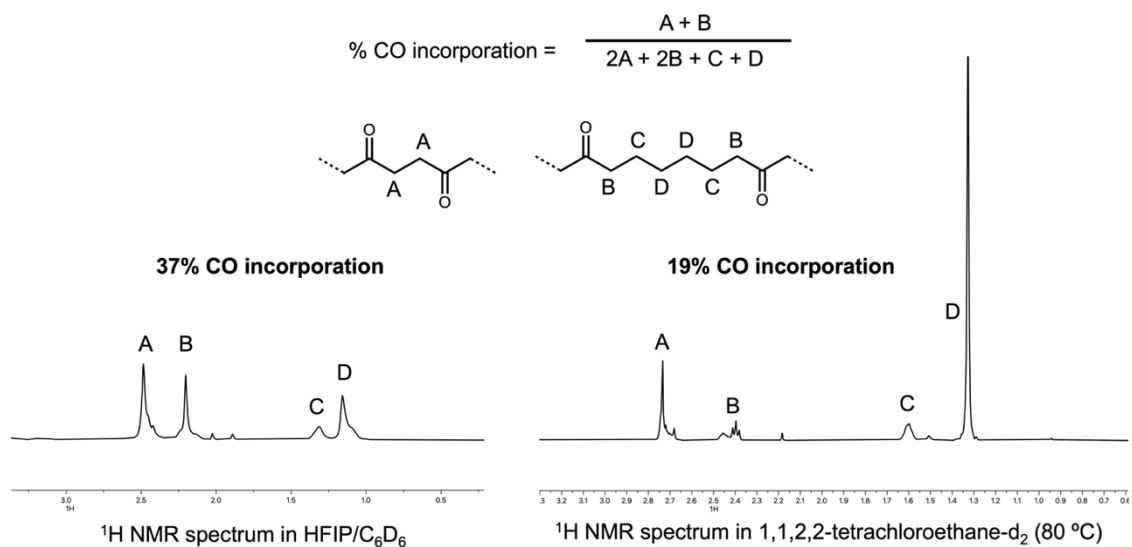


Figure S3.14 ^1H NMR spectra of non-alternating polyketone sample N from Table S3.4. Left: spectrum collected in HFIP/ C_6D_6 (4:1) mixture at 25 °C. Right: spectrum collected in TCE- d_2 at 80 °C. As CO incorporation decreases, polyketones become less soluble in HFIP and more soluble in 1,1,2,2-tetrachloroethane with heat. As the figure highlights, inaccurate % CO incorporation values will be obtained in HFIP for non-alternating polyketones.

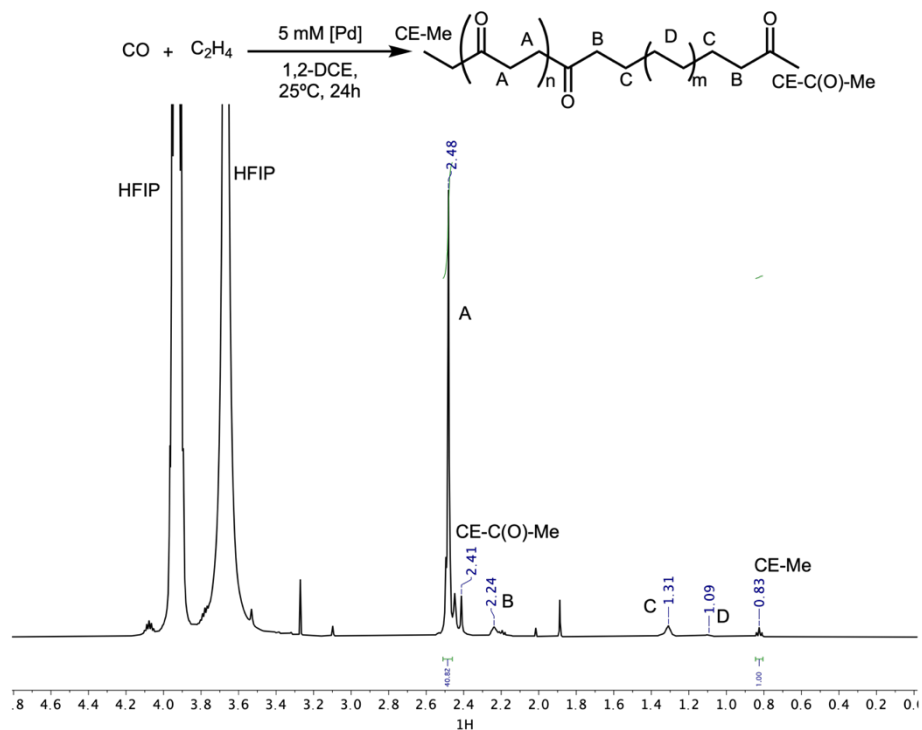


Figure S3.15 ^1H NMR spectrum of sample K from Table S3.4 in 4:1 HFIP: C_6D_6 at 25 °C.

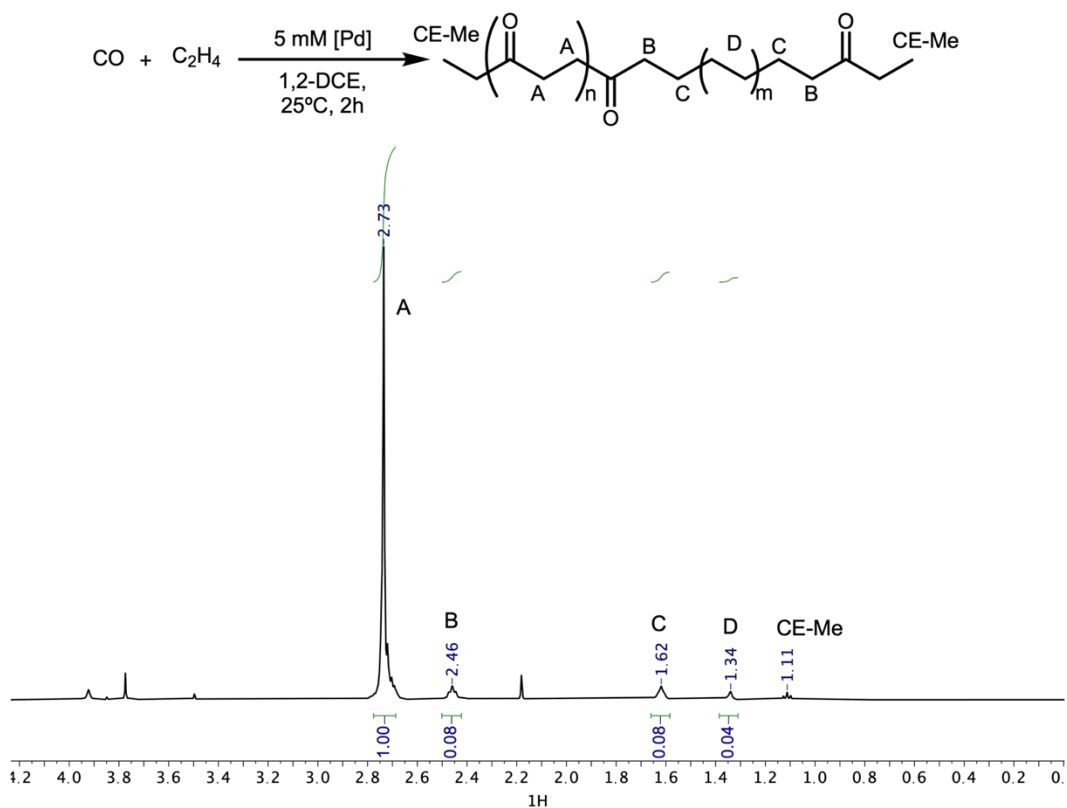


Figure S3.16 ^1H NMR spectrum of sample K from Table S3.4 in TCE- d_2 at 80°C .

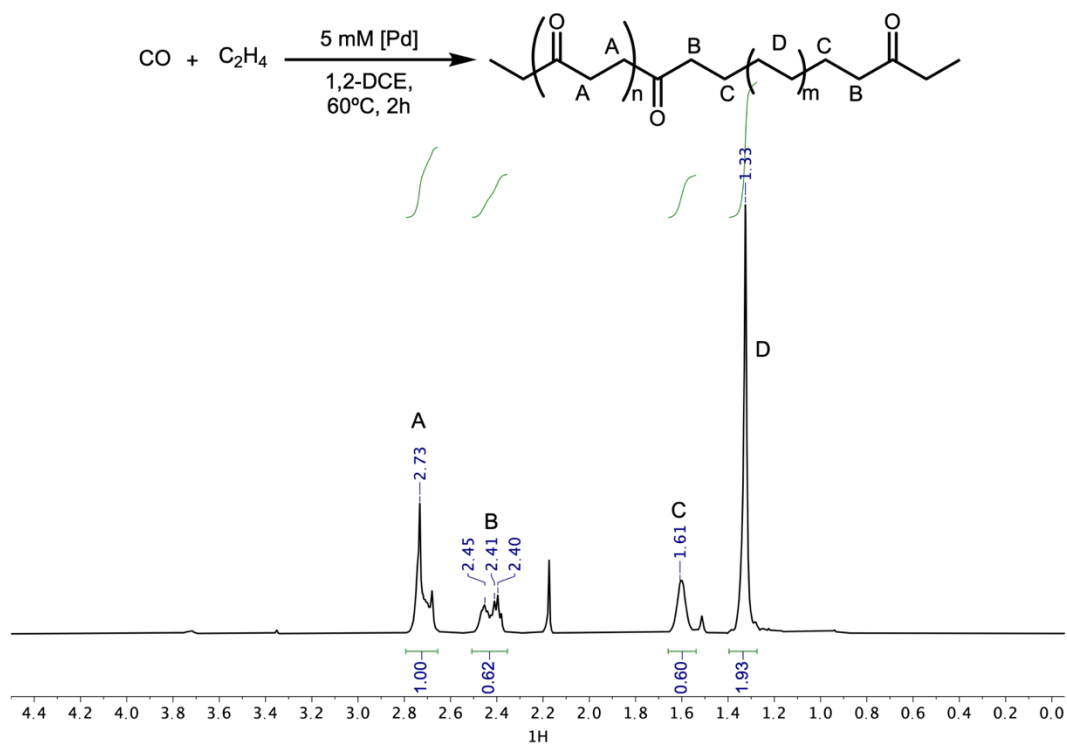


Figure S3.17 ^1H NMR spectrum of sample M from Table S3.4 in TCE- d_2 at 80°C .

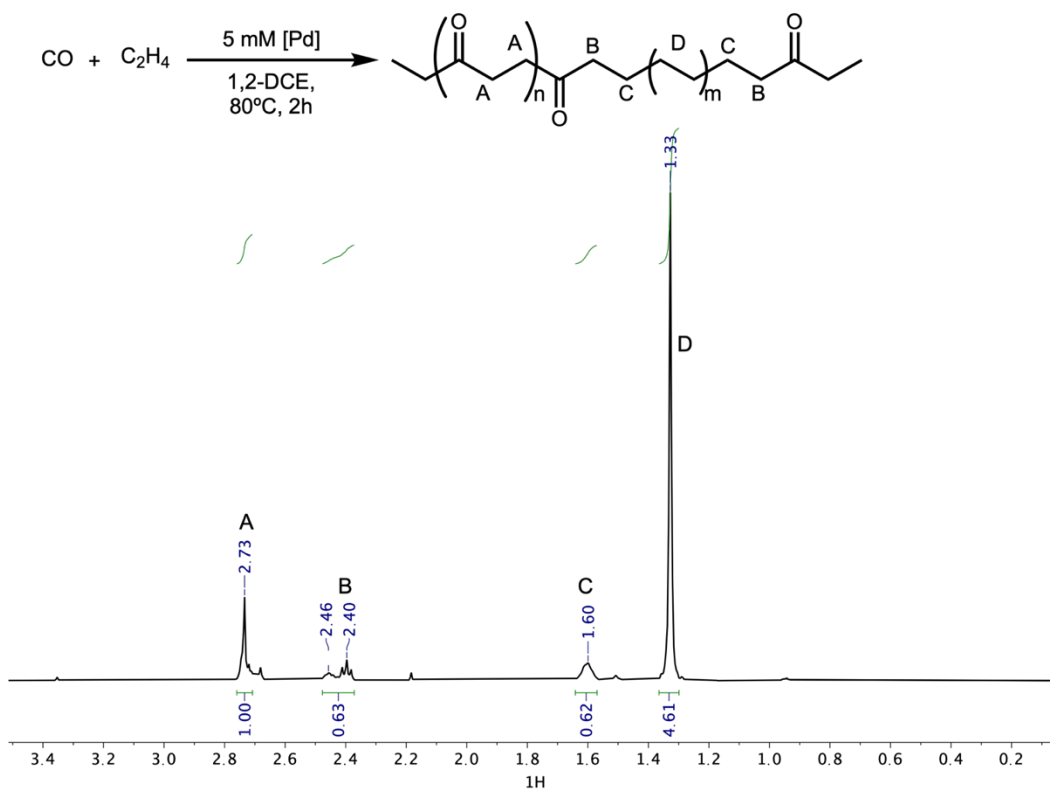


Figure S3.18 ^1H NMR spectrum of sample N from Table S3.4 in TCE- d_2 at 80°C .

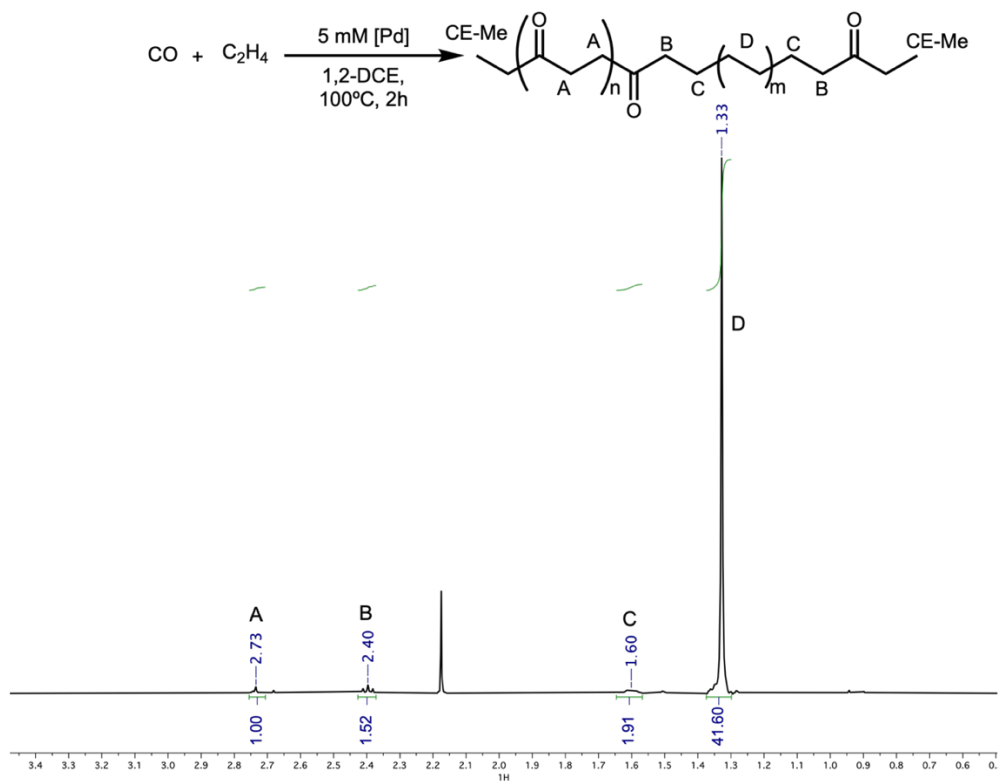


Figure S3.19 ^1H NMR spectrum of sample O from Table S3.4 in TCE- d_2 at 80°C .

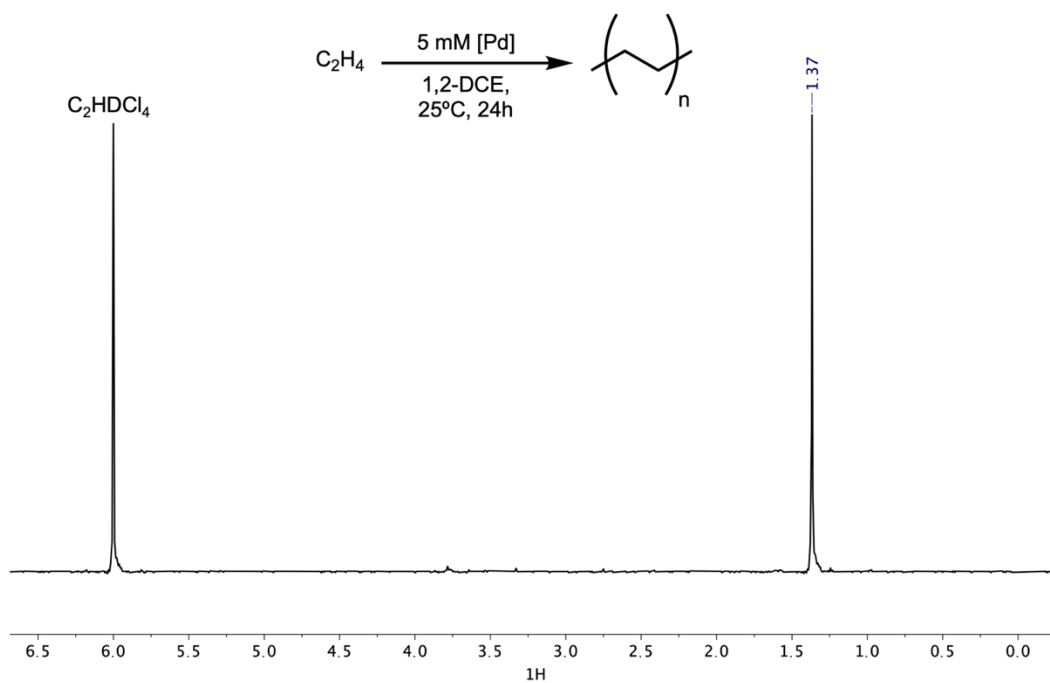


Figure S3.20 ^1H NMR spectrum of polyethylene from Table S3.3 in TCE- d_2 at 100 $^\circ\text{C}$.

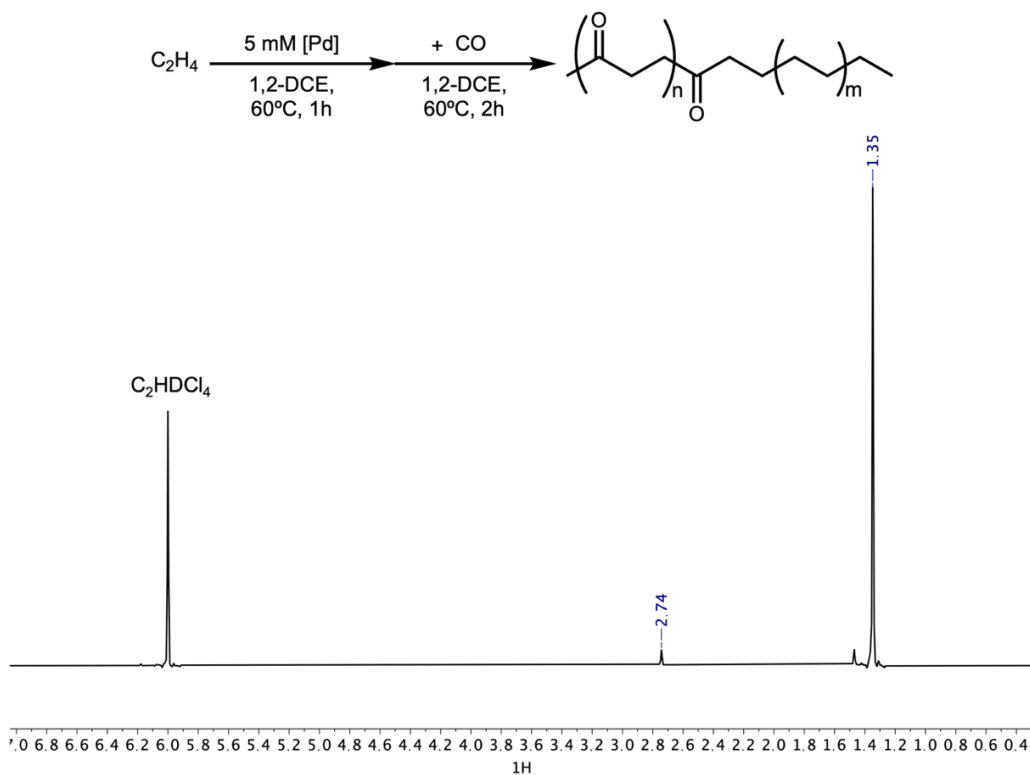


Figure S3.21 ^1H NMR spectrum of *block*-polyethylene-*block*-*alt*-polyketone from Table S3.3 in TCE- d_2 at 100 $^\circ\text{C}$.

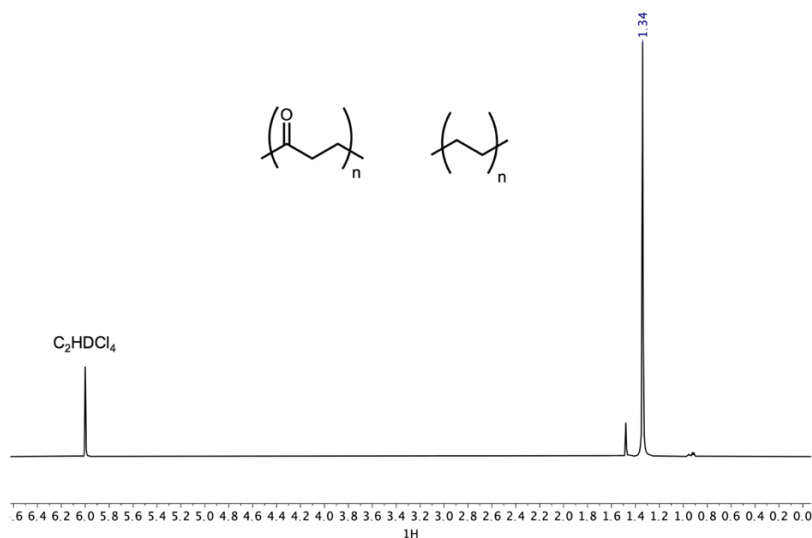


Figure S3.22 ^1H NMR spectrum of a blend of polyethylene and alternating polyketone in TCE-d_2 at 100°C . The blend was made manually by mixing two separate polymer samples.

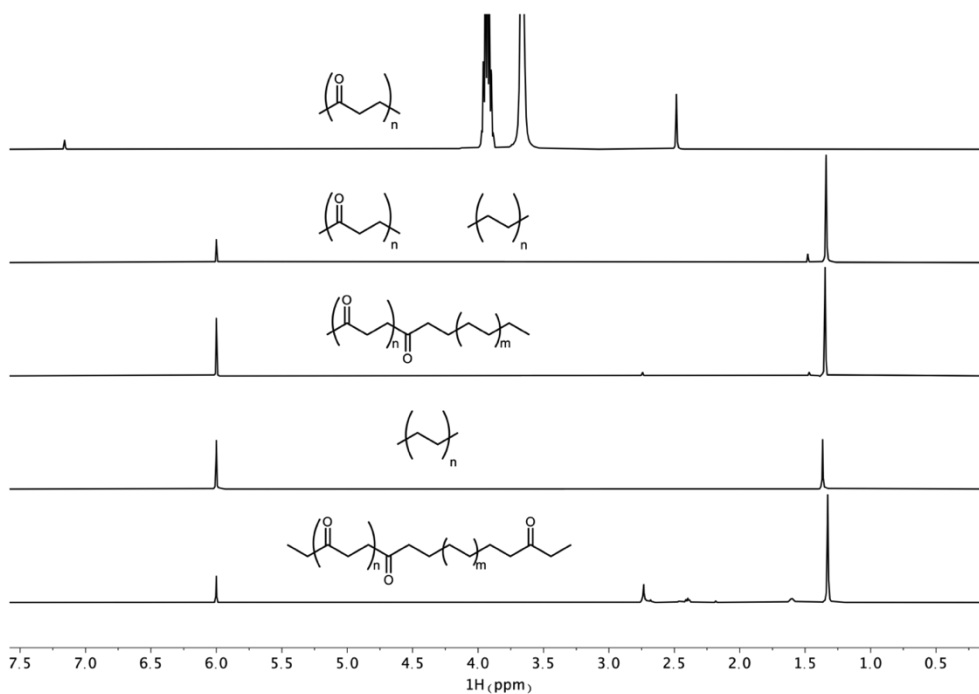


Figure S3.23 Stack of ^1H NMR spectra in TCE-d_2 at 100°C showing (from bottom to top): non-alt-polyketone, polyethylene, *block-polyethylene-block-alt-polyketone*, a blend of polyethylene and alt-polyketone, and alt-polyketone. The top spectrum of alt-polyketone was collected in 4:1 HFIP: C_6D_6 at 25°C .

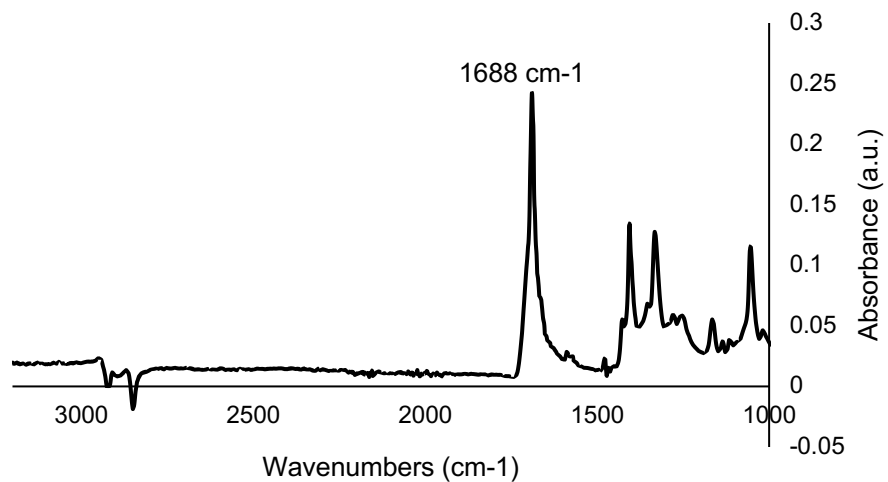


Figure S3.24 ATR-IR spectrum of sample K from Table S3.4.

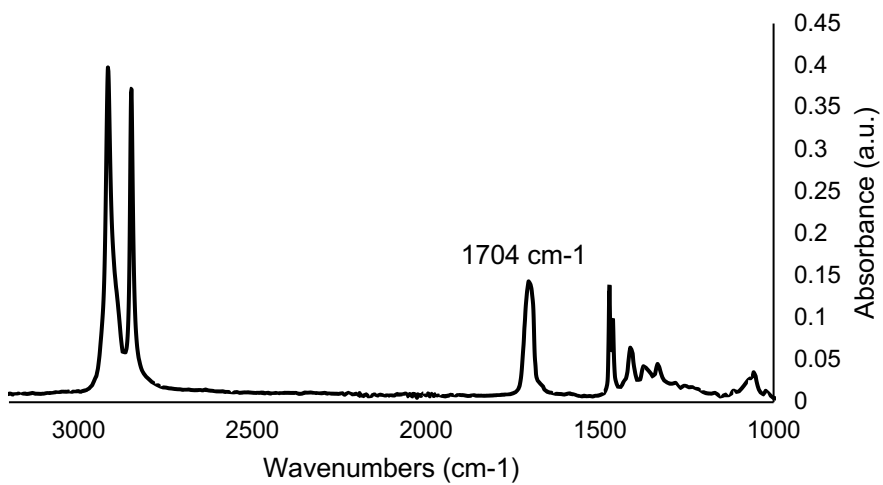


Figure S3.25 ATR-IR spectrum of sample M from Table S3.4.

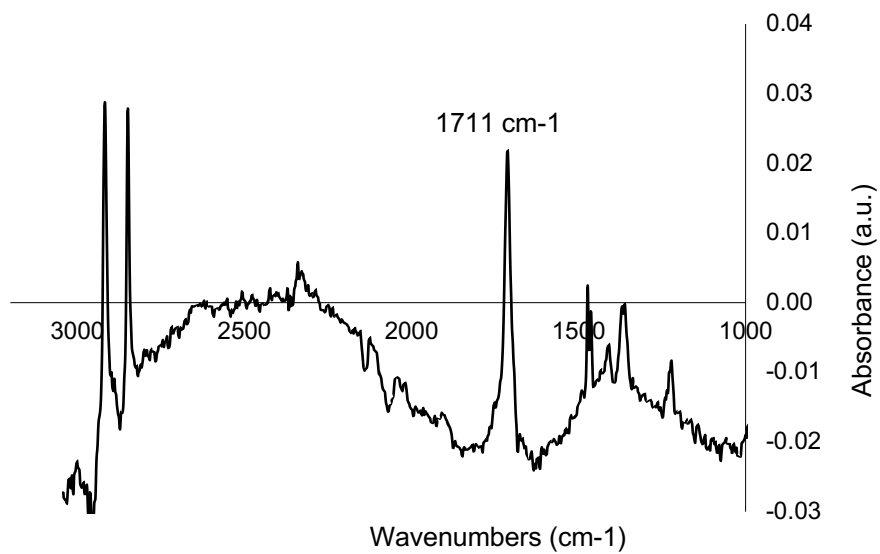


Figure S3.26 ATR-IR spectrum of sample O from Table S3.4.

Integrated Catalysis Methods

Integrated catalysis combining electrochemical CO₂ reduction and CO/C₂H₄ copolymerization.

Electrolysis measurements were performed using a Gamry Instruments Interface 1000-E or Biologic VMP3 potentiostat. The integrated reaction utilized the high-pressure reactor fitted with electrochemical feedthroughs (Figure S3.1 above), with an additional glass vial to house the polymerization catalyst solution (Figure S3.1B). The electrolyte solution was composed of ca. 200 mL 0.25 M TBAPF₆ in DMF, from which gaseous electrolysis products may diffuse out of and into the polymerization vial. Both the high-pressure reactor and polymerization vial were positioned carefully to allow stirring, while preventing the larger stir bar in the electrolyte from hitting the polymerization vial. In a typical experiment, a two-electrode cell was used. The working and counter/reference electrodes were both Pd foil with an average surface area of ~130 cm². The constant current electrolysis was conducted for 24 h under a constant I_{appl} of 90 mA resulting in a current density of 0.7 mA·cm⁻². For current densities of 0.5, 0.3, 0.2, and 0.1 mA·cm⁻² the applied current was 65, 39, 26, and 13 mA, respectively. The polymerization vessel contained 5 mM of the Pd complex dissolved in either DMF or 1,2-DCE. CO₂ gas (Airgas, 99.999 %) and C₂H₄ gas (Airgas, 99.9 %) were charged into the high-pressure reactor such that the total pressure was 14 bar and $P_{\text{CO}_2}/P_{\text{C}_2\text{H}_4} = 1$. Control experiments were conducted with N₂ in place of CO₂ at the same total pressure, but $P_{\text{N}_2} = 5$ bar and $P_{\text{C}_2\text{H}_4} = 9$ bar. The gas headspace of the reactor was sampled via online detection with a gas chromatograph before and after electrolysis. After the reaction, the Pd foil electrodes were sequentially rinsed and sonicated in acetone, DI water, and dilute nitric acid. Upon completion of the integrated catalysis, the contents of the polymerization compartment were transferred to a 50 mL centrifuge tube, and 15 mL of methanol and 3 mL of concentrated hydrochloric acid (HCl) were added. This mixture was sonicated overnight to facilitate the

dissolution of Pd and then the mixture was centrifuged at 7500 rpm for 15 min using a Thermo Scientific Sorvall ST 8 Centrifuge. Once the solid was concentrated to the bottom of the tube, the supernatant was discarded. The process of solid suspension and centrifugation was repeated 3 more times. The resulting off-white precipitate was collected and dried under vacuum overnight.

Synthesis of ^{13}C labeled polyketone using $^{13}\text{CO}_2$. A high-pressure reactor fitted with electrochemical feedthroughs was purged with nitrogen at least five times to remove air from the setup, leaving 1 bar N_2 was left in the reactor. The reactor was charged with 7 bar ^{13}C -labeled CO_2 . The reactor was continuously stirred during this time until no pressure dropped after stopping $^{13}\text{CO}_2$ input. After $^{13}\text{CO}_2$ saturation, the reactor was charged with 7 bar C_2H_4 , and the total pressure in the reactor reached 15 bar. Galvanostatic electrolysis (to 210 C) at $0.7 \text{ mA}\cdot\text{cm}^{-2}$ and 25°C was applied to the reactor, after which time the reactor was kept stirring for 24 h without any current passed. The reaction was worked up as described for other integrated catalysis experiments and analyzed by ^1H and $^{13}\text{C}\{^1\text{H}\}$ NMR spectroscopy.

Table S3.5 Polyketone samples made from $\text{CO}_2/\text{C}_2\text{H}_4$ (using integrated catalysis).

Sample	Current density (mA/cm ²)	P _{co} (bar)	FE _{co} (%)	FE _{H₂} (%)	Polymer catalyst (solvent)	Polymer yield (mg)	IR CO stretch (cm ⁻¹)	%CO NMR	M _n (Đ) (g/mol)
PO-1	0.7	0.466	38.7	16.2	Pd-PO (1,2-DCE)	39.1	1692	36.2	1260 (1.71)
PO-2	0.7	0.517	42.9	29.2	Pd-PO (1,2-DCE)	61.5	1692	45.3	1650 (2.08)
PO-3	0.7	0.315	26.2	24.3	Pd-PO (DMF)	29.2	1691	>49 ^a	1550 (1.41)
PO-4	0.5	0.254	29.5	25.0	Pd-PO (1,2-DCE)	35.5	1692	42.1	740 (2.49)
PO-5	0.3	0.133	24.9	22.5	Pd-PO (1,2-DCE)	29.0	1695	22.1	-
PO-6	0.3	0.133	17.1	48.5	Pd-PO (1,2-DCE)	22.5	1692	31.8	-

PO-7	0.3	0.08	14.1	27.5	Pd-PO (1,2-DCE)	130	1695	15.0	-
PO-8	0.2	0.058	14.6	37.4	Pd-PO (1,2-DCE)	19.0	1707	20.3	-
PO-9	0.15	0.032	12.4	37.2	Pd-PO (1,2-DCE)	84.0	1697	18.5	5030 (1.78)
PO-10	0.1	0.002	0.9	24.7	Pd-PO (1,2-DCE)	47.1	1709	5.8	-
PO-11	0.1	0.006	3.4	58.7	Pd-PO (1,2-DCE)	26.3	-	4.3	1250 (1.3 0)
PO-12	0.1	0.008	6.2	21.2	Pd-PO (1,2-DCE)	34.0	1713	3.1	-
PO-13	0	0	-	-	Pd-PO (1,2-DCE)	39.0	none	0	4630 (1.18)
PP-1	0.7	0.370	30.7	38.5	Pd-PP (DMF)	278.9	1692	>49 ^a	18120 (1.60) 4880 (1.07) 2060 (1.07)
PP-2	0.7	0.234	19.5	14.7	Pd-PP (1,2-DCE)	110	1692	>49 ^a	6170 (1.66)
PP-3	0.2	0.031	8.0	36.6	Pd-PP (DMF)	15.3	1691	>49 ^a	-
PP-4	0.2	0.063	18.2	21.5	Pd-PP (1,2-DCE)	2.1	1692	>49 ^a	-
PP-5	0.1	0.0021	1.24	51.6	Pd-PP (DMF)	0	-	-	-
PP-6	0.1	0.0047	2.7	66.4	Pd-PP (DMF)	0	-	-	-
PP-7 ^b	0.7	0.224	32.7	13.2	Pd-PP (DMF)	1.5	-	>49 ^a	-

^a The %CO incorporation calculated from the ¹H NMR spectrum at 25°C in HFIP. ^b ¹³CO₂ used in electrolysis to make ¹³CO

Table S3.6 Integrated catalysis control experiments.

Entry	Gas mixture	Current density (mA/cm ²)	Polymerization catalyst (solvent in compartment)	P_{Total} (bar)	P_{CO} (bar)	FE _{CO} (%)	Polymer yield (mg)
1	CO ₂ + C ₂ H ₄	0.7	None (DMF)	14	0.422	35.0	0
2	CO ₂ + C ₂ H ₄	0	Pd-PP (DMF)	14	0.0	0.0	0
3	N ₂ + C ₂ H ₄	0.7	Pd-PP (DMF)	14	0.0002	0.01	0
4	CO ₂ + C ₂ H ₄	0.7	None (1,2-DCE)	14	0.471	39.2	0
5	CO ₂ + C ₂ H ₄	0	Pd-PO (1,2-DCE)	14	0.0	0.0	39.0 (polyethylene)
6	N ₂ + C ₂ H ₄	0.7	Pd-PO (1,2-DCE)	14	0.0001	0.01	25.5 (polyethylene)
7 ^a	CO ₂ + C ₂ H ₄	0.7	Pd-PO (n/a)	25	0.083	2.2	2.1

^a**Pd-PO** was dissolved directly in the electrolyte solution, in contact with Pd electrodes.

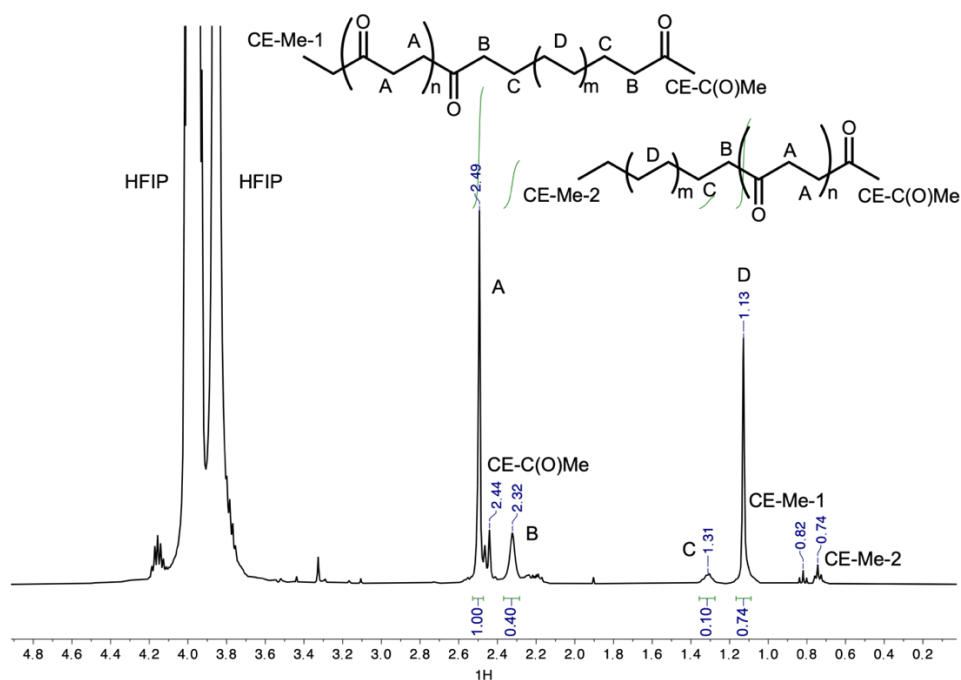


Figure S3.27 ^1H NMR spectrum of polyketone sample PO-1 from Table S3.5 in 4:1 HFIP: C_6D_6 at 25 $^\circ\text{C}$.

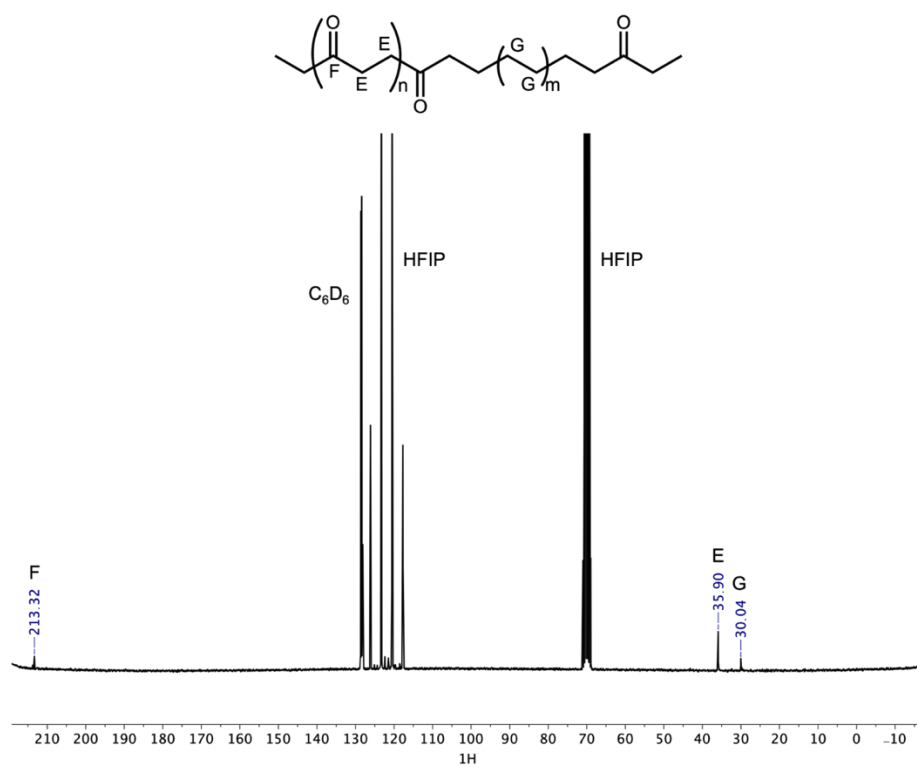


Figure S3.28 $^{13}\text{C}\{^1\text{H}\}$ NMR spectrum of sample PO-1 from Table S3.5 in 4:1 HFIP: C_6D_6 at 25 $^\circ\text{C}$.

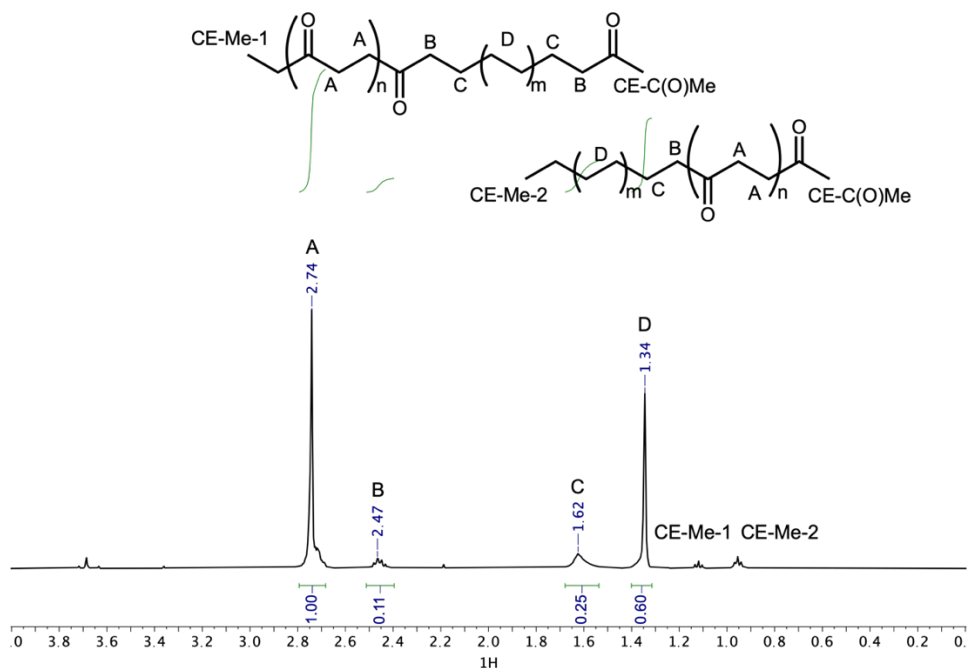


Figure S3.29 ^1H NMR spectrum of polyketone sample PO-1 from Table S3.5 in TCE-d_2 at 100 $^\circ\text{C}$.

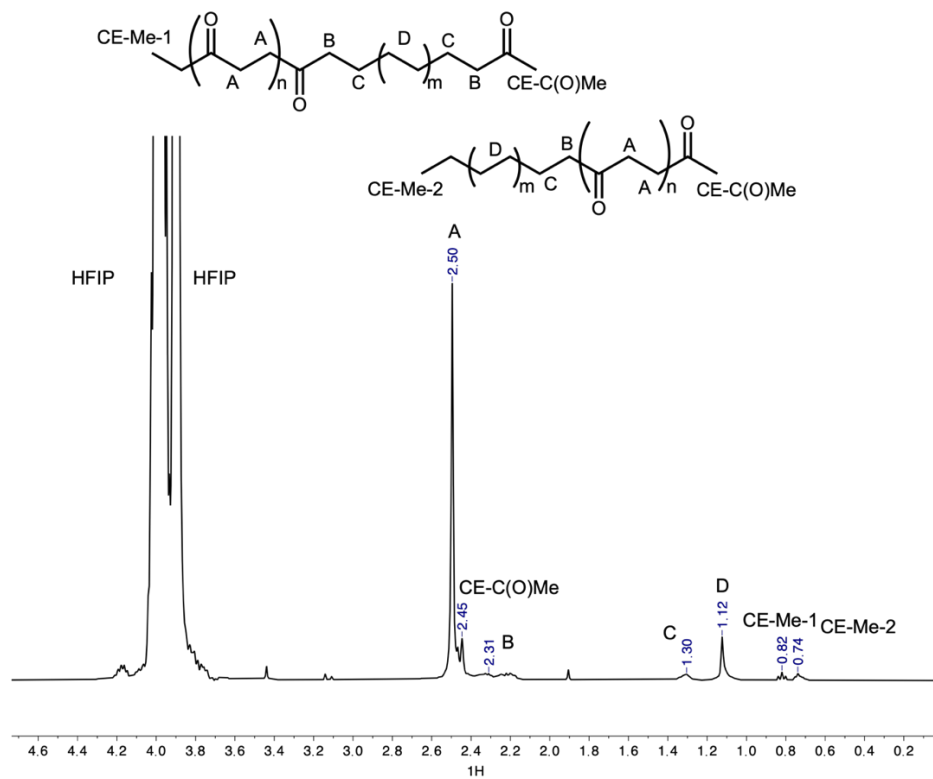


Figure S3.30 ^1H NMR spectrum of polyketone sample PO-2 from Table S3.5 in 4:1 HFIP: C_6D_6 at 25 $^\circ\text{C}$.

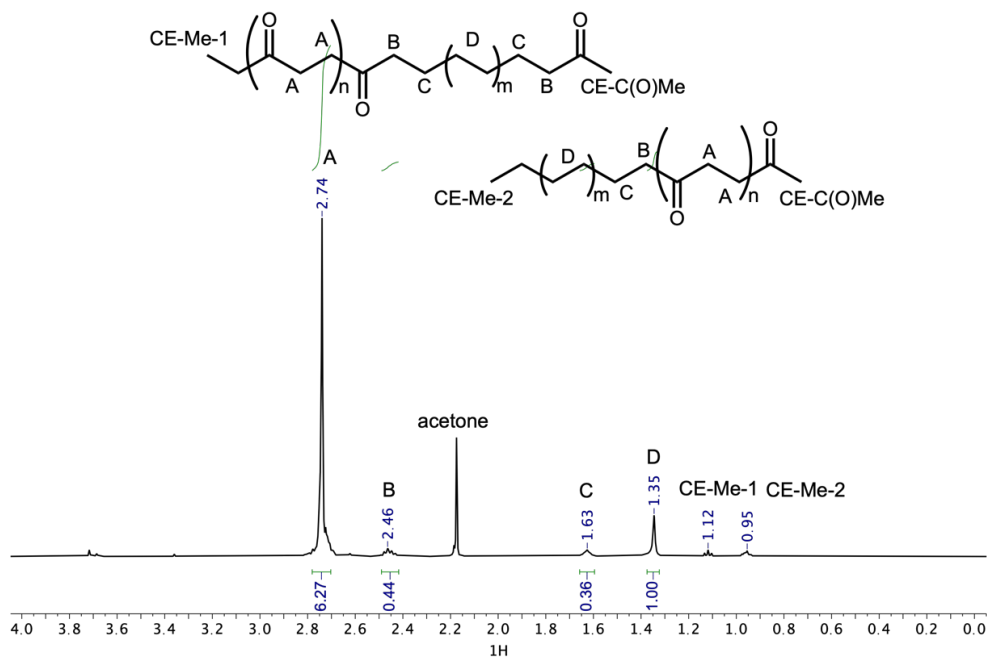


Figure S3.31 ^1H NMR spectrum of polyketone sample PO-2 from Table S3.5 in TCE-d_2 at 100 $^\circ\text{C}$.

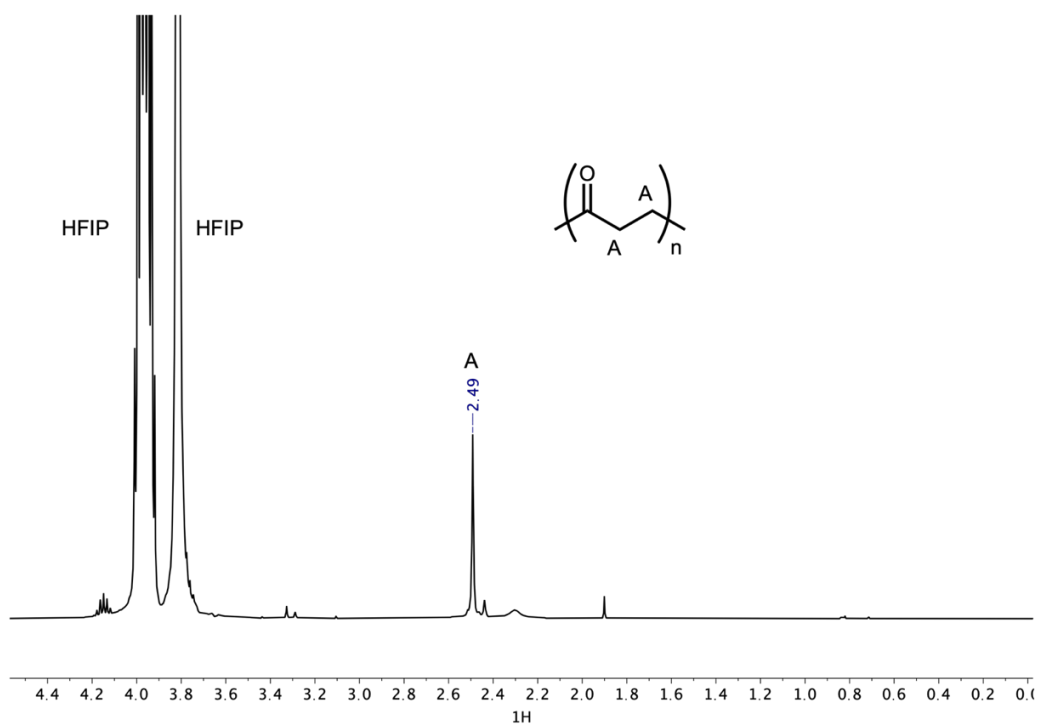


Figure S3.32 ^1H NMR spectrum of polyketone sample PO-3 from Table S3.5 in 4:1 $\text{HFIP}:\text{C}_6\text{D}_6$ at 25 $^\circ\text{C}$.

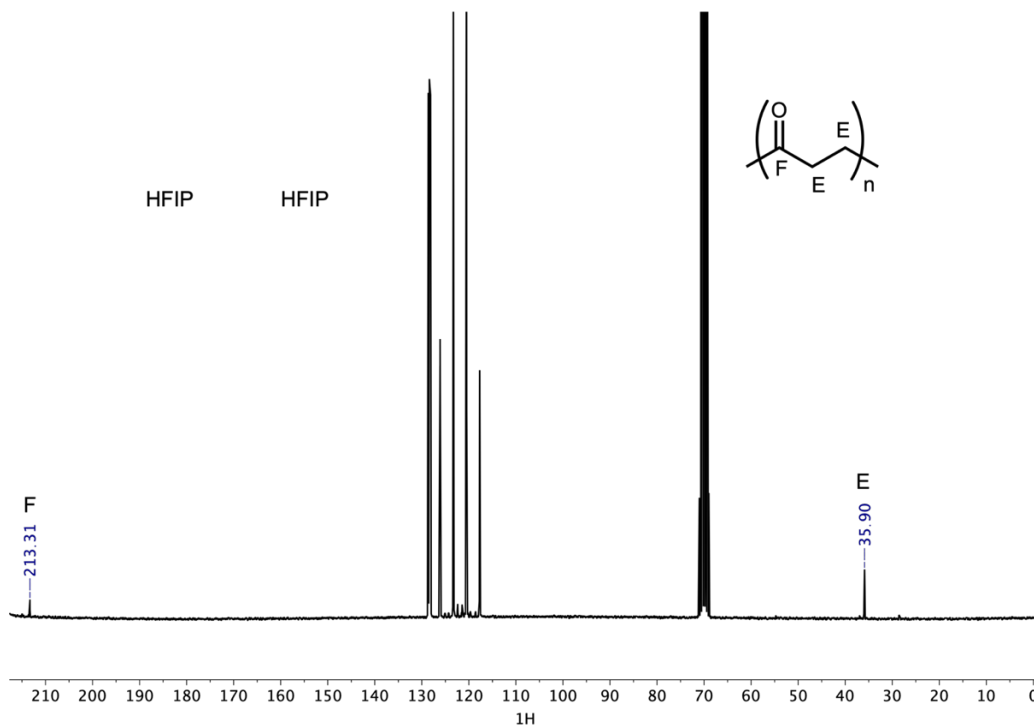


Figure S3.33 $^{13}\text{C}\{^1\text{H}\}$ NMR spectrum of sample PO-3 from Table S3.5 in 4:1 HFIP: C_6D_6 at 25 $^\circ\text{C}$.

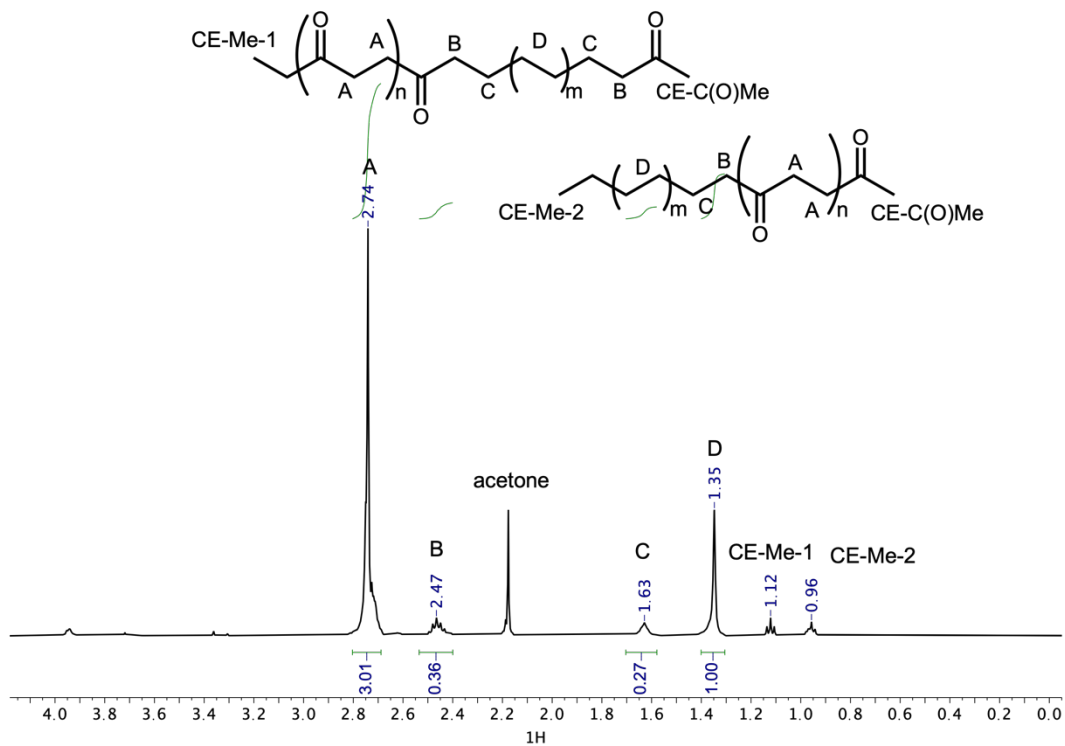


Figure S3.34. ^1H NMR spectrum of polyketone sample PO-4 from Table S3.5 in TCE- d_2 at 100 $^\circ\text{C}$.

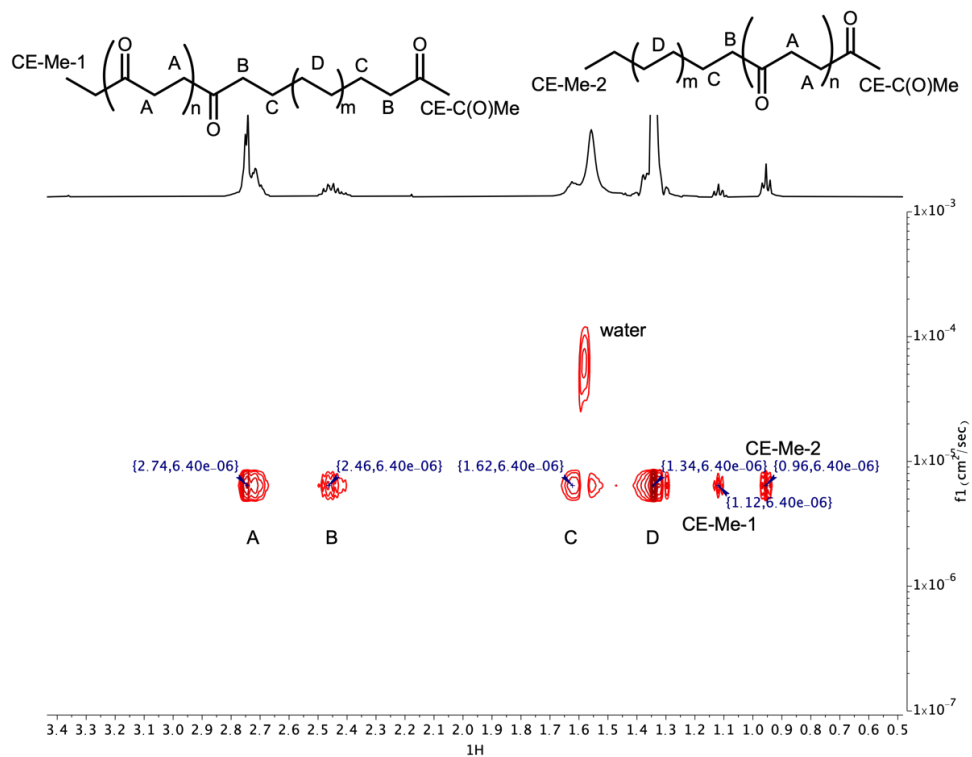


Figure S3.37 2D DOSY NMR spectrum of polyketone sample PO-7 from Table S3.5 in TCE-d₂ at 100 °C.

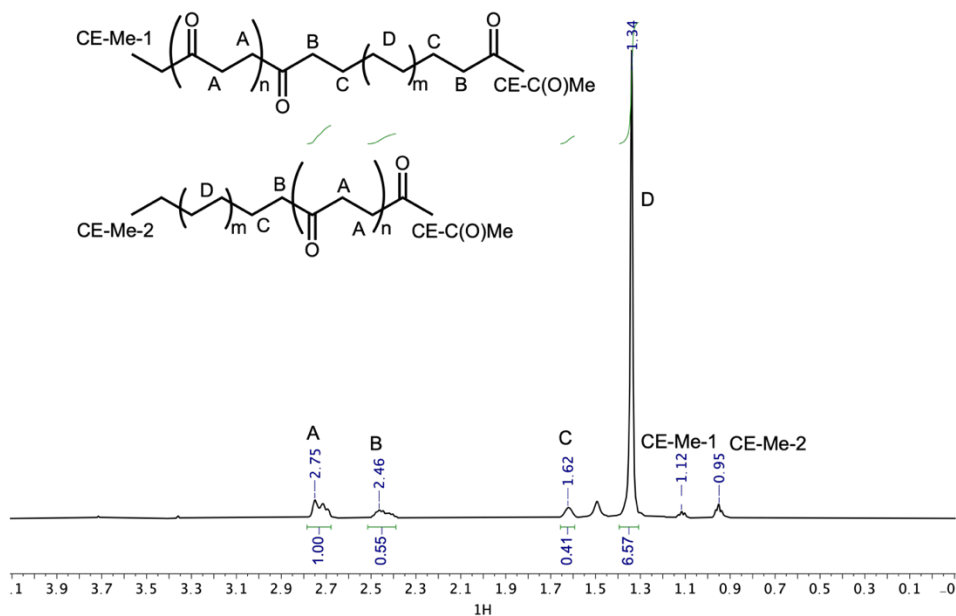


Figure S3.38. ¹H NMR spectrum of polyketone sample PO-9 from Table S3.5 in TCE-d₂ at 100 °C.

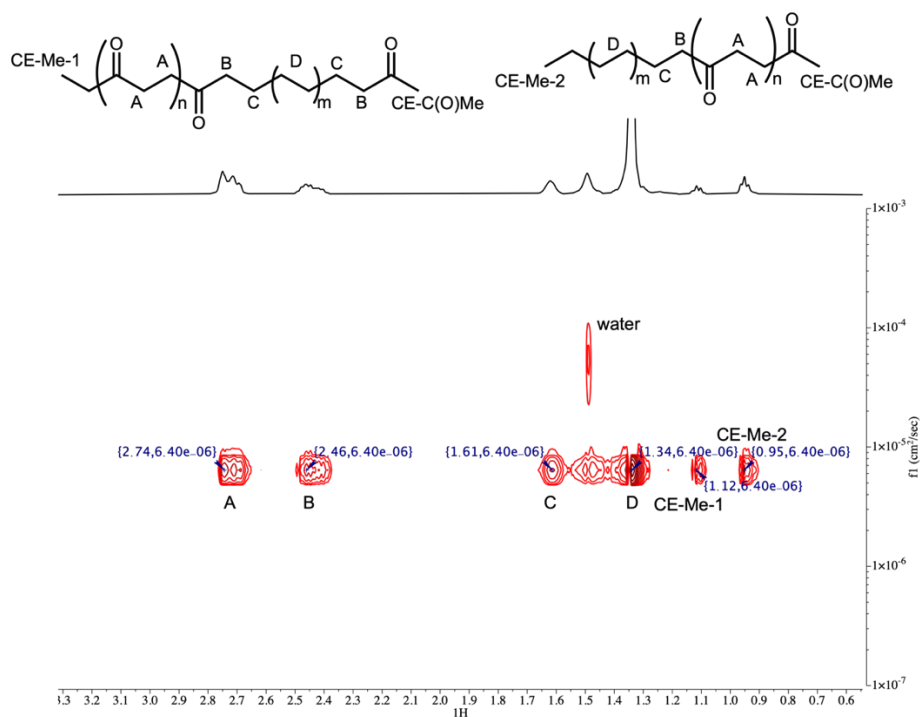


Figure S3.39 2D DOSY NMR spectrum of polyketone sample PO-9 from Table S3.5 in TCE-d₂ at 100 °C.

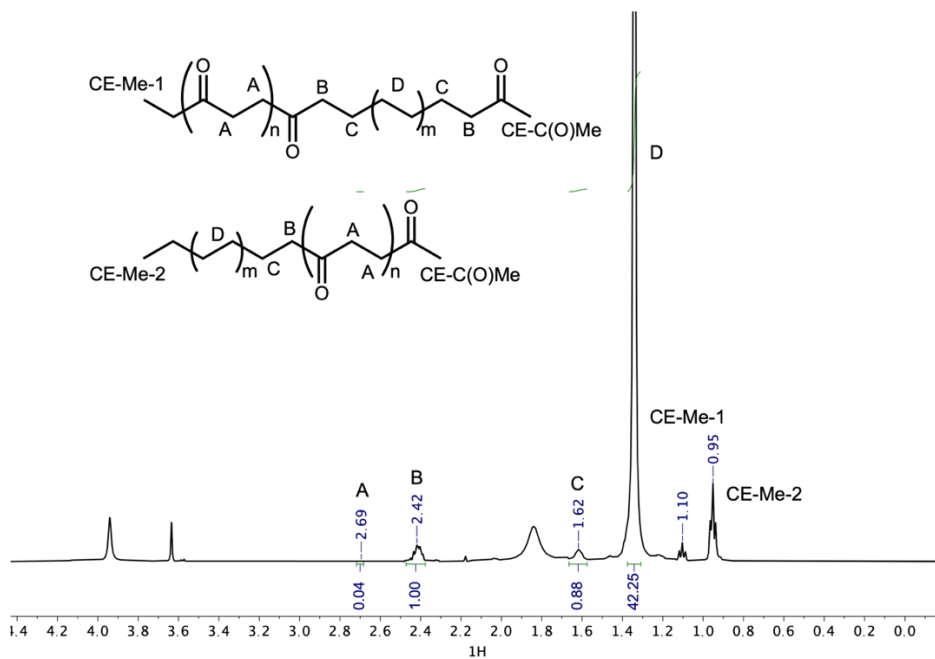


Figure S3.40. ¹H NMR spectrum of polyketone sample PO-12 from Table S3.5 in TCE-d₂ at 100 °C.

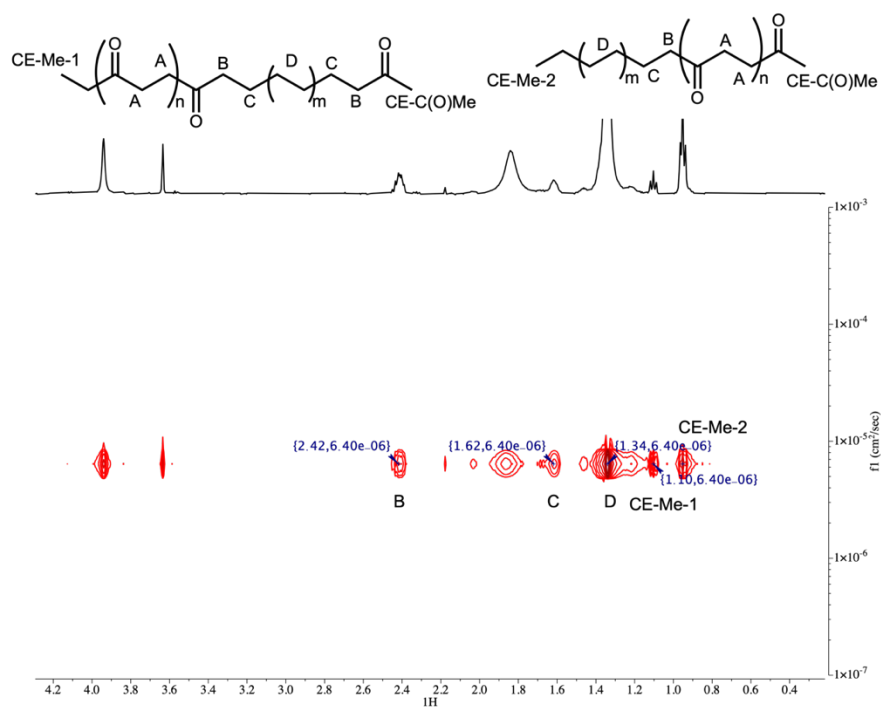


Figure S3.41 2D DOSY NMR spectrum of polyketone sample PO-12 from Table S3.5 in TCE-d₂ at 100 °C.

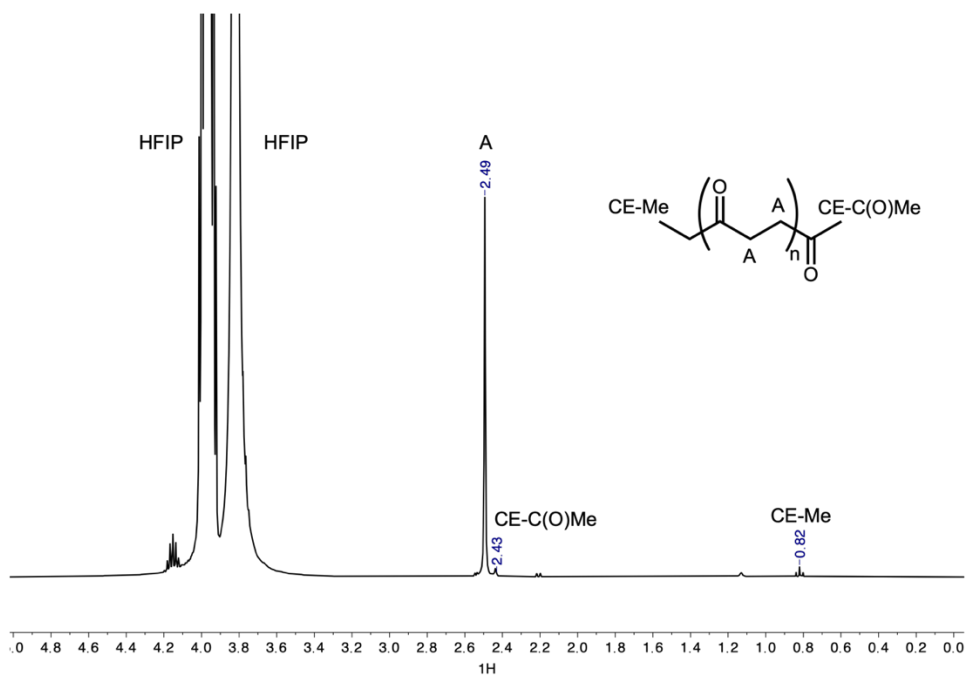


Figure S3.42 ¹H NMR spectrum of polyketone sample PP-2 from Table S3.5 in 4:1 HFIP:C₆D₆ at 25 °C.

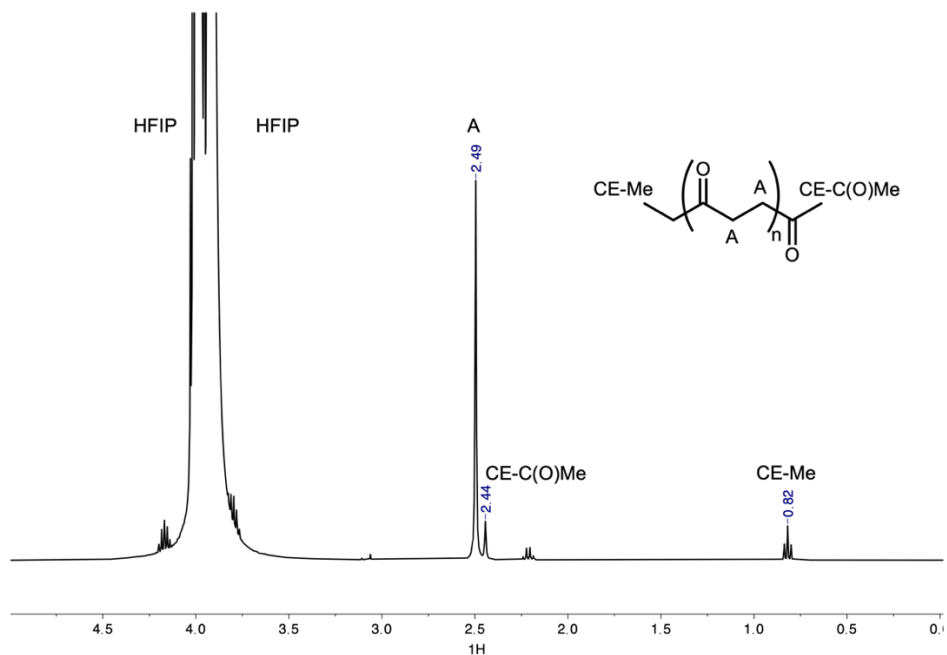


Figure S3.43 ^1H NMR spectrum of polyketone sample PP-3 from Table S3.5 in in 4:1 HFIP: C_6D_6 at 25 $^\circ\text{C}$.

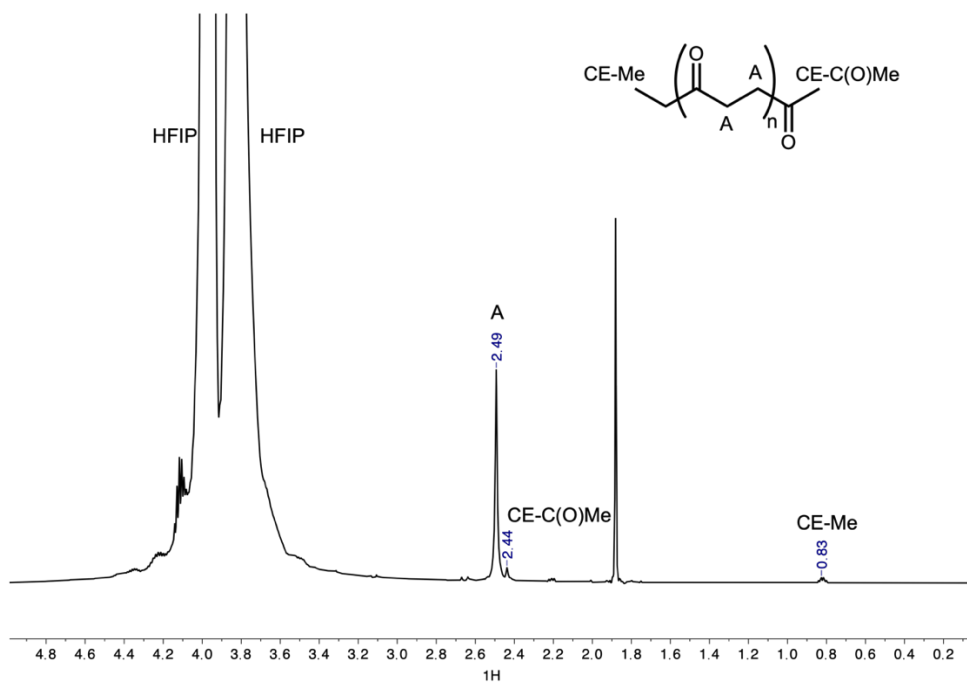


Figure S3.44 ^1H NMR spectrum of polyketone sample PP-7 from Table S3.5 in in 4:1 HFIP: C_6D_6 at 25 $^\circ\text{C}$ (from $^{13}\text{CO}_2$).

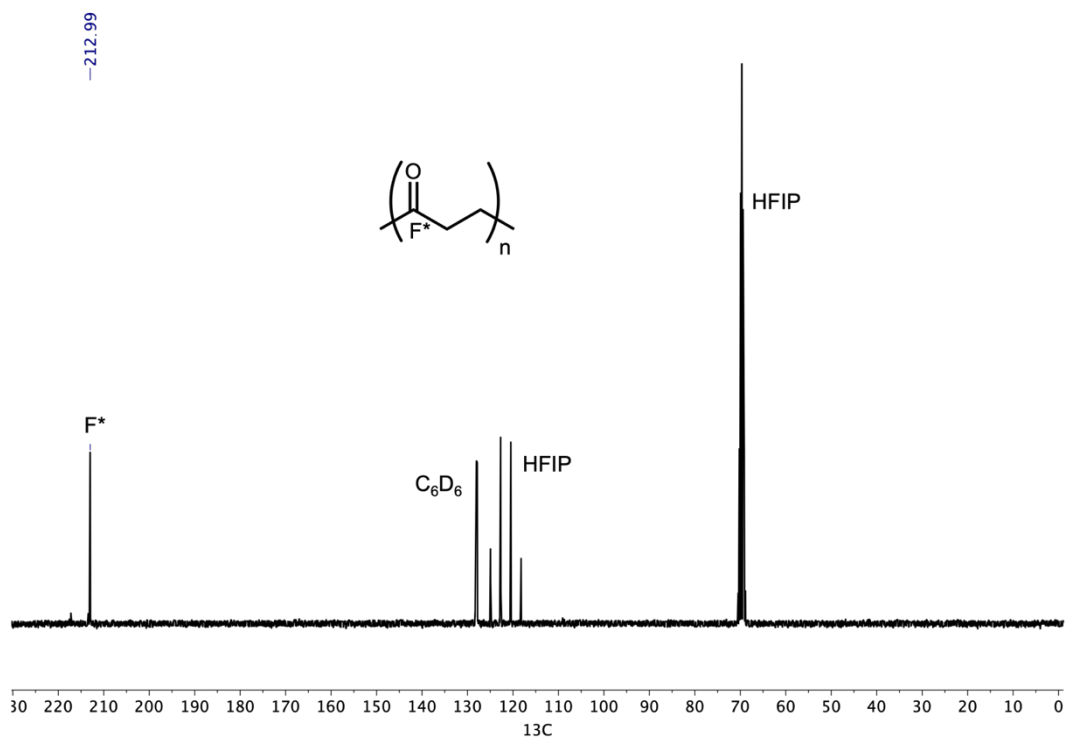


Figure S3.45 $^{13}\text{C}\{^1\text{H}\}$ NMR spectrum of polyketone PP-7 from Table S3.5 in 4:1 HFIP: C_6D_6 at 25°C (from $^{13}\text{CO}_2$).

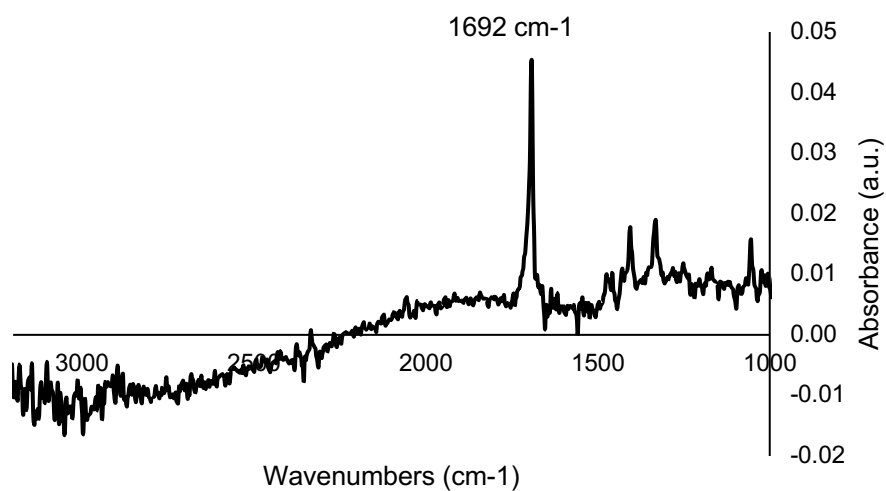


Figure S3.46 ATR-IR spectrum of sample PO-1 from Table S3.5.

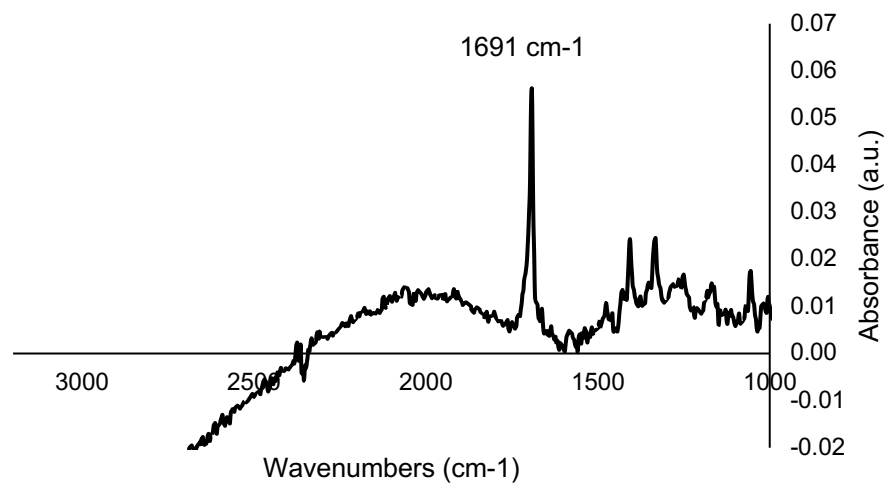


Figure S3.47 ATR-IR spectrum of sample PO-3 from Table S3.5.

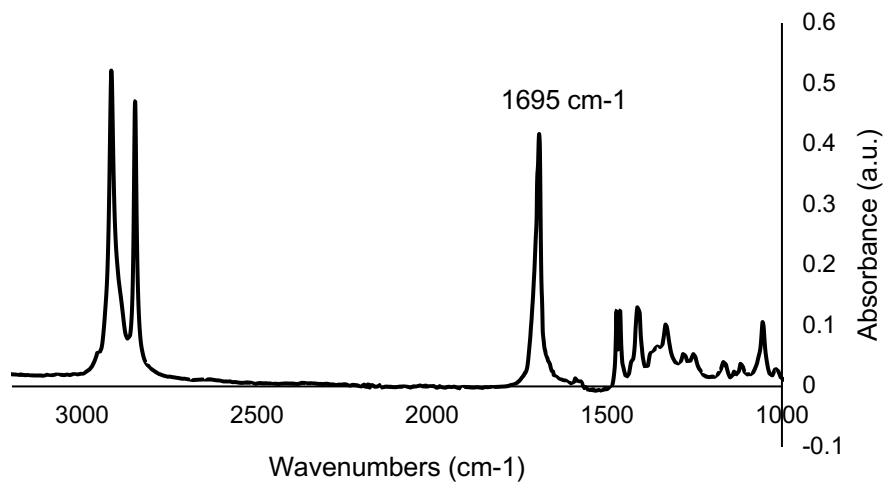


Figure S3.48 ATR-IR spectrum of sample PO-7 from Table S3.5.

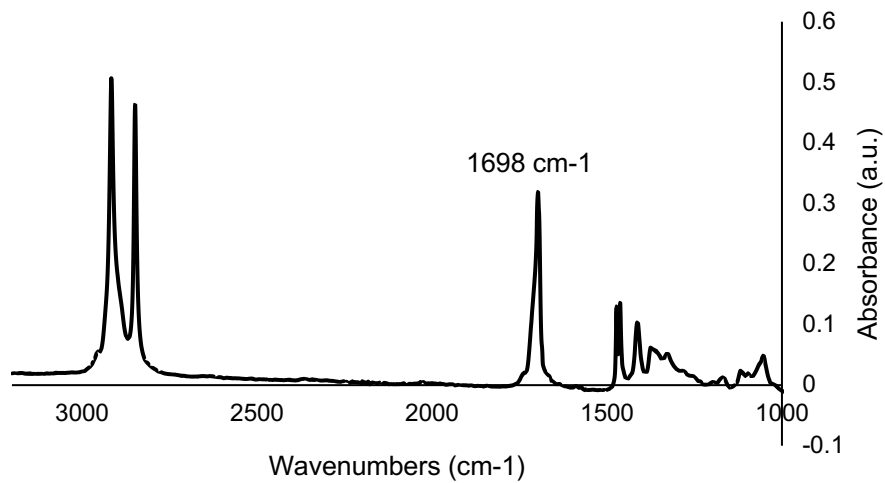


Figure S3.49 ATR-IR spectrum of sample PO-9 from Table S3.5.

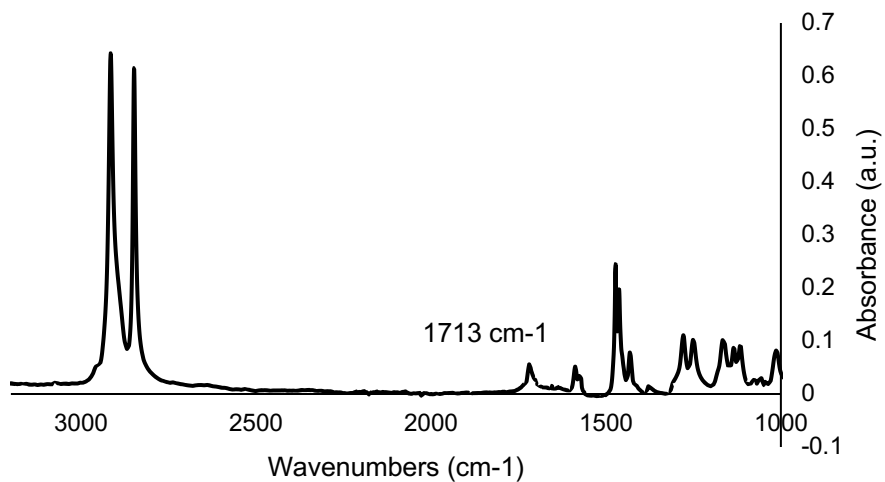


Figure S3.50 ATR-IR spectrum of sample PO-12 from Table S3.5.

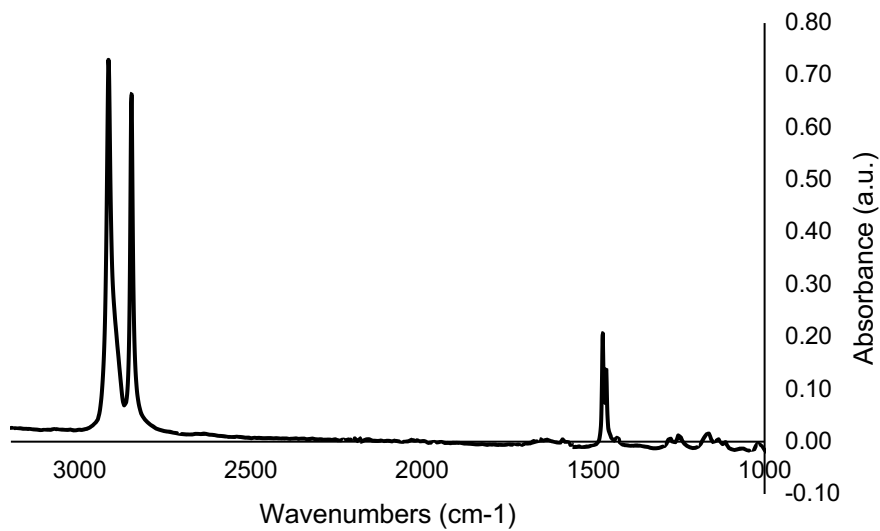


Figure S3.51 ATR-IR spectrum of sample PO-13 from Table S3.5.

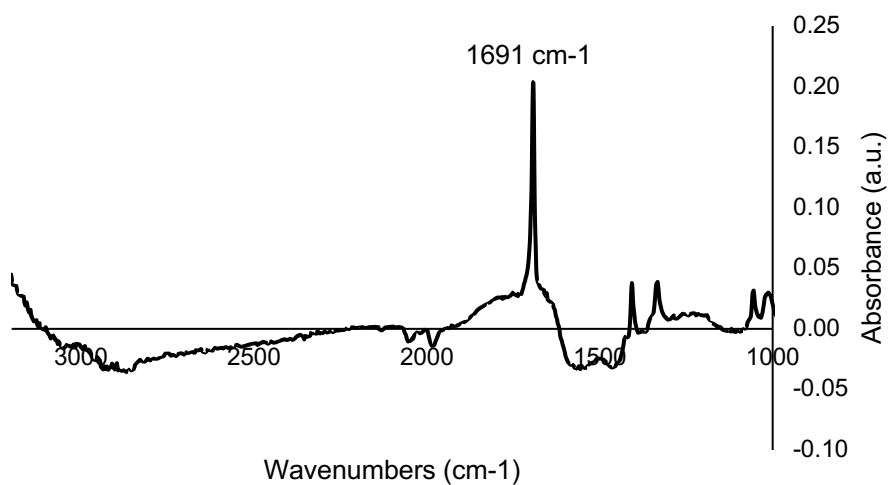


Figure S3.52 ATR-IR spectrum of sample PP-1 from Table S3.5.

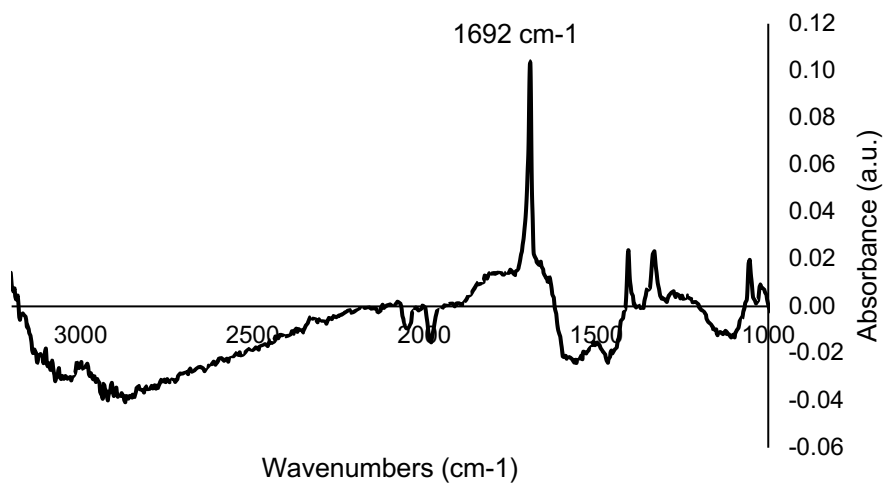


Figure S3.53 ATR-IR spectrum of sample PP-2 from Table S3.5.

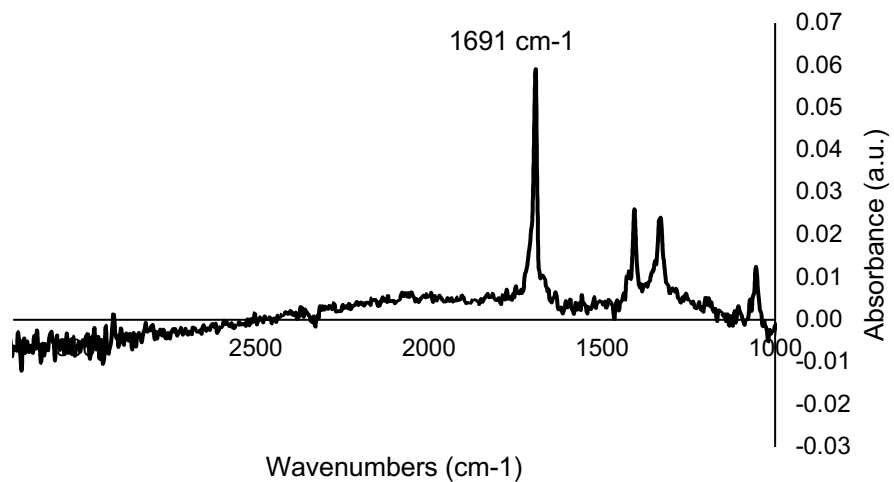


Figure S3.54 ATR-IR spectrum of sample PP-3 from Table S3.5.

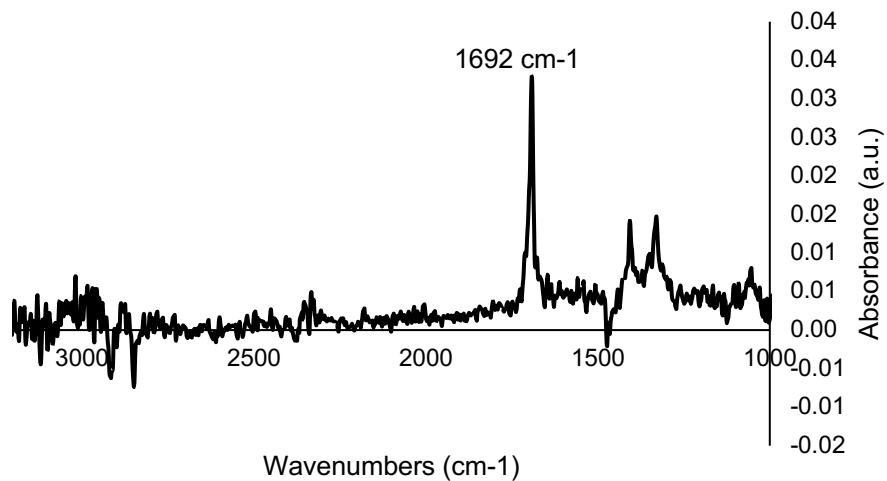


Figure S3.55 ATR-IR spectrum of sample PP-4 from Table S3.5.

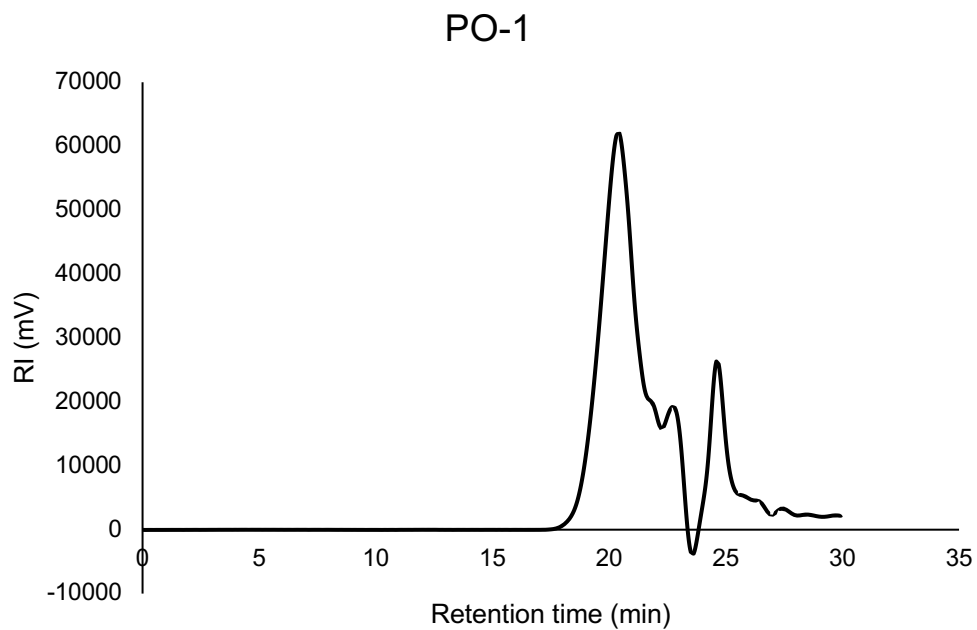


Figure S3.56 SEC trace for sample PO-1 from Table S3.5.

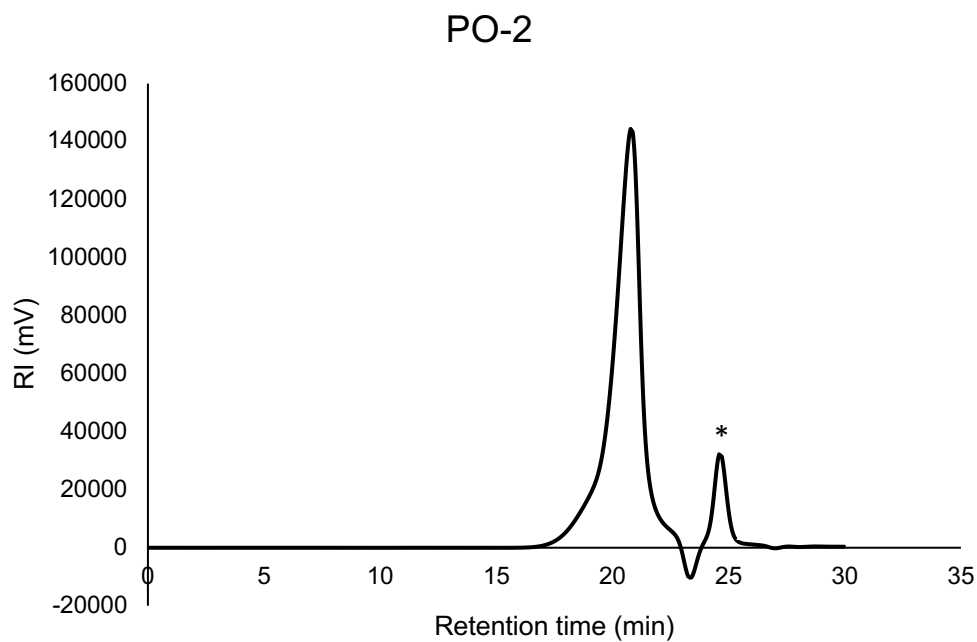


Figure S3.57. SEC trace for sample PO-2 from Table S3.5.

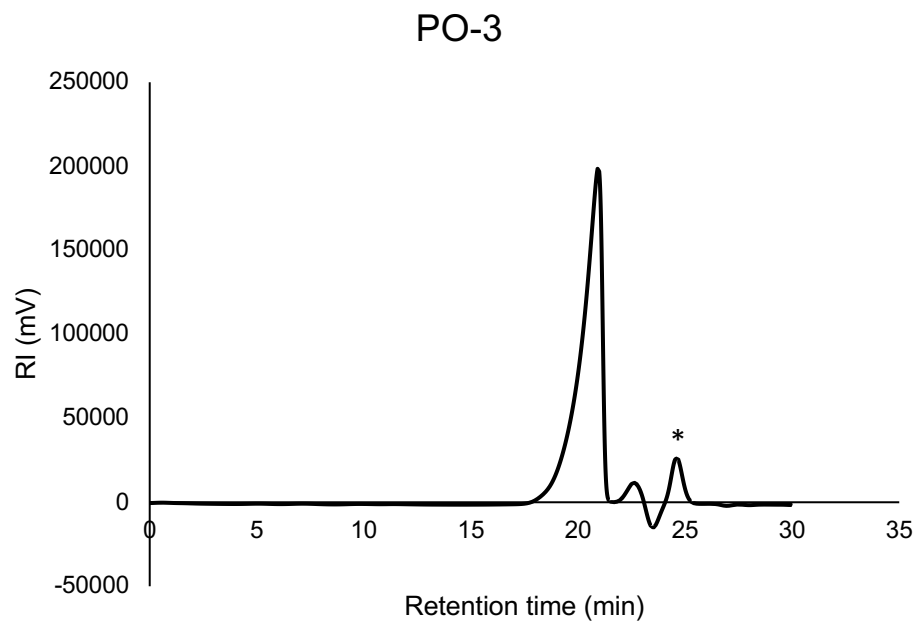


Figure S3.58 SEC trace for sample PO-3 from Table S3.5.

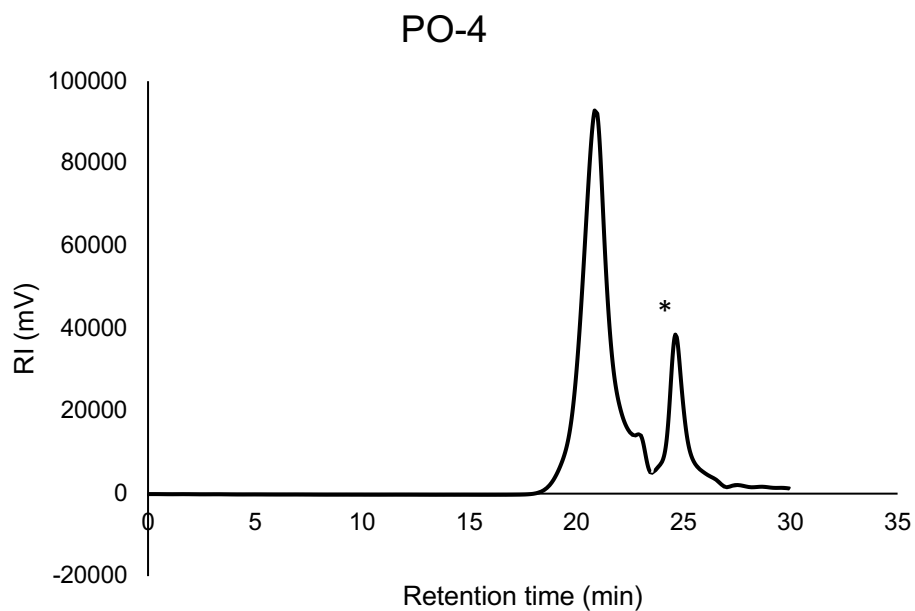


Figure S3.59 SEC trace for sample PO-4 from Table S3.5.

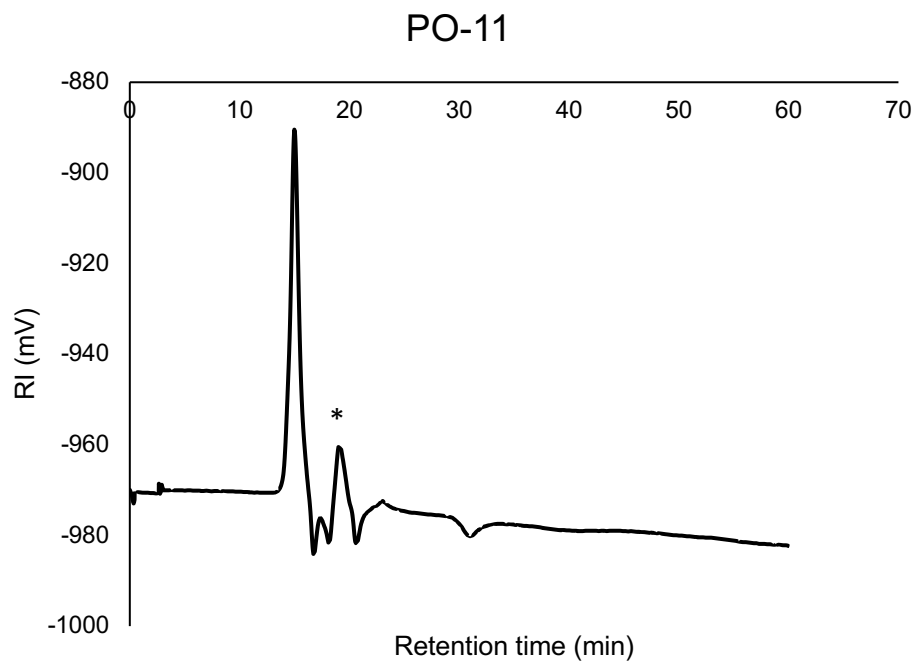


Figure S3.60 SEC trace for sample PO-11 from Table S3.5.

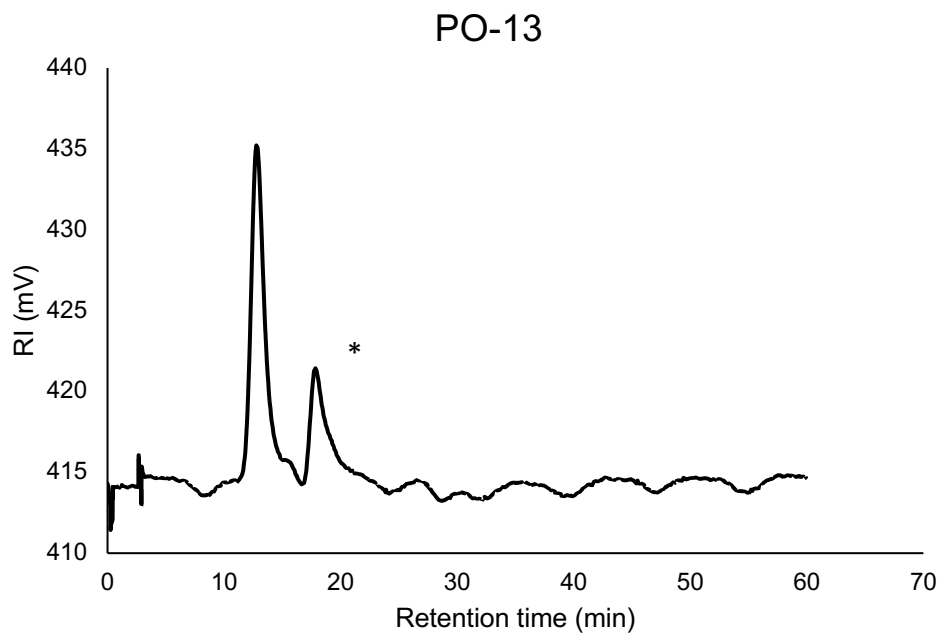


Figure S3.61 SEC trace for sample PO-13 from Table S3.5.

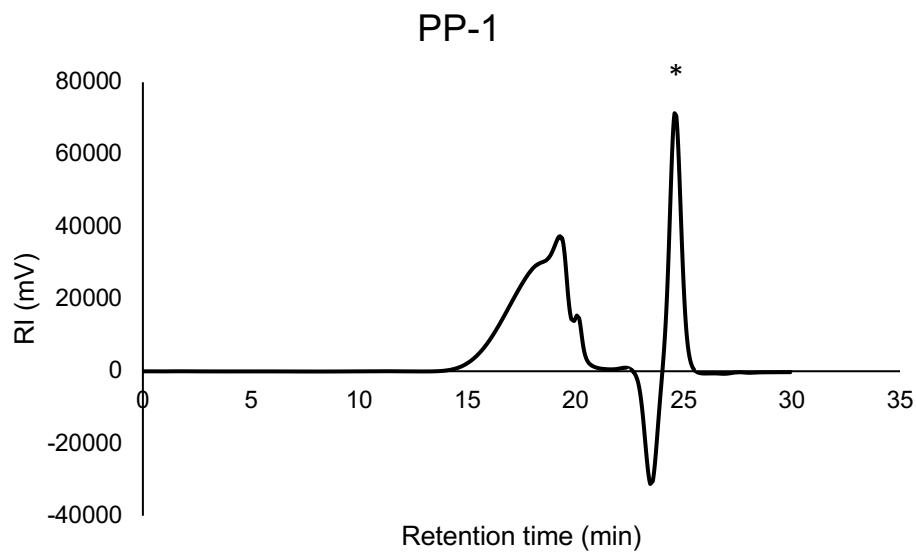


Figure S3.62 SEC trace for sample PP-1 from Table S3.5.

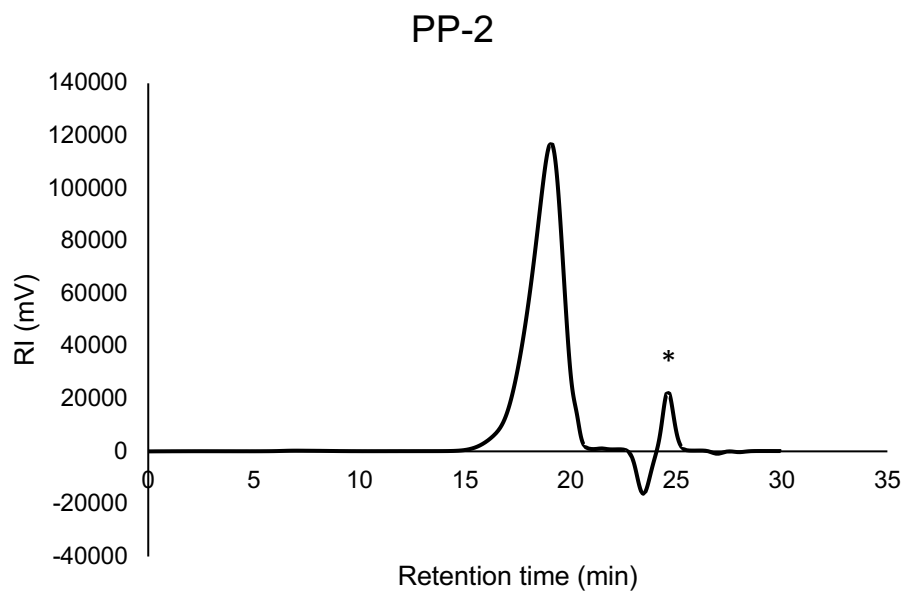


Figure S3.63 SEC trace for sample PP-2 from Table S3.5.

Supplementary references

1. Vela, J.; Lief, G. R.; Shen, Z.; Jordan, R. F., Ethylene polymerization by palladium alkyl complexes containing bis (aryl) phosphino-toluenesulfonate ligands. *Organometallics* **2007**, 26, 6624-6635.
2. Dekker, G. P.; Elsevier, C. J.; Vrieze, K.; Van Leeuwen, P. W., Influence of ligands and anions on the rate of carbon monoxide insertion into palladium-methyl bonds in the complexes (PP)Pd(CH₃)Cl and [(PP)Pd(CH₃)(L)]⁺SO₃CF₃⁻ (PP = dppe, dppp, dppb, dppf; L= CH₃CN, PPh₃). *Organometallics* **1992**, 11, 1598-1603.
3. Kacker, S.; Sen, A., Palladium (II)-Catalyzed Alternating Copolymerization of Allene with Carbon Monoxide and the Synthesis of Terpolymer with Alt-Allene-Carbon Monoxide and Alt-Ethene-Carbon Monoxide Blocks. Synthetic and Mechanistic Aspects. *J. Am. Chem. Soc.* **1997**, 119, 10028-10033.
4. Fujita, T.; Nakano, K.; Yamashita, M.; Nozaki, K., Alternating Copolymerization of Fluoroalkenes with Carbon Monoxide. *J. Am. Chem. Soc.* **2006**, 128, 1968-1975.
5. Elgrishi, N.; Chambers, M. B.; Fontecave, M., Turning it off! Disfavouring hydrogen evolution to enhance selectivity for CO production during homogeneous CO₂ reduction by cobalt-terpyridine complexes. *Chem. Sci.* **2015**, 6, 2522-2531.
6. Gonell, S.; Miller, A. J., Carbon Dioxide Electroreduction Catalyzed by Organometallic Complexes. *Adv. Organomet, Chem.* **2018**, 70, 1-69.
7. Williams, D. B. G.; Lawton, M., Drying of Organic Solvents: Quantitative Evaluation of the Efficiency of Several Desiccants. *J. Org. Chem.* **2010**, 75, 8351-8354.

8. Luo, R.; Newsham, D. K.; Sen, A., Palladium-Catalyzed Nonalternating Copolymerization of Ethene and Carbon Monoxide: Scope and Mechanism. *Organometallics* **2009**, *28*, 6994-7000.
9. Soomro, S. S.; Cozzula, D.; Leitner, W.; Vogt, H.; Müller, T. E., The microstructure and melt properties of CO–ethylene copolymers with remarkably low CO content. *Polym. Chem.* **2014**, *5*, 3831-3837.

Chapter 4. Integrated electrochemical CO₂ reduction and hydroformylation

This chapter is a version of Jolly, B. J.; Pung, M. J.; and Liu, C., "Integrated electrochemical CO₂ reduction and hydroformylation." *Dalton Trans.* **2024**. DOI: 10.1039/d4dt00423j.

Abstract

The development of integrated multi-catalyst processes has become of high interest to transform abundant feedstocks or environmental pollutants to commodity chemicals in a one pot, one pass fashion. Specifically, CO₂ poses a large environmental burden and would thus be a desirable, relatively abundant C1 source in multi-step synthetic chemistry. Herein we disclose the synthesis of aldehydes from CO₂ via the integration of electrochemical CO₂ reduction (CO₂RR) and hydroformylation, taking advantage of the typically unwanted concomitant hydrogen evolution (HER) to generate the necessary CO and H₂ needed for hydroformylation. Though typical hydroformylation catalysts based on Rh would be deactivated under CO₂RR conditions, we circumvent this limitation by spatially segregating our CO₂RR and hydroformylation systems in a vial-in-vial reactor, while allowing CO and H₂ transport between catalyst sites. In this manner, 97% aldehyde yield from CO₂RR and styrene was achieved selectively using a classic homogeneous hydroformylation catalyst in HRh(CO)(PPh₃)₃, and 43% aldehyde yield was obtained using a heterogenized version of this Rh catalyst onto mesoporous silica. This work not only repurposes undesired HER in CO₂RR and prepares aldehydes from CO₂ without added H₂, but expands the scope of processes that transform feedstocks all the way to commodity chemicals in a one pass manner.

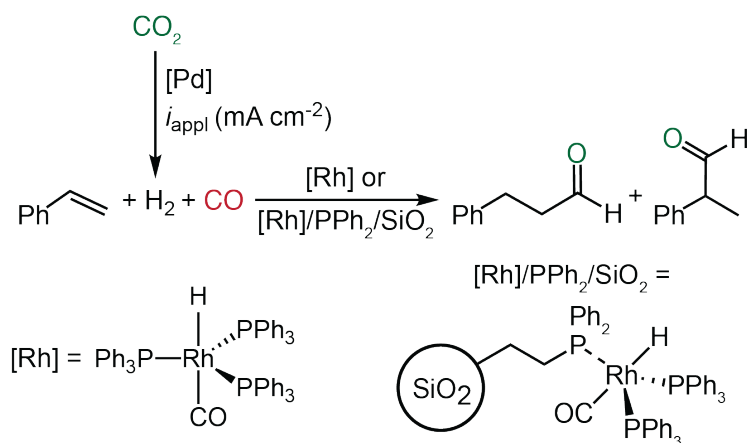
Introduction

The development of cascade, tandem, or integrated catalytic processes wherein multiple catalysts carry out simultaneous or sequential transformations without any intermediary work up have attracted significant attention in recent years.¹⁻¹⁰ Such processes present the opportunity to transform abundant feedstocks and/or prevalent environmental pollutants to commodity chemicals, while obviating time and resource wasteful purifications or various work up. To this end, numerous multi-catalyst systems operating in concert have emerged in recent years. Seminal examples of such systems include tandem Co and Rh based alkyne hydration and asymmetric transfer hydrogenation,^{11, 12} and three step conversion of CO₂ to CH₃OH synthesis via two separate Ru catalysts and a Lewis acid site in a metal organic framework,^{13, 14} amongst others. Though this field is relatively in its infancy, it presents an exciting area of research that may positively influence chemical manufacturing at the industrial scale in the near future.

One common pitfall of multi-catalyst systems is often catalyst-catalyst, substrate-substrate, catalyst-substrate interference, or some combination thereof.¹ Such limitations may be circumvented by spatial control, wherein incompatible species of a multi-catalyst process may be co-localized, yet spatially segregated to avoid interference with one another. Catalyst may be co-localized either in the same reaction medium, or in separate compartments of an integrated setup in different mediums. While the former presents challenges in overcoming differences in optimal compatibility, it presents little concern for transport limitations as species are in the same medium. The latter avoids a requisite of compatible conditions but poses a potential hurdle in transport limitations between catalysts in different mediums. This may be avoided with judicious catalyst co-localization or additional means of transport such as flow chemistry. Nonetheless, catalyst integration via spatial control remains attractive for multi-catalyst processes.

Our lab, in collaboration, previously reported the integration of electrochemical CO₂ reduction (CO₂RR) to polyketone synthesis enabled by spatial separation of the CO₂RR and polyketone catalysts.¹⁵ This was achieved without interference between CO₂RR and polyketone formation sites by localizing the catalysts for each process in separate compartments within one reactor. Relying on the gaseous nature of the intermediate CO between the two processes, CO₂ incorporation into polyketones was observed for the first time enabled by spatial control, with control over polymer microstructure via applied current density. Encouraged by this work, we were motivated to apply our spatially controlled integrated catalysis platform to construct additional multi-catalyst processes via spatial control to utilize CO₂ in chemical synthesis, as well as study the role of spatial separation in such processes. Much progress has been made in the field of electrocatalytic CO₂ reduction spanning catalyst, electrode and reactor design, to interfacial CO₂ transport processes, amongst other topics.¹⁶⁻²⁶ However, a major challenge in CO₂RR is concomitant hydrogen evolution (HER), one which was prevalent in our prior work. Thus, a significant focal point in CO₂RR research has been the development of methods to prevent HER.

A. Targeted integrated reaction



B. Vial-in-vial reactor design

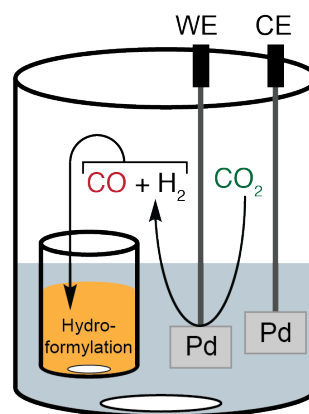


Figure 4.1 Integrated electrochemical CO₂ reduction (CO₂RR) and hydroformylation with a homogeneous and heterogeneous Rh catalyst (A), and spatial control of Pd and Rh sites for CO₂RR and hydroformylation respectively in a vial-in-vial reactor (B).

We posit that such CO and H₂ evolution from CO₂RR may actually be useful in transformations that use syngas. Though great work towards hydroformylation fueled by CO₂ hydrogenation or electroreduction to CO and H₂ have been reported,²⁷⁻³² they often employ high temperature/pressure and additionally may require the handling of H₂, or only have moderate aldehyde selectivity. Though we note some groups have remarkably generated the necessary CO, H₂, and ethylene required for hydroformylation towards propionaldehyde.^{30, 32} An electrochemical approach to generating the necessary CO and H₂ from CO₂RR utilizing a classic Rh based hydroformylation catalyst can operate at less harsh conditions for both the electrochemical and thermochemical processes, selectively producing the desired aldehyde products. Further, electrocatalysis may soon be solar powered as the development of sunlight to electricity converting

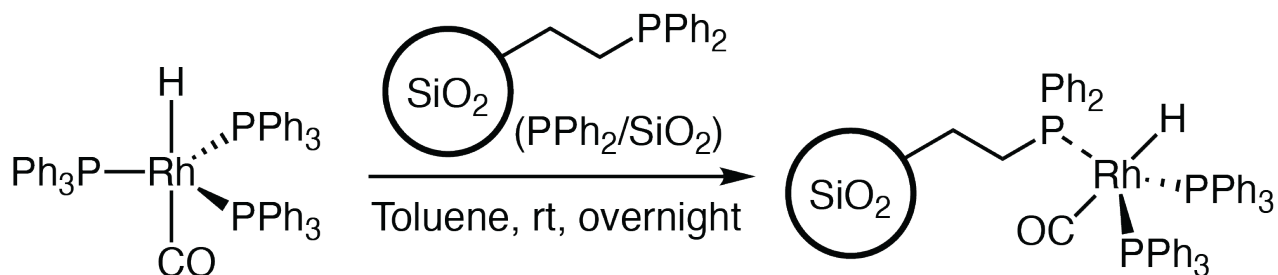
devices continue to advance, potentially improving the sustainability of an electrochemical rather than thermal approach.³³

Here, we report the re-purposing of the typically undesired HER in CO₂RR systems to provide the necessary equivalents for the synthesis of aldehydes via hydroformylation in an integrated catalysis fashion (Figure 4.1A). We employ a vial-in-vial reactor design (VIV, Figure 4.1B) wherein CO from CO₂RR and H₂ from adventitious H⁺ are generated in one component of a high pressure reactor, then allowed to diffuse into another component (vial) for the synthesis of aldehydes. Both a classic homogeneous Rh based hydroformylation catalyst, as well as a heterogeneous analogue immobilized onto mesoporous silica (SiO₂), maintain hydroformylation activity when using a CO/H₂ feedstock provided from CO₂RR to synthesize 2-, and 3-phenylpropionaldehyde from styrene and CO₂. This work serves to expand the landscape of CO₂ as a C1 source in synthetic chemistry via spatial control in a multi-catalyst process.

Results and Discussion

We elected to employ HRh(CO)(PPh₃)₃ ([Rh]) as an exemplary hydroformylation catalyst due to commercial availability, as well as its extensively studied and benchmarked hydroformylation activity in a variety of solvent mediums and reaction conditions, specifically towards styrene.³⁴⁻³⁷ Further, [Rh] demonstrates feasible activity at ambient temperature and CO/H₂ pressure, compatible with our lab's prior reported non-aqueous CO₂RR which operates at room temperature and can generate ~1 bar of ~1:1 CO/H₂ with moderate fluctuations in CO:H₂. In addition to our aim of spatially controlling and separating CO₂RR and hydroformylation catalyst systems in separate components of one reactor, we were also interested in spatially localizing [Rh] at the molecular level onto a solid support to aid in future, more precise spatially controlled hydroformylation coupled to CO₂RR. To this end, we immobilized [Rh] onto phosphine coated

silica (PPh₂/SiO₂) via ligand exchange (Scheme 4.1, Supplementary Information). The grafting [Rh] on PPh₂/SiO₂ (abbreviated as [Rh]/PPh₂/SiO₂) was confirmed via ICP-MS, ¹H, ¹³C,



Scheme 4.1 Immobilization of HRh(CO)(PPh₃)₃ onto phosphine coated silica (PPh₂/SiO₂) via overnight grafting.

³¹P, and ²⁹Si solid state NMR (SSNMR), and IR spectroscopy (Supplementary Figures S4.1-4.5).

With both [Rh] and its heterogeneous analogue [Rh]/PPh₂/SiO₂ in hand, we explored compatible conditions between Rh based hydroformylation and CO₂RR for integration.

Our prior report in non-aqueous electrochemical CO₂RR demonstrated that dimethylformamide (DMF) as solvent, tetrabutylammonium hexafluorophosphate (TBAPF₆), and Pd foil working and counter/reference electrodes work best as a simple, non-aqueous CO₂RR system achieving ~40% faradaic efficiency (FE) for CO generation (FE_{CO}).¹⁵ Further, typically 1:1 - 1:2 FE_{CO}:FE_{H₂} (or P_{CO}:P_{H₂}) with P_{CO} + P_{H₂} ~ 1 bar was achieved at -0.5 mA cm⁻² for 24 h. Comparable HER to CO₂RR was ascribed to adventitious H⁺ from residual moisture.³⁸ Applied current was maintained at -0.5 mA cm⁻² for comparisons to prior reports at ~1:1 CO:H₂ and P_{CO} + P_{H₂} ~ 1 bar, though in an industrial context higher current densities should be explored for competent aldehyde production. Thus, we tested Rh based hydroformylation using the classic HRh(CO)(PPh₃)₃ (abbreviated as [Rh]) catalyst in DMF containing TBAPF₆ and at 0.5 mA cm⁻². Fortunately, [Rh] maintained essentially the same phenylpropionaldehyde yield of a maximum of 64% (Table S4.1,

Entry 2) in DMF and an appreciable drop to 48% in DMF/TBAPF₆, compared to 71% in the typically employed toluene for [Rh] hydroformylation (Table S4.1, Entries 1 and 4). With this promising preliminary result, integration of CO₂RR and hydroformylation was then studied in our vial-in-vial reactor.

The results of integrating CO₂RR to hydroformylation via spatial control in our VIV reactor are displayed in Figure 4.2. Increasing CO₂RR electrolysis time at -0.5 mA cm^{-2} up to 24 h when using [Rh] results in increase in phenylpropionaldehyde yield from styrene, with a slight lag phase at the onset of electrolysis time points, presumably due to slow buildup of CO and H₂ and their mass transport into the hydroformylation compartment. Further, capping electrolysis time to 24 h but leaving the multi-catalyst system for an additional day under the CO/H₂ atmosphere from CO₂RR results in near 100% phenylpropionaldehyde yield. The linear:branched (l:b) ratio of phenylpropionaldehyde species primarily remained between 0.5:1 - 1:1 for [Rh] in our integrated system, a minimal variation from the typical 0.11:1 - 0.5:1 observed for [Rh] in benzene at similar overall pressure and ratio of CO:H₂.³⁵ This suggests that catalyst selectivity is negligibly altered when using a feed of CO/H₂ from CO₂RR than when pressurized directly. CO:H₂ varied slightly from experiment to experiment, and did not manifest in drastic changes in product regioselectivity (Supplementary Tables S4.1, S4.2). Further, chronopotentiometry traces typically show stable voltage over a 24 h electrolysis, suggesting negligible change in the CO:H₂ ratio during electrolysis (Figure S4.6). In repeat trials using [Rh] at -0.5 mA cm^{-2} for 24 h with a slight variation in CO:H₂ from 0.2 to 0.4, the l:b ratios were 1:1 and 0.6:1 respectively, in line with prior reports that lower CO:H₂ gas compositions lead to more linear aldehyde.³⁵

On the other hand, [Rh]/PPh₂/SiO₂ demonstrates lower hydroformylation activity compared to its [Rh], likely due to mass transport and/or changes in [Rh] coordination environment when

immobilized. Nonetheless, capping electrolysis time at 24 h for comparison to the [Rh] time study, but allowing additional reaction time leads to an increase in phenylpropionaldehyde yield up to 43% within 72 h total reaction time. Interestingly, the l:b ratio decreases to 0.07:1 – 0.22:1 for [Rh]/PPh₂/SiO₂, with some trials leading to no detectable linear aldehyde. This appears rather counterintuitive as one would suspect the branched aldehyde to be less favorable to form within a mesoporous support from a steric argument. However, an in depth analysis of the effect of reaction conditions and coordination environment on the l:b is beyond the scope of this report, and the reader is referred to other reports on this subject.³⁹⁻⁴² Control experiments using the bare PPh₂/SiO₂ support lead to no detectable aldehyde in our integrated system (Table S4.1, entry 9). We note that the use of DMF as a solvent for hydroformylation introduced additional benefits in adequately dispersing [Rh]/PPh₂/SiO₂, in line with previous studies of dispersing and coating mesoporous SiO₂ materials.⁴³

The results of our time study suggest that mass transport is the major limiting factor in integrating CO₂RR and hydroformylation in our VIV reactor, as evidenced by the need for additional reaction time post electrolysis to allow CO to transport from our CO₂RR to hydroformylation compartments. Therefore, we attempted to co-localize yet still spatially separate the Pd foil for CO₂RR from our [Rh]/PPh₂/SiO₂ in one compartment to circumvent catalyst-catalyst interference, while shortening the distance for CO transport. To this end, spin coating of [Rh]/PPh₂/SiO₂ onto Pd foil with an insulating SiO₂ layer in between was explored (Supplementary Information), amongst other coating methods. Such a hierarchical material design would allow for close spatial co-localization of the Pd and Rh sites and would take advantage of the mesoporous nature of SiO₂ materials to allow gas diffusion to and from the electrode surface. This would allow for more a more in depth investigation of how intercatalyst distance affects spatially controlled, multi-catalyst

systems in accordance with prior literature in analyzing mass transport in chemical transformations.^{44, 45} Unfortunately, [Rh]/PPh₂/SiO₂ appeared to lose hydroformylation activity within a reasonable time scale when coated onto Pd foil (Table S4.1, entry 9). Additionally, drop casting or doctor blading were unsuccessful in yielding a hydroformylation active [Rh]/PPh₂/SiO₂ species coated onto Pd. Thus, future work will focus on alternative electrode configurations and coating methods.

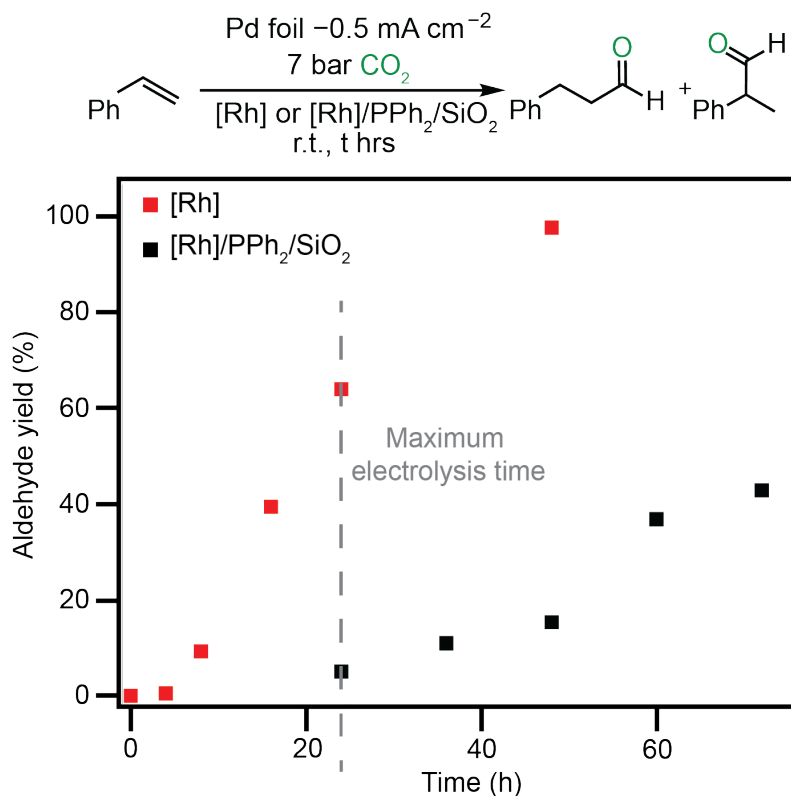


Figure 4.2 Time course study of integrated electrochemical CO₂ reduction (CO₂RR) and hydroformylation using a homogeneous ([Rh] = HRh(CO)(PPh₃)₃) and heterogeneous ([Rh]/PPh₂/SiO₂) Rh catalyst in a vial-in-vial reactor. [Rh] concentration was kept at 15 mM, [Rh]/PPh₂/SiO₂ loading was kept at 40 mg mL⁻¹, styrene concentration was kept at 0.5 M. CO₂ pressure was 7 bar. Applied current density (*i*) was 0.5 mA cm⁻² for 24 hours, resulting in an average of 0.206 bar CO and 0.44 bar H₂. Electrolyte solution consisted of 0.25 M TBAPF₆ in DMF. Total aldehyde yield was determined from GCMS using a naphthalene internal standard.

Conclusions

CO₂ as a C1 source for aldehyde synthesis was achieved via the integration of electrochemical CO₂ reduction (CO₂RR) to hydroformylation by spatial separation within a vial-in-vial reactor (VIV). Using styrene as a substrate and the classic HRh(CO)(PPh₃)₃ ([Rh]) catalyst or its heterogeneous analogue immobilized onto mesoporous silica ([Rh]/PPh₂/SiO₂) in our VIV reactor resulted in 97 and 43% phenylpropionaldehyde yield with minimal deviations in linear:branched (l:b) ratio compared to prior literature. The limiting factor in this integrated CO₂RR-hydroformylation system is likely CO generation and transport from the electrochemical zone to the hydroformylation compartment. Attempts to spatially localize in closer proximity yet still separate Rh and Pd sites via spin coating, drop casting, or doctor blading appeared to shut down hydroformylation activity. Thus, future work will focus on alternative working electrode configurations and coating methods to generate an active [Rh] species on an electrode surface, allowing the study of the role of inter-catalyst distance in integrated catalytic processes. Further, we aim to explore the role that a widely varied ratio of electrogenic CO:H₂ controlled by applied current has on product distributions, building off of deep prior mechanistic understandings of hydroformylation at Rh sites. Nonetheless, this work expands the landscape of multi-catalyst, one pass systems that take abundant, environmentally detrimental pollutants such as CO₂ to commodity chemicals like aldehydes by generating and utilizing both CO/H₂ from CO₂RR at ambient temperature and low pressure.

References

1. Deng, S.; Jolly, B. J.; Wilkes, J. R.; Mu, Y.; Byers, J. A.; Do, L. H.; Miller, A. J.; Wang, D.; Liu, C.; Diaconescu, P. L., Spatiotemporal control for integrated catalysis. *Nat. Rev. Methods Primers* **2023**, *3*, 28.
2. Schmidt, S.; Castiglione, K.; Kourist, R., Overcoming the Incompatibility Challenge in Chemoenzymatic and Multi-Catalytic Cascade Reactions. *Chem. Eur. J.* **2018**, *24*, 1755-1768.
3. Vriezema, D. M.; Garcia, P. M. L.; Sancho Oltra, N.; Hatzakis, N. S.; Kuiper, S. M.; Nolte, R. J. M.; Rowan, A. E.; van Hest, J. C. M., Positional Assembly of Enzymes in Polymersome Nanoreactors for Cascade Reactions. *Angew. Chem. Int. Ed.* **2007**, *46*, 7378-7382.
4. Quin, M. B.; Wallin, K. K.; Zhang, G.; Schmidt-Dannert, C., Spatial organization of multi-enzyme biocatalytic cascades. *Org. Biomol. Chem.* **2017**, *15*, 4260-4271.
5. Zhang, Y.; Hess, H., Toward Rational Design of High-efficiency Enzyme Cascades. *ACS Catal.* **2017**, *7*, 6018-6027.
6. Tsitkov, S.; Hess, H., Design Principles for a Compartmentalized Enzyme Cascade Reaction. *ACS Catal.* **2019**, *9*, 2432-2439.
7. Vázquez-González, M.; Wang, C.; Willner, I., Biocatalytic Cascades Operating on Macromolecular Scaffolds and in Confined Environments. *Nat. Catal.* **2020**, *3*, 256-273.
8. Wang, C.; Yue, L.; Willner, I., Controlling biocatalytic cascades with enzyme–DNA dynamic networks. *Nat. Catal.* **2020**, *3*, 941-950.
9. Kracher, D.; Kourist, R., Recent developments in compartmentalization of chemoenzymatic cascade reactions. *Curr. Opin. Green Sustain. Chem.* **2021**, *32*, 100538.

10. Webb, D.; Jamison, T. F., Continuous flow multi-step organic synthesis. *Chem. Sci.* **2010**, *1*, 675.
11. Lu, J.; Dimroth, J.; Weck, M., Compartmentalization of Incompatible Catalytic Transformations for Tandem Catalysis. *J. Am. Chem. Soc.* **2015**, *137*, 12984-12989.
12. Qu, P.; Kuepfert, M.; Hashmi, M.; Weck, M., Compartmentalization and Photoregulating Pathways for Incompatible Tandem Catalysis. *J. Am. Chem. Soc.* **2021**, *143*, 4705-4713.
13. Rayder, T. M.; Adillon, E. H.; Byers, J. A.; Tsung, C.-K., A Bioinspired Multicomponent Catalytic System for Converting Carbon Dioxide into Methanol Autocatalytically. *Chem* **2020**, *6*, 1742-1754.
14. Rayder, T. M.; Bensalah, A. T.; Li, B.; Byers, J. A.; Tsung, C.-K., Engineering Second Sphere Interactions in a Host–Guest Multicomponent Catalyst System for the Hydrogenation of Carbon Dioxide to Methanol. *J. Am. Chem. Soc.* **2021**, *143*, 1630-1640.
15. Dodge, H. M.; Natinsky, B. S.; Jolly, B. J.; Zhang, H. C.; Mu, Y.; Chapp, S. M.; Tran, T. V.; Diaconescu, P. L.; Do, L. H.; Wang, D. W.; Liu, C.; Miller, A. J. M., Polyketones from Carbon Dioxide and Ethylene by Integrating Electrochemical and Organometallic Catalysis. *ACS Catal.* **2023**, *13*, 4053-4059.
16. Saeki, T.; Hashimoto, K.; Kimura, N.; Omata, K.; Fujishima, A., Electrochemical reduction of CO₂ with high current density in a CO₂⁺ methanol medium at various metal electrodes. *J. Electroanal. Chem.* **1996**, *404*, 299-302.
17. Appel, A. M.; Bercaw, J. E.; Bocarsly, A. B.; Dobbek, H.; DuBois, D. L.; Dupuis, M.; Ferry, J. G.; Fujita, E.; Hille, R.; Kenis, P. J., Frontiers, opportunities, and challenges in biochemical and chemical catalysis of CO₂ fixation. *Chem. Rev.* **2013**, *113*, 6621-6658.

18. Jones, J. P.; Prakash, G. S.; Olah, G. A., Electrochemical CO₂ reduction: recent advances and current trends. *Isr. J. Chem.* **2014**, *54*, 1451-1466.
19. Chen, C.; Zhang, B.; Zhong, J.; Cheng, Z., Selective electrochemical CO₂ reduction over highly porous gold films. *Journal of Materials Chemistry A* **2017**, *5*, 21955-21964.
20. Gao, D.; Zhou, H.; Cai, F.; Wang, D.; Hu, Y.; Jiang, B.; Cai, W.-B.; Chen, X.; Si, R.; Yang, F., Switchable CO₂ electroreduction via engineering active phases of Pd nanoparticles. *Nano Research* **2017**, *10*, 2181-2191.
21. Zhao, G.; Huang, X.; Wang, X.; Wang, X., Progress in catalyst exploration for heterogeneous CO₂ reduction and utilization: a critical review. *Journal of Materials Chemistry A* **2017**, *5*, 21625-21649.
22. Francke, R.; Schille, B.; Roemelt, M., Homogeneously catalyzed electroreduction of carbon dioxide—methods, mechanisms, and catalysts. *Chem. Rev.* **2018**, *118*, 4631-4701.
23. Gonell, S.; Miller, A. J., Carbon Dioxide Electroreduction Catalyzed by Organometallic Complexes. *Adv. Organomet. Chem.* **2018**, *70*, 1-69.
24. Grignard, B.; Gennen, S.; Jérôme, C.; Kleij, A. W.; Detrembleur, C., Advances in the use of CO₂ as a renewable feedstock for the synthesis of polymers. *Chem. Soc. Rev.* **2019**, *48*, 4466-4514.
25. Zhang, S.; Fan, Q.; Xia, R.; Meyer, T. J., CO₂ reduction: from homogeneous to heterogeneous electrocatalysis. *Acc. Chem. Res.* **2020**, *53*, 255-264.
26. Shi, R.; Guo, J.; Zhang, X.; Waterhouse, G. I.; Han, Z.; Zhao, Y.; Shang, L.; Zhou, C.; Jiang, L.; Zhang, T., Efficient wettability-controlled electroreduction of CO₂ to CO at Au/C interfaces. *Nat. Commun.* **2020**, *11*, 3028.

27. Ali, M.; Gual, A.; Ebeling, G.; Dupont, J., Ruthenium-Catalyzed Hydroformylation of Alkenes by using Carbon Dioxide as the Carbon Monoxide Source in the Presence of Ionic Liquids. *ChemCatChem* **2014**, *6*, 2224-2228.
28. Ren, X.; Zheng, Z.; Zhang, L.; Wang, Z.; Xia, C.; Ding, K., Rhodium-Complex-Catalyzed Hydroformylation of Olefins with CO₂ and Hydrosilane. *Angew. Chem. Int. Ed.* **2017**, *56*, 310-313.
29. Hua, K.; Liu, X.; Wei, B.; Shao, Z.; Deng, Y.; Zhong, L.; Wang, H.; Sun, Y., Chemo- and regioselective hydroformylation of alkenes with CO₂/H₂ over a bifunctional catalyst. *Green Chem.* **2021**, *23*, 8040-8046.
30. Biswas, A. N.; Xie, Z.; Xia, R.; Overa, S.; Jiao, F.; Chen, J. G., Tandem electrocatalytic–thermocatalytic reaction scheme for CO₂ conversion to C₃ oxygenates. *ACS Energy Lett.* **2022**, *7*, 2904-2910.
31. Biswas, A. N.; Winter, L. R.; Xie, Z.; Chen, J. G., Utilizing CO₂ as a reactant for C₃ oxygenate production via tandem reactions. *JACS Au* **2023**, *3*, 293-305.
32. Zhang, J.; Kang, X.; Yan, Y.; Ding, X.; He, L.; Li, Y., Cascade Electrocatalytic and Thermocatalytic Reduction of CO₂ to Propionaldehyde. *Angew. Chem. Int. Ed.* **2024**, *63*, e202315777.
33. Blanco, D. E.; Modestino, M. A., Organic electrosynthesis for sustainable chemical manufacturing. *Trends Chem.* **2019**, *1*, 8-10.
34. Evans, D.; Osborn, J. A.; Wilkinson, G., Hydroformylation of alkenes by use of rhodium complex catalysts. *J. Chem. Soc. A* **1968**, 3133-3142.

35. Brown, C. K.; Wilkinson, G., Homogeneous hydroformylation of alkenes with hydridocarbonyltris-(triphenylphosphine)rhodium(I) as catalyst. *J. Chem. Soc. A* **1970**, 2753-2764.
36. Bath, S.; Vaska, L., Five-coordinate hydrido-carbonyl complexes of rhodium and iridium and their analogy with $\text{CoH}(\text{CO})_4$. *J. Am. Chem. Soc.* **1963**, *85*, 3500-3501.
37. Dewhirst, K. C.; Keim, W.; Reilly, C. A., Preparation and nuclear magnetic resonance spectra of hydridophosphine complexes of ruthenium and rhodium. *Inorg. Chem.* **1968**, *7*, 546-551.
38. Williams, D. B. G.; Lawton, M., Drying of Organic Solvents: Quantitative Evaluation of the Efficiency of Several Desiccants. *The Journal of Organic Chemistry* **2010**, *75*, 8351-8354.
39. Breit, B., Recent advances in alkene hydroformylation. *Metal Catalyzed Reductive C–C Bond Formation* **2007**, 139-172.
40. Klosin, J.; Landis, C. R., Ligands for practical rhodium-catalyzed asymmetric hydroformylation. *Acc. Chem. Res.* **2007**, *40*, 1251-1259.
41. Watkins, A. L.; Landis, C. R., Origin of Pressure Effects on Regioselectivity and Enantioselectivity in the Rhodium-Catalyzed Hydroformylation of Styrene with (*S, S, S*)-BisDiazaphos. *J. Am. Chem. Soc.* **2010**, *132*, 10306-10317.
42. Tonks, I. A.; Froese, R. D.; Landis, C. R., Very Low Pressure Rh-Catalyzed Hydroformylation of Styrene with (*S,S,S*-Bisdiazaphos): Regioselectivity Inversion and Mechanistic Insights. *ACS Catal.* **2013**, *3*, 2905-2909.

43. Choi, J.-Y.; Alford, T. L.; Honsberg, C. B., Solvent-Controlled Spin-Coating Method for Large-Scale Area Deposition of Two-Dimensional Silica Nanosphere Assembled Layers. *Langmuir* **2014**, *30*, 5732-5738.
44. Weisz, P.; Hicks, J., The behaviour of porous catalyst particles in view of internal mass and heat diffusion effects. *Chem. Eng. Sci.* **1962**, *17*, 265-275.
45. Weisz, P. B., Diffusion and Chemical Transformation: An interdisciplinary excursion. *Science* **1973**, *179*, 433-440.

Supplementary Information

Chemicals and methods

Chemicals. All reagents were purchased from Sigma Aldrich and were used as received unless specified. *N,N*-dimethylformamide (DMF) was dried over 3 Å molecular sieves for at least 24 h prior to use. Styrene was distilled over MgSO₄ under an N₂ environment and stored in the glove box until use, purity was checked via NMR (Bruker, AV400 MHz) and GCMS (Agilent).

Synthesis of [Rh]/PPh₂/SiO₂. In an Ar glovebox, 78 mg of diphenylphosphinoethyl-functionalized onto silica gel (PPh₂/SiO₂, 0.7 mmol g⁻¹ of PPh₂ groups, 200 - 400 mesh) was added to 10 mL of anhydrous toluene in a Schlenk flask, then brought out of the glovebox to sonicate for 15 min, then brought back in. 50 mg of HRh(CO)(PPh₃)₃ ([Rh]) was then added and the mixture was allowed to stir overnight at ambient temperature. The [Rh] immobilized onto silica material ([Rh]/PPh₂/SiO₂) was isolated via vacuum filtration and washed with two volumes of toluene and one of dichloromethane (10 mL per wash). [Rh]/PPh₂/SiO₂ was then dried overnight in a Schlenk flask, yielding a yellow/gold material. 0.4 ± 0.02 wt% Rh was determined for the [Rh]/PPh₂/SiO₂ species via inductively coupled plasma - mass spectrometry (ICP-MS, Agilent QQQ).

Integrated CO₂RR and hydroformylation. Experiments in integrating CO₂RR and hydroformylation were carried out in a high pressure electrochemical reactor equipped with an additional glass vial housing the hydroformylation catalysts. Electrochemistry was performed using a Gamry Instruments Interface 1000-E potentiostat. The electrolyte solution consisted of 0.25 M TBAPF₆ dissolved in DMF. A custom-designed high-pressure electrochemical reactor (Parr Instruments) was used equipped with electrical leads.¹ The solution volume was 200 mL and the gas headspace volume was ca. 750 mL (the value used for Faradaic efficiency calculations¹). The reactor was purged three times, then pressurized using CO₂ (Airgas, 99.999%). A two-electrode

configuration was utilized under constant applied current (i_{appl}) and the headspace was sampled after electrolysis using a gas chromatograph (GC). Electrodes were cleaned post electrolysis via sequential rinsing and sonication in acetone, DI water, and dilute nitric acid. Unless noted otherwise, the average surface area of the Pd foil working electrodes was $\sim 130 \text{ cm}^2$.

Hydroformylation catalysts, both the homogeneous [Rh] and its heterogeneous analogue [Rh]/PPh₂/SiO₂, were handled and prepared in an Ar glovebox until ready for use in integrated experiments. Catalyst concentrations were kept at 15 mM of [Rh] or 40 mg mL⁻¹ of [Rh]/PPh₂/SiO₂, both in a 1 mL DMF solution. [Rh]/PPh₂/SiO₂ solutions were first prepared in a Schlenk flask, taken outside of the glovebox and sonicated for 30 min to disperse [Rh]/PPh₂/SiO₂, then brought back into the glovebox. Lastly, once the electrolyte and catalyst solutions were added to the high pressure reactor, styrene was then added to the hydroformylation compartment, with a fixed [styrene] = 0.5 M. The reactor was then sealed and pressurized with CO₂ as described above.

Gas product quantification. Gaseous products from CO₂ reduction electrolysis (CO₂RR) were quantified via online detection with a GC (SRI 8610C) equipped with both a flame ionization detector with a methanizer (FIDm), and a thermal conductivity detector (TCD). The concentration of CO and H₂ in the headspace were often too high and lead to detector saturation. Thus, headspace samples were diluted by 5/83 with air. The valve oven was set to 175 °C. Argon was used as a carrier gas at 15 psi and 40 mL min⁻¹. The GC method was as follows: 50 °C for 1 min, 20 °C min⁻¹ ramp rate up to 90 °C, hold at 90 °C for 3.75 min, then a 30 °C min⁻¹ ramp rate to a final temperature of 210 °C. Three columns employed: 0.5 m Haysep-D pre-column, 2 m MoleSieve5A column, and 2 m Haysep-D column in that order. H₂ was supplied to the FID via a H₂-100 Hydrogen Generator at 20 psi and a 30 mL min⁻¹ flow rate, air was also supplied at 5 psi and a 250 mL min⁻¹ flow rate. The retention times of CO was 5.45 min (FIDm), and H₂ was 1.25 min

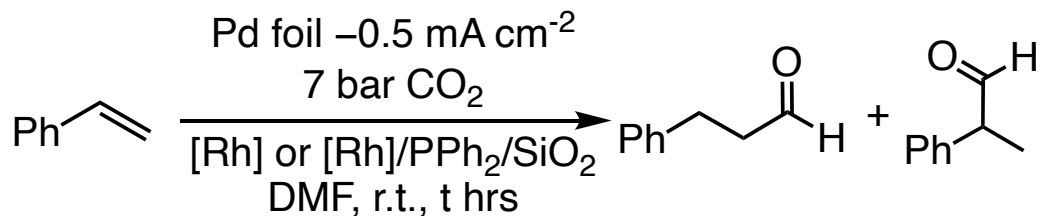
(TCD). A standard calibration gas mixture of consisting of 0.5% of CO₂, CO, H₂, and O₂ each in N₂.

Liquid product quantification. Products from the hydroformylation vial were detected and quantified via GCMS analysis and using a naphthalene internal standard. The temperature profile method for the GC was as follows: 100 °C for 5 min followed by a 4 °C min⁻¹ ramp up to 160 °C. For experiments using the [Rh]/PPh₂/SiO₂ catalyst, the hydroformylation solution was first centrifuged and decanted prior to sample preparation. 0.5 mL of the hydroformylation solution was diluted to 1 mL using 50 µL of a 20 mg mL⁻¹ naphthalene in acetone solution and 450 µL of acetone. Additionally, product quantification by GCMS was corroborated by conducting an integrated experiment using *d*₇-DMF. This was achieved by taking advantage of the diagnostic benzylic ¹H-NMR shifts between styrene and 2-/3-phenylpropionadelhyde, and using residual styrene as a pseudo internal standard.² Linear:branched ratios were assessed using the area under the curve or integral of their NMR of the respective isomer's.



Entry	Catalyst	Solvent composition ^a	CO/H ₂	Aldehyde yield (%) ^b	l:b ^c
1	[Rh]	Toluene	0.2	76	0.7:1
2	[Rh]	DMF	0.2	53±21	0.8:1
3	No [Rh]	DMF	0.1	0	–
4	[Rh]	0.25 M TBAPF ₆ , DMF	0.1	48	1:1
5	[Rh]	<i>d</i> ₇ -DMF	0.04	31 (25) ^d	0.9:1
6	[Rh]	DMF	0.4	97 ^e	0.6:1
7	[Rh]/PPh ₂ /SiO ₂	DMF	0.7	3±2	0.07:1
8	[Rh]/PPh ₂ /SiO ₂	DMF	0.3	43 ^f	0.2:1
9	Bare PPh ₂ /SiO ₂	DMF	0.6	0	–
10	[Rh]/PPh ₂ /SiO ₂ /Pd ^g	0.25 M TBAPF ₆ , DMF	0.6	0	–

Table S4.1 Experiments and controls in integrated CO₂RR - hydroformylation. [Rh] = HRh(CO)(PPh₃), kept at 15 mM, [Rh]/PPh₂/SiO₂ loading was kept at 40 mg mL⁻¹, styrene concentration was kept at 0.5 M. CO₂ pressure was 7 bar. Applied current density (*i*) was ± 0.5 mA cm⁻² for 24 hours, resulting in an average of 0.21 bar CO and 0.44 bar H₂. Pd foils were used as the working and counter electrode. Electrolyte solution consisted of 0.25 M TBAPF₆ in DMF. ^aSolvent composition for hydroformylation compartment. ^bYield for both phenylpropionaldehyde species was determined from GCMS using a naphthalene internal standard. ^cLinear:branched ratio of phenylpropionaldehyde isomers. ^dYield determined from NMR. ^e48 hours total reaction time, 24 hours electrolysis. ^f72 hours total reaction time, 24 hours electrolysis. ^gSee Supplementary Information for further details on [Rh]/PPh₂/SiO₂ coated onto Pd ([Rh]/PPh₂/SiO₂/Pd).



Catalyst	Electrolysis time (h)	Total time (h)	CO/H ₂	Aldehyde yield (%) ^a	l:b ^b
[Rh]	4	4	0.2	0.5	0.6:1
	8	8	0.3	9	0.9:1
	16	16	0.2	40	0.6:1
	24	24	0.2	64	0.8:1
	24	48	0.2	97	0.6:1
[Rh]/PPh ₂ /SiO ₂	24	24	0.9	5	0.07:1
	24	36	0.5	11	0.05:1
	24	48	0.7	15	0.05:1
	24	60	0.4	37	0.13:1
	24	72	0.4	43	0.22:1

Table S4.2 Integrated CO₂RR - hydroformylation time course study for both [Rh] and [Rh]/PPh₂/SiO₂. [Rh] = HRh(CO)(PPh₃), kept at 15 mM, [Rh]/PPh₂/SiO₂ loading was kept at 40 mg mL⁻¹, styrene concentration was kept at 0.5 M. CO₂ pressure was 7 bar. Applied current density (*i*) was $\pm 0.5 \text{ mA cm}^{-2}$ for 24 hours, resulting in an average of 0.21 bar CO and 0.44 bar H₂. Pd foils were used as the working and counter electrode. Electrolyte solution consisted of 0.25 M TBAPF₆ in DMF. ^aYield for both phenylpropionaldehyde species was determined from GCMS using a naphthalene internal standard. ^bLinear:branched ratio of phenylpropionaldehyde isomers.

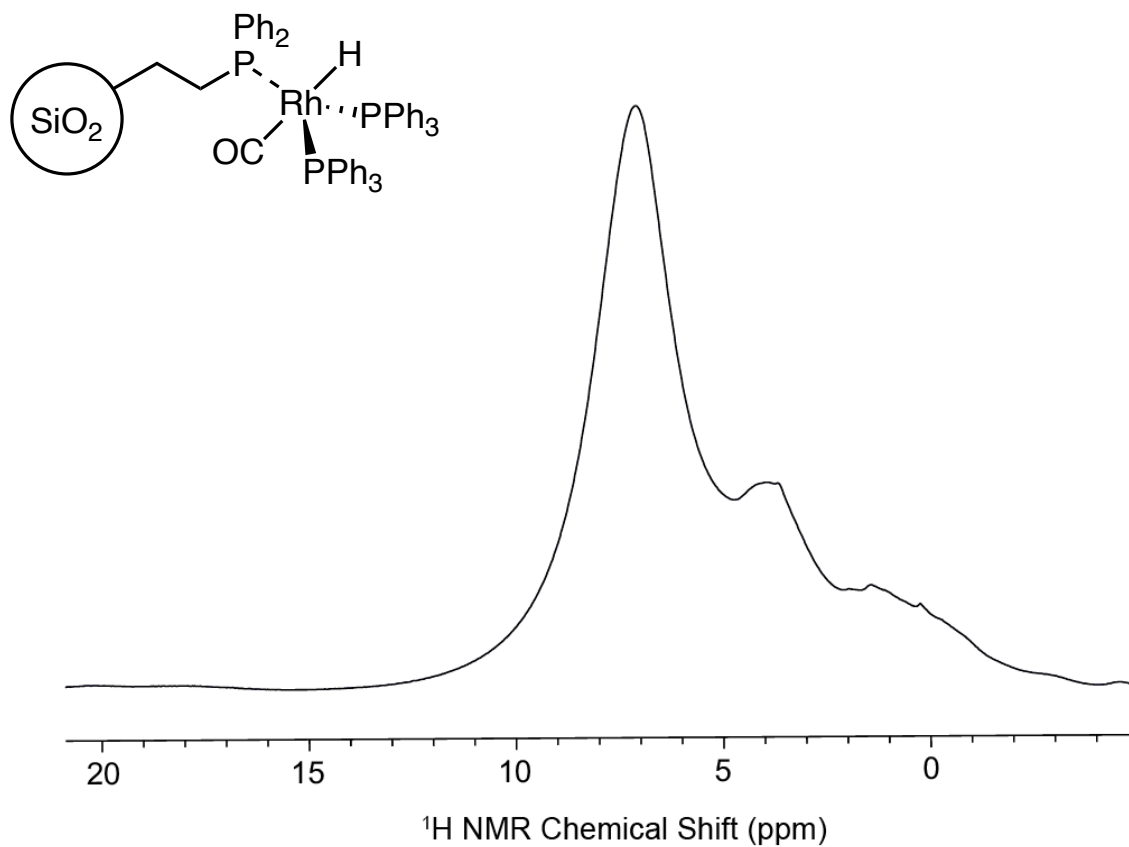


Figure S4.1 ¹H NMR (600 MHz, 10 kHz) of [Rh]/PPh₂/SiO₂, δ (ppm): 7.03 (Ph), 3.76, 1.35.

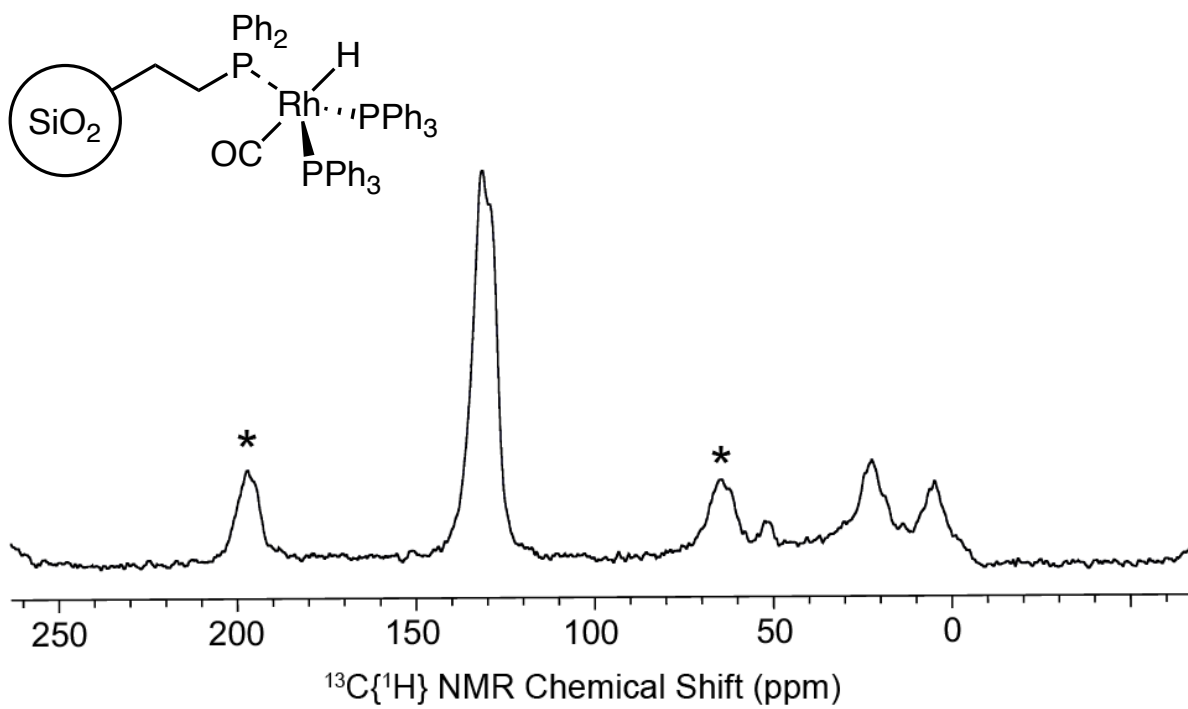


Figure S4.2 ¹³C NMR of [Rh]/PPh₂/SiO₂ (151 MHz, 10 kHz), δ (ppm): 131.1 (PPh), 128.9 (PPh), 52.0, 22.6, 5.0.

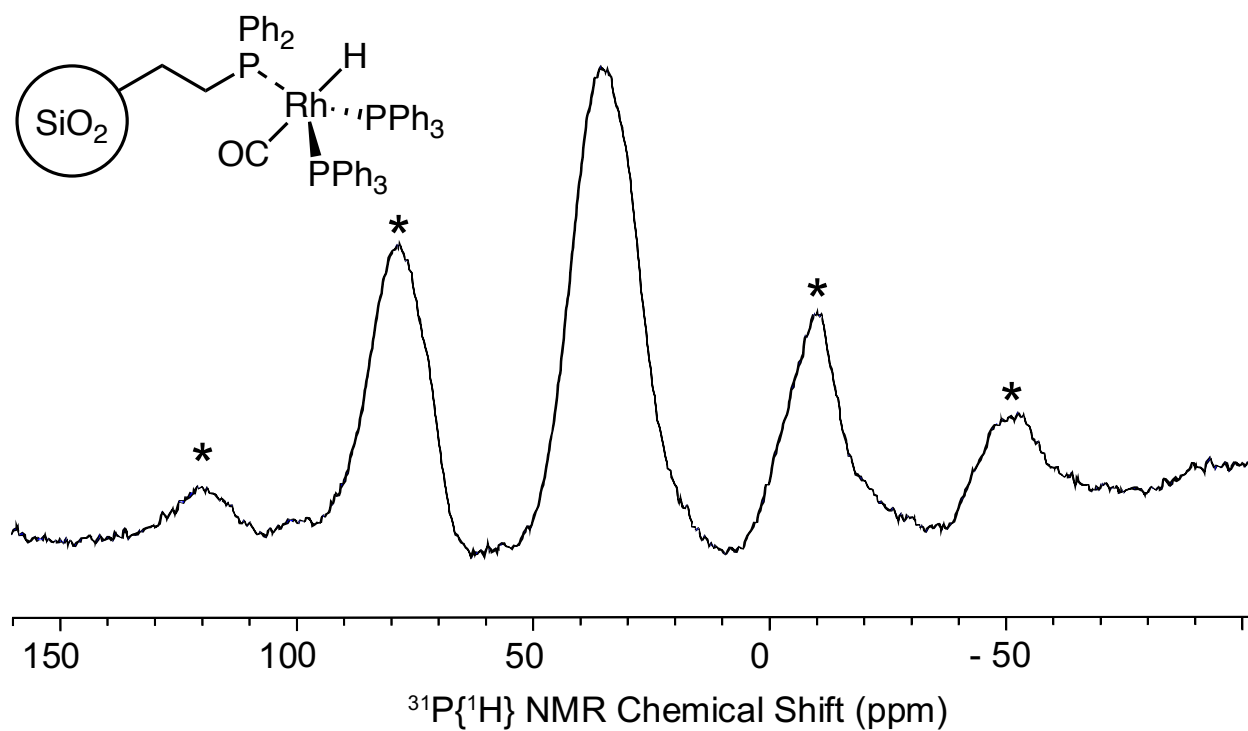


Figure S4.3 ^{31}P NMR of [Rh]/PPh₂/SiO₂ (243 MHz, 10 kHz), δ (ppm): 34.8 (PPh)

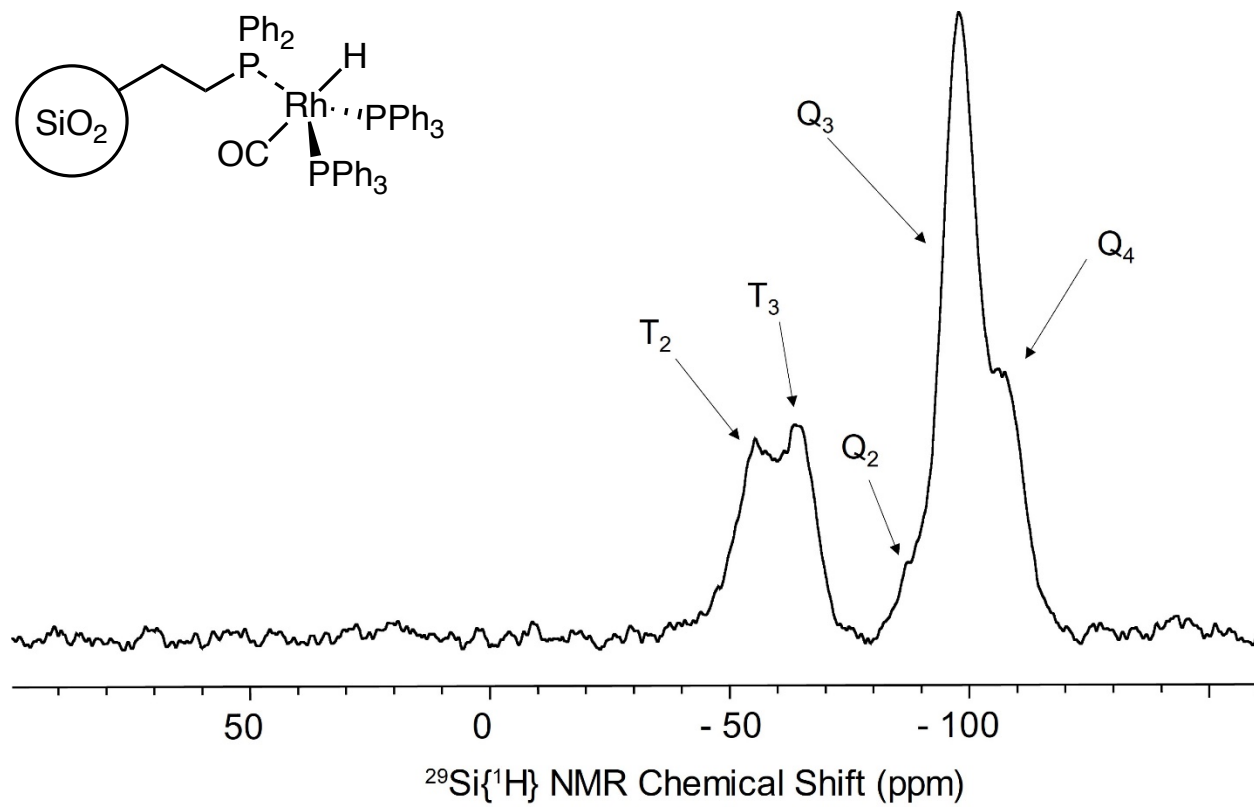


Figure S4.4 ²⁹Si NMR of [Rh]/PPh₂/SiO₂ (119 MHz, 10 kHz).

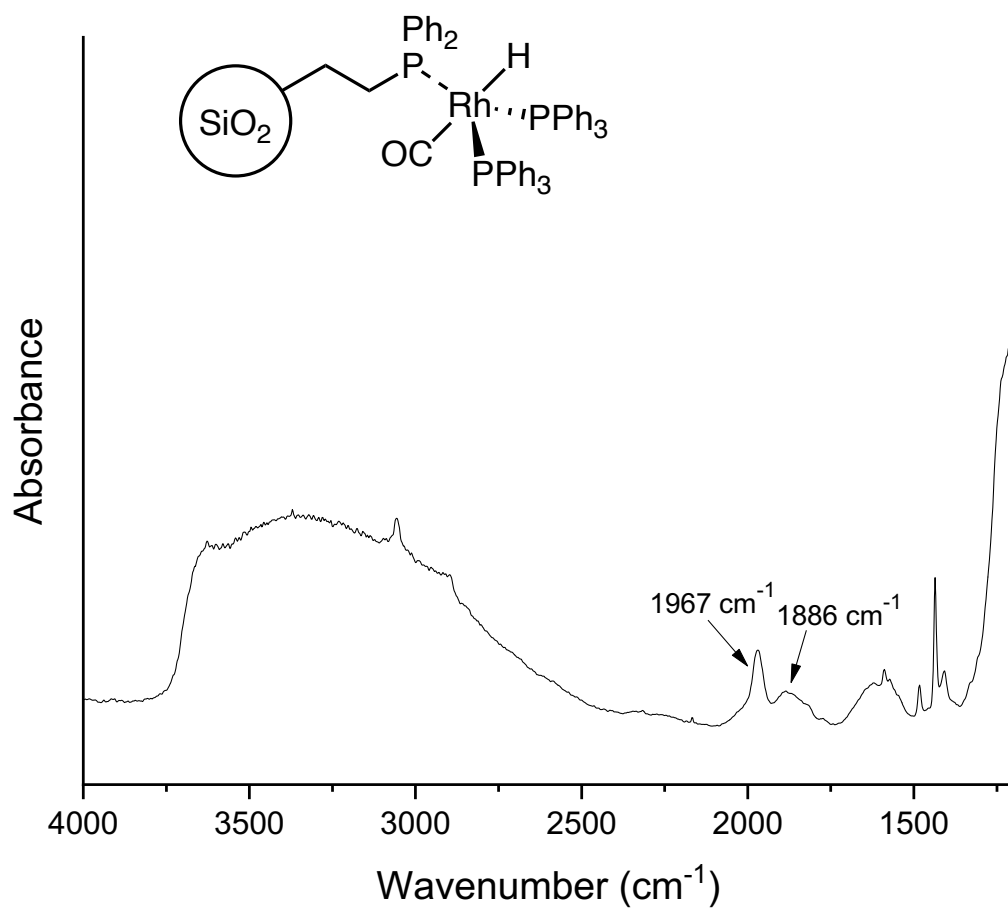


Figure S4.5 ATR-IR of [Rh]/PPh₂/SiO₂, Rh-H (1967 cm⁻¹), Rh-CO (1886 cm⁻¹).

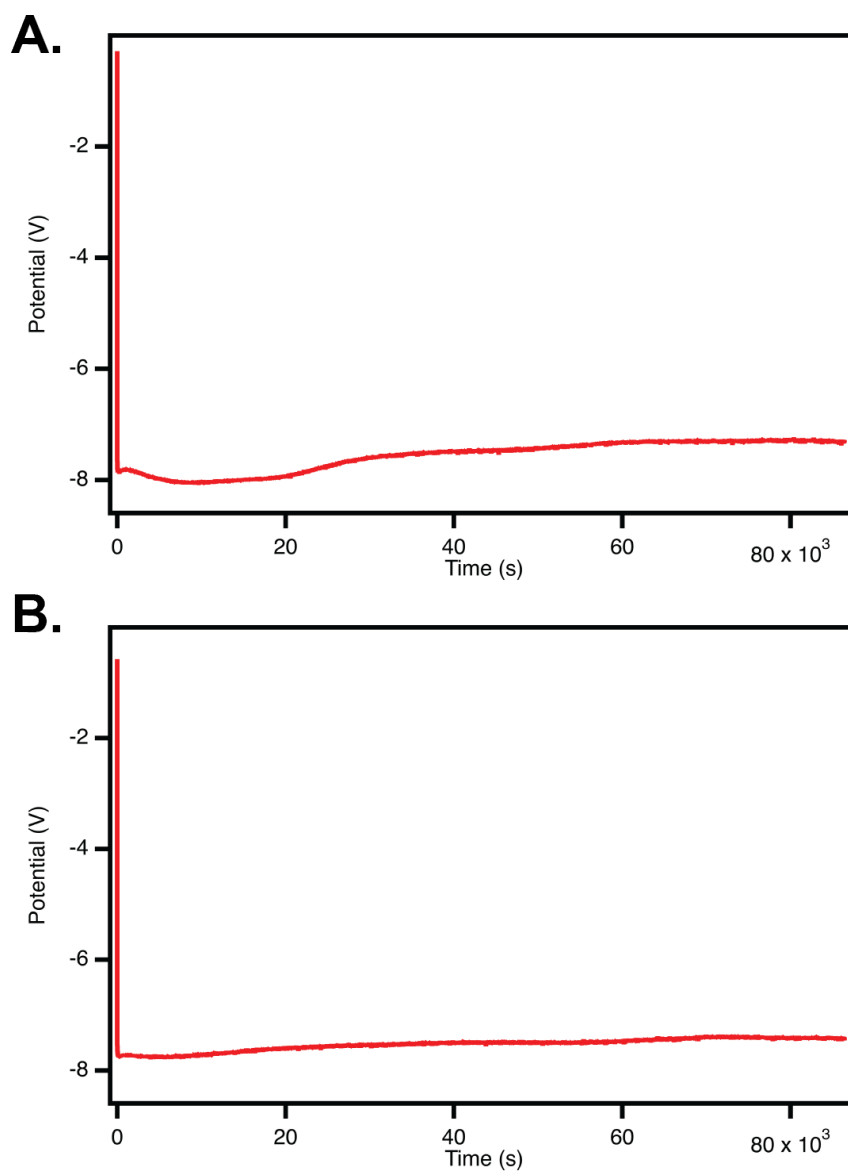


Figure S4.6 Chronopotentiometry traces from two separate experiments conducted at -0.5 mA cm^{-2} for 24 hours. Pd foils were used as the working and counter electrode. Electrolyte solution consisted of 0.25 M TBAPF_6 in DMF.

Coating of [Rh]/PPh₂/SiO₂ onto Pd foil

Spin coating, drop casting, and doctor blading were explored as methods of preparing a layer of [Rh]/PPh₂/SiO₂ onto Pd foil with an insulating layer of SiO₂ in between. Solutions of 1 - 5 wt% of either SiO₂ or [Rh]/PPh₂/SiO₂ in DMF, both with and without 2.5 wt% polyvinylidene fluoride (PVDF) as a binder, were tested. DMF was chosen on the basis of a prior report demonstrating superior dispersity and coating of SiO₂ compared to typical solvents such as H₂O. In a typical coating attempt, 50 - 600 μL of a particular wt% of SiO₂ first, then [Rh]/PPh₂/SiO₂ afterwards, were dispensed onto a sectioned 1 - 6 cm² area of a 5 x 5 cm² Pd foil, unless otherwise noted. For spin coating, Pd foil was taped down to a Si wafer, and spin rates between 200 - 800 rpm and 5 - 60 s were tested. For drop casting, the Pd foil was gently heated to 30 °C until all DMF had evaporated. For doctor blade, 500 μL of a 10 wt% [Rh]/PPh₂/SiO₂ solution was dispensed onto a Pd foil, with thickness controlled by the amount of layers of ~20 μm thick tape around the area designated for coating. The excess [Rh]/PPh₂/SiO₂ dispersed in DMF was then scraped off, and the Pd foil was gently heated at 30 °C until all DMF had evaporated. Thicknesses of Pd foil samples coated with [Rh]/PPh₂/SiO₂ (denoted as [Rh]/PPh₂/SiO₂/Pd) were measured via optical microscopy and SEM. Thicknesses varied from 40 - 200 μm. Unfortunately, no [Rh]/PPh₂/SiO₂/Pd demonstrated any hydroformylation activity in our integrated catalytic reactor.

Supplementary references

1. H. M. Dodge, B. S. Natinsky, B. J. Jolly, H. C. Zhang, Y. Mu, S. M. Chapp, T. V. Tran, P. L. Diaconescu, L. H. Do, D. W. Wang, C. Liu and A. J. M. Miller, *ACS Catal.*, 2023, **13**, 4053-4059.
2. I. A. Tonks, R. D. Froese and C. R. Landis, *ACS Catal.*, 2013, **3**, 2905-2909.

Chapter 5. Continuous flow *N*-carboxyanhydride synthesis and polymerization

This chapter is largely a collaborative effort between Prof Chong Liu's lab at UCLA, Prof Jeffery Byers' and Prof Dunwei Wang's lab at Boston College (BC), Prof Loi Do's lab at the University of Houston (UH), and Prof Paula Diaconescu's lab at UCLA, as part of the National Science Foundation Center for Integrated Catalysis. I give much thanks and acknowledgement to Thi Tran (Do, UH), Kexing Xiao, Matthew Thompson, Stephanie Johnson, and Connor Gallin (Byers, BC), Haochuan Zhang (Wang, BC), as well as Yi Shen and Shijie Deng (Diaconescu, UCLA). They all helped tremendously in preparing catalyst bound plates for polymerization experiments, and for all of their work in testing surface-initiated polymerizations in batch. I dedicate this chapter specifically to the late Prof Jeffery Byers.

Abstract

Carrying out multi-step processes in one pass is a particularly attractive approach for synthetic pathways that proceed through ephemeral intermediates. The synthesis of polypeptide materials from the ring opening polymerization of *N*-carboxyanhydrides (NCAs) is a process of great desire that requires the handling of unstable intermediates, as NCAs are often prone to hydrolysis. Here we disclose efforts made in the development and optimization of NCA synthesis and polymerization methods under continuous flow as a step towards carrying out both reactions sequentially. Continuous flow processing was chosen to allow for controlled transport of NCA intermediates between reaction sites via flow. Further, flow chemistry offers additional benefits in improved mass and heat transfer over batch processes. Utilizing a Ru catalyst, alkyne, and organic base, NCAs were synthesized at moderate yields (~30%) under flow conditions at greatly reduced CO₂ pressures and improved selectivity over batch conditions. Employing an immobilized Fe(I)

catalyst, surface-initiated polymerization (SIP) of NCAs was greatly accelerated through flow by over four orders of magnitude in observed rate over batch conditions., achieving ~40% conversion for flow compared to 9% for batch conditions. This represents the first example of overcoming documented mass transport limitations in SIP process by translation to a flow setting.

Introduction

The development of multi-step reaction pathways operating in one pass is of great desire in converting feedstocks to commodity chemicals, while obviating wasteful or problematic work ups.¹ The ability to generate and quickly consume an intermediate along a synthetic pathway would be especially beneficial in situations where said intermediate has a short shelf life, and/or is hazardous to handle. However, it is not trivial to carry out multiple successive reactions in one reaction vessel simultaneously owing to potentially complex cross reactivity between reaction systems. One approach to circumvent this limitation is to spatially separate reactions to be carried out in tandem, while allowing effective intermediate transport between reaction sites.¹ One method of achieving controlled, effective intermediate transport is through flow chemistry. Additionally, flow chemistry offers a large scale form a spatial in that individual reactions may be carried out in separate flow systems, while intermediates are flowed between separate flow components. Recent advancements in continuous flow processing have demonstrated flow as an effective approach to complex organic synthesis.²⁻⁸ Flow chemistry offers improved mass and heat transfer over batch processes, and can be highly tailored to a specific reactions' conditions.²

One attractive multi-step system wherein the synthetic pathway proceeds through an unstable intermediate is the synthesis of polypeptide (polyamide) materials via *N*-carboxyanhydrides. The preparation of synthetic polypeptides has been highly sought after for applications in biotechnology such as drug delivery, tissue engineering, amongst others.⁹⁻¹¹ Traditionally,

polypeptides have been synthesized via solid phase peptide synthesizers.¹¹ Though they offer great sequence control over amino acid incorporation, this method often suffers from numerous side reactions, and limitations in achievable molecular weight. Synthetic polypeptides via the ring opening polymerization (ROP) of *N*-carboxyanhydrides (NCA) is an alternative approach that reconciles some of these limitations, with drawbacks such as poor sequence control and the short shelf life of NCAs.^{9, 10, 12} ROP of NCAs also only releases CO₂ as the major byproduct. Currently, much focus is given to methods that would institute better sequence control in NCA ROP, which would lead to high molecular weight, diverse polypeptides in a synthetically cleaner fashion than solid phase peptide synthesizers.

NCA synthesis is typically carried out using the Fuchs-Farthing method wherein amino acids are cyclized to NCAs with hazardous phosgene, with prepared NCAs usually having short shelf lives due to hydrolysis.^{13, 14} Though this method has effectively prepared a variety of NCAs and allowed for extensive research into the resultant polypeptides from NCA ROP, the use of phosgene is far from ideal from a safety perspective. Given that NCA ROP releases CO₂, it would be ideal to

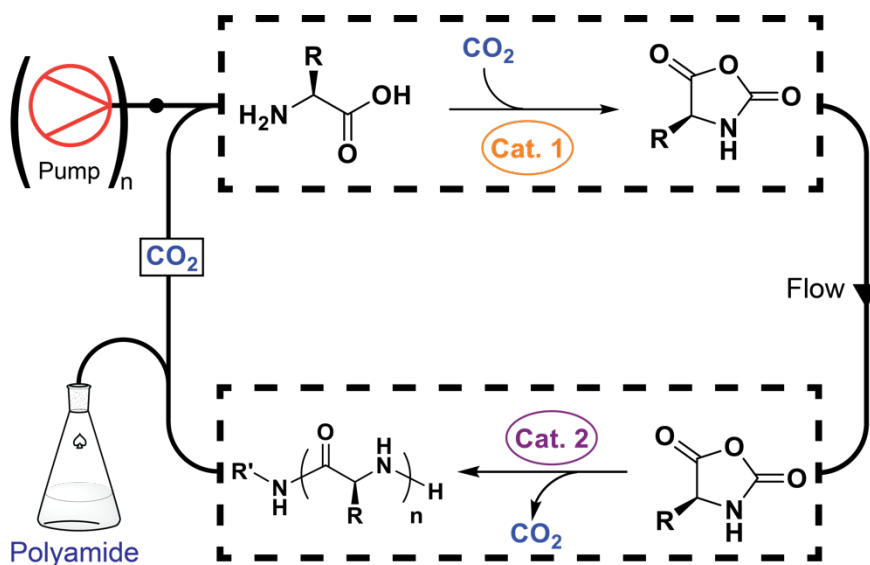


Figure 5.1 Targeted flow reactor scheme for integrated NCA synthesis and polymerization to recycle CO₂.

recycle the liberated CO₂ to drive NCA synthesis. One approach to achieving this goal is to spatially control NCA synthesis and polymerization within one integrated reactor setup to allow recycling of liberated CO₂ (Figure 5.1). This approach would also allow the *in situ* consumption of generated, unstable NCAs to prepare polypeptide materials.

One attractive use of polypeptide materials is the coating of surfaces to improve the biocompatibility of materials.^{15, 16} To generate polypeptide coated surfaces, grafting to and grafting from (surface initiated polymerization) techniques have been developed.¹⁷ In the former, well defined polypeptides (or polymers in general) are adhered to a surface post synthesis. However, this method is limited by steric hindrance of tethering materials to a surface. The grafting from, or surface initiated polymerization method circumvents this limitation by growing a polymer from a surface bound initiator. In this way, much higher surface grafting densities can be achieved, albeit with less well defined polymers. Thus, there lies a growing interest in surface grown polypeptide materials.

Herein, we disclose efforts made towards developing NCA synthesis and polymerization methods under flow conditions for reasons outlined above. In light of spatial control desired for integration of NCA synthesis and polymerization to polyamides, we elected to use the grafting from approach for NCA ROP employing a surface bound Fe(I) initiator. For NCA synthesis, we employed a synthetic method involving a Ru catalyst, alkyne, and organic base to activate CO₂ to cyclize amino acids to NCAs. Though we were not able to move forward with integrating the two processes together, achievements were made towards optimizing these processes in a flow setting for later integration. This work not only makes progress towards integrating NCA synthesis and polymerization by means of continuous flow, but also reveals the crucial role of mass transport in SIP processes.

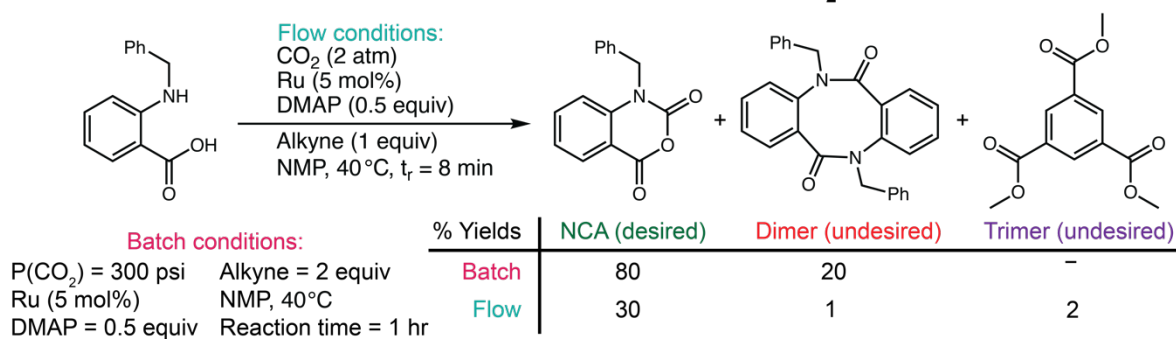
Results and Discussion

In collaboration with Professor Loi Do's lab at the University of Houston, conditions for NCA synthesis using CO₂ instead of phosgene were identified to be explored in flow, displayed in Figure 5.2. Six membered ring NCAs were chosen for method development as opposed to five membered analogues that form from amino acids, owing to increased stability of six membered ring NCAs and thus ease of characterization. A Ru catalyst (dichloro[(2,6,10-dodecatriene)-1,12-diyl]ruthenium), alkyne initiator (methyl propiolate), and organic base (dimethylaminopyridine, DMAP), were identified to form the carbamate with CO₂ and activate the carboxylic acid towards cyclization to an NCA. In preliminary studies of NCA synthesis using these reagents, two major side reactions were identified by gas chromatography - mass spectrometry (GCMS). Dimerization of the starting material was apparent and decreased with increasing CO₂ pressure. Trimerization of the alkyne by the Ru catalyst was also prevalent, in line with prior literature.¹⁸ Given these observations, high CO₂ pressures were targeted, and the alkyne was added last to the reaction. Further, the reaction was pressurized with CO₂ containing the starting material, the Ru catalyst, and DMAP. Then, the reaction was vented, the alkyne was added, then re-pressurized. Optimized batch conditions resulted in full conversion of *N*-benzylanthranillic acid to 80% desired NCA product (*N*-benzylisatoic anhydride), and a 4:1 ratio of NCA:dimer, with no detected trimer stemming from alkyne trimerization. With batch conditions in hand, and an understanding of prevalent side reactions, we then explored translating these conditions to a flow setting.

Numerous configurations of a flow system were explored employing two pumps to separate starting materials under a CO₂ atmosphere to be mixed via flow (Supplementary Information). Ultimately, a simple two pump system wherein *N*-benzylanthranillic acid and methyl propiolate were separated from the Ru catalyst in DMAP in separate pump solutions, both pressurized with

CO₂ at 2 bar (Figure 5.2) proved most successful. Given the breadth of parameters ranging from temperature and pressure, to equivalents of reagents, Design of Experiment (DoE) methods were employed to rapidly screen parameters and identify optimal conditions (Supplementary Information). Five key parameters were initially identified to be explored using DoE, being: flow rate (mL min⁻¹), temperature, equivalents of methyl propiolate and DMAP, and Ru mol%. CO₂

A. Flow N-carboxyanhydride (NCA) synthesis with CO₂ and comparison to batch



B. Schematic of flow reactor for NCA synthesis and reagents

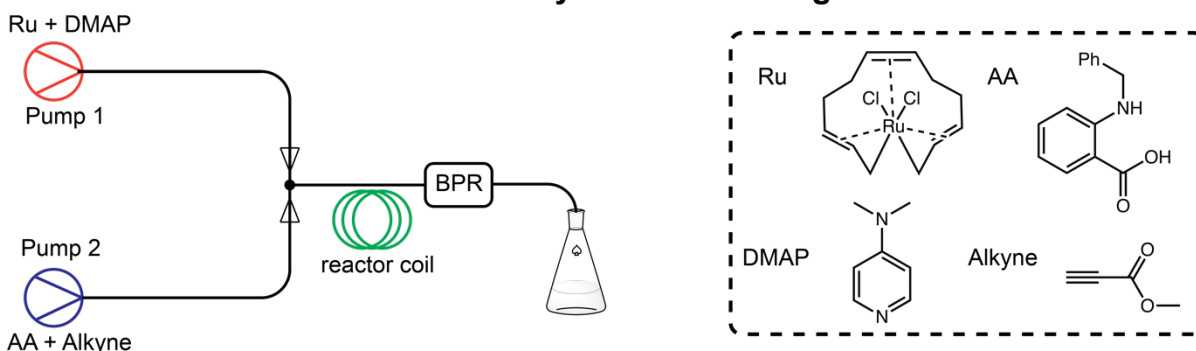


Figure 5.2 Optimized conditions and percent yield for batch and flow synthesis of NCAs from amino acids with CO₂, using *N*-benzylanthranilic acid as a model substrate. **(A)** Ru - dichloro[(2,6,10-dodecatriene)-1,12-diyl]ruthenium, DMAP - dimethylaminopyridine, alkyne - methyl propiolate, NMP - *N*-methylpyrrolidone, t_r - residence time, calculated from the volume of the reactor divided by the volumetric flow rate. Schematic of flow reactor design employed for NCA synthesis. **(B)** BPR - back pressure regulator, AA - amino acid analogue (*N*-benzylanthranilic acid).

pressure was not included, as 2 bar was the upper limit of P_{CO_2} achievable with our flow system, and prior experiments suggest higher P_{CO_2} is beneficial. Initial screening suggested flow rate or residence time (t_r , min), alkyne equivalents, and temperature were identified to have the most significant impact on yield and selectivity, whereas Ru mol% and DMAP equivalents had minimal impact under flow conditions.

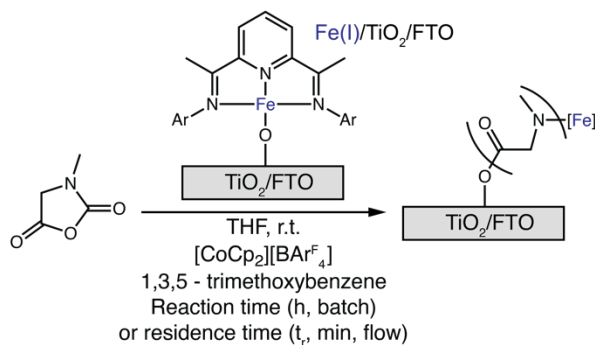
The result of a Custom Design DoE model using flow rate, alkyne equivalents, and temperature identified 40 °C, 1 equivalent of methyl propiolate, and 0.25 mL min⁻¹ ($t_r \sim 8$ min) yielded 30% desired NCA (*N*-benzylisatoic anhydride), with 1% dimer, and 2% trimerization product (Figure 5.2, Table S5.1). Increasing temperature up to 80 °C or alkyne equivalents marginally can improve NCA yield in some trials but leads to significant alkyne trimer formation. Thus, optimal conditions for NCA synthesis under flow conditions with the developed method were those displayed in Figure 5.2. Attempts to increase P_{CO_2} under flow conditions using a gas permeable tube-in-tube flow system were halted due to time constraints for this work. Such gas permeable tubing has been employed in synthetic flow chemistry where high gas pressures are desired,¹⁹⁻²¹ and would theoretically improve NCA yields here past 30%. Further, we explored alternate flow configurations wherein CO₂ was introduced directly to the flow reactor by means of gas - liquid segmented flow (Supplementary Information). Unfortunately, this proved unsuccessful, likely due to poor solvation of CO₂ at operable pressures and timeframe for dissolution. With NCA synthesis conditions under flow established, we turned our attention to explore NCA polymerization off a surface in flow.

In collaboration with Professor Jeff Byers' lab at Boston College, we employed a surface bound formally Fe(I) bisiminopyridine catalyst anchored to a titanium dioxide (TiO₂) coated fluorine doped tin oxide (FTO) plate for NCA ROP (Supplementary Information). Under batch conditions,

9% NCA conversion to polyamides was achieved using sarcosine-NCA as a model substrate. Extending reaction time to 168 hours marginally improves conversion to 27%. Compared to the Fe(I) catalyst not bound to any surface, 100% conversion is achieved within 10 min.²²

To carry out NCA surface initiated polymerization (SIP) (Figure 5.3A) in flow, we chose to build off of literature on parallel plate microfluidic devices, often employed in flow electrolysis,^{20, 23-28} as they are apt for carrying out heterogeneous reactions in flow off of surfaces. Our custom flow

A. NCA SIP by surface bound Fe(I) catalyst



B. Schematic of microfluidic reactor for NCA SIP

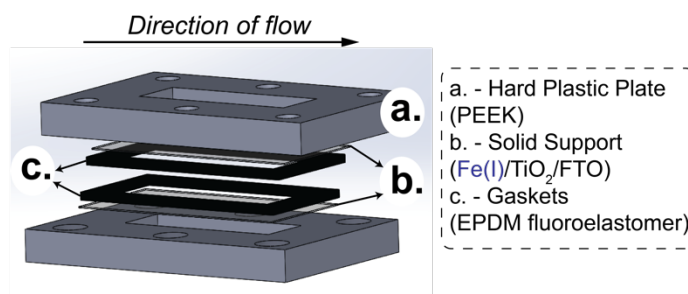


Figure 5.3 Reaction scheme of batch or flow surface initiated polymerization (SIP) of sarcosine-NCA (*N*-carboxyanhydride) by a formal Fe(I) bisiminopyridine catalyst bound to a TiO₂ coated FTO plate. (A) THF - tetrahydrofuran, r.t. - room temperature, [CoCp₂][BARF₄] - cobaltocenium tetrakis[3,5-bis(trifluoromethyl)phenyl]borate, 1,3,5 - trimethoxybenzene - internal standard, t_r - residence time, calculated from the volume of the reactor divided by the volumetric flow rate.. Schematic of custom designed microfluidic cell to incorporate Fe(I)/TiO₂/FTO plates to carry out NCA SIP in flow. (B) PEEK - polyether ether ketone, EPDM - ethylene propylene diene monomer.

cell consists of two PEEK (polyether ether ketone) plates that sandwich two FTO glass slides over EPDM (ethylene propylene diene monomer) gaskets, between which tubing can be inserted to flow solution through (Figure 5.3B). Further details about our custom flow cell design can be found in the Supplementary Information.

We initially tested the effect of flow on NCA SIP by flowing a sarcosine-NCA solution through our flow cell at 1 mL min^{-1} for roughly 1 day, which showed improved conversion compared to batch within the same time scale (*vide infra*). The monomer was recycled by connecting the outlet of the flow cell to the solution reservoir, as we suspected minimal conversion to ensue with each pass through the flow cell due the short residence time (t_r) of 1 min at 1 mL min^{-1} . Near 50% conversion was achieved at 1 mL min^{-1} within 22 hours, which is in stark contrast to the 11% conversion observed in batch within 1 day for the surface bound Fe(I) catalyst. However, polymer cleavage by MeI yielded no detectable removed polymer by NMR, making characterization challenging. A control flow experiment under the same conditions but without the Fe(I) catalyst yielded 3% conversion, presumably due to monomer adsorption to the TiO_2 surface. These results support the hypothesis that flow provides an additional means of monomer transport to surface catalyst sites, thus accelerating the observed rate of NCA SIP.

To gain a more in depth understanding of the effect of flow on NCA SIP, we carried out single pass NCA SIP under flow at various flow rates and residence times, which revealed an inverse relationship between conversion or observed rate constant (k_f , vide infra) and t_r (Fig. 6). Interestingly, we originally anticipated that longer t_r would favor higher conversion, giving more time for polymerization to occur within the flow channel. However, the results clearly demonstrate that shorter t_r , or faster flow rates, lead to higher conversion. Such a result supports our hypothesis that flow can alleviate mass transport limitations observed in batch. Ultimately, the application of continuous flow to NCA SIP is shown to assist in monomer transport to surface catalytic sites,

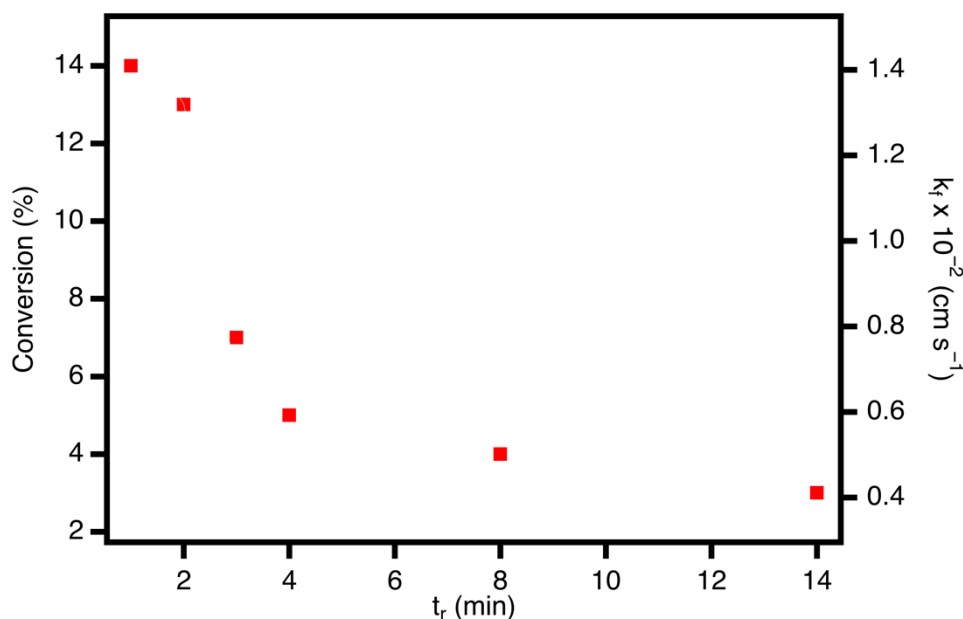


Figure 5.4 Effect of varying residence time (t_r) via flow rate on conversion and apparent rate constant k_f for a one pass NCA SIP using sarcosine-NCA, and a surface bound Fe(I) bisiminopyridine catalyst.

which improves conversion relative to the batch process.

As conversion alone between a batch and flow setting may not be an apples to apples comparison,²⁹ we next developed a kinetic model to draw direct comparisons between NCA SIP in batch and flow. Specifically, we derived expressions for a heterogeneous apparent rate constant k (subscript

b for batch, f for flow), which further supports that flow accelerates NCA SIP. In addition, we derived k such that it can be calculated from key parameters in batch and flow, namely surface area, volume, time, and flow rate. We arrived at the following expressions:

$$k_b = \frac{\ln(-\text{Conversion} + 1) V}{-SA * t} \quad (1)$$

$$k_f = \frac{2 * \text{Conversion} * Q}{SA(\text{Conversion} + 2)} \quad (2)$$

where V is the volume of the monomer solution, SA is the surface area of the Fe(I) anchored TiO₂ surface, and Q is the volumetric flow rate in mL min⁻¹. An in-depth discussion of our derivation can be found in Supplementary Information. Compared to the apparent rate constant for batch NCA SIP, which was calculated to be $k_b \sim 10^{-6}$ cm s⁻¹ for reaction times up to 168 hours, the apparent rate constant for flow (k_f) was determined to be several orders of magnitude higher, ranging from $10^{-3} - 10^{-2}$ cm s⁻¹. Therefore, based on the accelerated rate of NCA SIP in flow demonstrated by higher conversion and orders of magnitude faster apparent rate constant, we unequivocally conclude that flow effectively alleviates mass transport limitations observed in batch NCA SIP. This provides justification and motivation for the application of flow to other surface-initiated polymerization systems to improve conversion.

Conclusion

N-carboxyanhydride (NCA) synthesis and polymerization to polypeptide materials was explored in a continuous flow setting as a means for future integration to generate and consume ephemeral NCA intermediates in a one pass manner. Adapting conditions for NCA synthesis developed in a

batch setting using CO₂ instead of hazardous phosgene, improved selectivity was achieved with regards to NCA production over dimer formation in flow (~30:1) compared to batch conditions (4:1). This is ascribed to enhanced mass transfer of CO₂, as well as heat transfer in a flow system. Though reduced overall NCA yields of 30% were obtained in flow compared to 80% in batch, likely due to a ~2 bar upper limit of operable CO₂ pressure. For NCA surface-initiated polymerization (SIP), significantly enhanced conversion was achieved in flow compared to batch. This demonstrates flow's ability to circumvent mass transport limitations in a grafting from approach to coating surfaces with polymer materials. Further, in depth kinetic analysis reveals flow greatly accelerates the observed heterogeneous rate constant (k_b - batch, k_f - flow, both in cm s⁻¹) over four orders of magnitude. An inverse relationship between residence time (t_r , min) and conversion or k_f was observed, suggesting that enhanced transport via accelerated flow rate plays a larger role than longer reaction times (bestowed by longer t_r) in flow NCA SIP. Though integration of NCA synthesis and polymerization was not achieved due to time constraints, progress towards developing each process in flow was made. Additionally, fundamental insights into the role of mass transport in flow SIP processes was uncovered, aiding in future SIP work where mass transport limitations are observed.

References

1. Deng, S.; Jolly, B. J.; Wilkes, J. R.; Mu, Y.; Byers, J. A.; Do, L. H.; Miller, A. J.; Wang, D.; Liu, C.; Diaconescu, P. L., Spatiotemporal control for integrated catalysis. *Nat. Rev. Methods Primers* **2023**, *3*, 28.
2. Britton, J.; Jamison, T. F., The assembly and use of continuous flow systems for chemical synthesis. *Nature Protocols* **2017**, *12*, 2423-2446.
3. Marken, F.; Wadhawan, J. D., Multiphase Methods in Organic Electrosynthesis. *Acc. Chem. Res.* **2019**.
4. Bannock, J. H.; Krishnadasan, S. H.; Heeney, M.; de Mello, J. C., A gentle introduction to the noble art of flow chemistry. *Materials Horizons* **2014**, *1*, 373-378.
5. Akwi, F. M.; Watts, P., Continuous flow chemistry: where are we now? Recent applications, challenges and limitations. *Chem. Commun.* **2018**, *54*, 13894-13928.
6. Baumann, M.; Moody, T. S.; Smyth, M.; Wharry, S., A Perspective on Continuous Flow Chemistry in the Pharmaceutical Industry. *Organic Process Research & Development* **2020**, *24*, 1802-1813.
7. Webb, D.; Jamison, T. F., Continuous flow multi-step organic synthesis. *Chem. Sci.* **2010**, *1*, 675.
8. Hartman, R. L.; McMullen, J. P.; Jensen, K. F., Deciding Whether To Go with the Flow: Evaluating the Merits of Flow Reactors for Synthesis. *Angew. Chem. Int. Ed.* **2011**, *50*, 7502-7519.
9. Deming, T. J., Synthetic polypeptides for biomedical applications. *Prog. Polym. Sci.* **2007**, *32*, 858-875.

10. Cheng, J.; Deming, T. J., Synthesis of Polypeptides by Ring-Opening Polymerization of α -Amino Acid N-Carboxyanhydrides. *Top. Curr. Chem.* **2011**, *310*, 1-26.
11. Deming, T. J., Polypeptide Materials: New synthetic methods and applications. *Adv. Mater.* **1997**, *9*, 299-311.
12. Laconde, G.; Amblard, M.; Martinez, J., Synthesis of α -Amino Acid N-Carboxyanhydrides. *Organic Letters* **2021**, *23*, 6412-6416.
13. Poche, D. S.; Moore, M. J.; Bowles, J. L., An unconventional method for purifying the N-carboxyanhydride derivatives of γ -alkyl-L-glutamates. *Synth. Commun.* **1999**, *29*, 843-854.
14. Koga, K.; Sudo, A.; Nishida, H.; Endo, T., Convenient and useful synthesis of N-carboxyanhydride monomers through selective cyclization of urethane derivatives of α -amino acids. *J. Polym. Sci., Part A: Polym. Chem.* **2009**, *47*, 3839-3844.
15. Bozokalfa, G.; Akbulut, H.; Demir, B.; Guler, E.; Gumus, Z. P.; Odaci Demirkol, D.; Aldemir, E.; Yamada, S.; Endo, T.; Coskunol, H., Polypeptide functional surface for the aptamer immobilization: electrochemical cocaine biosensing. *Anal. Chem.* **2016**, *88*, 4161-4167.
16. Gao, Q.; Yu, M.; Su, Y.; Xie, M.; Zhao, X.; Li, P.; Ma, P. X., Rationally designed dual functional block copolymers for bottlebrush-like coatings: In vitro and in vivo antimicrobial, antibiofilm, and antifouling properties. *Acta biomaterialia* **2017**, *51*, 112-124.
17. Uyama, Y.; Kato, K.; Ikada, Y., Surface modification of polymers by grafting. *Grafting/Characterization Techniques/Kinetic Modeling* **1998**, 1-39.

18. Kawatsura, M.; Yamamoto, M.; Namioka, J.; Kajita, K.; Hirakawa, T.; Itoh, T., Ruthenium-Catalyzed Regioselective [2 + 2 + 2] Cyclotrimerization of Trifluoromethyl Group Substituted Internal Alkynes. *Org. Lett.* **2011**, *13*, 1001-1003.
19. He, Z.; Jamison, T. F., Continuous-Flow Synthesis of Functionalized Phenols by Aerobic Oxidation of Grignard Reagents. *Angew. Chem. Int. Ed.* **2014**, *53*, 3353-3357.
20. Folgueziras-Amador, A. A.; Philipps, K.; Guilbaud, S.; Poelakker, J.; Wirth, T., An Easy-to-Machine Electrochemical Flow Microreactor: Efficient Synthesis of Isoindolinone and Flow Functionalization. *Angew. Chem. Int. Ed.* **2017**, *56*, 15446-15450.
21. Seo, H.; Nguyen, L. V.; Jamison, T. F., Using carbon dioxide as a building block in continuous flow synthesis. *Advanced Synthesis & Catalysis* **2019**, *361*, 247-264.
22. Thompson, M. S.; Johnson, S. A.; Gonsales, S. A.; Brown, G. M.; Kristufek, S. L.; Byers, J. A., Adding Polypeptides to the Toolbox for Redox-Switchable Polymerization and Copolymerization Catalysis. *Macromolecules* **2023**, *56*, 3024-3035.
23. Laudadio, G.; Straathof, N. J.; Lanting, M. D.; Knoops, B.; Hessel, V.; Noël, T., An environmentally benign and selective electrochemical oxidation of sulfides and thiols in a continuous-flow microreactor. *Green Chem.* **2017**, *19*, 4061-4066.
24. Laudadio, G.; De Smet, W.; Struik, L.; Cao, Y.; Noël, T., Design and application of a modular and scalable electrochemical flow microreactor. *Journal of flow chemistry* **2018**, *8*, 157-165.
25. Pletcher, D.; Green, R. A.; Brown, R. C. D., Flow Electrolysis Cells for the Synthetic Organic Chemistry Laboratory. *Chem. Rev.* **2018**, *118*, 4573-4591.
26. Elsherbini, M.; Wirth, T., Electroorganic Synthesis under Flow Conditions. *Acc. Chem. Res.* **2019**, *52*, 3287-3296.

27. Gleede, B.; Selt, M.; Gütz, C.; Stenglein, A.; Waldvogel, S. R., Large, Highly Modular Narrow-Gap Electrolytic Flow Cell and Application in Dehydrogenative Cross-Coupling of Phenols. *Organic Process Research & Development* **2019**.
28. Noël, T.; Cao, Y.; Laudadio, G., The Fundamentals Behind the Use of Flow Reactors in Electrochemistry. *Acc. Chem. Res.* **2019**, *52*, 2858-2869.
29. Moore, J. S.; Jensen, K. F., “Batch” Kinetics in Flow: Online IR Analysis and Continuous Control. *Angew. Chem. Int. Ed.* **2014**, *53*, 470-473.

Supplementary Information

Chemicals and methods

Chemicals. For flow *N*-carboxyanhydride (NCA) synthesis, all reagents were purchased from Sigma Aldrich and used without further purification. For NCA surface initiated polymerization (SIP), all reagents were also purchased from Sigma Aldrich and used without further purification unless otherwise noted. Tetrahydrofuran (THF) was of anhydrous grade ($\geq 99.9\%$, inhibitor free), and was further dried over molecular sieves overnight prior to use. Molecular sieves were dried at 200 °C overnight prior to use. Sarcosine-NCA was synthesized from sarcosine according to prior literature,¹ and was sublimed twice prior to use. The synthesis of formally Fe(I) bisiminopyridine catalyst, its anchoring to TiO₂ coated fluorine doped tin oxide (FTO), and batch mechanistic experiments have been reported elsewhere.²

Continuous flow systems. For both flow NCA synthesis and SIP, single piston pumps (Teledyne ISCO Reaxus M1 Class, 0.1 - 10 mL min⁻¹, 2500 psi) were employed to control liquid flow rate. Reactor coil tubing (1/16" OD, 0.020" ID, fluoroethylene polymer), fittings/adapters/check valves, and a back pressure regulator (BPR, 20 psi) were purchased from IDEX - Health & Science.

Characterizations. For NCA synthesis, product quantification was determined by GCMS (Agilent 6890N GC HP-5 column equipped with Agilent 5975 Inert XL Mass Selective Detector) using a naphthalene internal standard. The temperature profile method for the GC was as follows: 80 °C for 1 minute, then 25 °C min⁻¹ until 140 °C, 30 °C min⁻¹ until 190 °C, 40 °C min⁻¹ until 270 °C, hold for 3 minutes, followed by 40 °C min⁻¹ until 300 °C, hold for 5 minutes.

For NCA polymerization, conversion of sarcosine-NCA was assessed by ¹H-NMR spectroscopy using 1,3,5-trimethoxybenzene as an internal standard.

Continuous flow NCA synthesis

A variety of flow system configurations were explored with either two or three pumps to separate and flow reagents together (Figures S5.1). In a typical flow NCA experiment, pump solutions consisted of 0.3 mmol *N*-benzylanthranillic acid (68.2 mg) and 1 equiv of methyl propiolate (27 μ L) in 5 mL *N*-methylpyrrolidone (NMP) for one pump, then 0.5 mol% Ru (dichloro[(2,6,10-dodecatriene)-1,12-diyl]ruthenium, 5 mg) and 0.5 equiv dimethylaminopyridine (DMAP, 18.3 mg) in 5 mL NMP for the other pump in media bottles with 1/4"-28 ports (GL25 - 45, Cole Parmer). Pump solutions were purged with CO₂ for 1 min per mL of solution, then all ports on the media bottle cap were sealed, except for CO₂ inlet and outlet tubing to the pump connections, allowing the solution to pressurize up to 2 bar CO₂. Solutions were then pumped at the desired flow rate into a reactor coil submerged in an H₂O bath. Fractions of product were collected at the outlet of the reactor coil every 2 - 5 mins and analyzed by GCMS to determine how many residence times (t_r) must pass for the yield to plateau. The pumps were flushed with copious acetone until the solution coming from the outlet of the flow system was clear.

Design of Experiment was carried out using JMP SAS. The results from a Custom Design DoE model using flow rate, alkyne equivalents, and temperature are displayed in Table S5.1.

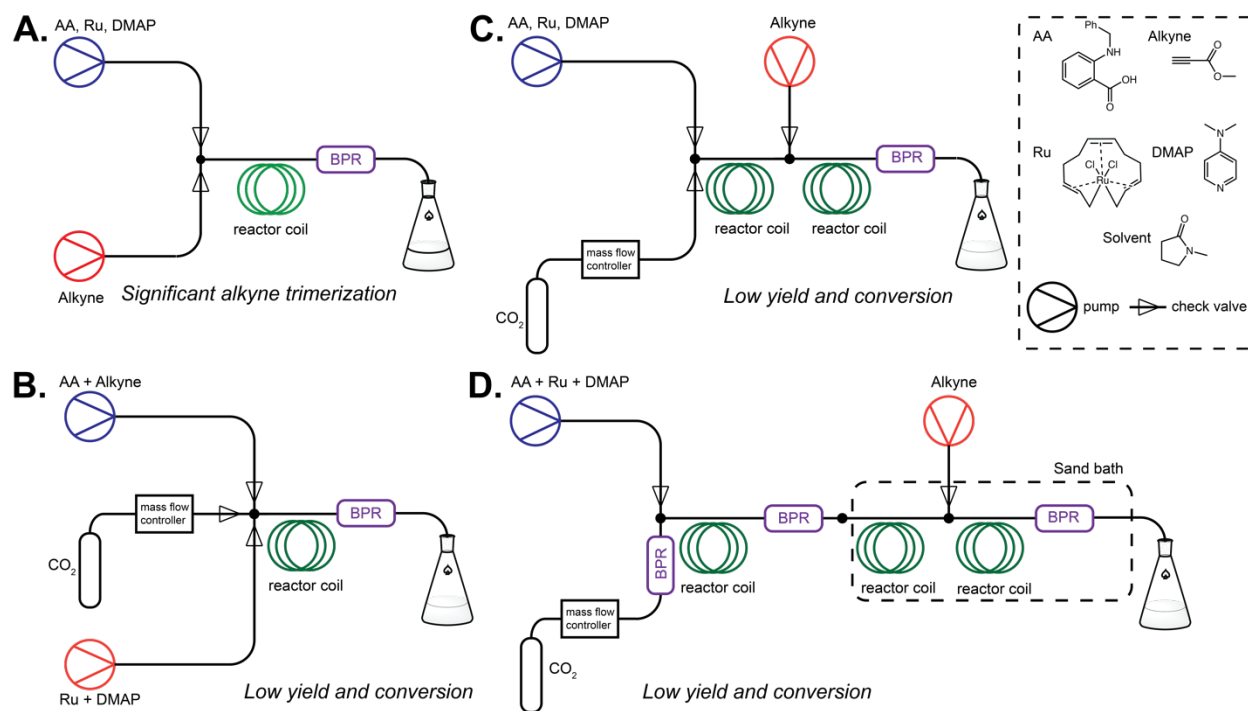
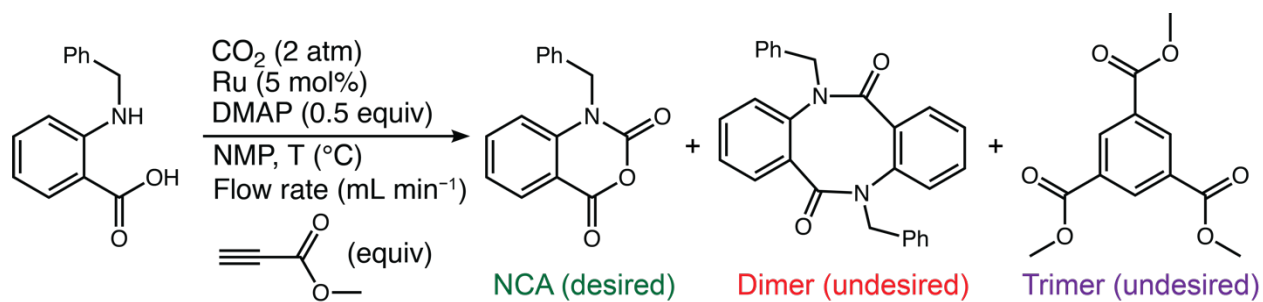


Figure S5.1. Alternate flow system configurations explored for flow *N*-benzylisatoic anhydride (model *N*-carboxyanhydride, NCA) synthesis. The configuration in panel **A** led to significant alkyne trimerization. Configurations in panels **B** - **D** resulted in poor yield and conversion, likely due to challenges in CO₂ within flow reaction time scales. AA - amino acid analogue, *N*-benzylanthranilic acid, Ru - dichloro[(2,6,10-dodecatriene)-1,12-diyl]ruthenium, DMAP - dimethylaminopyridine, alkyne - methyl propiolate, NMP - *N*-methylpyrrolidone, BPR - back pressure regulator.



Entry	Flow rate (mL min ⁻¹)	Alkyne equiv	Temperature (°C)	NCA yield (%)	Dimer yield (%)	Alkyne trimer yield (%)
1	1	1	30	0.65	0.5	0
2	0.1	1	30	5	0	0.5
3	1	4	30	0.6	0	0.2
4	0.1	4	30	8.5	0.4	3
5	1	1	80	7	1.2	0.8
6	0.1	1	80	20	5.3	30
7	1	4	80	21	1	11
8	0.1	4	80	30	3.5	57
9	0.5	2.5	55	17	0.6	4
10	0.25	1	40	30	1	2

Table S5.1. Conditions and yields for flow NCA synthesis of *N*-benzylisatoic anhydride from a Custom Design DoE model. Ru - dichloro[(2,6,10-dodecatriene)-1,12-diyl]ruthenium, DMAP - dimethylaminopyridine, NMP - *N*-methylpyrrolidone.

Continuous flow NCA SIP

Flow *N*-carboxyanhydride (NCA) surface-initiated polymerization (SIP) by a surface bound formally Fe(I) catalyst was carried out in a custom flow cell. Plates for a custom parallel plate flow reactor were designed using SolidWorks, and machined out of PEEK (polyether ether ketone) from Protolabs. A schematic of the flow cell assembly encompassing top and bottom plates to sandwich fluorine doped tin oxide (FTO) on glass plates coated with the Fe(I) catalyst bound to a TiO₂ layer (abbreviated as Fe(I)/TiO₂/FTO) is displayed in Figure 5.3B. A picture of the assembled parallel plate flow cell is displayed in Figure S5.2. To achieve a good seal when the PEEK plates are compressed over the Fe(I)/TiO₂/FTO plates, two EPDM (ethylene propylene diene monomer) gaskets were placed in between Fe(I)/TiO₂/FTO plates. NCA solutions were flowed into the flow channel by simply sandwiching 1/16" tubing in between the two gaskets.

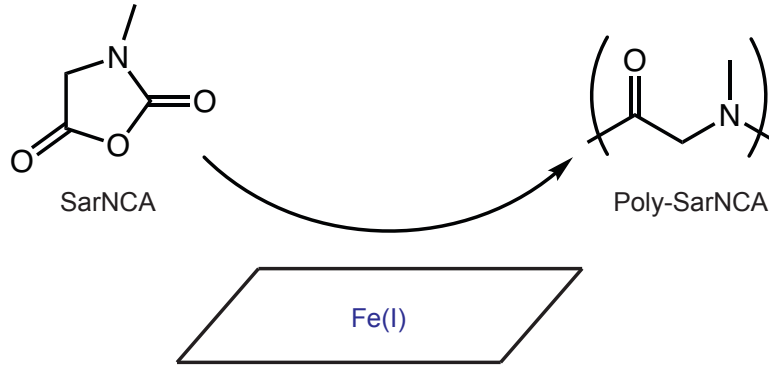
All flow NCA SIP experiments were carried out in an Ar glovebox. In a typical experiment, 50 mg of sarcosine-NCA, 15 mg of 1,3,5-trimethoxybenzene (internal standard), and 5 mg of [CoCp₂][BAR^F₄] (cobaltocenium tetrakis[3,5-bis(trifluoromethyl)phenyl]borate) were dissolved in 5 mL of tetrahydrofuran (THF). Solutions were then flowed into a custom parallel plate flow reactor at the desired flow rate. The bottom plate of the flow cell consisted of an Fe(I)/TiO₂/FTO plate, while the top plate was kept as just a bare FTO plate for optical transparency. Fractions of product were collected at the outlet of the flow reactor in time intervals equivalent to the residence time (t_r) and analyzed by NMR to determine how many residence times (t_r) must pass for the yield to plateau. Fractions were taken out of the glovebox, THF was removed using a rotary evaporator, and the resultant solid was re-dissolved in CDCl₃ for ¹H-NMR analysis.

Cleavage of surface grown polymers was carried out by soaking plates post flow NCA SIP with MeI for up to 72 hours, then dried by rotary evaporator. The presence of polymer was first checked

by $^1\text{H-NMR}$. Unfortunately, no polymer was detected, likely due to a multitude of reasons (vide supra).

Derivation of expressions for apparent rate constants for batch and flow NCA SIP k_b and k_f

Batch (b)



$$r_{poly} = k_b [NCA] \quad (1)$$

$$\frac{dV[NCA]}{dt} = -SA * k_b [NCA] \quad (2)$$

$$[NCA]_t = [NCA]_{t=0} \exp \left[-\frac{SA}{V} k_b t \right] \quad (3)$$

$$Conversion = \frac{[NCA]_0 - [NCA]_t}{[NCA]_0} = 1 - \frac{[NCA]_t}{[NCA]_0} \quad (4)$$

From eq 3:

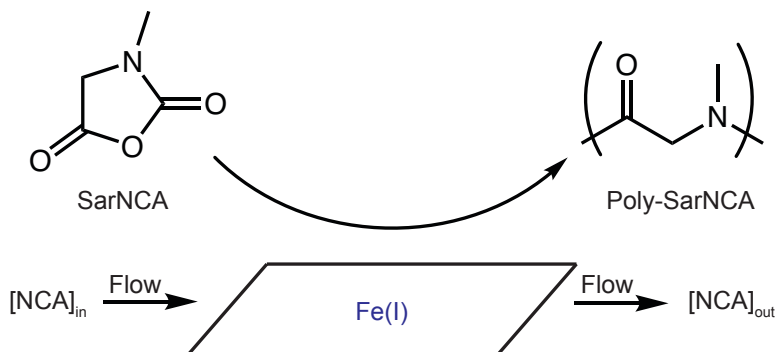
$$\frac{[NCA]_t}{[NCA]_0} = \exp \left[-\frac{SA}{V} k_b t \right] \quad (5)$$

$$\ln \left(\frac{[NCA]_t}{[NCA]_0} \right) = -\frac{SA}{V} k_b t \quad (6)$$

Incorporating eq 4 into eq 6:

$$k_b = \frac{\ln(-\text{Conversion} + 1) V}{-SA * t} \quad (7)$$

Flow (f)



At steady state, $[NCA]_{out}$ is a constant. At low conversions, amount of NCA consumed (right hand side of eq 8) is approximately equal to the amount replenished under flow (left hand side of eq 8).

$$([NCA]_{in} - [NCA]_{out})\Delta t * Q = SA * k_f \left(\frac{[NCA]_{in} - [NCA]_{out}}{2} \right) \Delta t \quad (8)$$

$$\left(1 - \frac{[NCA]_{out}}{[NCA]_{in}} \right) Q = SA * k_f * \frac{1}{2} \left(1 + \frac{[NCA]_{out}}{[NCA]_{in}} \right) \quad (9)$$

Analogous to eq 4, conversion is defined in flow as:

$$\text{Conversion} = 1 - \frac{[NCA]_{out}}{[NCA]_{in}} \quad (10)$$

To replace all concentration terms with conversion, the parenthetical term on the right hand side of eq 9 is re-written as:

$$1 + \frac{[NCA]_{out}}{[NCA]_{in}} = -\text{Conversion} + 2 \quad (11)$$

Inputting eq 10 and 11 into eq 9, the following expression is obtained:

$$k_f = \frac{2 * Conversion * Q}{SA(-Conversion + 2)} \quad (12)$$

Glossary of terms

r_{poly} – rate of polymerization

k_b – apparent rate constant in batch

k_f – apparent rate constant in flow

Both k values are heterogeneous rate constants cm s^{-1}

V – volume of NCA solution

SA – surface area of Fe(I)/TiO₂ section of FTO/glass slides

t – time

Q – flow rate (mL min^{-1})

Supplementary references

1. Klinker, K.; Schäfer, O.; Huesmann, D.; Bauer, T.; Capelôa, L.; Braun, L.; Stergiou, N.; Schinnerer, M.; Dirisala, A.; Miyata, K., Secondary-Structure-Driven Self-Assembly of Reactive Polypept(o)ides: Controlling Size, Shape, and Function of Core Cross-Linked Nanostructures. *Angew. Chem. Int. Ed.* **2017**, *56*, 9608-9613.
2. Xiao, K. Developing a Surface-initiated Polymerization System from a Redox-switchable Catalyst for Polyamide Synthesis. Boston College. Graduate School of Arts and Sciences, 2022.

Chapter 6. Concluding remarks

The research presented in this dissertation outlines work completed during my graduate career in employing various forms of spatial control and tailored mass transport in catalysis to construct multi-step, multi-catalyst processes. The major goal of this work was to generate and utilize intermediates along a reaction pathway in one pass, thereby obviating time and resource wasteful work ups, and to avoid challenges in multi-step processes with hazardous and/or ephemeral intermediates. We demonstrated that altering mass transport by spatially localizing but separating reagents for various processes, two tandem reactions can be carried out to transform feedstocks to commodity chemicals in one pass, instead of traditional iterative synthesis. Much of this work is inspired by biology's approach to executing efficient complex reaction pathways by compartmentalization, wherein key enzymes, co-factors, substrates, and intermediates are co-localized to augment reaction efficiency and prevent unwanted side reactions. We built off of this phenomenon to first study the effect of compartmentalization on organometallic catalysis as a model, simple multi-step process. From this work, we compartmentalized electrochemical CO₂ reduction to feed into co-polymerization with ethylene to polyketones, and to hydroformylation, re-purposing typically undesired H₂ generation. In a similar light, we also employed continuous flow processing to separate but connect *N*-carboxyanhydride (NCA) synthesis from amino acids and polymerization to polypeptide materials. Though this work was halted early due to time constraints, progress towards marrying the two processes was made by optimizing each in a flow setting. From a big picture perspective, the work presented in my dissertation serves to demonstrate the benefits of instituting some form of spatial control in constructing multi-step, multi-catalyst processes.

There lies a myriad of avenues that all of these projects could adventure through in the future. For the work presented on developing a model for compartmentalization, the extracted design principle of tailoring a compartment's geometry to yield mass transport that's slower than a multi-step process' kinetics remains to be further applied experimentally. Though we adapted the model to analyze previously established confined organometallics, it would greatly improve the broader impact of such a design principle if a systematic exploration of compartmentalized organometallics is carried out using the design principle as a starting point for experimental design. Additionally, we modeled a catalytic system wherein both the catalyst species and substrate/product were freely diffusing, and analyzed catalyst mass transport as limiting assuming the substrate/product diffuse far easier than the catalyst. However, numerous confined organometallic systems involve a catalyst immobilized within a confinement (e.g., a mesoporous material's pores), which generates a system where substrate/product transport play a much more significant role. It would be interesting to see how the conclusions of a model where compartmentalized organometallic catalysis has a fixed catalyst.

Keeping mass transport in mind for spatially controlled multi-step and/or multi-catalyst processes, a limiting factor in the work integrating electrochemical CO₂ reduction (CO₂RR) to organometallic catalysis likely suffered from intermediate CO and H₂ transport from one compartment medium to another. One approach to circumventing this would be to immobilize the organometallic catalyst employed for the second reaction onto a surface which may then be submerged in the same reaction medium as CO₂RR. Though progress towards this effort was made for a Rh catalyst used for hydroformylation, we encountered loss of activity when the catalyst was immobilized onto silica coated onto an electrode surface, even when the electrode containing the catalyst was not used for electrolysis. There exists a wealth of research in immobilizing transition metal catalysts onto

materials and supports, thus this avenue would be feasible. Further, this would allow the studying of inter-catalyst distance on observed overall reactivity, a phenomenon often implicated in biology for efficient multi-enzyme cascades.

For our work in flow NCA synthesis and polymerization, a major next step would be on flow system re-design to improve overall conversion based on fundamental understandings of the reaction mechanisms. In NCA synthesis, a limiting factor was the operable maximum CO₂ pressure, which was capped at 2 bar. To reach higher pressures, gas permeable tubing should be used to directly pressure the outer tubing from a gas cylinder to higher pressures and relying on the permeable nature of the inner tubing for gas diffusion and dissolution. In NCA surface-initiated polymerization, the challenges experienced pertained to polymer detection. Assuming the origin was incomplete cleavage, reaching higher conversions in flow could help facilitate obtaining more material to characterize. More broadly, once limitations in each step are overcome, integrating the two processes together to take amino acids and CO₂ to polypeptide materials using flow chemistry would be the next avenue.